Journal of Mechanics of Materials and Structures

Volume 1, Nº 3

March 2006

mathematical sciences publishers

JOURNAL OF MECHANICS OF MATERIALS AND STRUCTURES

http://www.jomms.org

mathematical sciences publishers

JOURNAL OF MECHANICS OF MATERIALS AND STRUCTURES
Vol. 1, No. 3, 2006

AN OFF-RESONANCE SYNCHRONOUS VIBRATION BASED METHOD FOR ROTOR SYSTEM DAMAGE DETECTION

HUAGENG LUO, HECTOR RODRIGUEZ AND DARREN HALLMAN

This paper presents a methodology for detecting rotor imbalances, such as mass imbalance and crack-induced imbalance, using shaft synchronous vibrations. A vibration detection algorithm is derived based on the first order synchronous vibration response. A detection system was integrated by using state-of-the-art commercial analysis equipment. A laboratory rotor test rig with controlled mass imbalances was used to verify the integrated system. The system was then deployed to an engine subassembly test setup. Four specimens were used in the subassembly test and the test results are reported in the final section.

1. Introduction

1.1. ***Mass imbalance in rotors.*** The physics of the mass imbalance induced vibration response in rotors can be explained using a simplified shaft-disk assembly. As shown in Figure 1, a simple Jeffcott rotor is represented by a spring-mass system restricted to vibrations along the vertical y-axis. In this model, the disk is represented by its mass m, and the stiffness of the shaft is represented by k_s. This simplified representation of a rotor is typically used to model the response of single-disk rotor assemblies under relatively rigid bearings (for example, ball bearings) at relatively low speeds (that is, near or below the first bending critical speed). The response at a sensor with respect to a reference, such as a synchrophaser or a tachometer, can be represented by the response from a single-degree-of-freedom system. The amplitude of a displacement sensor response Y, at the center of the disk due to mass imbalance, is given as [Thomson and Dahleh 1998]

$$Y(j\omega) = \frac{U_m \omega^2}{m(\omega_0^2 - \omega^2 + 2j\xi_0\omega_0\omega)}, \tag{1}$$

where

Y is the Laplace transform of time response $y(t)$. $Y(j\omega) = L[y(t)]\big|_{s=j\omega}$;

j is the complex symbol, $j = \sqrt{-1}$;

Keywords: off-resonance, synchronous vibration, damage detection, rotor system, mass imbalance, crack induced imbalance.

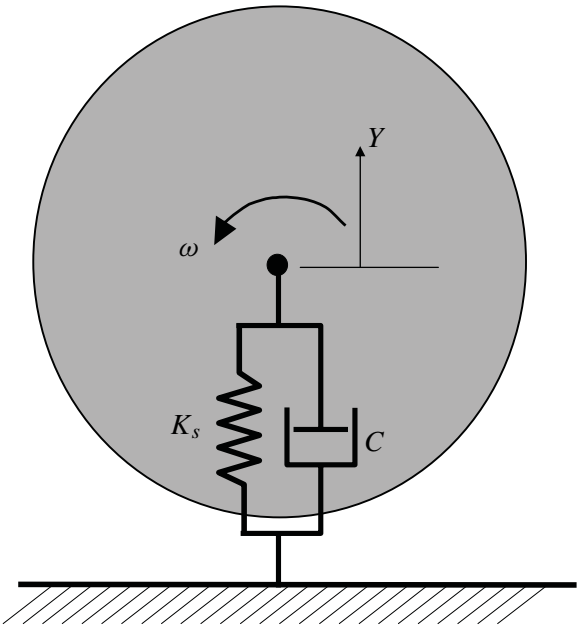

Figure 1. Jeffcott model of rotor assembly.

m is the mass of the system;

U_m is the mass imbalance in frequency domain;

$\omega_0 = \sqrt{k_s/m}$ is the natural frequency of the system;

$\xi_0 = c/2\omega_0 m$ is the damping ratio of the system.

Equation (1) shows that at speeds below the critical speed (that is, $\omega/\omega_0 \ll 1.0$), the vibration response due to mass imbalance is proportional to ω^2.

1.2. ***Crack-induced imbalance.*** Cracks in rotor disks have been identified as the cause of a distinct behavior in the vibration response of rotor assemblies [Imam and DeLorenzi 1988; Sonnichsen 2000]. Radial-axial cracks induce a unique vibration response as they open due to tensile hoop stresses caused by centrifugal loading. The crack, which opens as a function of the square of the rotor speed, forces a redistribution of the disk mass. This redistribution results in an additional imbalance that is also proportional to the square of the speed, and hence the resulting crack-induced imbalance force is proportional to the fourth power of the shaft speed. This unique imbalance force characteristic contrasts with the force due to standard mass imbalance, which is related to the square of the shaft speed.

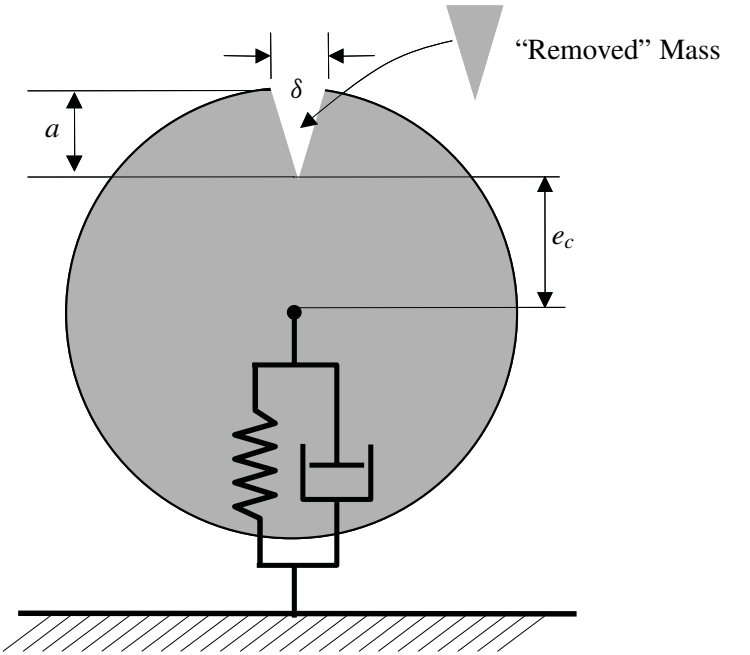

Figure 2. Jeffcott rotor showing "removed" mass concept.

In the case of a radial-axial crack with length a in a disk rotating at speed ω, the induced imbalance can be expressed as

$$U_c(a, \omega) = m_c(a, \omega)e_c, \tag{2}$$

where the effective change in mass distribution due to the crack opening $m_c(a, \omega)$ is a function of the crack size and speed, and e_c is the effective radius of rotation of $m_c(a, \omega)$. The hoop stress in a rotating disk is a function of the square of the shaft speed ω. Therefore, the effective change in mass distribution due to the crack opening is also a function of the square of the shaft speed. The response of a Jeffcott type rotor with a radial-axial crack can be obtained after substituting $U_c(a, \omega)$ for U_m in Equation (1). Due to the dependence of $U_c(a, \omega)$ on ω^2, the resulting displacement response in the low-speed regime (that is, below the critical speed) will be proportional to the fourth power of the speed.

An approximate expression for Equation (2) can be obtained if the effective change in mass distribution due to the crack opening is represented as a "removed" mass while e_c is the radial distance to the crack tip as shown in Figure 2. In the case of a radial-axial crack, the removed mass is proportional to the opening of the crack δ as a function of speed. The opening of a small crack in a large-diameter disk can be approximated using the analogy of an edge crack in a plate strip, for

which a closed-form solution exists. The opening of the crack due to tensile hoop stress level in the neighborhood of the crack is given as [Tada et al. 1985]

$$\delta = \frac{4\sigma_h a}{E} V\left(\frac{a}{D}\right), \tag{3}$$

where the empirical function $V(\frac{a}{D})$ is given as [Tada et al. 1985]

$$V\left(\frac{a}{D}\right) = \frac{1.46 + 3.42 \times \left(1 - \cos(\frac{\pi a}{2D})\right)}{\left(\cos(\frac{\pi a}{2D})\right)^2}, \tag{4}$$

where the disk diameter is used instead of the plates width, as considered in the reference. As we see in Equation (4), $V(\frac{a}{D})$ approaches the constant value of 1.46 for small ratios of $\frac{a}{D}$.

The hoop stress in a constant thickness disk at a distance e_c is given as [NASA 1975]

$$\sigma_h = \frac{\rho D^2 \omega^2 (3+\mu)}{32g}\left(1 - \frac{(1+3\mu)}{3+\mu} \times \left(\frac{2e_c}{D}\right)^2\right), \tag{5}$$

where g is the gravity constant. Finally, the removed mass can be approximated as

$$m_c = \frac{\delta a t \rho}{2g}. \tag{6}$$

Therefore, the crack-induced imbalance is given as [Rodriguez et al. 2001]

$$U_c = K\rho^2 a^2 t D^2 \omega^2 e_c = K_C \omega^2, \tag{7}$$

where

$$K_C = \frac{(3+\mu)}{16g^2 E}\left[1 - \frac{(1+3\mu)}{3+\mu} \times \left(\frac{2e_c}{D}\right)^2\right] V\left(\frac{a}{D}\right) \rho^2 a^2 t D^2 e_c. \tag{8}$$

In the case of values of $\frac{a}{D}$ less than 0.05, Equation (8) becomes $K_C \sim 0.5/E$.

Equation (7) clearly establishes the dependence of the crack-induced imbalance on the physical parameters of the disk and the rotational speed. As shown in the equation, the crack-induced imbalance is proportional to the second power of the speed, the weight density, the crack length, and the disk diameter, respectively. In addition, for the case of relatively small cracks, e_c approximates $D/2$, introducing a stronger dependence of the imbalance on the disk diameter. Refer to references [Butz and Rodriguez 1999] and [Rodriguez et al. 2001] for more numerical simulations and analyses.

1.3. ***Multi-DOF modeling.*** It has been well established that the mass-induced synchronous vibration is proportional to the square of the rotational speed, that is, ω^2, in the region where $\omega \ll \omega_0$, where ω_0 is the first resonant frequency of the machinery system. The radial-axial cracks in the rotating disk or shaft can cause

a synchronous vibration that is proportional to ω^4, under the same assumption of $\omega \ll \omega_0$. Several groups have developed detection systems based on these assumptions [Imam and DeLorenzi 1988; Sonnichsen 2000]. However, in reality, there are several major difficulties in implementing the traditional algorithms:

(i) It is difficult to satisfy the $\omega \ll \omega_0$ condition without significantly reducing the signal to noise ratio, because the first natural frequency in many rotational machinery systems is usually low. Especially in soft-mounted rotor systems, where the first natural frequency can be so low that it prevents such monitoring systems from getting meaningful results.

(ii) It is difficult to simplify real rotor machinery into a single degree of freedom (SDOF) system. On top of the bearing DOFs, the vibration sensors are usually mounted on the bearing case or engine case, so that additional structural resonances, besides rotor-shaft resonances, may be picked up, thus destroying the polynomial relationship established for low frequency region.

(iii) The operational frequency range is not always below first resonance frequency of the rotor machinery system.

In the next section, a nonresonant synchronous vibration based detection algorithm is developed for any operational speed region between two consecutive natural frequencies of a machinery system. The development is based on multi-degree of freedom (MDOF) rotor machinery assumptions.

2. Nonresonant synchronous vibration based approach

In the simplest possible model for rotor vibration analysis, the system is described by a spring-mass-damper single-degree-of-freedom (SDOF) system as shown in Figure 1. If there are both mass and crack-induced imbalances, by combining Equation (1) and (7), we have

$$Y(j\omega) = \frac{U_m \omega^2}{m(\omega_0^2 - \omega^2 + 2j\xi_0\,\omega_0\,\omega)} + \frac{K_C \omega^4}{m(\omega_0^2 - \omega^2 + 2j\xi_0\,\omega_0\,\omega)}. \tag{9}$$

In the region where $\omega \ll \omega_0$, Equation (9) can be simplified as

$$Y(j\omega) = \frac{U_m \omega^2}{m\omega_0^2} + \frac{K_C \omega^4}{m\omega_0^2} = C_2\omega^2 + C_3\omega^4, \tag{10}$$

where

$$C_2 = \frac{U_m}{m\omega_0^2} \quad \text{and} \quad C_3 = \frac{K_C}{m\omega_0^2} \tag{11}$$

are the imbalance and system parameter related complex constants.

In many cases, the rotor system response has to be modified into a multi-degree-of-freedom (MDOF) system, assuming the system has distinct natural frequencies for simplicity, as

$$Y(j\omega) = \sum_{i=1}^{\infty} \frac{U_{mi}\omega^2}{m_i(\omega_i^2 - \omega^2 + 2j\xi_i\omega_i\omega)} + \sum_{i=1}^{\infty} \frac{K_{C_i}\omega^4}{m_i(\omega_i^2 - \omega^2 + 2j\xi_i\omega_i\omega)}, \tag{12}$$

where U_{mi} is the i-th modal response coefficient due to mass imbalance; K_{C_i} is the i-th modal response coefficient due to the crack induced imbalace; m_i is the i-th modal mass; ξ_i is the i-th modal damping ratio, and

$$\omega_1 < \omega_2 < \cdots < \omega_{k-1} < \omega_k < \cdots \tag{13}$$

are natural frequencies of the machinery system.

In the frequency region of $\omega_{k-1} < \omega < \omega_k$, the variables

$$\frac{\omega_i}{\omega}, \quad i = 1, 2, \ldots, k-1 \quad \text{and} \quad \frac{\omega}{\omega_i}, \quad i = k, k+1, \ldots \tag{14}$$

are less than 1. If these quantities are much less than unity, Equation (12) can be approximated as

$$\begin{aligned} Y(j\omega) = &\sum_{i=1}^{k-1} \frac{U_{mi}\omega^2}{m_i} \frac{1}{\omega^2\left[\left(\frac{\omega_i}{\omega}\right)^2 - 1 + 2j\xi_i\left(\frac{\omega_i}{\omega}\right)\right]} + \sum_{i=k}^{\infty} \frac{U_{mi}\omega^2}{m_i} \frac{1}{\omega_i^2\left[1 - \left(\frac{\omega}{\omega_i}\right)^2 + 2j\xi_i\left(\frac{\omega}{\omega_i}\right)\right]} \\ &+ \sum_{i=1}^{k-1} \frac{K_{C_i}\omega^4}{m_i} \frac{1}{\omega^2\left[\left(\frac{\omega_i}{\omega}\right)^2 - 1 + 2j\xi_i\left(\frac{\omega_i}{\omega}\right)\right]} + \sum_{i=k}^{\infty} \frac{K_{C_i}\omega^4}{m_i} \frac{1}{\omega_i^2\left[1 - \left(\frac{\omega}{\omega_i}\right)^2 + 2j\xi_i\left(\frac{\omega}{\omega_i}\right)\right]}. \end{aligned} \tag{15}$$

Using the Taylor series expansion and retaining up to the second order of small terms, we have

$$\begin{aligned} Y(j\omega) = &\sum_{i=1}^{k-1} -\frac{U_{mi}}{m_i}\left[1 + 2j\xi_i\left(\frac{\omega_i}{\omega}\right) + (1 - 4\xi_i^2)\left(\frac{\omega_i}{\omega}\right)^2 + O\left(\frac{\omega_i}{\omega}\right)^3\right] \\ &+ \sum_{i=k}^{\infty} \frac{U_{mi}}{m_i}\left[\left(\frac{\omega}{\omega_i}\right)^2 + O\left(\frac{\omega}{\omega_i}\right)^3\right] \\ &+ \sum_{i=1}^{k-1} -\frac{K_{C_i}\omega^2}{m_i}\left[1 + 2j\xi_i\left(\frac{\omega_i}{\omega}\right) + (1 - 4\xi_i^2)\left(\frac{\omega_i}{\omega}\right)^2 + O\left(\frac{\omega_i}{\omega}\right)^3\right] \\ &+ \sum_{i=k}^{\infty} \frac{K_{C_i}\omega^2}{m_i}\left[\left(\frac{\omega}{\omega_i}\right)^2 + O\left(\frac{\omega}{\omega_i}\right)^3\right]. \end{aligned} \tag{16}$$

2.1. ***Zero order approximation.*** By omitting the first and higher orders of small terms in Equation (16), we get a zero order approximation as

$$Y(j\omega) = -\sum_{i=1}^{k-1} \frac{U_{mi}}{m_i} - \sum_{i=1}^{k-1} \frac{K_{C_i}\omega^2}{m_i}. \tag{17}$$

In the case of $k = 2$, which means the operation speed range is between the first and second resonant frequencies, Equation (17) is further simplified as

$$Y(j\omega) = -\frac{U_{m1}}{m_1} - \frac{K_{C1}\omega^2}{m_1}. \tag{18}$$

Keep in mind that in Equation (18), U_{m1} and K_{C1} are complex variables. Their amplitudes reflect the imbalance amounts while the phases reflect the circumferential locations. The negative signs in Equation (18) reflect the 180° phase shift after the first resonance.

2.2. ***First order approximation.*** By omitting the second and higher orders of small terms in Equation (16), we get a first order approximation as

$$Y(j\omega) = \sum_{i=1}^{k-1} -\frac{U_{mi}}{m_i}\left[1 + 2j\xi_i\left(\frac{\omega_i}{\omega}\right)\right] + \sum_{i=1}^{k-1} -\frac{K_{C_i}\omega^2}{m_i}\left[1 + 2j\xi_i\left(\frac{\omega_i}{\omega}\right)\right]. \tag{19}$$

In a lightly damped case, ξ_i is small, thus Equation (19) can be further reduced to Equation (17), that is, the zero order case. Therefore, in a lightly damped case, zero order and first order approximations have the same formula.

2.3. ***Higher order approximation.*** Using the Taylor series expansion, any higher-order approximation can be derived. For example, by omitting the third and higher order of small terms, we have the second order approximation:

$$\begin{aligned} Y(j\omega) = &\sum_{i=1}^{k-1} -\frac{U_{mi}}{m_i}\left[1 + 2j\xi_i\left(\frac{\omega_i}{\omega}\right) + (1 - 4\xi_i^2)\left(\frac{\omega_i}{\omega}\right)^2\right] + \sum_{i=k}^{\infty} \frac{U_{mi}}{m_i}\left(\frac{\omega}{\omega_i}\right)^2 \\ &+ \sum_{i=1}^{k-1} -\frac{K_{C_i}\omega^2}{m_i}\left[1 + 2j\xi_i\left(\frac{\omega_i}{\omega}\right) + (1 - 4\xi_i^2)\left(\frac{\omega_i}{\omega}\right)^2\right] + \sum_{i=k}^{\infty} \frac{K_{C_i}\omega^2}{m_i}\left(\frac{\omega}{\omega_i}\right)^2. \end{aligned} \tag{20}$$

In a lightly damped case, Equation (20) can be further reduced to

$$\begin{aligned} Y(j\omega) = &\sum_{i=1}^{k-1} -\frac{U_{mi}}{m_i}\left[1 + 2j\xi_i\left(\frac{\omega_i}{\omega}\right) + \left(\frac{\omega_i}{\omega}\right)^2\right] + \sum_{i=k}^{\infty} \frac{U_{mi}}{m_i}\left(\frac{\omega}{\omega_i}\right)^2 \\ &+ \sum_{i=1}^{k-1} -\frac{K_{C_i}\omega^2}{m_i}\left[1 + 2j\xi_i\left(\frac{\omega_i}{\omega}\right) + \left(\frac{\omega_i}{\omega}\right)^2\right] + \sum_{i=k}^{\infty} \frac{K_{C_i}\omega^2}{m_i}\left(\frac{\omega}{\omega_i}\right)^2. \end{aligned} \tag{21}$$

Rearranging Equation (21), we have

$$\begin{aligned} Y(j\omega) &= -\tfrac{1}{\omega^2}\sum_{i=1}^{k-1}\tfrac{U_{mi}}{m_i}\omega_i^2 - \tfrac{1}{\omega}\sum_{i=1}^{k-1}\tfrac{U_{mi}}{m_i}2j\xi_i\omega_i - \left(\sum_{i=1}^{k-1}\tfrac{U_{mi}}{m_i} + \sum_{i=1}^{k-1}\tfrac{K_{C_i}}{m_i}\omega_i^2\right) \\ &\quad - \omega\sum_{i=1}^{k-1}\tfrac{K_{C_i}}{m_i}2j\xi_i\omega_i + \omega^2\left(\sum_{i=k}^{\infty}\tfrac{U_{mi}}{m_i\omega_i^2} - \sum_{i=1}^{k-1}\tfrac{K_{C_i}}{m_i}\right) + \omega^4\sum_{i=k}^{\infty}\tfrac{K_{C_i}}{m_i\omega_i^2} \\ &= \frac{C_{-2}}{\omega^2} + \frac{C_{-1}}{\omega} + C_0 + C_1\omega + C_2\omega^2 + C_4\omega^4, \end{aligned} \tag{22}$$

where

$$\begin{cases} C_{-2} = -\sum_{i=1}^{k-1}\tfrac{U_{mi}}{m_i}\omega_i^2, \\ C_{-1} = -\sum_{i=1}^{k-1}\tfrac{U_{mi}}{m_i}2j\xi_i\omega_i, \\ C_0 = -\left(\sum_{i=1}^{k-1}\tfrac{U_{mi}}{m_i} + \sum_{i=1}^{k-1}\tfrac{K_{C_i}}{m_i}\omega_i^2\right), \\ C_1 = -\sum_{i=1}^{k-1}\tfrac{K_{C_i}}{m_i}2j\xi_i\omega_i, \\ C_2 = \left(\sum_{i=k}^{\infty}\tfrac{U_{mi}}{m_i\omega_i^2} - \sum_{i=1}^{k-1}\tfrac{K_{C_i}}{m_i}\right), \\ C_4 = \sum_{i=k}^{\infty}\tfrac{K_{C_i}}{m_i\omega_i^2}, \end{cases} \tag{23}$$

are the imbalance and system parameter related complex constants.

3. System integration

The proposed algorithm was integrated into an accelerated engine test system. In the accelerated test, it was designed to simulate an engine cycle, which consists of speed-up, dwell, and coast-down segments simulating aircraft taking-off, cruise, and landing, in a short time. For example, the speed-up process in our accelerated test was only 15 seconds. Thus, it is very important to have a system that can handle data acquisition, pre- and post-processing, and data management in a short time. In addition, the signal from such tests is usually noisy, thus it is also critical to have a processing technique to improve the signal to noise ratio.

After a careful market search, the Pulse system by B&K was selected as the hardware platform, the Production Test Advisor (PTA) by Signalysis, Inc. was selected as the database management system, and a MATLAB-based post-processing system was developed in-house and integrated into the system for real-time health monitoring.

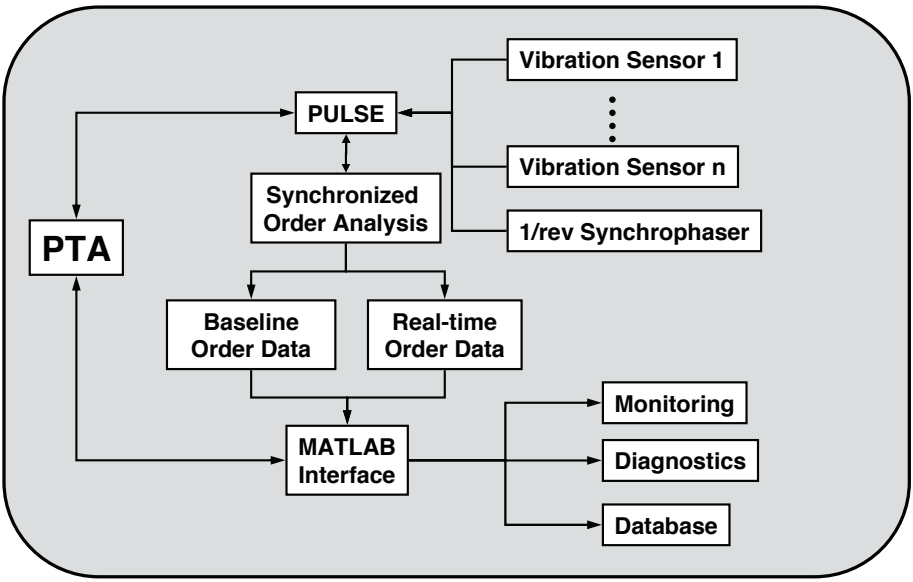

Figure 3. System diagram.

A brief system diagram is shown in Figure 3. In system integration, any vibration sensors, such as accelerometers, velocity sensors, or displacement probes, can be used to pick up vibration signals for the system. Appropriate signal conditioners are needed for the sensors. A once-per-revolution (1/rev) signal from the rotating shaft is also required for order analysis and extraction.

The B&K Pulse system was used as a data acquisition and signal processing system. The Order Analyzer of the Pulse system was activated for our integrations. In order to improve the signal-to-noise ratio, a synchronous averaging technique was also employed.

Data management for the system was carried out by the PTA, which is a special version of SigQC developed by Signalysis Inc. The SigQC was originally designed for manufacturer quality assurance. It is a production line test that responds to the demand among manufacturers to automate a process for accepting or rejecting units on the assembly line based on measured noise and vibration data. The SigQC provides basic statistics, criteria, strategies and pass/fail methods. The major functions of the PTA include Database Management (Database tree) and Production Line Interface (traffic control).

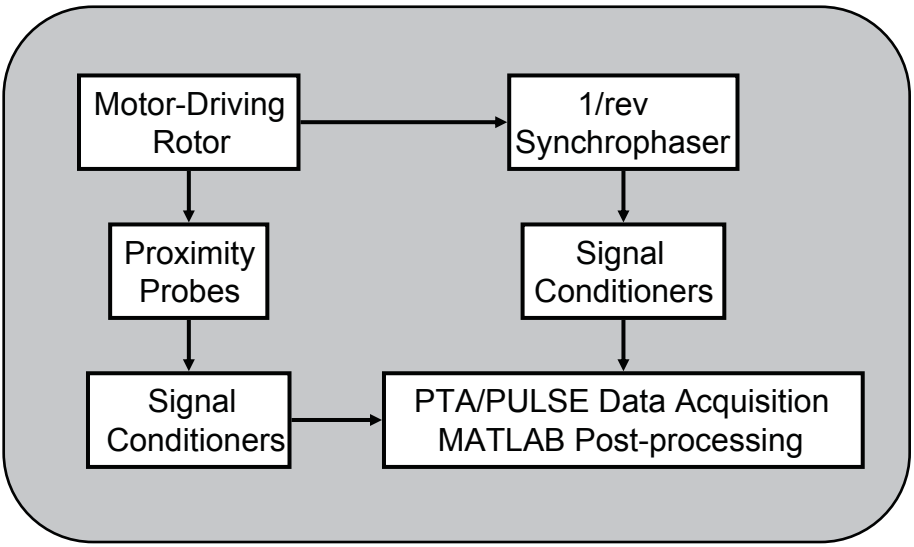

Figure 4. Small rotor rig test diagram.

Though the PTA provides basic statistics, criteria, strategies and pass/fail methods, it is very difficult, if not infeasible, to use these basic functions in constructing a diagnostic algorithm for our crack detection applications. Thus, MATLAB codes for mass and crack imbalance detection functions were developed according to equations in Section 2 for nonresonant synchronous vibrations. The codes were incorporated into the crack detection system by utilizing the interface between PTA and MATLAB.

4. Small rotor test

To verify the crack detection system integration and algorithms, a Bently Nevada RK 4 rotor kit was used as a test bench.

4.1. ***Setup.*** The test rig diagram and instrument setup are shown in Figure 4 and Figure 5, respectively. A single rotor disk with two bearings was used. The rotor disk has a weight of 810 g. The balance slots was located at radius of 30.5 mm with 22.5° resolution in circumference (refer to Figure 6). The rotor shaft has a diameter of 10 mm. The bearing span is 400 mm with additional 200 mm overhang. With such setup, the fundamental frequency of the system is at 2000 rpm. Modal test indicates that the second bending resonance is above 167 Hz, or over 10,000 rpm.

Proximity probes were used as the signal pick-up. Sensor #1 (vib1) is in the vertical direction, while sensor #2 (vib2) is in the horizontal direction. Typical

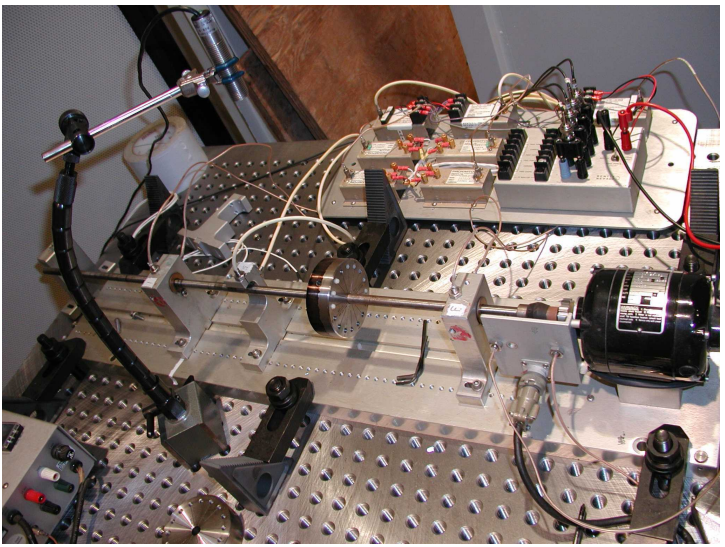

Figure 5. BN RK 4 rotor kit.

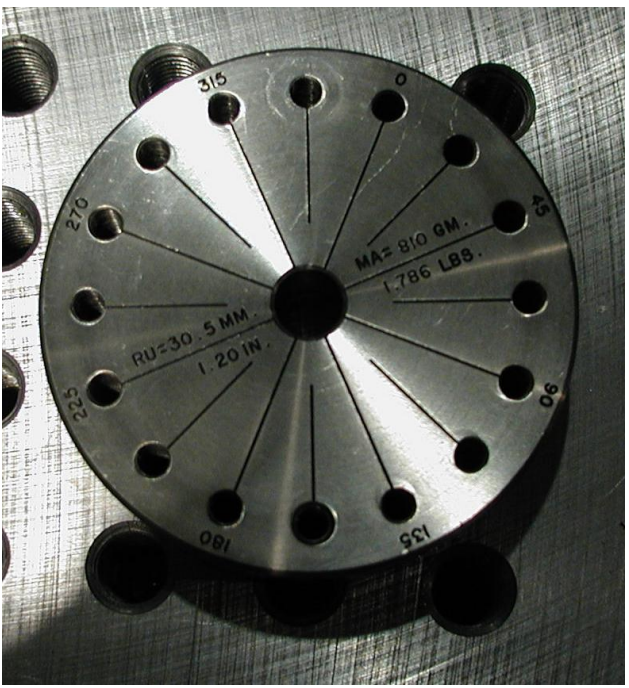

Figure 6. Rotor kit disk with balance slots.

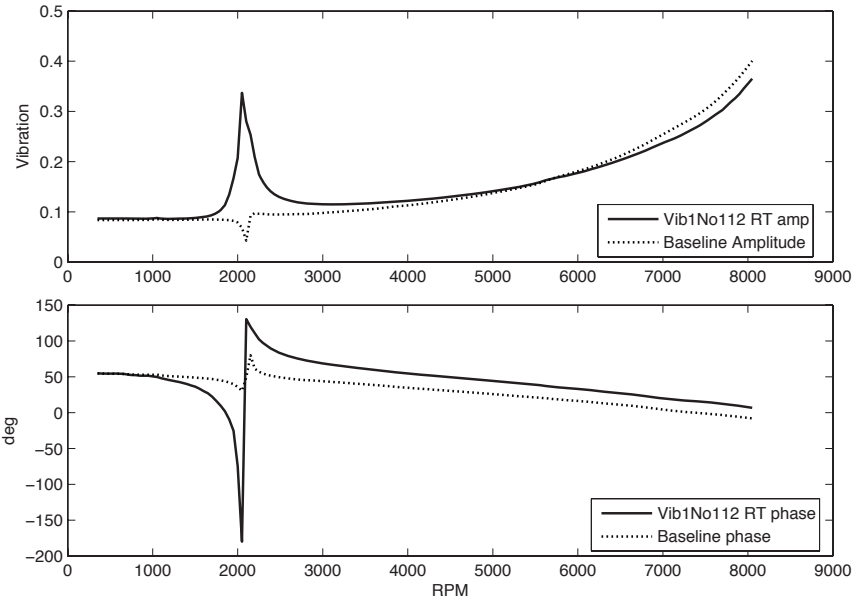

Figure 7. Typical synchronous response, vertical.

synchronous responses of the system are shown in Figure 7 and Figure 8, respectively.

Nylon (instead of steel) set screws were used as imbalance weights to improve the imbalance resolution. As a result, the smallest imbalance unit is 3.416 g-mm.

The disk 0° position was aligned with the center of the notch on the rotor shaft. A mechanical 1/rev signal (shaft notch detected by proximity probe) was used as the trigger. The rising edge of the signal was used as the trigger for data acquisition, which turned out to be the trailing edge of the shaft notch. Later, a laser calibration indicated that the actual triggering point corresponded to approximately the 30° rotor disk circumferential position.

4.2. ***Tests.*** The initial system was balanced first using the influence coefficient method. To verify the system integration and algorithms, imbalances were added at two circumferential positions: nominal 0° and 90° on the rotor disk. The 1/rev signal came from a notch at the shaft near the 0° mark. The actual notch was a filing-off of the shaft, which covered approximately 60° of the shaft circumference. According to the calibration, the nominal 0° and 90° circumferential positions corresponded to approximately 30° and 120° with respect to the 1/rev trigger. At each circumferential location, 4 different imbalance amounts were added: 1, 2, 3,

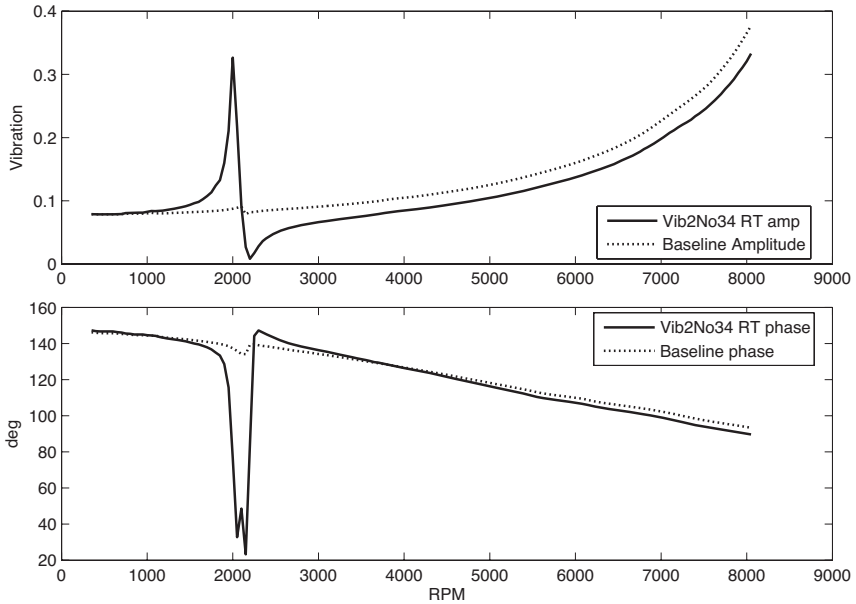

Figure 8. Typical synchronous response, horizontal.

and 4 set screws, which correspond to 3.416, 6.832, 10.248, and 13.664 g-mm imbalances.

The motor speed was controlled between 350 rpm to 8050 rpm, and 25 baseline runs were recorded. For each imbalance case, 5 repeated runs were recorded for further analysis. After that, the tests were repeated for 10 baseline conditions and 5 imbalanced runs for each imbalance case for the purpose of verification.

4.3. ***Data reduction.*** For nonresonant based analysis, the data in the speed range of 4000 to 4500 rpm were used. With this speed range, the variables in Equation (14) satisfy

$$\frac{\omega_1}{\omega} \leq 0.5 \quad \text{and} \quad \frac{\omega}{\omega_2} < 0.5.$$

Equation (19) (the first order approximation) was used in the data processing. Before curve fitting, the baseline response was subtracted from a real-time measurement in the complex domain. The difference was then used in the complex domain curve fitting for extracting the mass imbalance coefficient and the crack-induced imbalance coefficient.

The magnitudes of the typical real time measurement, the baseline, and the difference are shown in Figure 9. As can be seen from the figure, in the difference signal, the "slow roll" effect introduced by the shaft geometric imperfection has been removed after complex domain baseline subtraction. The curve fitting was

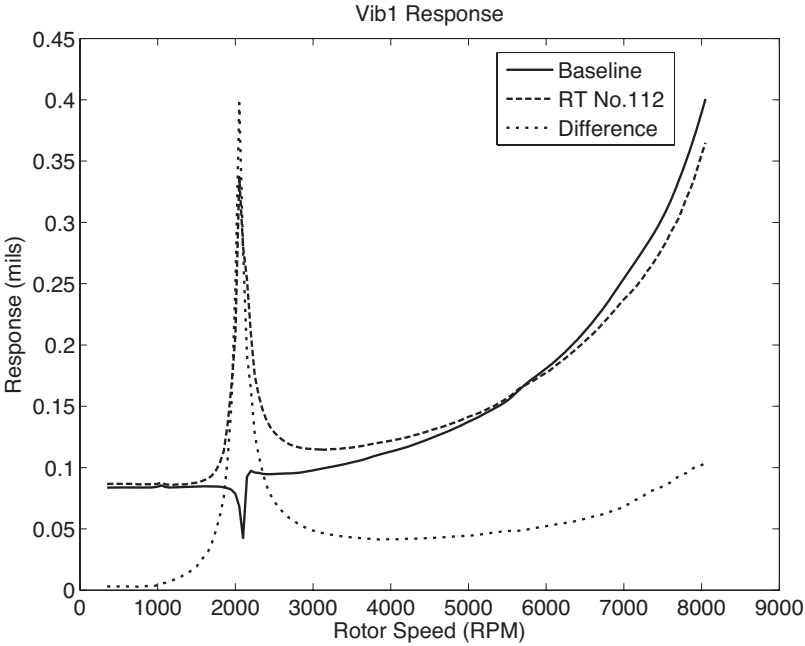

Figure 9. A typical speed-up run.

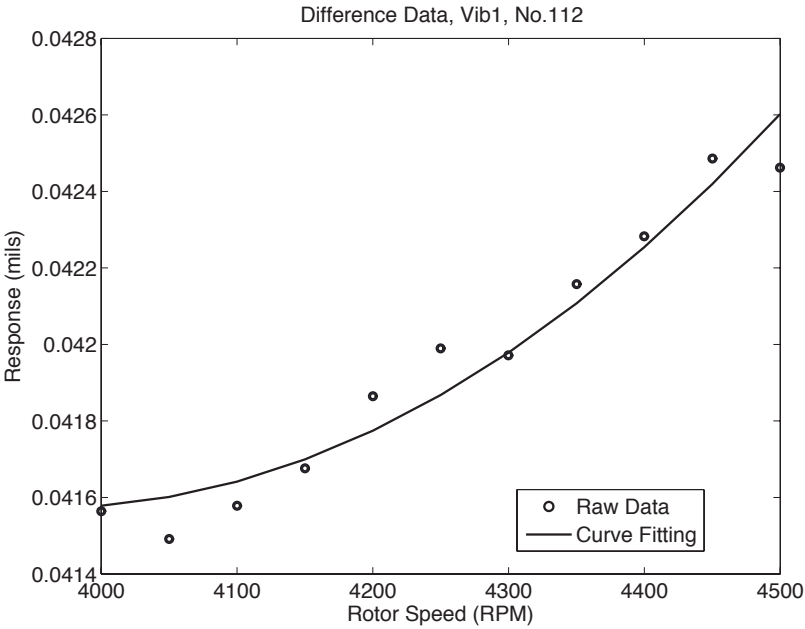

Figure 10. Curve fitting results.

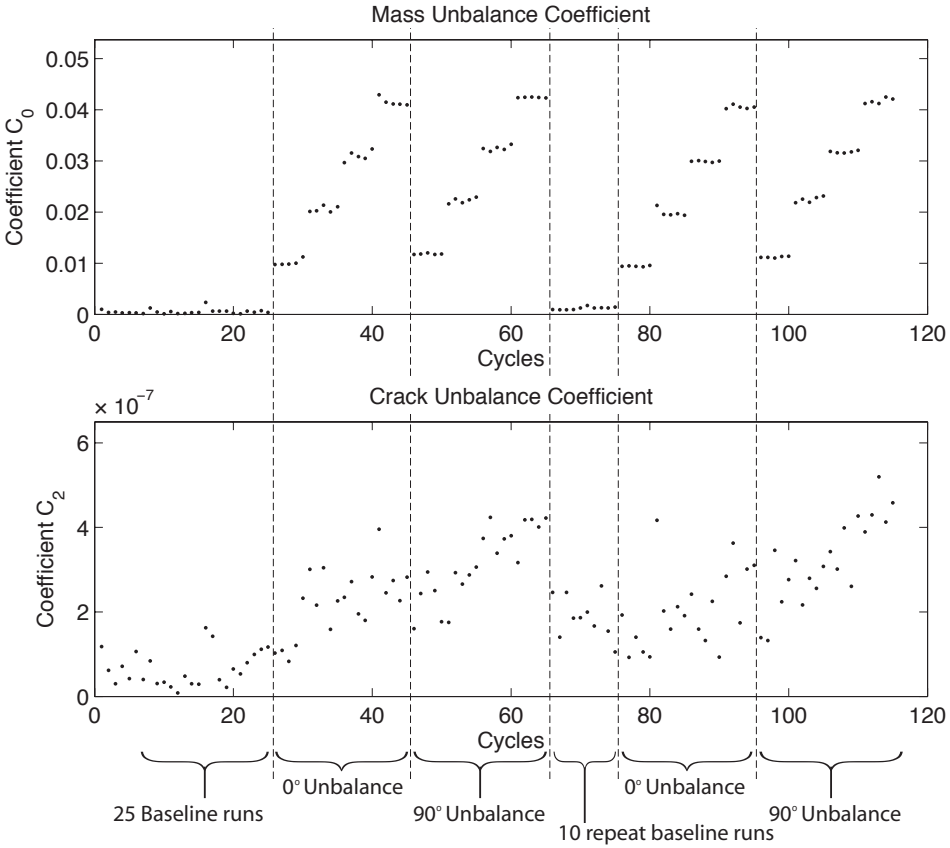

Figure 11. Nonresonance-based analysis, vertical sensor.

carried out in the complex domain with least-square minimization of the difference between the raw data and the fitting curve in the specified RPM range. A typical example of the curve fitting results is shown in Figure 10, where the solid line is the curve fitting results and the dots are the test data.

The result from the vertical sensor is shown in Figure 11, where C_0 is the mass imbalance indicator and C_2 is the crack-induced imbalance indicator. This test had 115 speed-up runs. The first 25 runs are the baseline runs. The mean of these 25 runs are the reference of the rotor health condition. The next 20 runs were the nominal 0° unbalanced runs. 1, 2, 3 and 4 nylon set crews were added to the 0° mark on the rotor. For each unbalanced case, five runs were repeated.

The next 20 runs were the nominal 90° unbalanced runs. In this case, the imbalance masses were removed from the 0° location. 1, 2, 3 and 4 nylon set crews were added to the 90° mark on the rotor. For each unbalanced case, five runs were repeated.

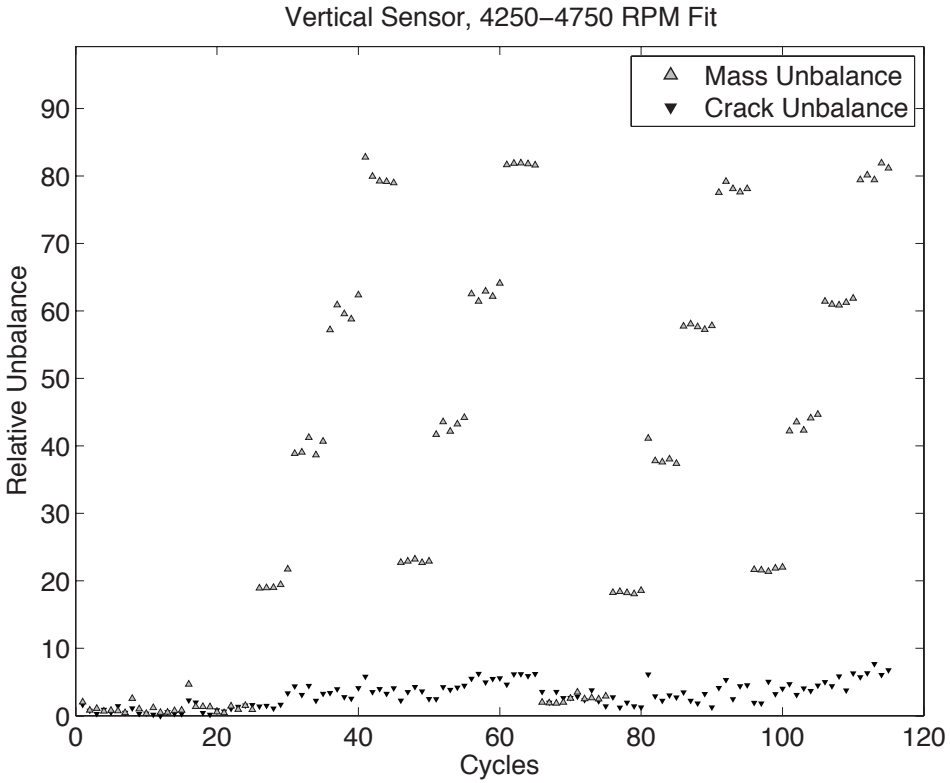

Figure 12. Identified imbalances normalized w.r.t. baseline.

To double-check the test, the procedure was repeated with 10 baseline runs, 20 nominal 0° unbalanced runs, and 20 nominal 90° unbalanced runs at different imbalance levels.

In Figure 11, the top half of the figure displays the mass imbalance parameter C_0 and the bottom half is the crack-induced imbalance parameter C_2. We see that that the mass imbalance indicator C_0 is proportional to the imbalance added, while the crack-induced imbalance indicator C_2 does not have obvious trend. The slight upward trend is probably due to test and curve-fitting numerical variations.

In Figure 12, the normalized C_0 and C_2 are shown for comparison. In the figure, C_0 is normalized with respect to the mean of the C_0 in the first 25 baseline runs, while C_2 is normalized with respect to the mean of the C_2 in the first 25 baseline runs. Again, the normalized C_0 is also clearly proportional to the mass imbalance added. The crack-induced imbalance indicator C_2 is small. In theory, C_2 should be a small constant. The slight increase could be due to fitting errors.

		Vertical Sensor		Horizontal Sensor	
	Ref.	0°	90°	0°	90°
3.4	3.416	3.14 (−8.2%)	3.69 (+8.2%)	3.60 (+5.3%)	3.23 (−5.3%)
6.8	6.832	6.49 (−5.0%)	7.18 (+5.1%)	6.99 (+2.2%)	6.60 (−3.4%)
10.2	10.248	9.77 (−4.7%)	10.31 (+0.6%)	10.12 (−1.3%)	9.72 (−5.1%)
13.7	13.664	13.17 (−4.6%)	13.50 (−1.2%)	13.43 (−1.7%)	12.85 (−5.9%)

Table 1. Normalized mass imbalance identification. All values in g mm; percentages in parentheses indicate error relative to the reference value (second column).

To figure out the exact imbalance amount from C_0, the exact modal parameters, such as modal mass and mode shape, are required from the rotating system. For a quick examination, the imbalance amount can be normalized at the smallest imbalance at 0° and 90° positions. The normalized mass imbalance identification is shown in Table 1, where it can be seen that the identification error is less than 9% (for the horizontal sensor, less than 6%).

Similar data processing was carried out on the horizontal sensor. The results are shown in Table 1 and Figures 13 and 14. In this sensor, the fitting error is less than 6%. In this case, the C_2 upward trend is much less.

5. Engine subassembly spin-pit tests

The engine subassembly tests were set up at the Naval Air Warfare Center in Maryland. Tests included four F404 HPT disk subassemblies. Each disk was implanted with single/multiple flaws at known/unknown locations. Each cycle included a run-up from 1500 RPM to 18000 RPM, a dwell at high speed 18000 RPM, and a coast-down from 18000 RPM to 1500 RPM. In our system, only the speed-up synchronous data was collected and analyzed. The data acquisition diagram is shown in Figure 15. A light probe was used to pick up the 1/rev signal for synchronous data reduction. Two proximity probes were used as vibration sensors. Data acquisition and signal processing were carried out at the control room near the test laboratory. The operations were monitored through remote accesses.

The test #1 results are shown in Figure 16. The full cycle history of the mass imbalance coefficient and crack-induced imbalance coefficient are shown in Figure 16(a). In this test, the cooling plate crack was developed during the cycles. It ended up with a small piece being liberated at the cooling plate (see Figure 17). The last cycles of the mass imbalance and crack-induced imbalance coefficient are

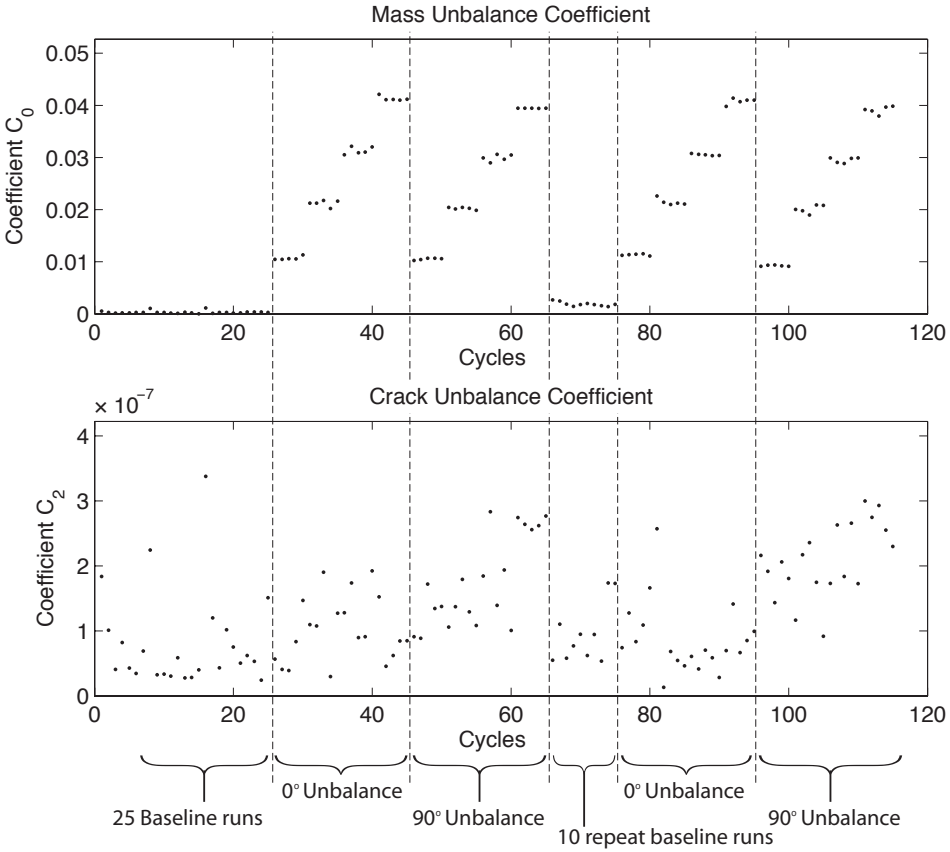

Figure 13. Nonresonance-based analysis, horizontal sensor.

shown in Figure 16(b), where both C_0 and C_2 coefficients increased significantly at the end of cycles.

The Test #2 results are shown in Figure 18. Similar to the Test #1, the test ended after a piece of mass being liberated from the cooling plate. Again, both mass imbalance and crack-induced imbalance coefficients are significantly increased at the end of the cycle history.

The Test #3 and Test #4 results are shown in Figure 19 and Figure 20, respectively. In both tests, the disk crack propagated. The disks were burst at the end due to crack propagation. As seen in Figure 19 and Figure 20, the mass imbalance coefficients are relatively quiet in the last cycles, while the crack-induced imbalance coefficient increased gradually.

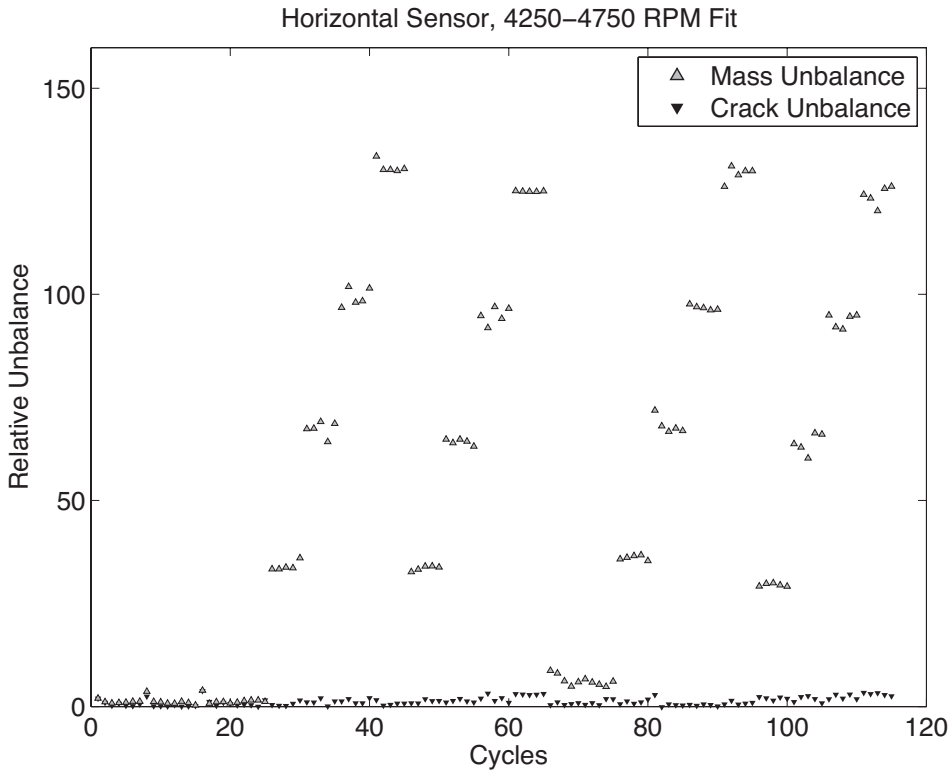

Figure 14. Identified imbalances normalized w.r.t baseline.

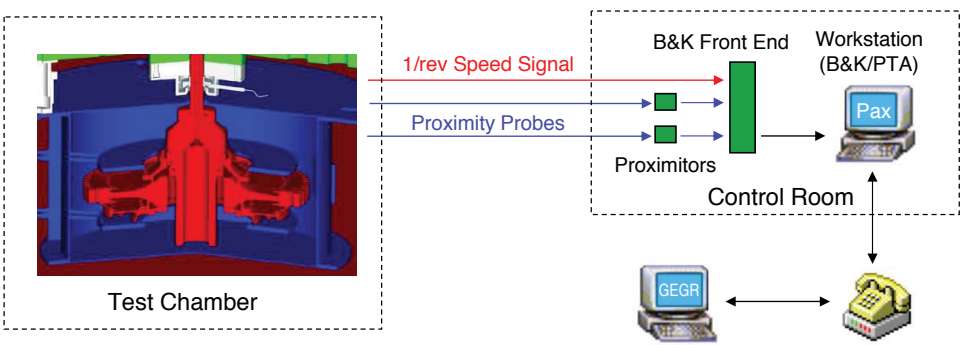

Figure 15. Engine subassembly data acquisition diagram.

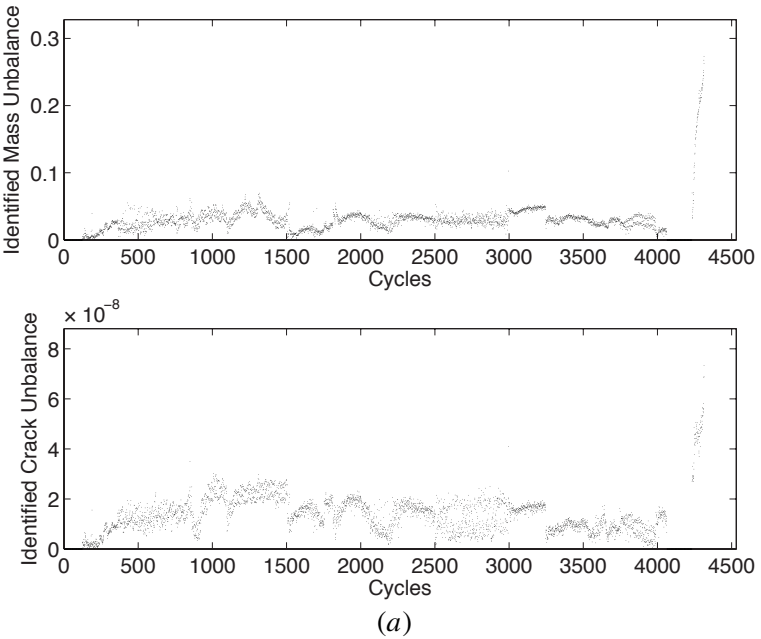

(*a*)

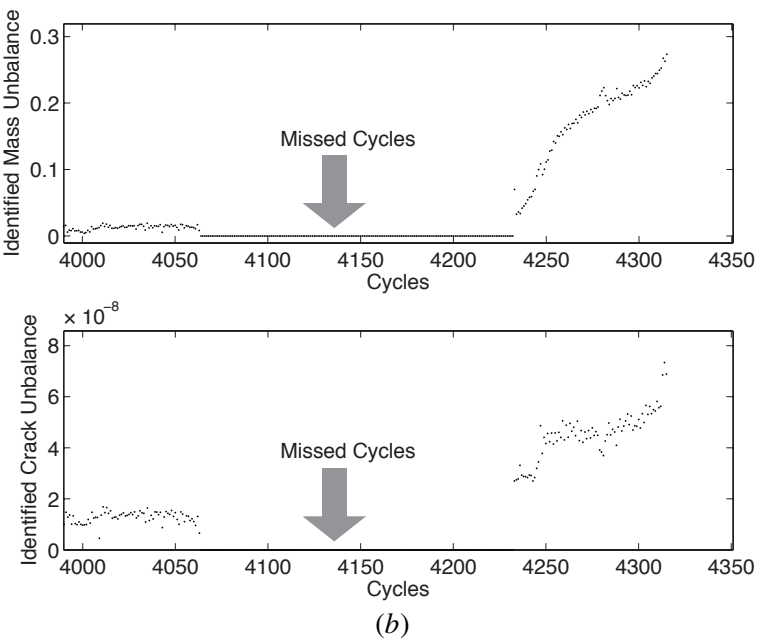

(*b*)

Figure 16. Test #1 results (a) all cycles and (b) last cycles.

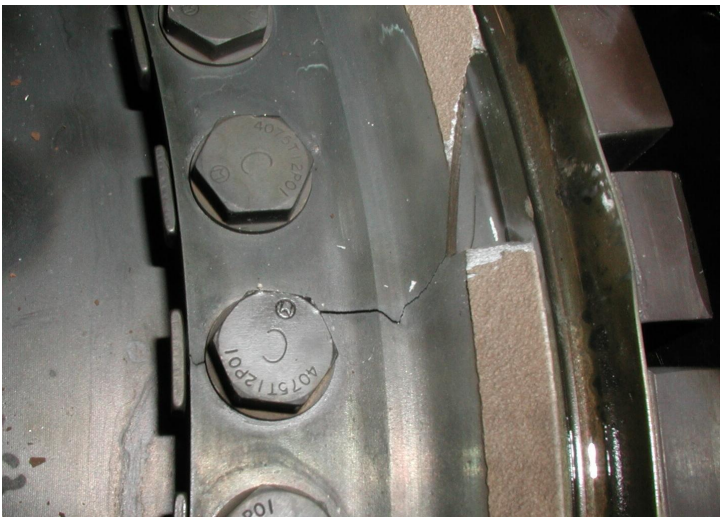

Figure 17. Crack and mass deliberation at the cooling plate.

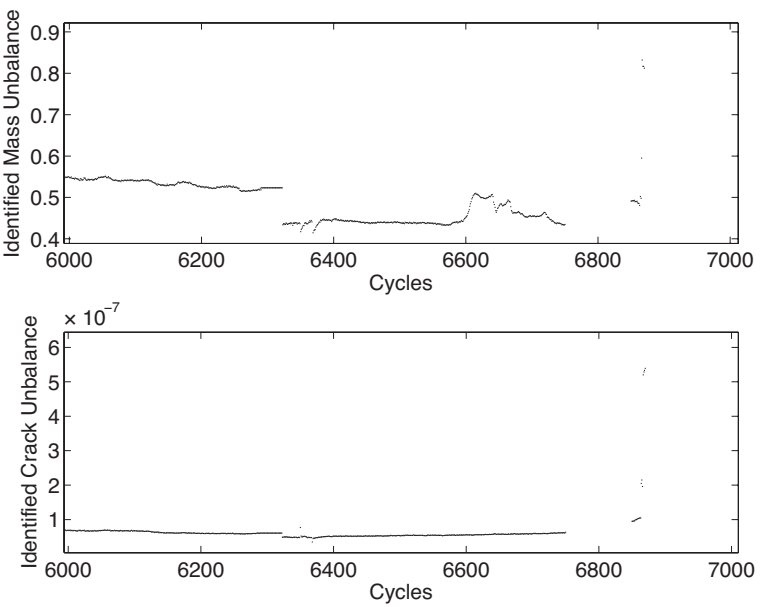

Figure 18. Test #2 results.

6. Conclusion

In this paper, an imbalance detection algorithm was derived based on rotor synchronous vibrations. Instead of an SDOF model, the multi-DOF model was used

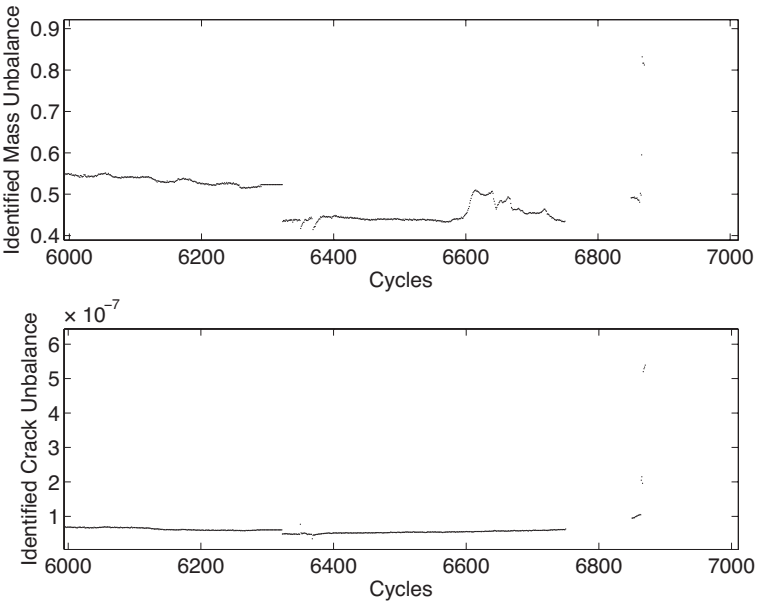

Figure 19. Test #3 results.

in the derivations. Thus, the algorithm was valid in a frequency region between any two critical speeds. The MDOF model reflected the more realistic conditions in many rotor operations. The algorithm was integrated into an automatic data collection and analysis system. The integrated system has been validated through a small rotor laboratory test rig with controlled mass imbalance and an engine subassembly with embedded disk cracks. Laboratory rig test results indicated that a good agreement between the embedded and identified imbalances can be achieved. An engine subassembly test also indicated the feasibility of trending the mass imbalance and crack-induced imbalance from the engine cycle history. Initial test results indicated that it is promising to use vibration diagnostic techniques for the online detection of engine rotor disk cracks and other anomalies. However, the sensitivity of the system needs to be improved. The precision of the 1/rev signal is also a key to the success of the algorithm.

Acknowledgments

The authors gratefully acknowledge the support of Dr. Leo Christodoulou of the Defense Advanced Research Projects Agency (DARPA), much of this work was accomplished as part of DARPA's Materials Damage Prognosis program. The authors would like to acknowledge Dennis Corbly of GE Aircraft Engines for his

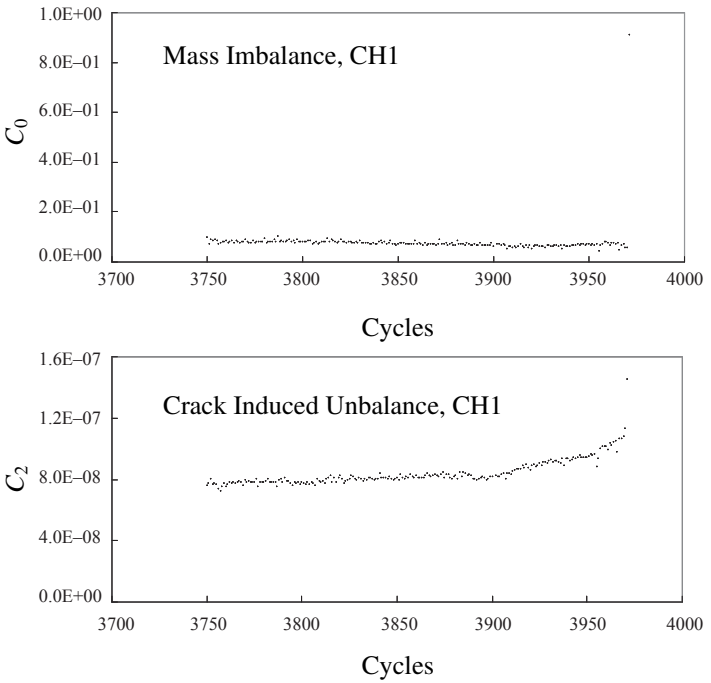

Figure 20. Test #4 results

support and leadership in the program, and Greg Muschlitz of NAWCAD for his help in the disk subassembly tests.

References

[Butz and Rodriguez 1999] M. Butz and H. Rodriguez, "Propulsion wealth monitoring for enhanced safety", Contract NAS3-99203, NASA, Houston, TX, 1999.

[Imam and DeLorenzi 1988] I. Imam and H. G. DeLorenzi, "Method and apparatus for detecting axial cracks in rotors for rotating machinery", *United States Patent* **4** (June 14 1988), 751,657.

[NASA 1975] NASA, "Astronautics structures manual", NASA, Houston, TX, 1975.

[Rodriguez et al. 2001] H. Rodriguez, D. Hallman, M. Butz, and V. Dhar, "A physics-based approach for the detection of cracks in rotating disks", Paper presented at the ISABE, 15th International Symposium on Air Breathing Engines (Bangalore, India), 2001.

[Sonnichsen 2000] H. E. Sonnichsen, "Real-time detection of developing cracks in jet engine rotors", pp. 173–183 in *IEEE Conference*, vol. 6, 2000.

[Tada et al. 1985] H. Tada, P. Paris, and G. Irwin, *The stress analysis of cracks handbook*, 2nd ed., Del Research Corp. and Paris Productions, St. Louis, MO, 1985.

[Thomson and Dahleh 1998] W. T. Thomson and M. D. Dahleh, *Theory of vibration with applications*, 5th ed., Prentice-Hall, Englewood Cliffs, NJ, 1998.

Received 29 Sep 2005. Revised 19 Dec 2005.

HUAGENG LUO: luoh@research.ge.com
GE Global Research Center, K1 3A 30B, One Research Circle, Niskayuna, NY 12309, United States

HECTOR RODRIGUEZ: hector.m.rodriguez@pw.utc.com
Infotech Aerospace Services, Inc., Structures Department, 699 Industrial Ave., Isabela, PR 00662, United States

DARREN HALLMAN: hallman@research.ge.com
GE Global Research Center, K1 3A 30B, One Research Circle, Niskayuna, NY 12309, United States

JOURNAL OF MECHANICS OF MATERIALS AND STRUCTURES
Vol. 1, No. 3, 2006

A HIGHER-ORDER THEORY FOR CRACK GROWTH IN FIBER-METAL LAMINATES UNDER GENERALIZED PLANE-STRESS CONDITIONS

XIJIA WU, ZHONG ZHANG AND J. LALIBERTÉ

Fiber-metal laminates (FML) are hybrid materials that consist of alternating layers of metal and fiber-reinforced prepreg. The classical plane-stress theory has difficulty in dealing with the fatigue fracture of such materials where the crack only grows in the metal layers, while the prepreg layers remain intact. In this paper, a new theoretical treatment is given to FML under generalized plane-stress conditions. The new theory introduces a harmonic anti-plane-stress potential p to describe the interlaminar stresses near the crack tips and the "bridging" effect of the unbroken fibers along the crack wakes. An analytical solution is derived for GLARE-3 (3/2) containing collinear cracks with length $2a_0$ (the initial crack length) in the prepreg and length $2a$ in the aluminum layer. The effective stress intensity factor is obtained in a closed form, and the theoretical prediction is compared with the experimental behavior obtained from fatigue crack growth testing of center-notched specimens.

1. Introduction

Fiber-metal laminates (FML) consisting of alternating layers of aluminum and fiber-reinforced prepreg are being considered as a potential alternative to replace traditional aluminum alloys for more light-weight and damage tolerant aerospace structural applications [Gunnink et al. 1982]. FML have excellent fatigue crack growth resistance plus improved impact and corrosion resistances because the fiber reinforcement plays a role in crack bridging and also insulates the inner metal from any corrosive species. It has been recognized that the damage tolerance characteristics of FML are largely attributed to the load transfer mechanism via interfacial shear stresses from the cracked aluminum layers to fiber-reinforced (unbroken) prepregs [Gunnink et al. 1982; Roebroeks 1994]. Regarding the fiber-bridging effect, Marissen [1988] assumed that a constant "bridging stress" exists in the fibers along the crack wake. Guo and Wu [1999] offered a numerical method to derive the

Keywords: fiber-metal laminate, stress intensity factor.

"bridging stress" based on the displacement condition at the boundary of delamination. Their treatment rests on two assumptions: (i) each fiber within the delamination region is individually under uniform tension, and (ii) the displacement profile at the delamination boundary is equal to the crack opening displacement along the crack wake. The error associated with the assumed displacement condition would be proportional to the size of delamination (that is, $\Delta v \propto \varepsilon f(x)$, where $f(x)$ is the delamination boundary away from the crack line $y = 0$), if a constant strain existed across the region. The aforementioned theoretical treatments attempted to patch the shortcomings of the classical crack mechanics for monolithic materials, but they were not derived from the stress equilibrium and compatibility equations of elasticity. For laminated materials, the existence of parallel cracks of different length in different layers poses a significant challenge to the classical two-dimensional theories dealing with plates and laminates, and the general solution has not been found.

Traditionally, composite materials are considered as homogeneous and anisotropic materials and hence are solved with the classical theory [Tsai and Hahn 1980; Whitney 1987; Ashbee 1993], where the anti-plane shear stresses are absent because of the simplification. Except for some 3D or quasi-3D numerical methods—such as the finite element method, the hybrid and displacement superposition method [Pagano 1978; Iarve and Pagano 2001]—that could be used to describe cracks in FML where layer-to-layer interaction cannot be ignored, there is no analytical theory to formulate stresses in cracked FML. It is the intention of this paper to present such a theory.

A higher-order theory has been developed for generalized plane-stress states in isotropic materials with the introduction of two conjugated harmonic stress potentials for anti-plane stresses by the requirement of 3D strain compatibility [Wu and Cheng 1999]. This theory is now extended to FML whereby the interlaminar stress interaction is reduced to equivalent body forces. As an example, the boundary-value problem of fatigue crack growth in GLARE-3 (3/2) is solved, using the complex variable method. The effective stress intensity factor of a crack in FML, propagating only in the aluminum layers, is obtained in a closed form and the prediction is then compared with the experimental behavior observed from fatigue crack growth testing of center-notched specimens.

2. The theory of FML

Consider a typical fiber-metal laminate, which consists of alternating metal (isotropic) and prepreg (orthotropic) layers. The configuration of GLARE-3 (3/2) is shown in Figure 1. The reference coordinate system is also given in 1 by way of

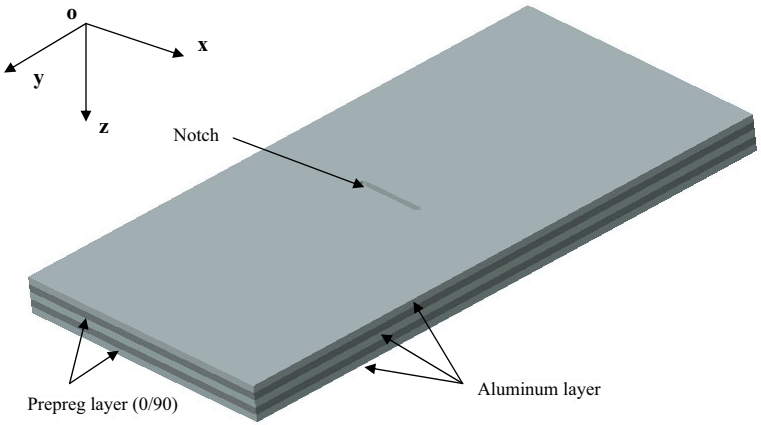

Figure 1. Schematic configuration of GLARE-3 (3/2) consisting of three layers of 2024-T3 aluminum alloy and two layers of glass fiber-epoxy prepreg.

describing the problem. For the panel, the thickness of the laminate is small compared to the planar dimensions. The body forces are ignored and the stress normal to the laminate, σ_z, is zero. In the following, we shall derive the stress formulation for metal and prepreg layers separately and then consider their interactions by the requirement of displacement continuity across the interface.

2.1. ***The metal layer.*** Under the generalized plane stress condition, the stress equilibrium in the metal layer can be expressed as

$$\frac{\partial \sigma_x}{\partial x} + \frac{\partial \tau_{xy}}{\partial y} + \frac{\partial \tau_{xz}}{\partial z} = 0, \tag{1a}$$

$$\frac{\partial \tau_{xy}}{\partial x} + \frac{\partial \sigma_y}{\partial y} + \frac{\partial \tau_{yz}}{\partial z} = 0, \tag{1b}$$

$$\frac{\partial \tau_{xz}}{\partial x} + \frac{\partial \tau_{yz}}{\partial y} = 0. \tag{1c}$$

It has been shown that the three-dimensional stress equilibrium and strain compatibility conditions can be all met when the in-plane and anti-plane shear stresses are expressed as [Wu and Cheng 1999]

$$\sigma_x = \frac{\partial^2 \Psi}{\partial y^2} + p, \qquad \sigma_y = \frac{\partial^2 \Psi}{\partial x^2} + p, \qquad \tau_{xy} = -\frac{\partial^2 \Psi}{\partial x\, \partial y}, \tag{2}$$

$$\tau_{xz} = -z\frac{\partial p}{\partial x} = -z\frac{\partial q}{\partial y}, \qquad \tau_{yz} = -z\frac{\partial p}{\partial y} = z\frac{\partial q}{\partial x}, \tag{3}$$

where Ψ is a bi-harmonic function ($\nabla^4\Psi = 0$), p and q are conjugated harmonic functions ($\nabla^2 p = 0$ and $\nabla^2 q = 0$, satisfying the Cauchy–Riemann condition).

For each individual layer, the neutral plane ($z = 0$) is set at either the free surface, for a surface metal layer, or the median plane for a middle layer. Therefore, the free surface is truly free of any anti-plane shear traction. Alternatively, the laminate can also be viewed as a portion of periodical stacking of the constituent lamina, in which the surface layer becomes an inner layer with twice the thickness. When the lay-up is symmetrical, as in GLARE 3, the net anti-plane shear stress across the laminate is zero, and the laminate is under the generalized plane-stress condition. When the lay-up is asymmetrical, a coupled bending is induced, because the net anti-plane shear is not always zero. Here we consider only the former case. For that, the inter-laminar shear stresses at the interfaces of metal/prepreg can be obtained from Equation (3) as

$$\tau_{xz}^i = \mp\frac{h_i}{2}\frac{\partial p_i}{\partial x}, \qquad \tau_{yz}^i = \mp\frac{h_i}{2}\frac{\partial p_i}{\partial y}, \qquad i = 1, 3, 5, \ldots, \tag{4}$$

where h_i is the thickness of the i-th layer. The detailed lay-up is shown in Figure 2 and the sign convention is observed accordingly.

2.2. ***The prepreg layer.*** For a prepreg layer between metal layers ($i = 2, 4, 6, \ldots$), the action of the inter-laminar shear stresses would produce an effect equivalent to that of the in-plane body forces, as defined by

$$X_i = -\frac{\tau_{xz}^{i+1} - \tau_{xz}^{i-1}}{h_i} = -\frac{1}{2h_i}\frac{\partial}{\partial x}\left(h_{i+1}p_{i+1} + h_{i-1}p_{i-1}\right) = -\frac{\partial U}{\partial x}, \tag{5a}$$

$$Y_i = -\frac{\tau_{yz}^{i+1} - \tau_{yz}^{i-1}}{h_i} = -\frac{1}{2h_i}\frac{\partial}{\partial y}\left(h_{i+1}p_{i+1} + h_{i-1}p_{i-1}\right) = -\frac{\partial U}{\partial y}, \tag{5b}$$

where U is defined as the equivalent body-force potential:

$$U = \frac{1}{2h_i}\left(h_{i+1}p_{i+1} + h_{i-1}p_{i-1}\right). \tag{5c}$$

Therefore, the equilibrium equations for the prepreg reduce to

$$\frac{\partial \sigma_x}{\partial x} + \frac{\partial \tau_{xy}}{\partial y} + X_i = 0, \tag{6a}$$

$$\frac{\partial \tau_{xy}}{\partial x} + \frac{\partial \sigma_y}{\partial y} + Y_i = 0. \tag{6b}$$

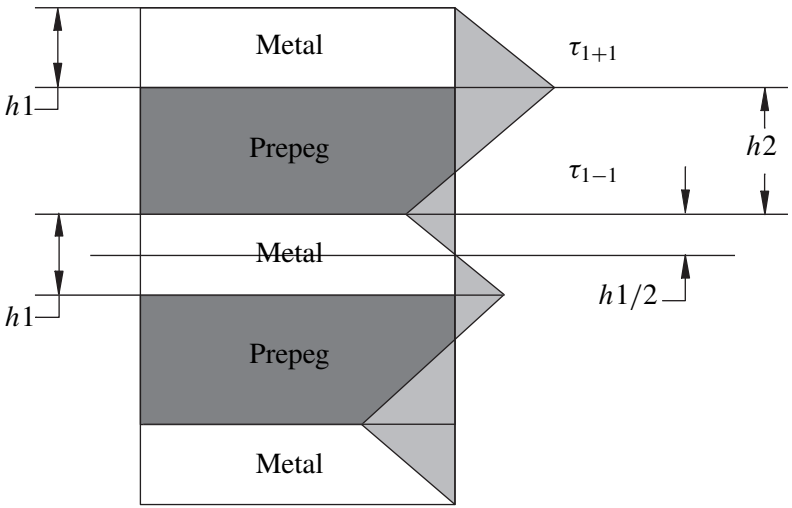

Figure 2. Schematic of inter-laminar shear stress distribution through the thickness of an FML.

By satisfying the equilibrium conditions, the in-plane stresses in a prepreg can be obtained as

$$\sigma_x = \frac{\partial^2 F}{\partial y^2} + U, \qquad \sigma_y = \frac{\partial^2 F}{\partial x^2} + U, \qquad \tau_{xy} = -\frac{\partial^2 F}{\partial x\, \partial y}, \tag{7}$$

where F is the stress potential of the prepreg and should satisfy the compatibility condition for an orthotropic material [Lekhnitskiĭ 1981]:

$$a_{22}\frac{\partial^4 F}{\partial x^4} + (a_{66} + 2a_{12})\frac{\partial^4 F}{\partial x^2\, \partial y^2} + a_{11}\frac{\partial^4 F}{\partial y^4} = -(a_{22} + a_{12})\frac{\partial^2 U}{\partial x^2} - (a_{11} + a_{12})\frac{\partial^2 U}{\partial y^2}, \tag{8}$$

where a_{ij} are the compliance coefficients of the prepreg.

For FML of symmetrical layout, the anti-plane shear stresses counteract each other across the entire thickness of the laminate such that the net result is zero. Thus, the stress-state of FML, as defined by the stress functions Ψ, F, U, p and q, falls into the category of the generalized plane stress.

In summary, the stresses in a metal (isotropic) layer can be obtained from the stress function Ψ and either of the conjugated harmonic functions p and q; the stresses in a prepreg (orthotropic) layer can be obtained from the stress functions F and U. The inter-laminar stresses can be calculated using Equation (4). These stress potentials, when satisfying the necessary compatibility conditions, should lead to a complete description of the stresses in the laminate. By the theorem of unique solution of elasticity, the stress potentials should represent the true stress-state of the laminate under a given generalized plane-stress condition. The problem, then, reduces to finding stress functions (or potentials) that meet the boundary-value conditions of the particular loading configuration. The mathematical approach to seeking such solutions is discussed along with the presentation of solving a practical case of fatigue crack growth in GLARE-3 (3/2) in the section below.

3. The complex variable solution for GLARE-3 containing a crack

Consider a GLARE-3 (3/2) panel containing central collinear cracks of length $2a$ in the aluminum and $2a_0$in the prepreg. The panel is remotely subjected to uniform tension, as shown schematically in Figure 3. The crack in the prepreg represents

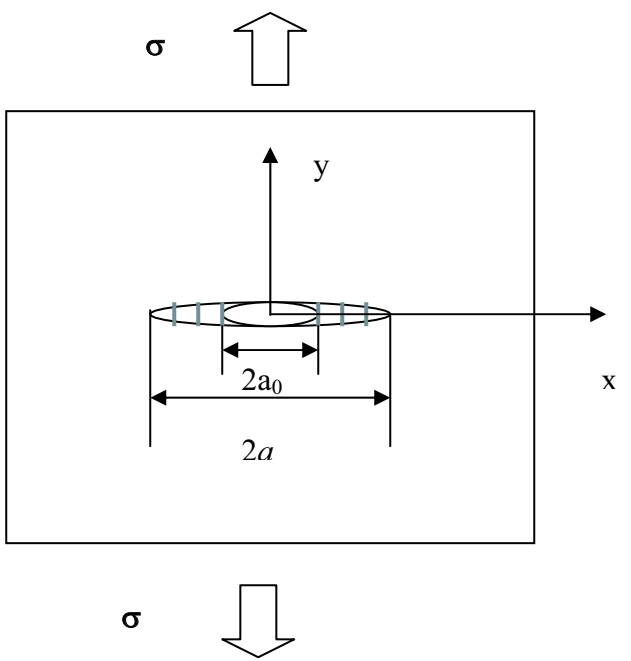

Figure 3. Schematic of a FML panel containing a center-located crack: a_0 is the half-length of the initial through-the-thickness crack; a is the half-length of the crack in the metal layer.

the initial notch, the ones in the metal layers extend to the current length a due to fatigue crack growth. As such, the crack wakes in the region $[a_0, a]$ are bridged with unbroken fibers. The aluminum layers are 2024-T3 sheets, which are considered to be isotropic materials. The prepreg layers in GLARE-3 have equal volume fraction of 0°/90° cross-ply glass fibers, and therefore are also treated as a quasi- isotropic material, for simplicity. This greatly reduces the complexity of the problem and allows one set of stress potential functions to be used for both aluminum and prepreg in GLARE-3, as detailed below. For other FML with anisotropic prepregs, the solution has to be obtained by solving Equation (8).

First, the Westergaard function is adopted as the in-plane stress potential ψ, as defined by

$$\psi = \operatorname{Re} \tilde{\tilde{Z}}(\xi) + y \operatorname{Im} \tilde{Z}(\xi), \tag{9}$$

where $\xi = x + iy$ is the complex coordinate variable and

$$\begin{aligned} \tilde{Z} &= \int Z(\xi)\, d\xi, \\ \tilde{\tilde{Z}} &= \int \tilde{Z}(\xi)\, d\xi = \iint Z(\xi)\, d\xi\, d\xi. \end{aligned} \tag{10}$$

Then, a new analytic function $\chi(\xi)$ is introduced to express the anti-plane shear stress potential p as

$$2p = \chi(\xi) + \bar{\chi}(\bar{\xi}) = \varphi'(\xi) + \bar{\varphi}'(\bar{\xi}), \tag{11}$$

where $\bar{\xi}$ denotes the conjugate of ξ, and the same meaning also applies to complex functions.

Hence, according to Equations (2) and (3), the stress components can be obtained as

$$\begin{aligned} \sigma_x + \sigma_y &= 2 \operatorname{Re}\left[Z(\xi) + \chi(\xi)\right], \\ \sigma_y - \sigma_x + i2\tau_{xy} &= -i2yZ'(\xi), \\ \tau_{xz} + i\tau_{yz} &= \mp \frac{h}{2} \bar{\chi}'(\bar{\xi}). \end{aligned} \tag{12}$$

The displacements (at $z = 0$) can be obtained as

$$2G(u + iv) = \frac{2}{1+\mu} \tilde{Z}(\xi) - \operatorname{Re} \tilde{Z}(\xi) - iy\bar{Z}(\bar{\xi}) + \frac{1-\mu}{1+\mu} \varphi(\xi). \tag{13}$$

Because of symmetry, the solution for the half plane $x > 0$ can be tentatively represented by the following functions:

$$Z(\xi) = \frac{A\xi}{\sqrt{\xi^2 - a^2}}, \qquad \chi(\xi) = \frac{B}{\sqrt{\xi - a}}, \tag{14}$$

where A and B are constants to be determined by the stress boundary conditions and displacement compatibility conditions.

Substituting Equation (14) into Equations (12) and (13), we obtain the in-plane stresses as

$$\sigma_x = \frac{\partial^2 \psi}{\partial y^2} + p = \operatorname{Re}\left[Z(\xi) + \chi(\xi)\right] - y \operatorname{Im} Z'(\xi),$$

$$\sigma_y = \frac{\partial^2 \psi}{\partial x^2} + p = \operatorname{Re}\left[Z(\xi) + \chi(\xi)\right] + y \operatorname{Im} Z'(\xi), \tag{15}$$

$$\tau_{xy} = -y \operatorname{Re} Z'(\xi),$$

and the displacements as

$$u = \frac{1}{2G}\left(\frac{1-\mu}{1+\mu} \operatorname{Re}\left[\tilde{Z}(\xi) + \varphi(\xi)\right] - y \operatorname{Im} Z(\xi)\right), \tag{16a}$$

$$v = \frac{1}{2G}\left(\frac{2}{1+\mu} \operatorname{Im} \tilde{Z}(\xi) - y \operatorname{Re} Z(\xi) + \frac{1-\mu}{1+\mu} \operatorname{Im} \varphi(\xi)\right). \tag{16b}$$

It is easy to verify that the crack surface condition, that is, $\tau_{xy} = \sigma_y = 0$, at $y = 0$, $|x| < a$, is satisfied and the displacement v along the line of $(x > a,\ y = 0)$ is zero. To satisfy the remote stress condition, $A = \sigma_\infty$. These stress/displacement formulations will be used to deal with two cracks in an FML: one crack of length $2a_0$ in the prepreg and one of length $2a$ in the aluminum.

For displacement continuity, it is assumed that the crack opening displacements at the center of both cracks in metal and prepreg are equal, due to the perfect bonding condition. Mathematically, this condition can be expressed as: $v^{(1)} = v^{(2)}$ at the point $(x = 0,\ y = 0)$. In the rest of the plane of the interface, displacement discontinuities or sliding may occur, particularly around the crack tips. The assumed condition is a simplification for the convenience of deriving a closed-form solution as shown in the following, yet it adheres to the fact that delamination does not occur at the center point. The above description is only a two-dimensional simplification of the delamination problem in a real case, a complete description of which would have to be based on a 3D theory.

From Equation (16b), the crack-center opening displacements in the metal (with a crack of half-length a) and prepreg (with a crack of half-length a_0) can be obtained, respectively, as

$$\begin{aligned} v^{(1)} &= \frac{1}{G_1}\left(\frac{A^{(1)}a}{1+\mu} + \frac{(1-\mu)B^{(1)}\sqrt{a}}{1+\mu}\right), \\ v^{(2)} &= \frac{1}{G_2}\left(\frac{A^{(2)}a_0}{1+\mu} + \frac{(1-\mu)B^{(2)}\sqrt{a_0}}{1+\mu}\right), \end{aligned} \tag{17}$$

where $v^{(1)}$ and $v^{(2)}$ are the displacements in the y direction for the metal and prepreg layers. $A^{(1)}$, $B^{(1)}$ and $A^{(2)}$, $B^{(2)}$ are constants for metal and prepreg layers, respectively. Since both layers are subjected to remote uniform tension, $A^{(1)} = \sigma^{(1)}$ and $A^{(2)} = \sigma^{(2)}$, where $\sigma^{(1)}$ and $\sigma^{(2)}$ are the remote stresses in the metal and prepreg layer, respectively. Then, only the constants $B^{(1)}$ and $B^{(2)}$ need to be determined to complete the solution.

There are two stress singularity points in the FML containing a fiber-bridged crack—one at $x = a_0$ and the other at $x = a$—which may cause local delamination due to incompatibility. This has indeed been observed in numerous experiments. At remote locations, however, it is believed that the bonding between the prepreg and the metal layers should remain intact such that the antiplane shear stresses are continuous across the interface. Thus, at the interface between the surface metal layer and an immediate inner prepreg layer, it should hold that

$$-h_1\bar{\chi}_1'(\bar{\xi}) = \frac{h_2}{2}\bar{\chi}_2'(\bar{\xi}), \qquad (\xi \to \infty), \tag{18}$$

where h_1 and h_2 are the thickness of the surface metal layer and the immediate prepreg layer, respectively. Equation (18) will hold true when $r = |\xi| \gg a_0$ and a, only if

$$2h_1 B^{(1)} = -h_2 B^{(2)}. \tag{19}$$

Then, by solving the displacement continuity condition at the crack center, that is, $v^{(1)} = v^{(2)}$ (at $x = 0$, $y = 0$), with the substitution of Equation (19) into Equation (17), we obtain

$$B^{(1)} = \frac{1}{1-\mu}\frac{A^{(2)}a_0 - \frac{G_2}{G_1}A^{(1)}a}{\frac{G_2}{G_1}\sqrt{a} + 2\frac{h_1}{h_2}\sqrt{a_0}} = -\frac{h_2}{2h_1}B^{(2)}. \tag{20}$$

We note here that the displacement continuity condition imposed at the crack-center is obviously an approximation of the more complicated interfacial continuity/discontinuity conditions around the crack in the real laminates. However, the major mechanical characteristics of the simplified condition agree with the real case, as elucidated in a later section.

From stress expression, Equation (15), the stress intensity factor in the metal layer can be obtained as:

$$K_{\text{eff}} = \lim_{\substack{x_1 \to 0 \\ y=0}} \sqrt{2\pi x_1}\sigma_y^{(1)} = K_\infty^{(1)} - \frac{\sqrt{2}}{1-\mu} \frac{K_\infty^{(1)} - \frac{G_1}{G_2}\sqrt{\frac{a_0}{a}} K_\infty^{(2)}}{1 + 2\frac{G_1 h_1}{G_2 h_2}\sqrt{\frac{a_0}{a}}}, \tag{21}$$

where, $x_1 = x - a$, and

$$K_\infty^{(1)} = A^{(1)}\sqrt{\pi a} = \sigma_\infty^{(1)}\sqrt{\pi a}, \qquad K_\infty^{(2)} = A^{(2)}\sqrt{\pi a_0} = \sigma_\infty^{(2)}\sqrt{\pi a_0}.$$

$\sigma_\infty^{(1)}$ and $\sigma_\infty^{(2)}$ are the remote stresses in the metal layer and prepreg layer.

4. Experiment

GLARE-3 3/2 specimens, which consist of three sheets of 2024-T3 aluminum alloy (0.3 mm thick) and two layers of glass/epoxy prepreg (0.25 mm thick) with a stacking sequence of (0°/90°), were machined (water-jet cut) in the form of center-crack tension specimen (CCT) configuration. The specimen has a length of 300 mm in the loading direction, a width of 100 mm and it contains a 24 mm long central notch with a notch root radius of 0.2 mm. The total thickness of the specimen is 1.4 mm. Fatigue crack growth rate testing was performed according to the ASTM-E647 standard. The testing was conducted at room temperature using a computer-controlled MTS servohydraulic testing machine under constant amplitude sinusoid loading with a frequency of 5 Hz and stress ratio $R = 0.1$. The crack length was measured using a traveling microscope (±0.01 mm). Fatigue testing was automatically stopped at a predetermined cycle interval to take measurements of the half-crack length on both sides of the specimen. An a-N curve is shown in Figure 4 (a). Details of the testing program were reported elsewhere [Zhang et al. 2002].

5. Discussion

Fatigue crack growth in FML has been investigated by many researchers, using semi-empirical approaches [Marissen 1988], experimental methods [Ritchie et al. 1989] and numerical methods [Guo and Wu 1998]. All these treatments used the concept of *bridging stress* to account for the reduction of stress intensity factor in FML, but it is empirically introduced. According to the present higher-order theory, it is the interlaminar shear stress that provides the bridging effect, as opposed to the in-plane "bridging stress" acting along the crack wake. The existence of these anti-plane shear stresses modifies the in-plane stresses through the interaction of stress potentials, as expressed in Equations (2) and (3). As a result, the stress intensity factor of the crack in the metal layer is changed, as shown in Equation (21), in

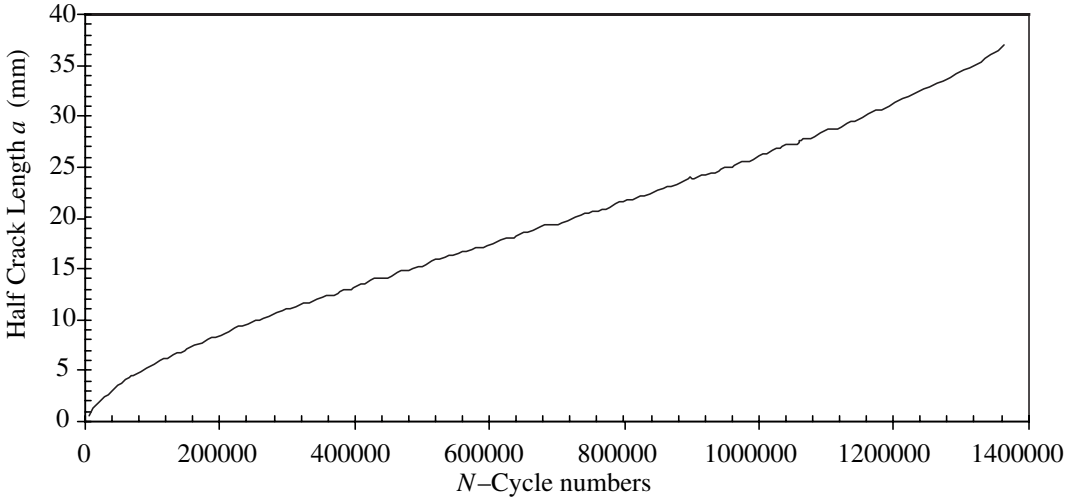

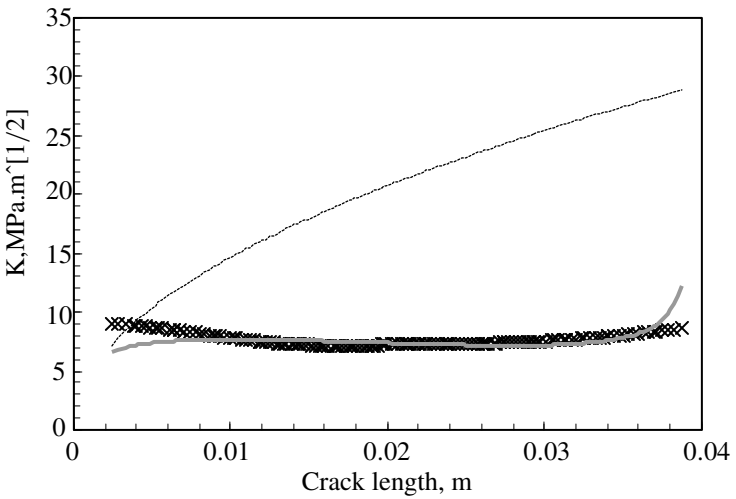

Figure 4. (a) Measured crack length as a function of fatigue cycle number; (b) comparison of the theoretical stress intensity factors with the experimental values: thin black line indicates monolithic K; thick black line shows FML-K; black X's indicate experimental values.

comparison with the solution for monolithic materials. Apparently, (21) can be broken into two parts, as

$$K_{\text{eff}} = K_m - K_{br}, \tag{22}$$

where K_m is the apparent stress intensity factor as if in the monolithic metal, and K_{br} is the stress intensity reduction due to fiber-bridging, as defined by

$$K_{br} = \frac{\sqrt{2}}{1-\mu} \frac{K_\infty^{(1)} - \frac{G_1}{G_2}\sqrt{\frac{a_0}{a}} K_\infty^{(2)}}{1 + 2\frac{G_1 h_1}{G_2 h_2}\sqrt{\frac{a_0}{a}}}. \tag{23}$$

Equation (22) bears a physical meaning similar to that perceived by other researchers, but only K_{br} is derived from anti-plane stresses and is explicitly expressed in Equation (23).

From the a-N curve, Figure 4 (a), fatigue crack growth rates can be evaluated. The effective stress intensity factors in the FML are thus found as compared with the metal fatigue crack growth behavior, that is, from the da/dN versus ΔK relationship, assuming that the fatigue crack, propagating in the aluminum alloy layer of an FML, experiences the same stress intensity at the same growth rate as it would were it propagating in the monolithic alloy alone. For the finite panel specimen configuration, a correction was made to Equation (21), replacing $K_\infty^{(1)}$ with

$$K_\infty^{(1)} \sqrt{\sec \frac{\pi a}{W}},$$

where W is the width of the specimen, to account for the effect of finite width.

In matching (21) with the real case, the value of a_0 has to be adjusted to account for the effect of bluntness of the initial machine notch in the specimen. Note that fatigue precracking in this case would only sharpen the metal crack but not the prepreg crack (notch). The comparison of (21) with the evaluated ΔK is shown in Figure 4 (b). The elastic properties of the FML, as input to the calculation, are: $G_1 = 27.7$ GPa, $h_1 = 0.3$ mm, for aluminum; and $G_2 = 5.6$ GPa, $h_2 = 0.25$ mm, for prepreg. The stress intensity factor of a crack in an infinite monolithic aluminum sheet is also shown in the figure for comparison purposes. It may be seen that a crack without fiber-bridging exhibits very high stress intensities as the crack grows, while the one in the FML tends to level off to a fairly constant value until the very end of the panel. Excellent agreement between the theoretical and experimental values can be found for the FML over 90% of crack growth range, except in the initial stage where the crack is perhaps under the influence of the notch plasticity.

To check the compatibility conditions at the interface, the difference between the displacements in the aluminum and the prepreg, $v_1 - v_2$, is calculated and mapped onto the panel plane (the x-y plane), as shown in Figure 5. We see that there is a discernible region of discontinuity, with a maximum occurring at $x = a_0$ (the tip of

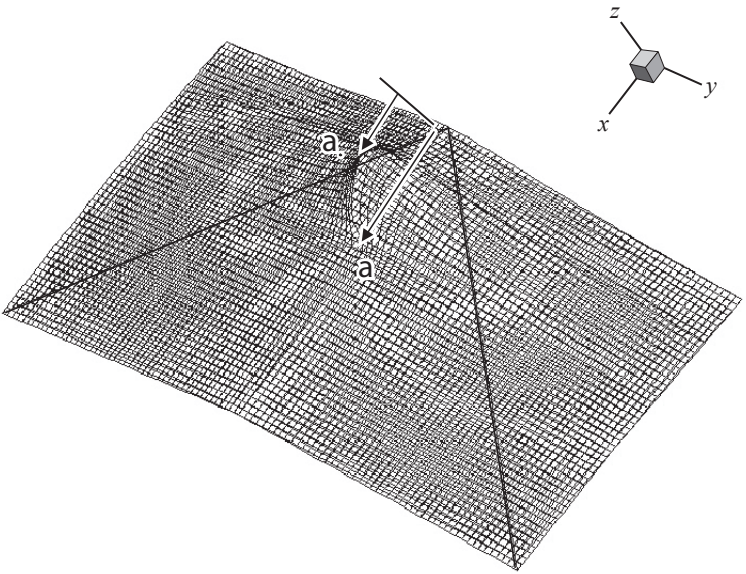

Figure 5. A map of displacement discontinuity at the interface between metal and prepreg layers. $X - Y$ represent the panel plane and Z represents the absolute value of $v_1 - v_2$.

the prepreg crack). This displacement discontinuity region actually corresponds to the shape of the delamination region rather well, as observed in the FML specimens both in our testing program and in others [Guo and Wu 1998]. It should be understood that the delamination problem in the present context within the framework of 2D elasticity is depicted as interfacial sliding, that is, relative in-plane displacement, as shown in Figure 5. Therefore, the criterion of delamination may be defined by how much the delta sliding can be accommodated by the gluing agent, which is determined by the physical properties of the interface. Such properties can be called the interfacial delamination resistance. Beyond that, interfacial breaking may occur, and thus physical delamination occurs. However, descriptions of the physical delamination process are beyond the scope of the theory of elasticity.

In summary, a higher-order laminate plate theory has been developed for fiber-metal laminates that consist of alternating metal and fiber-reinforced prepreg layers. The theory is an extension of the previous higher-order theory for generalized plane-stress problems of isotropic materials, which employs two harmonic anti-plane stress potentials, p and q, in addition to the bi-harmonic plane stress potential. When the displacement compatibility condition is set at the interlaminar interface, these anti-plane stress potentials play the role of load transfer between adjacent layers, particularly when one of them contains a crack. By taking advantage of

the complex variable method that has been developed and matured for monolithic isotropic materials [Muskhelishvili 1953; Lekhnitskiĭ 1981], one can easily extend the complex variable treatment, with the inclusion of an additional analytical function for the anti-plane stress potential to multi-layered bodies, as shown in the previous section. As an example, one mathematical solution is presented in this paper for GLARE-3 containing a fatigue crack, to show the application of the theory to practical problems.

6. Conclusion

1. A higher-order lamination theory has been developed for the plane-stress elasticity of fiber-metal laminates. The new theory employs anti-plane stress potentials to take into consideration possible interlaminar interactions, particularly when defects exist in certain layers, which tend to break the compatibility with the adjacent lamina. In this case, the anti-plane stress potentials produce an additional in-plane stress component that modifies the original (by the classical theory) stress state to re-establish the strain/displacement compatibility.
2. The complex variable representation of the plane-stress problem is modified to include the anti-plane shear stress function and a solution is derived for GLARE-3 (3/2) containing a fiber-bridged fatigue crack.
3. An effective stress intensity factor for GLARE-3 (3/2) is derived in closed form, which agrees with the test results, provided that the initial notch effect for the specimen is appropriately corrected.

Acknowledgment

The work was done under the NRC-IAR, research code 46_QJ0_18, with partial financial support from Bombardier Aerospace.

References

[Ashbee 1993] K. H. G. Ashbee, *Fundamental principles of fiber reinforced composites*, Technomic, Lancaster, PA, 1993.

[Gunnink et al. 1982] J. W. Gunnink, L. B. Vogelesang, and J. Schijve, "Application of a new material (ARALL) in aircraft structures", pp. 990–1000 in *Proc. 13th Congress of the International Council of the Aeronautical Sciences (ICAS)*, Seattle, WA, 1982.

[Guo and Wu 1998] Y. J. Guo and X. R. Wu, "A theoretical model for predicting fatigue crack growth rates in fibre-reinforced metal laminates", *Fatigue Fract. Eng. Mater. Struct.* **21**:9 (1998), 1133–1145.

[Guo and Wu 1999] Y. J. Guo and X. R. Wu, "Bridging stress distribution in center-cracked fiber reinforced metal laminates: modeling and experiment", *Eng. Fract. Mech.* **63**:2 (1999), 147–163.

[Iarve and Pagano 2001] E. V. Iarve and N. J. Pagano, "Singular full-field stresses in composite laminates with open holes", *Int. J. Solids Struct.* **38**:1 (2001), 1–28.

[Lekhnitskiĭ 1981] S. G. Lekhnitskiĭ, *Theory of elasticity of an anisotropic body*, Mir, Moscow, 1981. MR 82d:73001

[Marissen 1988] R. Marissen, *Fatigue crack growth in ARALL: a hybrid aluminum-aramid composite material–crack growth mechanisms and quantitative predictions of the crack growth rates*, Ph.D. thesis, Delf University of Technology, The Netherlands, 1988.

[Muskhelishvili 1953] N. I. Muskhelishvili, *Some basic problems of the mathematical theory of elasticity. Fundamental equations, plane theory of elasticity, torsion and bending*, P. Noordhoff Ltd., Groningen, 1953. MR 15,370d

[Pagano 1978] N. J. Pagano, "Stress fields in composite laminates", *Int. J. Solids Struct.* **14**:5 (1978), 385–400.

[Ritchie et al. 1989] R. O. Ritchie, W. Yu, and R. J. Bucci, "Fatigue crack propagation in ARALL laminates: measurement of the effect of crack-tip shielding from crack bridging", *Eng. Fract. Mech.* **32**:3 (1989), 361–377.

[Roebroeks 1994] G. H. J. J. Roebroeks, "Fibre-metal laminates: recent developments and applications", *Int. J. Fatigue* **16**:1 (1994), 33–42.

[Tsai and Hahn 1980] S. W. Tsai and H. T. Hahn, *Introduction to composite mechanics*, Technomic, Lancaster. PA, 1980.

[Whitney 1987] J. M. Whitney, *Structural analysis of laminated anisotropic plates*, Technomic, Lancaster, PA, 1987.

[Wu and Cheng 1999] X. J. Wu and S. M. Cheng, "A higher-order theory for plane stress conditions of laminates consisting of isotropic layers", *J. Appl. Mech.* (*Trans. ASME*) **66** (1999), 95–100.

[Zhang et al. 2002] Z. Zhang, J. Laliberté, X. J. Wu, and C. Poon, "Generating da/dN curves", Progress Report LM-SMPL-2002-0191, Structures, Materials and Propulsion Laboratory, Institute for Aerospace Research, National Research Council of Canada, 2002.

Received 10 Oct 2005.

XIJIA WU: xijia.wu@nrc-cnrc.gc.ca
Structures and Materials Performance Laboratory, Institute for Aerospace Research, National Research Council of Canada, 1200 Montreal Road, M-13, Ottawa, ON K1A OR6, Canada

ZHONG ZHANG: Zhong.Zhang@nrc-cnrc.gc.ca
Department of Mechanical and Aerospace Engineering, Carleton University, 1125 Coloniel By Drive, Ottawa, ON K1S 5B6, Canada

J. LALIBERTÉ: Jeremy.Laliberte@nrc-cnrc.gc.ca
Structures and Materials Performance Laboratory, Institute for Aerospace Research, National Research Council of Canada, 1200 Montreal Road, M-13, Ottawa, ON K1A OR6, Canada

JOURNAL OF MECHANICS OF MATERIALS AND STRUCTURES
Vol. 1, No. 3, 2006

THE NONLOCAL THEORY SOLUTION OF A MODE-I CRACK IN FUNCTIONALLY GRADED MATERIALS SUBJECTED TO HARMONIC STRESS WAVES

ZHEN-GONG ZHOU, JUN LIANG AND LIN-ZHI WU

In this paper, the dynamic behavior of a finite crack in functionally graded materials subjected to harmonic stress waves is investigated by means of nonlocal theory. The traditional concepts of nonlocal theory are extended to solve the dynamic fracture problem of functionally graded materials. To overcome mathematical difficulties, a one-dimensional nonlocal kernel is used instead of a two-dimensional one for the dynamic problem to obtain the stress fields near the crack tips. To make the analysis tractable, it is assumed that the shear modulus and the material density vary exponentially and vertically with respect to the crack. Using the Fourier transform and defining the jumps of the displacements across the crack surfaces as the unknown functions, two pairs of dual integral equations are derived. To solve the dual integral equations, the jumps of the displacements across the crack surfaces are expanded in a series of Jacobi polynomials. Unlike classical elasticity solutions, it is found that no stress singularities are present near crack tips. Numerical examples are provided to show the effects of the crack length, the parameter describing the functionally graded materials, the frequency of the incident waves, the lattice parameter of the materials and the material constants upon the dynamic stress fields near crack tips.

1. Introduction

A new class of engineered materials, functionally gradient materials (FGMs), has been developed primarily for use in high temperature applications [Koizumi 1993]. The composition of these FGMs, prepared using techniques like power metallurgy, chemical vapor deposition, centrifugal casting, etc., is graded along the thickness. The spatial variation of the material composition results in a medium with varying elastic and physical properties and calls for investigation into the fracture of FGMs under different loading conditions. In particular, the use of the graded material as interlayers in bonded media is one of the highly effective and promising applications to eliminate various shortcomings resulting from stepwise property

Keywords: crack, harmonic stress waves, functionally graded materials, nonlocal theory, dual integral equations.

mismatch inherent in piecewise homogeneous composite media [Lee and Erdogan 1994; Suresh and Mortensen 1977; Choi 2001].

From the viewpoint of fracture mechanics, the presence of a graded interlayer would play an important role in determining crack driving forces and fracture resistance parameters. In an attempt to address the issues pertaining to fracture analysis of bonded media with such transitional interfacial properties, a series of solutions to certain crack problems was obtained by Erdogan and his associates [Delae and Erdogan 1988; Ozturk and Erdogan 1996].

The dynamic crack problem for non-homogeneous composite materials was considered in [Wang et al. 2000] but they considered the FGM layer as a multi-layered homogeneous medium. The crack problem in FGM layers under thermal stresses was studied by Erdogan and Wu [1996]. They considered an unconstrained elastic layer under statically self-equilibrating thermal or residual stresses. More recently, the scattering of harmonic stress waves by a Mode-I crack in functionally graded materials was investigated by use of the Schmidt method in [Zhou et al. 2004]. However, it is found that all the solutions in [Koizumi 1993; Lee and Erdogan 1994; Suresh and Mortensen 1977; Choi 2001; Delae and Erdogan 1988; Ozturk and Erdogan 1996; Wang et al. 2000; Erdogan and Wu 1996; Zhou et al. 2004] contain stress singularities at the crack tips, which is not reasonable according to physical nature. As a result of this, beginning with Griffith, all fracture criteria in use today are based on other considerations, for example, energy, the J-integral [Rice 1968], and strain gradient theory [Xia and Hutchinson 1996].

To overcome the stress singularity in classical elastic fracture theory, Eringen [1977; 1978; 1979] used nonlocal theory to study the stress near tips of a sharp line crack in an isotropic elastic plate subject to uniform tension, shear, and anti-plane shear, and the resulting solutions did not contain any stress singularities. This allows us to use maximum stress as a fracture criterion. Modern nonlocal continuum mechanics has originated and developed in the last four decades as an alternative to these local approaches of zero-range internal interactions. Edelen [1976] contributed some mathematical formalism while Green and Rivlin [1965] simply enunciated some postulates for nonlocal theory. On the other hand, Eringen [1976] contributed not only the complete physics and mathematics of nonlocal theory but also shaped the theory into concrete form, making it viable for practical applications to boundary value problems.

According to nonlocal theory, the stress at a point X in a body depends not only on the strain at point X but also on that at all other points of the body. This is contrary to the classical theory that the stress at a point X in a body depends only on the strain at point X. In [Pan and Takeda 1998], the basic theory of nonlocal elasticity was stated with emphasis on the difference between nonlocal theory and classical continuum mechanics. The basic idea of nonlocal elasticity is to build a

relationship between macroscopic mechanical quantities and microscopic physical quantities within the framework of continuum mechanics.

The constitutive theory of nonlocal elasticity has been developed in [Edelen 1976], in which the elastic modulus is influenced by the microstructure of the material. Other results have been given by the application of nonlocal elasticity to the fields such as a dislocation near a crack [Pan 1992;1994] and fracture mechanics problems [Pan 1995; Pan and Fang 1993]. The literature on the fundamental aspects of nonlocal continuum mechanics is extensive. The results of those concrete problems that have been solved display a remarkable agreement with experimental evidence. This can be used to predict cohesive stress for various materials and the results are close to those obtained in atomic lattice dynamics [Eringen and Kim 1974;1977].

Likewise, a nonlocal study of the secondary flow of viscous fluid in a pipe furnishes a streamlined pattern similar to that obtained experimentally by Eringen [Eringen 1977]. Other examples of the effectiveness of the nonlocal approach are: (i) prediction of the dispersive character of elastic waves demonstrated experimentally (and lacking in classical theory) [Eringen 1972] and (ii) calculation of the velocity of short Love waves whose nonlocal estimates agree better with seismological observations than the local ones [Nowinski 1984b].

Several nonlocal theories have been formulated to address strain-gradient and size effects [Nowinski 1984b]. Recently, some fracture problems [Zhou et al. 1999b; 2002; Zhou and Wang 2002a] in an isotropic elastic material and piezoelectric material have been studied by use of nonlocal theory with a somewhat different method. The traditional concepts of nonlocal theory are extended to solve the fracture problem of piezoelectric materials [Zhou et al. 1999b; 2002; 2002a]. More recently, the traditional concepts of nonlocal theory have also been extended to solve the anti-plane shear fracture problem of functionally graded materials [Zhou and Wang 2006], and the results of the solution in [Zhou and Wang 2006] did not contain any stress singularity. However, to our knowledge, the effect of the lattice parameter on the dynamic stress field near the Mode-I crack tips has not been studied by use of nonlocal theory in functionally graded materials, in which the shear modulus and material density vary exponentially and vertically with respect to the crack. The present work is an attempt to fill this gap in research. Here, we attempt to give a theoretical solution for this problem.

In the present paper, the effect of the lattice parameter of functionally graded materials on dynamic stress fields near Mode-I crack tips is investigated using nonlocal theory in functionally graded materials with the Schmidt method [Morse and Feshbach 1958; Yau 1967]. When the lattice parameter of materials tends to zero, the present problem will revert to the same problem as in [Zhou et al. 2004]. To make the analysis tractable, it is assumed that the shear modulus and the material

density vary exponentially and vertically with respect to the crack. To overcome the mathematical difficulties, a one-dimensional nonlocal kernel is used instead of a two-dimensional one for the dynamic problem of obtaining the stress fields near the crack tips.

The traditional concepts of nonlocal theory are extended to solve the dynamic fracture problem of functionally graded materials. The Fourier transform is applied and a mixed boundary value problem is reduced to two pairs of dual integral equations. To solve the dual integral equations, the jumps of displacements across crack surfaces are expanded in a series of Jacobi polynomials. Numerical solutions are obtained for the stress fields near the crack tips. Contrary to previous results, it is found that the solution does not contain any stress singularities at the crack tips.

2. Formulation of the problem

We assume that there is a crack of length 2ℓ along the x-axis in a functionally graded material plane, as shown in Figure 1. In this paper, the harmonic elastic stress wave is vertically incident. Let ω be the circular frequency of the incident wave, τ_0 a magnitude of the incident wave, and

$$u_0^{(j)}(x, y, t) \quad \text{and} \quad v_0^{(j)}(x, y, t)$$

are components of the displacement vectors. $\tau_{ik0}^{(j)}(x, y, t)$, $(i, k = x, y)$ are components of stress fields. Note that the superscript $j = 1, 2$ corresponds to the half-planes $y \le 0$ and $y \ge 0$ throughout this paper and as shown in Figure 1. Because the incident wave is an harmonic stress wave, all field quantities of

$$u_0^{(j)}(x, y, t), \quad v_0^{(j)}(x, y, t) \quad \text{and} \quad \tau_{ik0}^{(j)}(x, y, t)$$

can be assumed to be of the following forms:

$$[u_0^{(j)}(x, y, t), v_0^{(j)}(x, y, t), \tau_{ik0}^{(j)}(x, y, t)] = [u^{(j)}(x, y), v^{(j)}(x, y), \tau_{ik}^{(j)}(x, y)]e^{-i\omega t}. \quad (1)$$

In what follows, the time dependence of $e^{-i\omega t}$ will be suppressed but understood. Here, the standard superposition technique was used. As discussed in [Eringen et al. 1977] and [Srivastava et al. 1983], the boundary conditions can be written as

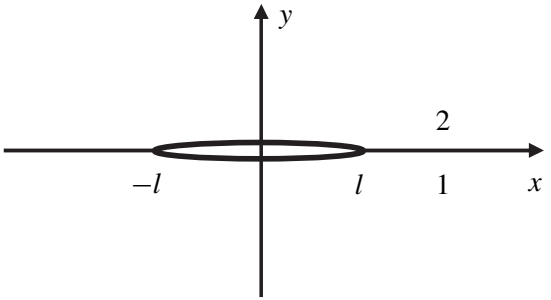

Figure 1. Geometry of a finite crack in the functionally graded materials.

follows. (In this paper, we consider just the perturbation fields.)

$$\tau_{yy}^{(1)}(x,0) = \tau_{yy}^{(2)}(x,0) = -\tau_0,\ \tau_{xy}^{(1)}(x,0) = \tau_{xy}^{(2)}(x,0) = 0,\ |x| \le \ell \tag{2}$$

$$\tau_{yy}^{(1)}(x,0) = \tau_{yy}^{(2)}(x,0),\ \tau_{xy}^{(1)}(x,0) = \tau_{xy}^{(2)}(x,0),\ |x| > \ell \tag{3}$$

$$u^{(1)}(x,0) = u^{(2)}(x,0),\ v^{(1)}(x,0) = v^{(2)}(x,0),\ |x| > \ell \tag{4}$$

$$u^{(j)}(x,y) = 0,\ v^{(j)}(x,y) = 0,\ (j = 1,2) \text{ for } \sqrt{x^2+y^2} \to \infty \tag{5}$$

3. Basic equations of nonlocal functionally graded materials

The basic equations of a plane of linear, non-homogeneous, isotropic, nonlocal functionally graded materials with variable shear modulus, variable material density and vanishing body force are given by Equations (6) and (7) [Suresh and Mortensen 1977; Nowinski 1984b]. (We assume here that the shear modulus and density function vary exponentially and vertically with respect to the crack.)

$$\frac{\partial \tau_{xx}^{(j)}(x,y)}{\partial x} + \frac{\partial \tau_{xy}^{(j)}(x,y)}{\partial y} = -\rho(y)\omega^2 u^{(j)}(x,y), \quad (j = 1,2) \tag{6}$$

$$\frac{\partial \tau_{xy}^{(j)}(x,y)}{\partial x} + \frac{\partial \tau_{yy}^{(j)}(x,y)}{\partial y} = -\rho(y)\omega^2 v^{(j)}(x,y). \quad (j = 1,2) \tag{7}$$

The following relationships were used in Equations (6)–(7)

$$-\rho(y)\omega^2 u^{(j)}(x,y)e^{-i\omega t} = \rho(y)\frac{\partial^2 u_0^{(j)}(x,y,t)}{\partial t^2} = \rho(y)\frac{\partial^2 (u^{(j)}(x,y)e^{-i\omega t})}{\partial t^2}, \tag{8}$$

$$-\rho(y)\omega^2 v^{(j)}(x,y)e^{-i\omega t} = \rho(y)\frac{\partial^2 v_0^{(j)}(x,y,t)}{\partial t^2} = \rho(y)\frac{\partial^2 (v^{(j)}(x,y)e^{-i\omega t})}{\partial t^2}, \tag{9}$$

$$\begin{cases} \tau_{xx}^{(j)}(x,y) = \int_{-\infty}^{\infty}\int_{-\infty}^{\infty} \mu^*(|x'-x|,|y'-y|) \\ \qquad \left[\frac{1+k}{k-1}\frac{\partial u^{(j)}(x',y')}{\partial x'} + \frac{3-k}{k-1}\frac{\partial v^{(j)}(x',y')}{\partial y'}\right]dx'dy', \\ \tau_{yy}^{(j)}(x,y) = \int_{-\infty}^{\infty}\int_{-\infty}^{\infty} \mu^*(|x'-x|,|y'-y|) \\ \qquad \left[\frac{1+k}{k-1}\frac{\partial v^{(j)}(x',y')}{\partial y'} + \frac{3-k}{k-1}\frac{\partial u^{(j)}(x',y')}{\partial x'}\right]dx'dy', \\ \tau_{xy}^{(j)}(x,y) = \int_{-\infty}^{\infty}\int_{-\infty}^{\infty} \mu^*(|x'-x|,|y'-y|) \\ \qquad \left[\frac{\partial v^{(j)}(x',y')}{\partial x'} + \frac{\partial u^{(j)}(x',y')}{\partial y'}\right]dx'dy', \end{cases} \quad (j=1,2), \tag{10}$$

where $k = 3-4\eta$ for the plane strain state and $k = (3-\eta)/(1+\eta)$ for the generalized plane stress state. $\mu^*(|x'-x|,|y'-y|)$ is the shear modulus, $\rho(y)$ is the material density. In this paper, we consider only the plane strain problem. η is the Poisson's ratio, and is taken to be a constant, owing to the fact that its variation within a practical range has a rather insignificant influence on the stress fields near the crack tips.

In the constitutive Equations (10), the only difference from classical elastic theory is that the stress

$$\tau_{ik}^{(j)}(x,y)(i,k=x,y)$$

at a point (x, y) depends on

$$u_{,k}^{(j)}(x,y) \quad \text{and} \quad v_k^{(j)}(x,y)$$

at all points of the body. As discussed in [Eringen and Kim 1974; 1977; Eringen 1977], it can be assumed in the form for which the dispersion curves of plane elastic waves coincide with those known in lattice dynamics. Among several possible curves the following has been found to be very useful.

$$\mu^*(|x'-x|,|y'-y|) = \mu(y')\alpha(|x'-x|,|y'-y|), \tag{11}$$

where $\alpha(|x'-x|,|y'-y|)$ is known as the influence function.

Crack problems in functionally graded materials do not appear to be analytically tractable for arbitrary variations of material properties. Usually one tries to generate forms of non-homogeneity for which the problem becomes tractable. As with

the treatment of the crack problem for isotropic non-homogeneous materials in [Koizumi 1993; Lee and Erdogan 1994; Suresh and Mortensen 1977; Choi 2001; Delae and Erdogan 1988; Ozturk and Erdogan 1996], we assume that the shear modulus and the material density are described by

$$\mu(y) = \mu_0\, e^{\gamma y}, \qquad \rho(y) = \rho_0\, e^{\gamma y}, \tag{12}$$

where γ is a constant that describes the functionally graded materials; μ_0 and ρ_0 are the shear modulus and the material density along $y = 0$, respectively; and $\gamma \neq 0$ is the case for the functionally graded materials. When $\gamma = 0$, it returns to the homogeneous material case.

Substituting Equations (10) for Equations (6)–(7) and using Equations (11)–(12) and the Green–Gauss theorem leads to

$$\begin{aligned}
&\mu_0 \int_{-\infty}^{\infty}\int_{-\infty}^{\infty} \alpha|x'-x|, |y'-y|)\, e^{\gamma y'} \\
&\left[(1+k)\frac{\partial^2 u^{(j)}}{\partial x'^2} + (k-1)\,\frac{\partial^2 u^{(j)}}{\partial y'^2} + 2\,\frac{\partial^2 v^{(j)}}{\partial x'\partial y'} + (k-1)\gamma\left(\frac{\partial u^{(j)}}{\partial y'} + \frac{\partial v^{(j)}}{\partial x'}\right)\right] dx'dy' \\
&\qquad - \int_{-\ell}^{\ell} \alpha|x'-x|, |0|)\big[\sigma_{xy}^{(j)}(x',0)\big]dx' \;=\; -\rho(y)\omega^2 u^{(j)}(x,y)
\end{aligned} \tag{13}$$

$$\begin{aligned}
&\mu_0 \int_{-\infty}^{\infty}\int_{-\infty}^{\infty} \alpha|x'-x|, |y'-y|)\, e^{\gamma y'} \\
&\left\{(1+k)\frac{\partial^2 v^{(j)}}{\partial y'^2} + (k-1)\,\frac{\partial^2 v^{(j)}}{\partial x'^2} + 2\frac{\partial^2 u^{(j)}}{\partial x'\partial y'} + \gamma\left[(1+k)\frac{\partial v^{(j)}}{\partial y'} + (3-k)\frac{\partial u^{(j)}}{\partial x'}\right]\right\} dx'dy' \\
&\qquad - \int_{-\ell}^{\ell} \alpha|x'-x|, |0|)\,\big[\sigma_{yy}^{(j)}(x',0)\big]dx' = -\rho(y)\omega^2 v^{(j)}(x,y),
\end{aligned} \tag{14}$$

where

$$\sigma_{yy}^{(j)}(x,y) = \mu_0 e^{\gamma y}\left[\frac{1+k}{k-1}\,\frac{\partial v^{(j)}(x,y)}{\partial y} + \frac{3-k}{k-1}\,\frac{\partial u^{(j)}(x,y)}{\partial x}\right] \tag{15}$$

and

$$\sigma_{xy}^{(j)}(x,y) = \mu_0 e^{\gamma y}\left[\frac{\partial v^{(j)}(x,y)}{\partial x} + \frac{\partial u^{(j)}(x,y)}{\partial y}\right]. \tag{16}$$

The bold brackets in Equations (13)–(14) indicate a jump at the crack line, that is,

$$\big[\sigma_{xy}^{(j)}(x,0)\big] = \sigma_{xy}^{(2)}(x,0^+) - \sigma_{xy}^{(1)}(x,0^-), \tag{17}$$

$$\big[\sigma_{yy}^{(j)}(x,0)\big] = \sigma_{yy}^{(2)}(x,0^+) - \sigma_{yy}^{(1)}(x,0^-); \tag{18}$$

Expressions (15)–(16) are the classical constitutive equations. Here the surface integral may be dropped since the displacement field vanishes at infinity as shown in Equations (13)–(14).

4. The dual integral equations

As discussed in [Eringen et al. 1977], we see that

$$[\sigma_{xy}^{(j)}(x,0)] = 0\,, \qquad [\sigma_{yy}^{(j)}(x,0)] = 0. \tag{19}$$

What remains now is to solve the integrodifferential equations (13)–(14) for functions $u^{(j)}(x, y)$ and $v^{(j)}(x, y)$, $(j = 1, 2)$. It is impossible to obtain a rigorous solution at the present stage. It seems obvious that in the solution of such a problem we encounter serious, if not insurmountable, mathematical difficulties and must resort to an approximation procedure. In the given problem, as discussed in [Nowinski 1984b; 1984a; Zhou and Wang 2002b], we assume that the nonlocal interaction in the y direction is ignored. This is purely an assumption for mathematical tractability. In view of our assumptions, we can state that

$$\begin{cases} \alpha|x'-x|, |y'-y|) = \alpha_0(|x'-x|)\delta(y'-y), \\ \alpha_0(|x'-x|) = \frac{1}{\sqrt{\pi}}\ (\beta\alpha \exp[-(\beta/\alpha^2(x'-x)^2], \end{cases} \tag{20}$$

where β is a constant and can be determined by experiment, and where a is the characteristic length. The characteristic length may be selected according to the range and sensitivity of the physical phenomena. For instance, for a perfect crystal, a may be taken as the lattice parameter. For a granular material, a may be considered to be the average granular distance and, for a fiber composite, the fiber distance, etc. In the present paper, a is taken to be the lattice parameter. From Equations (13)–(14), we have

$$\int_{-\infty}^{\infty} \alpha_0(|x'-x|)e^{\gamma y}\left[(1+k)\frac{\partial^2 u^{(j)}}{\partial x'^2} + (k-1)\frac{\partial^2 u^{(j)}}{\partial y^2} + 2\frac{\partial^2 v^{(j)}}{\partial x'\partial y} + (k-1)\gamma\left(\frac{\partial u^{(j)}}{\partial y} + \frac{\partial v^{(j)}}{\partial x'}\right)\right]dx' = -\frac{\rho_0}{\mu_0}\omega^2 u^{(j)}, \tag{21}$$

$$\int_{-\infty}^{\infty} \alpha_0(|x'-x|)e^{\gamma y}\left\{(1+k)\frac{\partial^2 v^{(j)}}{\partial y^2} + (k-1)\frac{\partial^2 v^{(j)}}{\partial x'^2} + 2\frac{\partial^2 u^{(j)}}{\partial x'\partial y} + \gamma\left[(1+k)\frac{\partial v^{(j)}}{\partial y} + (3-k)\frac{\partial u^{(j)}}{\partial x'}\right]\right\}dx' = -\frac{\rho_0}{\mu_0}\omega^2 v^{(j)}. \tag{22}$$

To solve the problem, the Fourier transform of Equations (21)–(22) with x can be given as follows:

$$-s^2(1+k)\bar{u}^{(j)} + (k-1)\frac{\partial^2 \bar{u}^{(j)}}{\partial y^2} - 2s\frac{\partial \bar{v}^{(j)}}{\partial y} + (k-1)\gamma\left(\frac{\partial \bar{u}^{(j)}}{\partial y} - s\bar{v}^{(j)}\right) = -\frac{\rho_0}{\mu_0\bar{\alpha}_0}\omega^2\bar{u}^{(j)}, \quad (23)$$

$$(1+k)\frac{\partial^2 \bar{v}^{(j)}}{\partial y^2} - s^2(k-1)\bar{v} + 2s\frac{\partial \bar{u}^{(j)}}{\partial y} + \gamma\left[(1+k)\frac{\partial \bar{v}^{(j)}}{\partial y} + s(3-k)\bar{u}\right] = -\frac{\rho_0}{\mu_0\bar{\alpha}_0}\omega^2\bar{v}^{(j)}. \quad (24)$$

Throughout the paper a superposed bar indicates the Fourier transform.

Because of the symmetry, it suffices to consider the problem for $x \geq 0$, $|y| < \infty$. The above systems governing Equations (23)–(24) are solved using the Fourier integral transform to obtain the general expressions for the displacement components as

$$\begin{cases} u^{(1)}(x, y) = \frac{2}{\pi}\int_0^\infty \sum_{i=1}^2 A_i(s)\, e^{-\lambda_{i+2}y}\sin(sx)\, ds, \\ v^{(1)}(x, y) = \frac{2}{\pi}\int_0^\infty \sum_{i=1}^2 m_{i+2}(s)A_i(s)\, e^{-\lambda_{i+2}y}\cos(sx)\, ds\ , \end{cases} \quad (y \geq 0) \quad (25)$$

$$\begin{cases} u^{(2)}(x, y) = \frac{2}{\pi}\int_0^\infty \sum_{i=1}^2 B_i(s)\, e^{-\lambda_i y}\sin(sx)\, ds, \\ v^{(2)}(x, y) = \frac{2}{\pi}\int_0^\infty \sum_{i=1}^2 m_i(s)B_i(s)\, e^{-\lambda_i y}\cos(sx)\, ds, \end{cases} \quad (y \geq 0) \quad (26)$$

and from Equations (15) and (16), the stress components are obtained as

$$\begin{cases} \sigma_{yy}^{(1)}(x, y) = \frac{2\mu_0 e^{\gamma y}}{\pi(k-1)}\int_0^\infty \sum_{i=1}^2 [-(k+1)m_{i+2}(s)\lambda_{i+2}], \\ \qquad +s(3-k)]A_i(s)\, e^{-\lambda_{i+2}y}\cos(sx)\, ds, \\ \sigma_{xy}^{(1)}(x, y) = \frac{2\mu_0 e^{\gamma y}}{\pi}\int_0^\infty \sum_{i=1}^2 [-\lambda_{i+2} - m_{i+2}(s)s]A_i(s)e^{-\lambda_{i+2}y}\sin(sx)\, ds, \end{cases} \quad (y \leq 0) \quad (27)$$

$$\begin{cases} \sigma_{yy}^{(2)}(x, y) = \frac{2\mu_0 e^{\gamma y}}{\pi(k-1)}\int_0^\infty \sum_{i=1}^2 [-(k+1)m_i(s)\lambda_i, \\ \qquad +s(3-k)]B_i(s)\, e^{-\lambda_i y}\cos(sx)\, ds, \\ \sigma_{xy}^{(2)}(x, y) = \frac{2\mu_0 e^{\gamma y}}{\pi}\int_0^\infty \sum_{i=1}^2 [-\lambda_i - m_i(s)s]B_i(s)e^{-\lambda_i y}\sin(sx)\, ds, \end{cases} \quad (y \geq 0) \quad (28)$$

where s is the transform variable. A_1, A_2, B_1 and B_2 are arbitrary unknowns, and $\lambda_i(s)$ $(i = 1, 2, 3, 4)$ are the roots of the characteristic equation

$$\lambda^4 - 2\lambda^3\gamma + (\gamma^2 - 2s^2)\lambda^2 + 2\gamma s^2\lambda + s^4 + \frac{3-k}{k+1}\gamma^2 s^2 + \frac{2k\rho_0\omega^2}{(k+1)\mu_0\alpha_0(s)}(-s^2 + \lambda^2 - \gamma\lambda) + \frac{k-1}{k+1}\left(\frac{\rho_0\omega^2}{\mu_0\alpha_0(s)}\right)^2 = 0, \quad (29)$$

and $m_i(s)$ $(i = 1, 2, 3, 4)$ is expressed for each root $\lambda_i(s)$ as

$$m_i(s) = \frac{-(k+1)s^2 + (k-1)\lambda_i^2 - \gamma(k-1)\lambda_i}{-2s\lambda_i + s\gamma(k-1)}. \quad (30)$$

Equation (29) can be rewritten in the following form

$$(\lambda^2 - \lambda\gamma - s^2)^2 + \frac{3-k}{k+1}\gamma^2 s^2 + \frac{2kc_1^2(\lambda^2 - \gamma\lambda - s^2)}{k+1} + \frac{c_1^4(k-1)}{k+1} = 0, \quad (31)$$

where

$$c_1^2 = \frac{c^2}{\alpha_0(s)} \quad \text{and} \quad c^2 = \frac{\rho_0\omega^2}{\mu_0}.$$

The roots may be obtained as

$$\lambda_1 = \frac{1}{2}\left(\gamma + \sqrt{\gamma^2 - 4\left(\frac{kc_1^2}{k+1} - s^2 - \sqrt{\frac{c_1^4}{(k+1)^2} - \frac{s^2\gamma^2(3-k)}{k+1}}\right)}\right), \quad (32)$$

$$\lambda_2 = \frac{1}{2}\left(\gamma + \sqrt{\gamma^2 - 4\left(\frac{kc_1^2}{k+1} - s^2 + \sqrt{\frac{c_1^4}{(k+1)^2} - \frac{s^2\gamma^2(3-k)}{k+1}}\right)}\right), \quad (33)$$

$$\lambda_3 = \frac{1}{2}\left(\gamma - \sqrt{\gamma^2 - 4\left(\frac{kc_1^2}{k+1} - s^2 - \sqrt{\frac{c_1^4}{(k+1)^2} - \frac{s^2\gamma^2(3-k)}{k+1}}\right)}\right), \quad (34)$$

$$\lambda_4 = \frac{1}{2}\left(\gamma - \sqrt{\gamma^2 - 4\left(\frac{kc_1^2}{k+1} - s^2 + \sqrt{\frac{c_1^4}{(k+1)^2} - \frac{s^2\gamma^2(3-k)}{k+1}}\right)}\right). \quad (35)$$

From Equations (25)–(28), we can see that there are four unknown constants (in Fourier space they are functions of s), that is, A_1, A_2, B_1, and B_2, which can be obtained from the boundary conditions (2)–(4). To solve the present problem, the

jumps of the displacements across the crack surfaces can be defined as follows:

$$f_1(x) - u^{(2)}(x,0) - u^{(1)}(x,0), \tag{36}$$

$$f_2(x) - v^{(2)}(x,0) - v^{(1)}(x,0), \tag{37}$$

where $f_1(x)$ is an odd function and $f_2(x)$ an even one.

Applying the Fourier transforms and the boundary conditions (2)–(4), we obtain

$$[X_1]\begin{bmatrix} B_1(s) \\ B_2(s) \end{bmatrix} - [X_2]\begin{bmatrix} A_1(s) \\ A_2(s) \end{bmatrix} = \begin{bmatrix} \bar{f}_1(s) \\ \bar{f}_2(s) \end{bmatrix}, \tag{38}$$

$$[X_3]\begin{bmatrix} B_1(s) \\ B_2(s) \end{bmatrix} = [X_4]\begin{bmatrix} A_1(s) \\ A_2(s) \end{bmatrix}, \tag{39}$$

where the matrices $[X_i]$ $(i = 1, 2, 3, 4)$ can be seen in the Appendix.

From Equations (10), and using Equations (20), we have

$$\tau_{yy}^{(2)}(x, y) = \int_{-\infty}^{\infty} \alpha_0(|x' - x|)\sigma_{yy}^{(2)}(x', y)\, dx', \tag{40}$$

$$\tau_{xy}^{(2)}(x, y) = \int_{-\infty}^{\infty} \alpha_0(|x' - x|)\sigma_{xy}^{(2)}(x', y)\, dx'. \tag{41}$$

Using the relations as follows [Gradshteyn and Ryzhik 1980]

$$I_1 = \int_{-\infty}^{\infty} \exp(-px'^2) \begin{Bmatrix} \sin\xi(x'+x) \\ \cos\xi(x'+x) \end{Bmatrix} dx' = (\pi/p)^{\frac{1}{2}} \exp\left(\frac{-\xi^2}{4p}\right) \begin{Bmatrix} \sin(\xi x) \\ \cos(\xi x) \end{Bmatrix}, \tag{42}$$

we have

$$\tau_{yy}^{(2)}(x, y) = \frac{2\mu_0 e^{\gamma y}}{\pi(k-1)} \int_0^{\infty} e^{-\frac{s^2}{4p}} \left[\sum_{i=1}^{2} g_i(s)B_i(s) + \sum_{i=1}^{2} g_{i+2}(s)A_i(s) \right] \cos(sx)\, ds, \tag{43}$$

$$\tau_{xy}^{(2)}(x, y) = \frac{2\mu_0 e^{\gamma y}}{\pi} \int_0^{\infty} e^{-\frac{s^2}{4p}} \left[\sum_{i=1}^{2} h_i(s)B_i(s) + \sum_{i=1}^{2} h_{i+2}(s)A_i(s) \right] \sin(sx)\, ds, \tag{44}$$

where

$$g_i(s) = -(k+1)m_i(s)\lambda_i + s(3-k) \quad \text{and} \quad h_i(s) = -\lambda_i - m_i(s)s,$$

with $(i = 1, 2, 3, 4)$, $p = \left(\frac{\beta}{a}\right)^2$.

By solving the four expressions in Equations (38)–(39) with four unknown functions A_1, A_2, B_1 and B_2, substituting those solutions for Equations (43)–(44), and applying the boundary conditions (2)–(4) to the results, we have

$$\begin{aligned}\tau_{yy}^{(1)}(x,0) &= \tau_{yy}^{(2)}(x,0)\\ &= \frac{2\mu_0}{\pi(k-1)}\int_0^\infty e^{-\frac{s^2}{4p}}[d_1(s)\bar{f}_1(s)+d_2(s)\bar{f}_2(s)]\cos(sx)\,ds\\ &= -\tau_0, \qquad 0\le x\le \ell, \end{aligned} \tag{45}$$

$$\begin{aligned}\tau_{xy}^{(1)}(x,0) &= \tau_{xy}^{(2)}(x,0)\\ &= \frac{2\mu_0}{\pi}\int_0^\infty e^{-\frac{s^2}{4p}}[d_3(s)\bar{f}_1(s)+d_4(s)\bar{f}_2(s)]\sin(sx)\,ds\\ &= 0, \qquad 0\le x\le \ell, \end{aligned} \tag{46}$$

$$\int_0^\infty \bar{f}_1(s)\sin(sx)ds = 0, \qquad x>\ell, \tag{47}$$

$$\int_0^\infty \bar{f}_2(s)\cos(sx)ds = 0, \qquad x>\ell, \tag{48}$$

where

$$\begin{aligned} d_1(s) &= g_1(s)e_{11}(s)+g_2(s)e_{21}(s)+g_3(s)c_{11}(s)+g_4(s)c_{21}(s),\\ d_2(s) &= g_1(s)e_{12}(s)+g_2(s)e_{22}(s)+g_3(s)c_{12}(s)+g_4(s)c_{22}(s),\\ d_3(s) &= h_1(s)e_{11}(s)+h_2(s)e_{21}(s)+h_3(s)c_{11}(s)+h_4(s)c_{21}(s),\\ d_4(s) &= h_1(s)e_{12}(s)+h_2(s)e_{22}(s)+h_3(s)c_{12}(s)+h_4(s)c_{22}(s), \end{aligned}$$

and where $e_{ij}(s)$ and $c_{ij}(s)$ $(i=1,2,\ j=1,2)$ are non-zero constants, as can be seen in the Appendix. To determine the unknown functions $\bar{f}_1(s)$ and $\bar{f}_2(s)$, the dual integral equations in (45)–(48) must be solved. For the lattice parameter $a\to 0$, then

$$d_1(s)e^{-\frac{s^2}{4p}}, \qquad (i=1,2,3,4)$$

is equal to a non-zero constant and Equations (45)–(48) reduce to two pairs of dual integral equations for the same problem in the classical functionally graded materials case.

5. Solution of the dual integral equations

The only difference between the classical and nonlocal equations is in the influence functions $d_i(s)$ $(i = 1, 2, 3, 4)$. It is logical to utilize the classical solution to convert the system of equations in (45)–(48) to two pairs of integral equations of the second kind, since the latter is generally better behaved. For the lattice parameter $a \to 0$, then

$$d_1(s)e^{-\frac{s^2}{4p}}, \qquad (i = 1, 2, 3, 4)$$

is equal to a non-zero constant and Equations (45)–(48) reduce to two pairs of dual integral equations for the same problem in classical elasticity. In the case of $(a \to 0)$, the present problem is the same as that discussed in [Zhou et al. 2004]. As we find in [Eringen et al. 1977], the dual integral equations (48)–(51) cannot be transformed into a Fredholm integral equation of the second kind, because

$$d_1(s)e^{-\frac{s^2}{4p}}/s, \qquad (i = 1, 2, 3, 4)$$

does not tend to a constant C $(C \neq 0)$ for $s \to \infty$. Of course, the dual equations (45)–(48) can be considered to be a single integral equation of the first kind with discontinuous kernel. It is well known in the literature that integral equations of the first kind are generally ill-posed in the sense of Hadamard, that is, small perturbations of the data can yield arbitrarily large changes in the solution. This makes the numerical solution of such equations quite difficult. To overcome this difficulty, the Schmidt method [Morse and Feshbach 1958; Yau 1967] is used to solve the dual integral equations (45)–(48).

From the nature of the displacement along the crack line, it can be shown that the jumps of the displacements across the crack surface are finite, differentiable, and continuum functions. Hence, the jumps of the displacements across the crack surface can be expanded by the following series:

$$f_1(x) = \sum_{n=0}^{\infty} a_n P_{2n+1}^{(\frac{1}{2},\frac{1}{2})}\left(\frac{x}{\ell}\right)\left(1 - \frac{x^2}{\ell^2}\right)^{\frac{1}{2}}, \qquad \text{for } 0 \le x \le \ell, \tag{49}$$

$$f_1(x) = 0, \qquad \text{for } x > \ell, \tag{50}$$

$$f_2(x) = \sum_{n=0}^{\infty} b_n P_{2n}^{(\frac{1}{2},\frac{1}{2})}\left(\frac{x}{\ell}\right)\left(1 - \frac{x^2}{\ell^2}\right)^{\frac{1}{2}}, \qquad \text{for } 0 \le x \le \ell, \tag{51}$$

$$f_2(x) = 0, \qquad \text{for } x > \ell, \tag{52}$$

where a_n and b_n are unknown coefficients and

$$P_n^{(\frac{1}{2},\frac{1}{2})}(x)$$

is a Jacobi polynomial [Gradshteyn and Ryzhik 1980].

The Fourier transforms of Equations (49)–(52) are [Erdelyi 1954]

$$\bar{f}_1(s) = \sum_{n=0}^{\infty} a_n G_n^{(1)} \frac{1}{s} J_{2n+2}(s\ell) \ , \quad G_n^{(1)} = \sqrt{\pi}\,(-1)^n \frac{\Gamma(2n+2+\frac{1}{2})}{(2n+1)!}, \tag{53}$$

$$\bar{f}_2(s) = \sum_{n=0}^{\infty} b_n G_n^{(2)} \frac{1}{s} J_{2n+1}(s\ell) \ , \quad G_n^{(2)} = \sqrt{\pi}\,(-1)^n \frac{\Gamma(2n+1+\frac{1}{2})}{(2n)!}, \tag{54}$$

where $\Gamma(x)$ and $J_n(x)$ are the Gamma and Bessel functions, respectively.

Substituting Equations (53)–(54) for Equations (45)–(48), it can be shown that Equations (47)–(48) are automatically satisfied. Equations (45)–(46) reduce to

$$\frac{2\mu_0}{\pi(k-1)} \sum_{n=0}^{\infty} \int_0^{\infty} \frac{1}{s} e^{-\frac{s^2}{4p}} [d_1(s) a_n G_n^{(1)} J_{2n+2}(sl) + d_2(s) b_n G_n^{(2)} J_{2n+2}(sl)] \cos(sx) ds = -\tau_0, \quad 0 \le x \le \ell, \tag{55}$$

$$\sum_{n=0}^{\infty} \int_0^{\infty} \frac{1}{s} e^{-\frac{s^2}{4p}} [d_3(s) a_n G_n^{(1)} J_{2n+2}(sl) + d_4(s) b_n G_n^{(2)} J_{2n+1}(sl)] \sin(sx) ds = 0 \ , \quad 0 \le x \le \ell. \tag{56}$$

The multi-valued functions $\lambda_1, \lambda_2, \lambda_3$ and λ_4 have branch points. We choose the branches such that $\Re(\lambda_1) \ge 0$, $\Re(\lambda_2) \ge 0$, $\Re(\lambda_3) \le 0$ and $\Re(\lambda_4) \le 0$ are on the path of integration. For large s, the integrands of Equations (55)–(56) almost all decrease exponentially. So the semi-infinite integral in Equations (55)–(56) can be evaluated numerically by Filon's method. Equations (55)–(56) can now be solved for the coefficients a_n and b_n by the Schmidt method [Morse and Feshbach 1958; Yau 1967]. Briefly, Equations (55)–(56) can be rewritten as

$$\sum_{n=0}^{\infty} a_n E_n^*(x) + \sum_{n=0}^{\infty} b_n F_n^*(x) = U_0(x) \ , \quad 0 \le x \le \ell, \tag{57}$$

$$\sum_{n=0}^{\infty} a_n G_n^*(x) + \sum_{n=0}^{\infty} b_n H_n^*(x) = 0 \ , \quad 0 \le x \le \ell, \tag{58}$$

where $E_n^*(x)$, $F_n^*(x)$, $G_n^*(x)$ and $H_n^*(x)$ and $U_0(x)$ are known functions, and a_n and b_n are unknown coefficients.

From Equation (58), we obtain

$$\sum_{n=0}^{\infty} b_n H_n^*(x) \ = \ -\sum_{n=0}^{\infty} a_n G_n^*(x) \ . \tag{59}$$

This can now be solved for coefficients b_n by the Schmidt method. Here, the form $-\sum_{n=0}^{\infty} a_n G_n^*(x)$ will be considered temporarily as a known function. A set of functions $P_n(x)$, which satisfies the orthogonality condition

$$\int_0^{\ell} P_m(x) P_n(x) dx = N_n \delta_{mn} \ , \quad N_n = \int_0^{\ell} P_n^2(x)\, dx, \tag{60}$$

can be constructed from the function, $H_n^*(x)$, such that

$$P_n(x) = \sum_{i=0}^{n} \frac{M_{in}}{M_{mn}}, H_i^*(x), \tag{61}$$

where M_{ij} is the cofactor of the element d_{ij} of D_n, which is defined as

$$D_n = \begin{bmatrix} d_{00}, d_{01}, d_{02}, \ldots, d_{0n} \\ d_{10}, d_{11}, d_{12}, \ldots, d_{1n} \\ d_{20}, d_{21}, d_{22}, \ldots, d_{2n} \\ \cdots \\ \cdots \\ \cdots \\ d_{n0}, d_{n1}, d_{n2}, \ldots, d_{nn} \end{bmatrix} \ , \quad d_{ij} = \int_0^{\ell} H_i^*(x) H_j^*(x)\, dx. \tag{62}$$

Using Equations (59)–(62), we obtain

$$b_n = \sum_{j=n}^{\infty} \frac{M_{nj}}{M_{jj}} \quad \text{with} \quad q_j = -\sum_{i=0}^{\infty} a_i \frac{1}{N_j} \int_0^{\ell} G_i^*(x) P_j(x)\, dx. \tag{63}$$

This can be rewritten as

$$b_n = \sum_{i=0}^{\infty} a_i K_{in}^* \ , \quad K_{in}^* = -\sum_{j=n}^{\infty} q_j \frac{M_{nj}}{N_j M_{jj}} \int_0^{\ell} G_i^*(x) P_j(x) dx \ . \tag{64}$$

Substituting Equation (64) for Equation (57), we obtain

$$\sum_{n=0}^{\infty} a_n Y_n^*(x) = U_0(x) \ , \quad Y_n^*(x) = E_n^*(x) + \sum_{i=0}^{\infty} K_{ni}^* F_i^*(x) \ . \tag{65}$$

This can now be solved for the coefficients a_n by the Schmidt method, again as mentioned above. With the aid of Equation (64), the coefficients b_n can be obtained.

6. Numerical calculations and discussion

The coefficients a_n and b_n are known, so that the entire stress field can be obtained. In the case of the present study, $\tau_{yy}^{(1)}(x, y)$ and $\tau_{xy}^{(1)}(x, y)$ along the crack line can

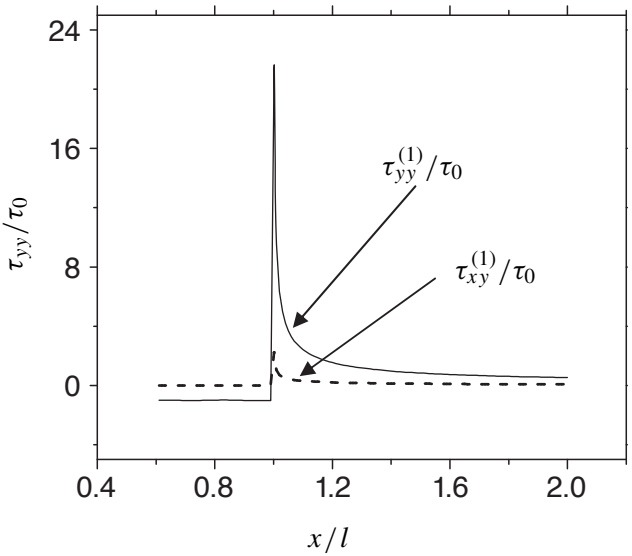

Figure 2. The stress along the crack line versus x/l for $l = 1.0$, $wl/c = 0.2$, $\gamma l = 0.4$, $\eta = 0.23$ and $a/\beta l = 0.003$.

be expressed as

$$\tau_{yy} = \tau_{yy}^{(1)}(x,0) = \frac{2\mu_0}{\pi(k-1)} \sum_{n=0}^{\infty} \int_0^{\infty} \frac{1}{s} e^{-\frac{s^2}{4p}} \tag{66}$$

$$[d_1(s) a_n G_n^{(1)} J_{2n+2}(s\ell) + d_2(s) b_n G_n^{(2)} J_{2n+2}(s\ell)] \cos(sx)\, ds,$$

$$\tau_{xy} = \tau_{xy}^{(1)}(x,0) = \frac{2\mu_0}{\pi} \sum_{n=0}^{\infty} \int_0^{\infty} \frac{1}{s} e^{-\frac{s^2}{4p}} \tag{67}$$

$$[d_3(s) a_n G_n^{(1)} J_{2n+2}(s\ell) + d_4(s) b_n G_n^{(2)} J_{2n+2}(s\ell)] \sin(sx)\, ds.$$

When the lattice parameter $a \neq 0$, the semi-infinite integration and the series in Equations (66)–(67) are convergent for any variable x, and they give finite stresses along $y = 0$, so there are no stress singularities at crack tips. For $-\ell < x < \ell$, $\tau_{yy}^{(1)}(x,0)/\tau_0$ is very close to negative unity. Hence, the solution of this paper can also be proved to satisfy the boundary conditions (2). For $x > \ell$, $\tau_{yy}^{(1)}(x,0)/\tau_0$ possesses finite values diminishing from a finite value at $x = \ell$ to zero at $x = \infty$. Since $a/\beta\ell > 1/100$ represents a crack length of less than 100 atomic distances [Eringen et al. 1977; Eringen 1978; 1979], and, for such submicroscopic sizes, other serious questions arise regarding the interatomic arrangements and force laws, we do not

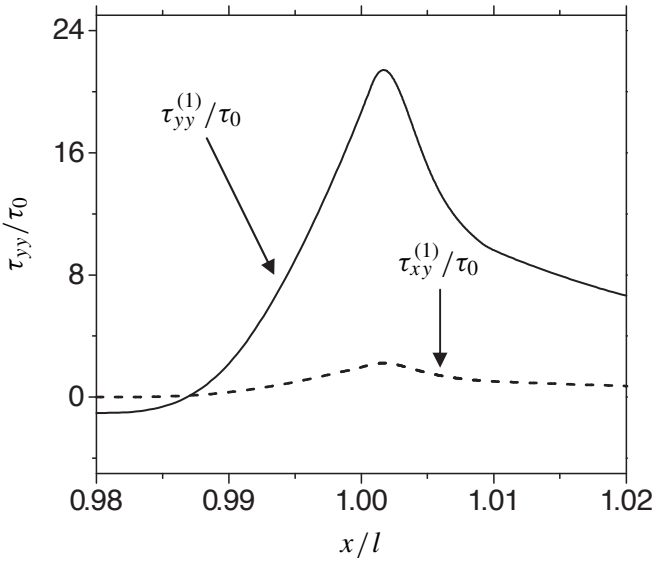

Figure 3. The locally enlarged graph of Figure 2 near the crack tip.

pursue valid solutions at such small crack sizes. The semi-infinite integrals that occur are easily evaluated because of the rapid diminution of the integrands. From [Itou 1978; Zhou et al. 1999a], it can be seen that the Schmidt method is performed satisfactorily if the first ten terms of the infinite series in Equations (57)–(58) are retained. The results of this paper are shown in Figures 2–8. From the results, the following observations are very significant:

(i) Nonlocal theory can be used to solve dynamic fracture problems in functionally graded materials subjected to harmonic stress waves. The traditional concepts of nonlocal theory can be extended to solve the fracture problem of functionally graded materials. When the lattice parameter, $a \to 0$ the present problem will revert to the same problem as discussed in [Zhou et al. 2004]. The dynamic stress fields can be directly obtained in the present paper. However, the dynamic stress fields cannot be directly obtained in [Zhou et al. 2004]; only the stress intensity factors are given there.

(ii For $a/\beta\ell \neq 0$, it can be proved that the semi-infinite integration in Equations (66)–(67) and the series in Equations (66)–(67) are convergent for any variable x. So the stresses give finite values all along the crack line, as shown in Figures 2 and 3. Contrary to the classical theory solution, we find that no stress singularities are present at the crack tips, and also that the present results converge to the classical ones when far away from the crack tips. The nonlocal

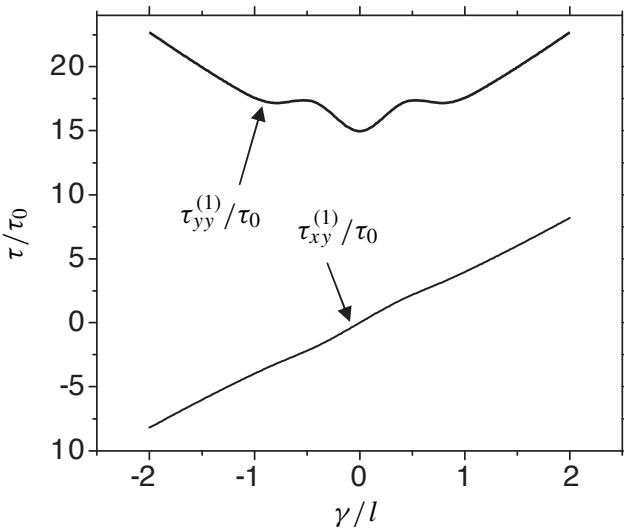

Figure 4. The stress at the crack tip versus γl for $a/\beta l = 0.003$, $wl/c = 0.2$, $\eta = 0.23$ and $l = 1.0$.

elastic solutions yield a finite hoop stress at the crack tips, thus allowing us to use the maximum stress as a fracture criterion. The maximum stress does not occur at the crack tips, but slightly away from it, as shown in Figure 3. This phenomenon has been thoroughly substantiated in [Eringen 1983]. The distance between the crack tip and the maximum stress point is very small, and it depends on the crack length, the lattice parameter, the parameter describing the functionally graded materials, and the frequency of the incident waves. As shown in Figures 2 and 3, it can be seen that the shear stress $\tau_{xy}^{(1)}$ is equal to zero for $|x| < \ell$. However, the shear stress $\tau_{xy}^{(1)}$ is not equal to zero for $x \geq \ell$. This inequality is caused by the shear modulus and mass density not being symmetric with respect to the cracked plane. The shear stress is smaller than the normal stress along the crack line.

(iii) Stresses at the crack tips become infinite as the lattice parameter $a \to 0$. This is the classical continuum limit of square root singularity. This can be shown from Equations (45)–(48). For $a \to 0$,

$$e^{-\frac{s^2}{4p}} = 1,$$

Equations (45)–(48) will reduce to the dual integral equations for the same problem in the classical functionally graded materials [Zhou et al. 2004].

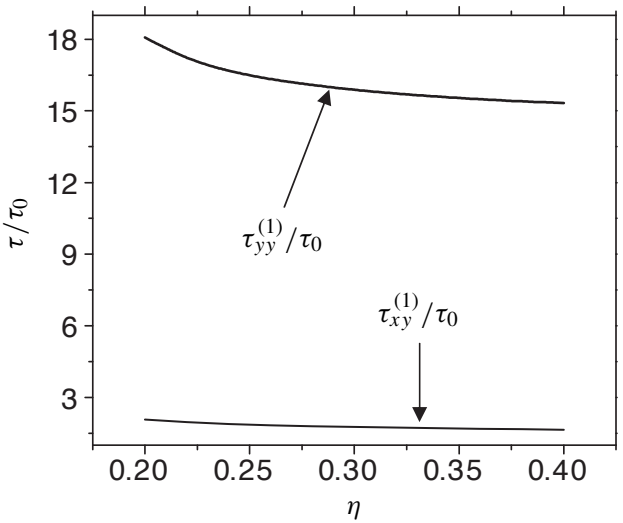

Figure 5. The stress at the crack tip versus η for $\gamma l = 0.4$, $a/\beta l = 0.003$, $wl/c = 0.3$, and $l = 1.0$.

These dual integral equations can be solved by using the singular integral equation for the same problem in the local functionally graded materials case. However, that stress singularities are present at the crack tips in the local functionally graded materials problem is well known.

(iv) The stress fields $\tau_{yy}^{(1)}$ at crack tips are symmetric about the line $\gamma\ell = 0$, as shown in Figure 4. The stress fields $\tau_{yy}^{(1)}$ at the crack tips decrease with an increase in the gradient parameter for $\gamma\ell < -1.0$, and increase with the gradient parameter reaching a peak near $\gamma\ell = -0.5$. They then decrease in magnitude for $\gamma\ell < 0$, as shown in Figure 4. In the case of $\gamma\ell > 0$, the stress fields $\tau_{yy}^{(1)}$ at the crack tips are symmetric, as in the case of $\gamma\ell < 0$. This means that by adjusting the gradient parameter of FGMs, dynamic stress fields near the crack tips can be reduced. However, the shear stress fields $\tau_{xy}^{(1)}$ at the crack tips increase almost linearly with an increase in the gradient parameter for all $\gamma\ell$. In this case, the shear stress $\tau_{xy}^{(1)}$ is smaller than the normal stress $\tau_{yy}^{(1)}$.

(v) The stress fields at the crack tips decrease with an increase in Poisson's ratio η, as shown in Figure 5. However, the changing ranges are small—that is, the variation of Poisson's ratio η within a practical range has a rather insignificant influence on the stress value near crack tips as discussed in [Delae and Erdogan 1988; Ozturk and Erdogan 1996].

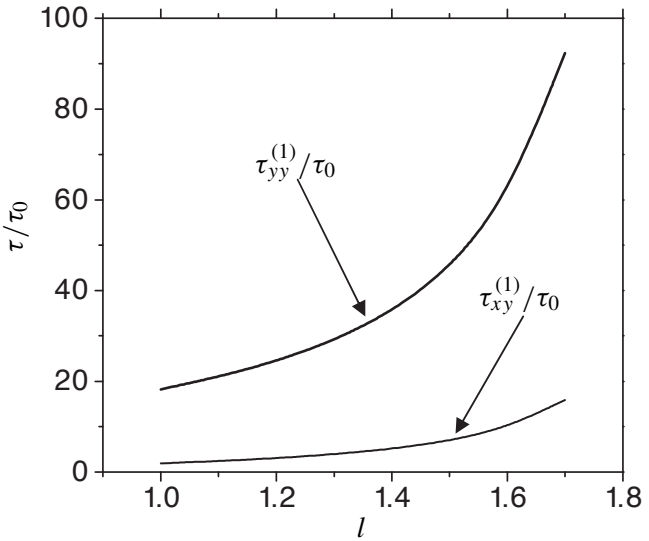

Figure 6. The stress at the crack tip versus l for $a/\beta = 0.003$, $\gamma = 0.4$, $\eta = 0.23$ and $w/c = 0.2$.

(vi) The stress fields at the crack tips increase non-linearly with an increase in crack length, as shown in Figure 6. This is similar to results of classical fracture theory. For classical fracture theory, the stress intensity factors increase with an increase in crack length.

(vii) The dynamic stresses of $\tau_{yy}^{(1)}$ and $\tau_{xy}^{(1)}$ at the crack tips in functionally graded materials tend to increase, with the frequency reaching a peak, and then decrease in magnitude, as shown in Figure 7. We can see that this conclusion is the same as that of the fracture problem in isotropic homogeneous materials.

(viii) The effect of the lattice parameter of functionally graded materials on the stress fields near the crack tips decreases with an increase in the lattice parameter, as shown in Figure 8. This phenomenon is discussed in [Eringen et al. 1977; 1978; 1979].

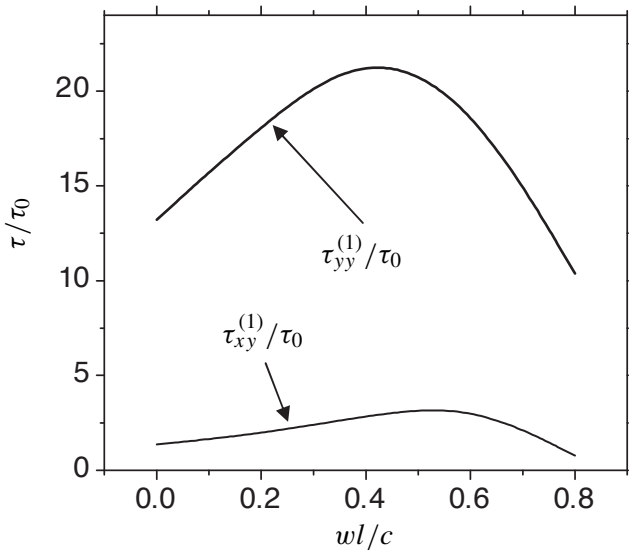

Figure 7. The stress at the crack tip versus wl/c for $a/\beta l = 0.0p03$, $\gamma l = -0.4$, $\eta = 0.23$ and $l = 1.0$.

Appendix

$$X_1 = \begin{bmatrix} 1 & 1 \\ m_1(s) & m_2(s) \end{bmatrix},$$

$$X_1 = \begin{bmatrix} 1 & 1 \\ m_3(s) & m_4(s) \end{bmatrix},$$

$$X_3 = \begin{bmatrix} g_1(s) & g_2(s) \\ h_1(s) & h_2(s) \end{bmatrix},$$

$$X_4 = \begin{bmatrix} g_3(s) & g_4(s) \\ h_3(s) & h_4(s) \end{bmatrix},$$

$$[X_5] = [X_1] - [X_2][X_4]^{-1}[X_3],$$

$$\begin{bmatrix} e_{11}(s) & e_{12}(s) \\ e_{21}(s) & e_{22}(s) \end{bmatrix} = [X_5]^{-1},$$

$$[X_6] = [X_4]^{-1}[X_3][X_5]^{-1} = \begin{bmatrix} c_{11}(s) & c_{12}(s) \\ c_{21}(s) & c_{22}(s) \end{bmatrix}.$$

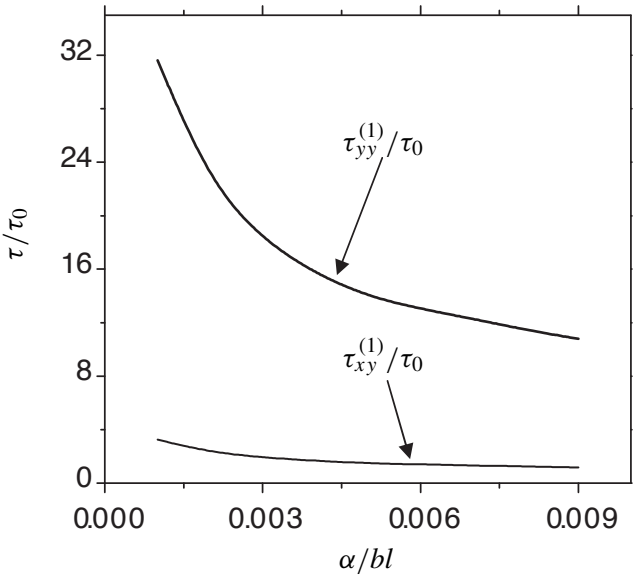

Figure 8. The stress at the crack tip versus $a/\beta l$ for $l = 1.0$, $\gamma l = 0.4$, $\eta = 0.23$ and $wl/c = 0.2$.

Acknowledgments

The authors are grateful for the financial support by the National Science Foundation for Excellent Young Investigators of Hei Long Jiang Province (JC04-08), the Natural Science Foundation of Hei Long Jiang Province(A0301), the National Science Foundation for Excellent Young Investigators (10325208), the National Natural Science Foundation of China (90405016, 10572043), and the National Natural Science Key Item Foundation of China (10432030).

References

[Choi 2001] H. J. Choi, "The problem for bonded half-planes containing a crack at an arbitrary angle to the graded interfacial zone", *Int. J. Solids Struct.* **38**:36-37 (2001), 6559–6588.

[Delae and Erdogan 1988] F. Delae and F. Erdogan, "On the mechanical modeling of the interfacial region in bonded half-planes", *J. Appl. Mech.* (*Trans. ASME*) **55** (1988), 317–324.

[Edelen 1976] D. G. B. Edelen, "Non-local field theory", pp. 75–204 in *Continuum physics*, vol. 4, edited by A. C. Eringen, Academic Press, New York, 1976.

[Erdelyi 1954] A. Erdelyi, *Tables of integral transforms*, vol. 1, McGraw-Hill, New York, 1954.

[Erdogan and Wu 1996] F. Erdogan and H. B. Wu, "Crack problems in FGM layer under thermal stress", *J. Therm. Stresses* **19** (1996), 237–265.

[Eringen 1972] A. C. Eringen, "Linear theory of nonlocal elasticity and dispersion of plane waves", *Int. J. Eng. Sci.* **10**:5 (1972), 425–435.

[Eringen 1976] A. C. Eringen, "Non-local polar field theory", pp. 205–267 in *Continuum physics*, vol. 4, edited by A. C. Eringen, Academic Press, New York, 1976.

[Eringen 1977] A. C. Eringen, "Continuum mechanics at the atomic scale", *Cryst. Latt. Def.* **7** (1977), 109–130.

[Eringen 1978] A. C. Eringen, "Line crack subject to shear", *Int. J. Fract.* **14**:4 (1978), 367–379.

[Eringen 1979] A. C. Eringen, "Line crack subject to antiplane shear", *Eng. Fract. Mech.* **12**:2 (1979), 211–219.

[Eringen 1983] A. C. Eringen, "Interaction of a dislocation with a crack", *J. Appl. Phys.* **54**:12 (1983), 6811–6817.

[Eringen and Kim 1974] A. C. Eringen and B. S. Kim, "On the problem of crack in non-local elasticity", pp. 81–113 in *Continuum mechanics aspects of geodynamics and rock fracture mechanics*, edited by P. Thoft-Christensen, Reidel, Dordrecht, Holland, 1974.

[Eringen and Kim 1977] A. C. Eringen and B. S. Kim, "Relation between non-local elasticity and lattice dynamics", *Cryst. Latt. Def.* **7** (1977), 51–57.

[Eringen et al. 1977] A. C. Eringen, C. G. Speziale, and B. S. Kim, "Crack-tip problem in non-local elasticity", *J. Mech. Phys. Solids* **25**:5 (1977), 339–355.

[Gradshteyn and Ryzhik 1980] I. S. Gradshteyn and I. M. Ryzhik, *Table of integrals, series and products*, Academic Press, New York, 1980. page 480.

[Green and Rivlin 1965] A. E. Green and R. S. Rivlin, "Multipolar continuum mechanics: functional theory. I", *P. Roy. Soc. Lond. A Mat.* **A 284**:1398 (1965), 303–324.

[Itou 1978] S. Itou, "Three dimensional waves propagation in a cracked elastic solid", *J. Appl. Mech.* (*Trans. ASME*) **45** (1978), 807–811.

[Koizumi 1993] M. Koizumi, "The concept of FGM", pp. 3–10 in *Functionally graded materials* (San Francisco, 1992), edited by J. B. Holt et al., Ceramic transactions **34**, American Ceramic Society, Westerville, OH, 1993.

[Lee and Erdogan 1994] Y. D. Lee and F. Erdogan, "Residual/thermal stresses in FGM and laminated thermal barrier coatings", *Int. J. Fract.* **69**:2 (1994), 145–165.

[Morse and Feshbach 1958] P. M. Morse and H. Feshbach, *Methods of theoretical physics*, M. G.aw-Hill, New York, 1958. page 926.

[Nowinski 1984a] J. L. Nowinski, "On non-local theory of wave propagation in elastic plates", *J. Appl. Mech.* (*Trans. ASME*) **51** (1984), 608–613.

[Nowinski 1984b] J. L. Nowinski, "On the nonlocal aspects of the propagation of Love waves", *Int. J. Eng. Sci.* **22**:4 (1984), 383–392.

[Ozturk and Erdogan 1996] M. Ozturk and F. Erdogan, "Axisymmetric crack problem in bonded materials with a graded interfacial region", *Int. J. Solids Struct.* **33**:2 (1996), 193–219.

[Pan 1992] J. Pan, K. L.and Fang, "The image force on a dislocation near an elliptic hole in nonlocal elasticity", *Arch. Appl. Mech.* **62**:8 (1992), 557–564.

[Pan 1994] K. L. Pan, "An image force theorem for a screw dislocation near a crack in non-local elasticity", *J. Phys. D: Appl. Phys.* **27**:2 (1994), 344–346.

[Pan 1995] K. L. Pan, "Interaction of a dislocation with a surface crack in nonlocal elasticity", *Int. J. Fract.* **69**:4 (1995), 307–318.

[Pan and Fang 1993] K. L. Pan and J. Fang, "Nonlocal interaction of a dislocation with a crack", *Arch. Appl. Mech.* **64**:1 (1993), 44–51.

[Pan and Takeda 1998] K. L. Pan and N. Takeda, "Nonlocal stress field of interface dislocations", *Arch. Appl. Mech.* **68**:3-4 (1998), 179–184.

[Rice 1968] J. R. Rice, "A path independent integral and the approximate analysis of strain concentrations by notches and cracks", *J. Appl. Mech.* (*Trans. ASME*) **35** (1968), 379–386.

[Srivastava et al. 1983] K. N. Srivastava, R. M. Palaiya, and D. S. Karaulia, "Interaction of shear waves with two coplanar Griffith cracks situated in an infinitely long elastic strip", *Int. J. Fract.* **23**:1 (1983), 3–14.

[Suresh and Mortensen 1977] S. Suresh and A. Mortensen, "Functionally graded metals and metal-ceramic composites: part 2, thermomechanical behaviour", *Int. Mater. Rev.* **29** (1977), 306–312.

[Wang et al. 2000] B. L. Wang, J. C. Han, and S. Y. Du, "Cracks problem for non-homogeneous composite material subjected to dynamic loading", *Int. J. Solids Struct.* **37**:9 (2000), 1251–1274.

[Xia and Hutchinson 1996] Z. C. Xia and J. W. Hutchinson, "Crack tip fields in strain gradient plasticity", *J. Mech. Phys. Solids* **44**:10 (1996), 1621–1648.

[Yau 1967] W. F. Yau, "Axisymmetric slipless indentation of an infinite elastic cylinder", *SIAM J. Appl. Math.* **15**:1 (1967), 219–227.

[Zhou and Wang 2002a] Z. G. Zhou and B. Wang, "Investigation of anti-plane shear behavior of two collinear cracks in the piezoelectric materials by using the non-local theory", *Int. J. Solids Struct.* **39**:7 (2002), 1731–1742.

[Zhou and Wang 2002b] Z. G. Zhou and B. Wang, "Investigation of the scattering of harmonic elastic waves by two collinear symmetric cracks using non-local theory", *J. Eng. Math.* **44**:1 (2002), 41–56.

[Zhou and Wang 2006] Z. G. Zhou and B. Wang, "Nonlocal theory solution of two collinear cracks in the functionally graded materials", *Int. J. Solids Struct.* **43**:5 (2006), 887–898.

[Zhou et al. 1999a] Z. G. Zhou, Y. Y. Bai, and X. W. Zhang, "Two collinear Griffith cracks subjected to uniform tension in infinitely long strip", *Int. J. Solids Struct.* **36**:36 (1999), 5597–5609.

[Zhou et al. 1999b] Z. G. Zhou, J. C. Han, and S. Y. Du, "Investigation of a Griffith crack subject to anti-plane shear by using the non-local theory", *Int. J. Solids Struct.* **36**:26 (1999), 3891–3901.

[Zhou et al. 2002] Z. G. Zhou, B. Wang, and S. Y. Du, "Investigation of antiplane shear behavior of two collinear permeable cracks in a piezoelectric material by using the nonlocal theory", *J. Appl. Mech.* (*Trans. ASME*) **69**:3 (2002), 388–390.

[Zhou et al. 2004] Z. G. Zhou, B. Wang, and Y. G. Sun, "Investigation of the dynamic behavior of a finite crack in the functionally graded materials by use of the Schmidt method", *Wave Motion* **39**:3 (2004), 213–225.

Received 22 Oct 2005. Revised 12 Dec 2005.

ZHEN-GONG ZHOU: zhouzhg@hit.edu.cn
Center for Composite Materials, Harbin Institute of Technology, P.O.Box 1247, Harbin 150001, P.R.China

JUN LIANG: *Center for Composite Materials, Harbin Institute of Technology, P.O.Box 1247, Harbin 150001, P.R.China*

LIN-ZHI WU: *Center for Composite Materials, Harbin Institute of Technology, P.O.Box 1247, Harbin 150001, P.R.China*

JOURNAL OF MECHANICS OF MATERIALS AND STRUCTURES
Vol. 1, No. 3, 2006

SEMI-ANALYTICAL SOLUTION FOR A VISCOELASTIC PLANE CONTAINING MULTIPLE CIRCULAR HOLES

YUN HUANG, SOFIA G. MOGILEVSKAYA AND STEVEN L. CROUCH

The paper considers the problem of an infinite, homogeneous, isotropic viscoelastic plane containing multiple circular holes. Constant or time-dependent loading is applied at infinity or on the boundaries of the holes. The sizes and locations of the holes are arbitrary provided they do not overlap. The solution of the problem is based on the use of the correspondence principle, and the governing equation in the Laplace domain is a complex hypersingular boundary integral equation written in terms of the unknown transformed displacements at the boundaries of the holes. The main feature of this equation is that the material parameters are only involved as multipliers for the terms other than the integrals of transformed displacements. The unknown transformed displacements are approximated by truncated complex Fourier series with coefficients dependent on the transform parameter. A system of linear algebraic equations is formulated using Taylor series expansion for determining these coefficients. The viscoelastic stresses and displacements are calculated through the viscoelastic analogs of Kolosov–Muskhelishvili potentials, and an inverse Laplace transform is used to provide the time domain solution. All the operations (space integration, Laplace transform and its inversion) are performed analytically. The method described in the paper enables the consideration of a variety of viscoelastic models. For the sake of illustration, examples are given for the cases where the viscoelastic solid responds as (*i*) a Boltzmann model in shear and elastically in dilatation, (*ii*) a Boltzmann model in both shear and dilatation, and (*iii*) a Burgers model in shear and elastically in dilatation. The accuracy and efficiency of the approach are demonstrated by comparing selected results with the solutions obtained by the finite element method (ANSYS) and the time stepping boundary element approach.

1. Introduction

Circular cavities are frequently present in various engineering applications. Time-independent problems involving multiple circular cavities have been extensively studied. A comprehensive review of the literature related to elastic problems can be found in [Crouch and Mogilevskaya 2003]. The solutions of various harmonic

Keywords: viscoelasticity, correspondence principle, boundary integral method, Laplace transform.

and biharmonic problems have been obtained in [Bird and Steele 1991; 1992; Bird 1992]. More recently, [Chen et al. 2006c; 2006a; 2006b] described a null-field integral equation approach for plane, anti-plane shear and torsion problems.

Efficient solutions of time-dependent problems involving a large number of circular cavities have not yet been published. The present paper aims to present such a solution for linear viscoelastic problems.

Traditional methods of solving problems in linear viscoelasticity fall into three categories. Methods in the first category are based on the use of the correspondence principle. For these methods, the reformulated problem in Laplace space is solved analytically or numerically (for example, using finite element or boundary element methods), and the results are inverted into the time domain using numerical Laplace transform inversion [Schapery 1962; Rizzo and Shippy 1971; Kusama and Mitsui 1982; Wang and Crouch 1982; Sun and Hsiao 1985; Carini and Gioda 1986; Lee et al. 1994]. The accuracy of these methods depends on the choice of the appropriate values for the transform parameters [Lee and Kim 1995], which changes with each problem under consideration. This disadvantage limits the application of these methods.

In the second category, a temporal integral equation is formulated using the time-dependent Green's functions, and the time history is divided into a number of discrete steps. By approximating time-dependent unknowns by some functions (for example, polynomials) at each time step and integrating them numerically or analytically, the time convolution is replaced by a sum of integrals for all steps. In general, the computation for one time step requires knowledge of the results from all the previous steps [Lee and Kim 1995; Sim and Kwak 1988]. The amount of computation therefore increases with time. If a linear or constant time interpolation function is used, the influence from all previous steps can be stored in a time-dependent function and updated after each step. In such cases, the computational expense can be decreased to some extent [Shinokawa et al. 1985].

In the third category of solution procedures for problems in linear viscoelasticity, a boundary integral equation involving time derivatives of the principal unknown variables (for example, the displacements) is obtained using the differential constitutive equation for a particular viscoelastic model and a weighted residual technique. A finite difference scheme is adopted to approximate the time derivatives, which results in a time stepping algorithm, and the space integrals are carried out using the boundary element method [Mesquita and Coda 2001; 2002b; 2003]. For the special case in which all of the geometric features are circular, we suggested a time stepping boundary integral method based on a truncated Fourier series approximation for the boundary variables [Huang et al. 2005c; 2005b; 2005a]. All the space integrals can be evaluated analytically in this method. However, such methods are based on the assumption of a constant viscoelastic Poisson's ratio,

which is physically unrealistic for practical materials. A volume integral must be included in the analysis if one wishes to consider a time-dependent Poisson's ratio, and this requires the adoption of a finite element type approach, as done for example in [Mesquita and Coda 2002a].

To overcome the disadvantages noted above for traditional methods of solution, a new approach is desired. As an attempt in this direction, we describe here a semi-analytical solution for the problem of an infinite viscoelastic plane containing multiple holes. The time-independent analog of this approach has been presented earlier in the series of papers [Mogilevskaya and Crouch 2001; 2002; Crouch and Mogilevskaya 2003; Wang et al. 2003a; 2003b; Mogilevskaya and Crouch 2004; Legros et al. 2004]. The technique presented in those papers was based on the use of complex or real versions of the two-dimensional Somigliana's formula. The unknown variables on the circular boundaries were approximated by truncated Fourier series. All the space integrals involved were evaluated analytically. In fact, infinite Fourier series provide the analytical solution for this class of problems; apart from round-off error, the only errors introduced in the numerical model are due to truncation of the series.

In the present paper, we extend this technique to the area of linear viscoelasticity. The solution presented in this paper is based on the correspondence principle and the analytical Laplace transform and its inversion, rather than the time stepping scheme used in our previous work [Huang et al. 2005c; 2005b; 2005a]. The governing equation for the problem in the Laplace domain is a complex hypersingular boundary integral equation written in terms of the unknown transformed displacements at the boundaries of the holes. A significant feature of this equation is that the space integrals involving the unknown variables (the transformed boundary displacements) do not include the material properties; the material parameters only appear as multipliers for the terms involving transformed far-field stress and pore pressures. The unknown transformed displacements on the circular boundary are approximated by truncated complex Fourier series with the coefficients dependent on the transform parameters. A system of linear algebraic equations is formed and solved for these Fourier coefficients. The solution for stresses and displacements anywhere in the viscoelastic plane is obtained in both the Laplace and time domains. No specific physical model is involved in the governing complex variable hypersingular integral equation, which means that the method is capable of handling a variety of viscoelastic models.

Several computational examples are given. In these examples, the viscoelastic solid responds as a Boltzmann model in shear and elastically in dilatation; a Boltzmann model in both shear and dilatation; and a Burgers model in shear and elastically in dilatation. Three loading cases are considered:

(i) the viscoelastic plane is subjected to constant far-field stresses;

(ii) the holes are subjected to constant pressure; and

(iii) the holes are subjected to time-dependent pressure.

The accuracy and efficiency of the method are examined by comparison to the numerical solution obtained by commercial finite element software (ANSYS) or by a time stepping boundary element approach [Huang et al. 2005b].

2. Problem formulation

Consider an infinite, isotropic, viscoelastic plane containing an arbitrary number of nonoverlapping circular holes, as shown in Figure 1. A plane strain condition is assumed. The holes are assumed to be either traction-free or subjected to time-dependent uniform normal traction. The viscoelastic plane is subjected to time-dependent far-field stress $\sigma^\infty(t)$. Let R_j, z_j and L_j denote the radius, center, and boundary of the jth hole, and let $p_j(t)$ denote the time-dependent uniform normal traction acting on L_j ($p_j < 0$ for compression). Any point of the plane is identified by the complex coordinate $z = x + iy$. The global and local Cartesian coordinate systems are shown in Figure 1. The direction of travel is clockwise for all the boundaries L_j. The unit tangent q points in the direction of travel and the unit outward normal n points to the right of this direction, away from the viscoelastic solid. The evolution of displacements and stresses in the perforated viscoelastic solid is to be determined.

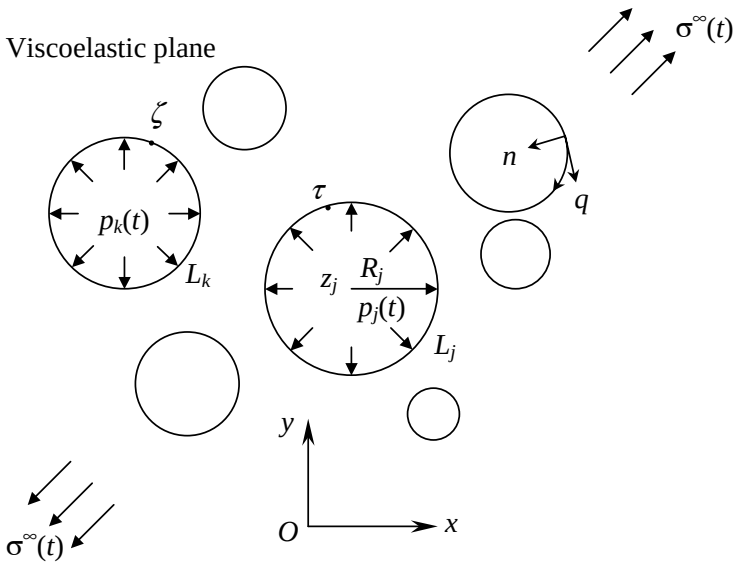

Figure 1. An infinite viscoelastic plane with multiple circular holes.

3. Correspondence principle

The correspondence principle allows the time domain solution for a linear viscoelastic problem to be obtained from the solution of a corresponding elastic problem by employing the following procedure. By using the Laplace transform, the time-dependent parameters for the original viscoelastic problem are removed by replacing them by s-varying analogs of these parameters. The resulting problem is formally equivalent to a linear elastic problem. However, the 'elastic constants' are functions of the transform parameter s, as are the transformed boundary conditions for the problem. By solving the corresponding elastic problem and taking the inverse Laplace transform, the time-dependent solution is found [Lee 1955; Findly et al. 1989].

The Laplace transform of a function $f(t)$ and its inversion are defined as [Haberman 1998]

$$\begin{aligned} f^*(s) &\equiv \Gamma[f(t)] = \int_0^\infty f(t)e^{-st}dt && (\operatorname{Re} s = \varsigma \geq 0), \\ f(t) &\equiv \Gamma^{-1}[f^*(s)] = \frac{1}{2\pi i}\int_{\varsigma-i\infty}^{\varsigma+i\infty} f^*(s)e^{st}ds && (t \geq 0,\ \varsigma \geq 0), \end{aligned} \tag{1}$$

where s is the transform parameter and ς is a vertical contour in the complex plane chosen in such a way that all singularities of $f^*(s)$ are located to the left of it.

The general way to obtain the s-varying analog of the Young's modulus $E^*(s)$ and Poisson's ratio $\nu^*(s)$ from the constitutive equations of a viscoelastic model is explained elsewhere (for example, [Wang and Crouch 1982]). Using the relations among elastic constants, one can easily obtain the s-varying shear modulus $G^*(s)$, bulk modulus $K^*(s)$ and s-varying Kolosov–Muskhelishvili parameter $\kappa^*(s)$ (which equals $3-4\nu^*(s)$ in plane strain and $(3-\nu^*(s))/(1+\nu^*(s))$ in plane stress). In Section 6, $G^*(s)$ and $\kappa^*(s)$ are given for three different viscoelastic models.

4. Basic equations

4.1. ***Basic hypersingular integral equation in the Laplace domain.*** The governing equation for the problem of a viscoelastic plane with holes (Figure 1) in the Laplace domain is an analog of the complex hypersingular integral equation for the corresponding elastic problems [Linkov and Mogilevskaya 1994; Mogilevskaya and Linkov 1998; Linkov and Mogilevskaya 1998; Linkov 2002]. To state the equation, let N be the number of holes; let i denote $\sqrt{-1}$ and $\bar{z}$ the complex conjugate of z; let $u_j^*(\tau; s) = u_{j,x}^*(\tau; s) + iu_{j,y}^*(\tau; s)$ be the result of the Laplace transform applied to the complex-valued displacement $u(\tau) = u_{j,x}(\tau) + iu_y(\tau)$ in the global coordinate system on the boundary of the j-th hole; let $\sigma_{ij}^{\infty,*}(s)$ (with i,

j representing x or y) be the components of far-field stress in the Laplace domain. The problem is then described by the N equations ($k = 1, 2, \ldots, N$)

$$\frac{1}{2\pi i}\sum_{j=1}^{N}\left(2\int_{L_j}\frac{u_j^*(\tau;s)}{(\tau-\zeta)^2}d\tau-\int_{L_j}u_j^*(\tau;s)\frac{\partial^2}{\partial\tau\,\partial\zeta}K_1(\tau,\zeta)\,d\tau\right.$$
$$-\int_{L_j}\overline{u_j^*(\tau;s)}\frac{\partial^2}{\partial\bar\tau\,\partial\zeta}K_2(\tau,\zeta)\,d\bar\tau$$
$$\left.+\frac{p_j^*}{2G^*}\left((1-\kappa^*)\int_{L_j}\frac{d\tau}{\tau-\zeta}-\kappa^*\int_{L_j}\frac{\partial}{\partial\zeta}K_1(\tau,\zeta)\,d\tau+\int_{L_j}\frac{\partial}{\partial\zeta}K_2(\tau,\zeta)\,d\bar\tau\right)\right)$$
$$=\frac{\kappa^*+1}{4G^*}\left(p_k^*-\left(\sigma_{xx}^{\infty,*}+\sigma_{yy}^{\infty,*}\right)-\frac{d\bar\zeta}{d\zeta}\left(\sigma_{yy}^{\infty,*}-\sigma_{xx}^{\infty,*}-2i\sigma_{xy}^{\infty,*}\right)\right),\quad(2)$$

where G^* stands for $G^*(s)$ and likewise p_j^*, p_k^*, κ^*, and the $\sigma_{ij}^{\infty,*}$; $d\bar\zeta/d\zeta = \exp(-2i\beta)$, where β is the angle between the axis Ox and the tangent at the point ζ; $\tau \in L_j$ and $\zeta \in L_k$ for $k = 1, 2, \ldots, N$; and the kernels K_1 and K_2 are

$$K_1(\tau,\zeta)=\ln\frac{\tau-\zeta}{\bar\tau-\bar\zeta},\qquad K_2(\tau,\zeta)=\frac{\tau-\zeta}{\bar\tau-\bar\zeta}.\quad(3)$$

4.2. ***The viscoelastic analog of the Kolosov–Muskhelishvili potentials.*** In the Laplace domain the displacements and stresses at any point of the viscoelastic plane can be calculated using the viscoelastic analogs of the Kolosov–Muskhelishvili potentials [Muskhelishvili 1963]

$$2G^*(s)u^*(z;s)=\kappa^*(s)\varphi^*(z;s)-z\overline{(\partial/\partial z)\varphi^*(z;s)}-\overline{\psi^*(z;s)},\quad(4)$$

$$\sigma_{xx}^*(z;s)+\sigma_{yy}^*(z;s)=4\mathrm{Re}(\partial/\partial z)\varphi^*(z;s),\quad(5)$$

$$\sigma_{yy}^*(z;s)-\sigma_{xx}^*(z;s)+2i\sigma_{xy}^*(z;s)=2\left(\bar z(\partial^2/\partial z^2)\varphi^*(z;s)+(\partial/\partial z)\psi^*(z;s)\right),\quad(6)$$

where, as in [Wang et al. 2003a],

$$\varphi^*(z;s)=\frac{G^*(s)}{\pi i(\kappa^*(s)+1)}\sum_{j=1}^{N}\int_{L_j}\frac{u_j^*(\tau;s)}{\tau-z}\,d\tau+\varphi^{\infty,*}(z;s)\quad(7)$$

and

$$\psi^*(z;s)$$
$$=\frac{G^*(s)}{\pi i(\kappa^*(s)+1)}\sum_{j=1}^{N}\left(\frac{p_j^*(s)}{2G^*(s)}\left(\int_{L_j}\frac{\bar\tau\,d\tau}{\tau-z}+\kappa^*(s)\int_{L_j}\ln(\tau-z)\,d\bar\tau\right)\right.$$
$$\left.+\int_{L_j}\frac{\overline{u_j^*(\tau;s)}}{\tau-z}\,d\tau-\int_{L_j}\frac{u_j^*(\tau;s)}{\tau-z}d\bar\tau+\int_{L_j}\frac{u_j^*(\tau;s)\bar\tau}{(\tau-z)^2}\,d\tau\right)+\psi^{\infty,*}(z;s),\quad(8)$$

with

$$\varphi^{\infty,*}(z;s) = \frac{\sigma_{xx}^{\infty,*}(s) + \sigma_{yy}^{\infty,*}(s)}{4} z, \tag{9}$$
$$\psi^{\infty,*}(z;s) = \frac{\sigma_{yy}^{\infty,*}(s) - \sigma_{xx}^{\infty,*}(s) + 2i\sigma_{xy}^{\infty,*}(s)}{2} z.$$

After the displacements $u_j^*(\tau;s)$ on boundary L_j $(j = 1,\ldots,N)$ have been obtained from the solution of Equation (2), the displacements and stresses in the Laplace domain at point z can be calculated using (4)–(6) and (7)–(9), provided that the integrals involved in (7) and (8) can be evaluated.

5. Numerical solution

The Laplace domain equation (2) is similar to the corresponding equation for elasticity (for example, equation (1) in [Wang et al. 2003a]). Thus, Equation (2) can be solved in the same way as its elastic counterpart [Wang et al. 2003a]. The main steps of the solution are outlined below.

5.1. ***Approximation of the boundary variables.*** The unknown displacement on the boundary L_j $(j = 1,\ldots,N)$ in the Laplace domain is approximated by a truncated complex Fourier series as

$$u_j^*(\tau;s) = \sum_{m=1}^{M_j} D_{-m,j}^*(s) g_j^m(\tau) + \sum_{m=0}^{M_j} D_{m,j}^*(s) g_j^{-m}(\tau), \tag{10}$$

where the function $g_j(\tau)$ is defined as

$$g_j(\tau) = \frac{R_j}{\tau - z_j}.$$

The unknown complex Fourier coefficients $D_{\pm m,j}^*(s)$ $(m = 1,\ldots,M_j)$ in (10) are functions of the Laplace transform parameter s. In the following discussion, we will omit the argument s in the expressions for the Fourier coefficients for notational convenience.

With the substitution of the Fourier series representation (10) into Equation (2), the unknown coefficients can be moved outside of the space integrals. The kernel space integrals are the same as those for the elastic problem [Wang et al. 2003a]. Thus, we can use the results of the space integrals provided in that article. In this way we obtain the following system of N complex algebraic equations, one for each hole:

$$\sum_{m=1}^{M_k} m D^*_{-m,k} g_k^{m+1}(\zeta) + \left(D^*_{1,k} + \overline{D^*_{1,k}}\right) + \sum_{m=2}^{M_k} m D^*_{m,k} g_k^{1-m}(\zeta)$$
$$+ \sum_{\substack{j=1\\ j\neq k}}^{N} \frac{R_k}{R_j}\Bigg(\sum_{m=1}^{M_j} m D^*_{-m,j} g_j^{m+1}(\zeta) + \left(D^*_{1,j} + \overline{D^*_{1,j}}\right) g_k^2(\zeta)\overline{g_j^2(\zeta)}$$
$$+ \sum_{m=2}^{M_j} m D^*_{m,j} g_k^2(\zeta)\overline{g_j^{m+1}(\zeta)}$$
$$+ \sum_{m=1}^{M_j} m \overline{D^*_{-m,j}}\Bigg(\overline{g_j^{m+1}(\zeta)} - (m+2) g_k^2(\zeta)\overline{g_j^{m+3}(\zeta)}$$
$$+ (m+1)\left(\frac{R_k}{R_j} g_k(\zeta) + \frac{g_k^2(\zeta)}{g_j(z_k)}\right)\overline{g_j^{m+2}(\zeta)}\Bigg)\Bigg)$$
$$= \frac{\kappa^*(s)+1}{4G^*(s)} R_k\left(\sigma^{\infty,*}_{xx} + \sigma^{\infty,*}_{yy} - g_k^2(\zeta)(\sigma^{\infty,*}_{yy} - \sigma^{\infty,*}_{xx} - 2i\sigma^{\infty,*}_{xy})\right)$$
$$- \frac{p_k^*}{G^*(s)} R_k - \frac{1-\kappa^*(s)}{2G^*(s)} R_k g_k^2(\zeta) \sum_{\substack{j=1\\ j\neq k}}^{N} p_j^* \overline{g_j^2(\zeta)} \tag{11}$$

Similarly, with the substitution of Fourier series approximation (10) into (7) and (8), and using the results of the space integrals provided in [Wang et al. 2003a], the viscoelastic analogs of the Kolosov–Muskhelishvili potentials $\varphi^*(z;s)$ and $\psi^*(z;s)$ are expressed as

$$\varphi^*(z;s) = \frac{2G^*(s)}{\kappa^*(s)+1} \sum_{j=1}^{N}\sum_{m=1}^{M_j} D^*_{-m,j} g_j^m(z) + \frac{\sigma^{\infty,*}_{xx}(s) + \sigma^{\infty,*}_{yy}(s)}{4} z, \tag{12}$$

$$\psi^*(z;s) = \frac{2G^*(s)}{\kappa^*(s)+1} \sum_{j=1}^{N}\Bigg(\left(g_j^2(z) + \frac{\overline{z_j}}{z-z_j}\right) \sum_{m=1}^{M_j} m D^*_{-m,j} g_j^m(z) \tag{13}$$
$$- \left(D^*_{1,j} + \overline{D^*_{1,j}}\right) g_j(z) - \sum_{m=2}^{M_j} \overline{D^*_{m,j}} g_j^m(z)\Bigg)$$
$$- \frac{1-\kappa^*(s)}{1+\kappa^*(s)} \sum_{j=1}^{N} p_j^*(s) R_j g_j(z) + \frac{\sigma^{\infty,*}_{yy}(s) - \sigma^{\infty,*}_{xx}(s) + 2i\sigma^{\infty,*}_{xy}(s)}{2} z.$$

5.2. ***Reduction to a linear algebraic system.*** To find the unknown coefficients $D^*_{-m,j}$ $(m = 1, \ldots, M_j)$ and $D^*_{m,j}$ $(m = 1, \ldots, M_j)$ for $j = 1, \ldots, N$, we need to reduce the system (11) to a linear algebraic system. We showed in a previous paper

[Wang et al. 2003a] that, excluding collocation, there are two equivalent methods to obtain the linear algebraic system: (i) the Galerkin weighted residual method and (ii) the Taylor series expansion method. Using a Taylor series expansion technique [Wang et al. 2003a] a linear algebraic equation system is obtained as follows:

$$
\begin{aligned}
&\sum_{m=2}^{M_k} m D^*_{m,k} g_k^{1-m}(\zeta) + \sum_{n=1}^{\infty}\sum_{\substack{j=1\\ j\neq k}}^{N} \frac{R_k}{R_j}\frac{g_k^n(z_j)}{g_k^n(\zeta)} \sum_{m=1}^{M_j} m\binom{m+n}{n} D^*_{-m,j} g_j^{m+1}(z_k) \\
&\quad + 2\,\mathrm{Re}(D^*_{1,k}) + \sum_{\substack{j=1\\ j\neq k}}^{N} \frac{R_k}{R_j} \sum_{m=1}^{M_j} m\left(D^*_{-m,j} g_j^{m+1}(z_k) + \overline{D^*_{-m,j}}\,\overline{g_j^{m+1}(z_k)}\right) \\
&\quad + \sum_{m=1}^{M_k} m D^*_{-m,k} g_k^{m+1}(\zeta) \\
&\quad + \sum_{n=1}^{\infty}\sum_{\substack{j=1\\ j\neq k}}^{N} \frac{R_k}{R_j}\overline{g_k^n(z_j)} g_k^n(\zeta) \sum_{m=1}^{M_j} m\binom{m+n}{n} \overline{D^*_{-m,j}}\,\overline{g_j^{m+1}(z_k)} \\
&\quad + \sum_{n=0}^{\infty}\sum_{\substack{j=1\\ j\neq k}}^{N} \frac{R_k}{R_j}\overline{g_k^n(z_j)} \Bigg(g_k^{n+2}(\zeta)\Bigg(2(n+1)\,\mathrm{Re}(D^*_{1,j})\overline{g_j^2(z_k)} \\
&\qquad\qquad + \sum_{m=2}^{M_j} m\binom{m+n}{n} D^*_{m,j}\overline{g_j^{m+1}(z_k)} \\
&\qquad\qquad - \sum_{m=1}^{M_j} m(m+2)\binom{m+n+2}{n}\overline{D^*_{-m,j}}\,\overline{g_j^{m+3}(z_k)} \\
&\qquad\qquad + \sum_{m=1}^{M_j} m(m+1)\binom{m+n+1}{n}\overline{D^*_{-m,j}}\,\frac{\overline{g_j^{m+2}(z_k)}}{g_j(z_k)}\Bigg) \\
&\qquad - g_k^{n+1}(\zeta)\sum_{m=1}^{M_j} m(m+1)\binom{m+n+1}{n}\overline{D^*_{-m,j}}\,\overline{g_j^{m+1}(z_k)}\,\overline{g_k(z_j)}\Bigg) \\
&= \frac{\kappa^*(s)+1}{4G^*(s)} R_k\left(\sigma^{\infty,*}_{xx} + \sigma^{\infty,*}_{yy}\right) - \frac{p_k^*}{G^*(s)} R_k \\
&\qquad - \frac{\kappa^*(s)+1}{4G^*(s)} R_k g_k^2(\zeta)\left(\left(\sigma^{\infty,*}_{yy} - \sigma^{\infty,*}_{xx} - 2i\sigma^{\infty,*}_{xy}\right)\right) \\
&\qquad - \frac{1-\kappa^*(s)}{2G^*(s)} R_k \sum_{n=0}^{\infty}(n+1) g_k^{n+2}(\zeta) \sum_{\substack{j=1\\ j\neq k}}^{N} p_j^*\overline{g_j^2(z_k)}\,\overline{g_k^n(z_j)}. \qquad (14)
\end{aligned}
$$

By equating the coefficients of the positive powers $g_k^{l+1}(t)$ $(1 \le l \le M_k)$, the constant terms, and the negative powers $g_k^{1-l}(t)$ $(2 \le l \le M_k)$ in (14), we obtain a system of $2M_k$ $(k = 1, \dots, N)$ linear complex algebraic equations for all the Fourier coefficients. To simplify the notation, we set

$$\mathrm{RHS}_1(s) = -\frac{\kappa^*(s)+1}{4G^*(s)} R_k(\sigma_{yy}^{\infty,*}(s) - \sigma_{xx}^{\infty,*}(s) - 2i\sigma_{xy}^{\infty,*}(s)) - \frac{1-\kappa^*(s)}{2G^*(s)} R_k \sum_{\substack{j=1 \\ j\neq k}}^{N} p_j^*(s)\overline{g_j^2(z_k)}$$

and, for $l = 2, \dots, M_k$,

$$\mathrm{RHS}_l(s) = -\frac{1-\kappa^*(s)}{2G^*(s)} R_k \sum_{\substack{j=1 \\ j\neq k}}^{N} p_j^*(s)\overline{g_j^2(z_k)}\,\overline{g_k^{l-1}(z_j)}.$$

The desired system is

$$D_{-l,k}^* - \sum_{\substack{j=1 \\ j\neq k}}^{N} \overline{g_k^l(z_j)} \Bigg(\sum_{m=1}^{M_j} (l+1) \binom{m+l}{l+1} \overline{D_{-m,j}^*}\,\overline{g_j^m(z_k)} \times \left(\frac{\overline{g_j(z_k)}}{g_j(z_k)} - \frac{m+l+1}{l+1}\overline{g_k^2(z_j)} - \frac{m+l+1}{m+1}\overline{g_j^2(z_k)} \right) + 2\,\mathrm{Re}(D_{1,j}^*)\overline{g_j(z_k)} + \sum_{m=2}^{M_j} \binom{m+l-1}{l} D_{m,j}^* \overline{g_j^m(z_k)} \Bigg) = \mathrm{RHS}_l(s), \quad (15)$$

$$\mathrm{Re}\, D_{1,k}^* + \frac{1}{2} \sum_{\substack{j=1 \\ j\neq k}}^{N} \frac{R_k}{R_j} \sum_{m=1}^{M_j} m\left(D_{-m,j}^* g_j^{m+1}(z_k) + \overline{D_{-m,j}^*}\,\overline{g_j^{m+1}(z_k)} \right) = \frac{\kappa^*(s)+1}{8G^*(s)} R_k\left(\sigma_{xx}^{\infty,*}(s) + \sigma_{yy}^{\infty,*}(s)\right) - \frac{p_k^*(s)}{2G^*(s)} R_k, \quad (16)$$

$$D_{l,k}^* - \sum_{\substack{j=1 \\ j\neq k}}^{N} g_k^l(z_j) \sum_{m=1}^{M_j} \binom{m+l-1}{l} D_{-m,j}^* g_j^m(z_k) = 0 \quad (l = 2, \dots, M_k). \quad (17)$$

The system (15)–(17) can be written in compact form as

$$AD = B. \quad (18)$$

The matrix A is s-independent and can be inverted directly and stored in computer memory. The unknown vector D is s-dependent and is defined as

$$D = \left[\, D_1^*(s) \;\; \dots \;\; D_N^*(s) \,\right]^T,$$

where each subvector, such as $D_j^*(s)$, is a vector of unknown Fourier coefficients for one hole, given by

$$D_j^*(s) = \begin{bmatrix} D_{-M_j,j}^*(s) & \dots & D_{-1,j}^*(s) & \operatorname{Re}(D_{1,j}^*(s)) & D_{2,j}^*(s) & \dots & D_{M_j,j}^*(s) \end{bmatrix}^T.$$

The vector B on the right is composed of loading terms multiplied by certain constants involving the transformed material parameters. The three constants are $\big(\kappa^*(s)+1\big)/\big(4G^*(s)\big)$, $\big(1-\kappa^*(s)\big)/\big(2G^*(s)\big)$, and $1/\big(2G^*(s)\big)$. We decompose B into three parts, each containing only one constant:

$$B = B^{(1)} + B^{(2)} + B^{(3)},$$

where, for $k = 1, \dots, N$, we have set

$$B_{l,k}^{(1)} = \begin{cases} -\dfrac{\kappa^*(s)+1}{4G^*(s)} R_k \big(\sigma_{yy}^{\infty,*}(s) - \sigma_{xx}^{\infty,*}(s) - 2i\sigma_{xy}^{\infty,*}\big)(s) & (l=-1), \\ \dfrac{\kappa^*(s)+1}{4G^*(s)} R_k \dfrac{\sigma_{xx}^{\infty,*}(s) + \sigma_{yy}^{\infty,*}(s)}{2} & (l=1), \\ 0 & (l=\pm 2, \dots, \pm M_k), \end{cases} \tag{19}$$

$$B_{l,k}^{(2)} = \begin{cases} -\dfrac{1-\kappa^*(s)}{2G^*(s)} R_k \sum_{\substack{j=1 \\ j\neq k}}^{N} p_j^*(s) \overline{g_j^2(z_k)} & (l=-1), \\ -\dfrac{1-\kappa^*(s)}{2G^*(s)} R_k \sum_{\substack{j=1 \\ j\neq k}}^{N} p_j^*(s) \overline{g_j^2(z_k) g_k^{-l-1}(z_j)} & (l=-M_k, \dots, -2), \\ 0 & (l=1, \dots, M_k), \end{cases} \tag{20}$$

$$B_{l,k}^{(3)} = \begin{cases} \dfrac{1}{2G^*(s)} \big(-p_k^*(s) R_k\big) & (l=1), \\ 0 & (l=-1, \pm 2, \dots, \pm M_k). \end{cases} \tag{21}$$

Assume for simplicity that all components of the far-field stress vary in the same time-dependent manner; for example,

$$\sigma_{ij}^{\infty}(t) = \tilde{\sigma}_{ij}^{\infty} \cdot f_{\infty}(t),$$

where i, j represent x, y. Thus, in the Laplace domain the far-field stress is expressed by

$$\sigma_{ij}^{\infty,*}(s) = \tilde{\sigma}_{ij}^{\infty} \cdot f_{\infty}^*(s), \tag{22}$$

where the s-dependent function $f_{\infty}^*(s)$ is given as

$$f_{\infty}^*(s) = \Gamma\big[f_{\infty}(t)\big] = \int_0^{\infty} f_{\infty}(t) e^{-st}\, dt.$$

Similarly we assume that the tractions on the boundaries of the holes vary as

$$p_j(t) = \tilde{p}_j \cdot f_p(t), \quad j = 1, \ldots, N.$$

Thus, in the Laplace domain the boundary tractions are expressed by

$$p_j^*(s) = \tilde{p}_j \cdot f_p^*(s).$$

Substituting this and (22) into (19)–(21) and separating the s-dependent terms, we get

$$B^{(1)} = \frac{\kappa^*(s)+1}{4G^*(s)}\langle B^{(1)}\rangle f_\infty^*(s),$$

$$B^{(2)} = \frac{1-\kappa^*(s)}{2G^*(s)}\langle B^{(2)}\rangle f_p^*(s),$$

$$B^{(3)} = \frac{1}{2G^*(s)}\langle B^{(3)}\rangle f_p^*(s),$$

where

$$\langle B_{l,k}^{(1)}\rangle = \begin{cases} -R_k\left(\tilde{\sigma}_{yy}^\infty - \tilde{\sigma}_{xx}^\infty - 2i\tilde{\sigma}_{xy}^\infty\right) & (l=-1), \\ \frac{1}{2}R_k(\tilde{\sigma}_{xx}^\infty + \tilde{\sigma}_{yy}^\infty) & (l=1), \\ 0 & (l=\pm 2, \ldots, \pm M_k), \end{cases}$$

$$\langle B_{l,k}^{(2)}\rangle = \begin{cases} -R_k \sum_{\substack{j=1 \\ j\neq k}}^N \tilde{p}_j \overline{g_j^2(z_k)} & (l=-1), \\ -R_k \sum_{\substack{j=1 \\ j\neq k}}^N \tilde{p}_j \overline{g_j^2(z_k) g_k^{-l-1}(z_j)}, & (l=-M_k, \ldots, -2), \\ 0 & (l=1, \ldots, M_k), \end{cases}$$

$$\langle B_{l,k}^{(3)}\rangle = \begin{cases} -\tilde{p}_k R_k & (l=1), \\ 0 & (l=-1, \pm 2, \ldots, \pm M_k). \end{cases}$$

Thus, the solution of equation system (18) can be written compactly as

$$D = \frac{\kappa^*(s)+1}{4G^*(s)}\langle D^{(1)}\rangle f_\infty^*(s) + \frac{1-\kappa^*(s)}{2G^*(s)}\langle D^{(2)}\rangle f_p^*(s) + \frac{1}{2G^*(s)}\langle D^{(3)}\rangle f_p^*(s), \quad (23)$$

where the s-independent vectors $\langle D^{(j)}\rangle$ $(j = 1, \ldots, 3)$ are the solution of the following equation systems

$$\langle D^{(j)}\rangle = A^{-1}\langle B^{(j)}\rangle. \quad (24)$$

We emphasize that A^{-1} is computed only once. The system (24) can also be solved (after separating the real and imaginary parts) using standard numerical methods (Gauss elimination, Gauss–Seidel iteration, etc.).

5.3. ***Solution in the Laplace domain.*** With the substitution of the solution for Fourier coefficients (23) into the expressions for the potentials (12), followed by substitution of those potentials and their derivatives into (4)–(6), one obtains the solution for the displacements and stresses at any point z in the Laplace domain:

$$u_x(z;s)+iu_y(z;s)=\sum_{k=1}^{3}\left(f_k^*(s)\Phi_k-zf_{k+3}^*(s)\overline{\Phi_k'}-f_{k+3}^*(s)\overline{\Psi_k}\right)+f_5^*(s)\overline{\Psi^{(p)}}$$
$$+f_7^*(s)\frac{\tilde\sigma_{xx}^\infty+\tilde\sigma_{yy}^\infty}{2}z-f_4^*(s)\left(\tilde\sigma_{yy}^\infty-\tilde\sigma_{xx}^\infty-2i\tilde\sigma_{xy}^\infty\right)\bar z, \quad (25)$$

$$\sigma_{xx}(z;s)+\sigma_{yy}(z;s)=4\,\mathrm{Re}\left(\tfrac{1}{2}f_\infty^*(s)\Phi_1'+f_8^*(s)\Phi_2'+f_9^*(s)\Phi_3'\right)$$
$$+\left(\tilde\sigma_{xx}^\infty+\tilde\sigma_{yy}^\infty\right)f_\infty^*(s), \quad (26)$$

$$\sigma_{yy}(z;s)-\sigma_{xx}(z;s)+2i\sigma_{xy}(z;s)$$
$$=2\Big(\bar z\left(\tfrac{1}{2}f_\infty^*(s)\Phi_1''+f_8^*(s)\Phi_2''+f_9^*(s)\Phi_3''\right)$$
$$+\left(\tfrac{1}{2}f_\infty^*(s)\Psi_1'+f_8^*(s)\Psi_2'+f_9^*(s)\Psi_3'\right)+f_8^*(s)s^{-1}\Psi^{(p)\prime}\Big)$$
$$+\left(\tilde\sigma_{yy}^\infty-\tilde\sigma_{xx}^\infty+2i\tilde\sigma_{xy}^\infty\right)f_\infty^*(s), \quad (27)$$

where $\Phi^{(k)}$, $\Psi^{(k)}$ $(k=1,\dots,3)$ and $\Psi^{(p)}$ are given by

$$\Phi^{(k)}=\sum_{j=1}^{N}\sum_{m=1}^{M_j}\left\langle D_{-m,j}^{(k)}\right\rangle g_j^m(z),$$

$$\Psi^{(k)}=\sum_{j=1}^{N}\left(\left(g_j^2(z)+\frac{\overline{z_j}}{z-z_j}\right)\sum_{m=1}^{M_j}m\left\langle D_{-m,j}^{(k)}\right\rangle g_j^m(z)\right.$$
$$\left.-\left(\left\langle D_{1,j}^{(k)}\right\rangle+\overline{\left\langle D_{1,j}^{(k)}\right\rangle}\right)g_j(z)-\sum_{m=2}^{M_j}\overline{\left\langle D_{m,j}^{(k)}\right\rangle}g_j^m(z)\right),$$

$$\Psi^{(p)}=\sum_{j=1}^{N}\tilde p_j R_j g_j(z).$$

Note that $\Phi^{(k)}$, $\Psi^{(k)}$ and $\Psi^{(p)}$ are independent of the transform parameter s.

In these equations the s-independent Fourier coefficients $\left\langle D_{m,j}^{(k)}\right\rangle$, for $m=\pm1,\dots,\pm M_j$, are the components of the vectors $\left\langle D^{(k)}\right\rangle$ $(k=1,\dots,3)$ obtained from the equation systems (24).

The s-dependent functions involved in Equations (25)–(27) are written as

$$f_1^*(s)=\frac{\kappa^*(s)}{4G^*(s)}f_\infty^*(s), \qquad f_2^*(s)=\frac{1}{2G^*(s)}\frac{\kappa^*(s)\left(1-\kappa^*(s)\right)}{\kappa^*(s)+1}f_p^*(s),$$

$$f_3^*(s) = \frac{1}{2G^*(s)}\frac{\kappa^*(s)}{\kappa^*(s)+1} f_p^*(s), \qquad f_4^*(s) = \frac{1}{4G^*(s)} f_\infty^*(s),$$

$$f_5^*(s) = \frac{1}{2G^*(s)}\frac{1-\kappa^*(s)}{\kappa^*(s)+1} f_p^*(s), \qquad f_6^*(s) = \frac{1}{2G^*(s)}\frac{1}{\kappa^*(s)+1} f_p^*(s),$$

$$f_7^*(s) = \frac{\kappa^*(s)-1}{4G^*(s)} f_\infty^*(s), \qquad f_8^*(s) = \frac{1-\kappa^*(s)}{\kappa^*(s)+1} f_p^*(s),$$

$$f_9^*(s) = \frac{1}{\kappa^*(s)+1} f_p^*(s).$$

Note again that the space functions $\Phi^{(k)}$, $\Psi^{(k)}$ $(k = 1, 2, 3)$ and $\Psi^{(p)}$ are independent of the viscoelastic model and the time-dependent behavior for the loadings: $f_\infty(t)$ and $f_p(t)$. Thus the procedure is universal for any viscoelastic model and any loading situation.

5.4. ***Solution in the time domain.*** Upon application of the analytical inverse Laplace transform, equations (25)–(27) become

$$u_x(z;t) + iu_y(z;t) = \sum_{k=1}^{3}\big(f_k(t)\Phi_k - zf_{k+3}(t)\overline{\Phi_k'} - f_{k+3}(t)\overline{\Psi_k}\big) + f_5(t)\overline{\Psi^{(p)}} + f_7(t)\frac{\tilde\sigma_{xx}^\infty + \tilde\sigma_{yy}^\infty}{2}z - f_4(t)\big(\tilde\sigma_{yy}^\infty - \tilde\sigma_{xx}^\infty - 2i\tilde\sigma_{xy}^\infty\big)\bar z, \quad (28)$$

$$\sigma_{xx}(z;t) + \sigma_{yy}(z;t) = 4\,\mathrm{Re}\big(\tfrac{1}{2}f_\infty(t)\Phi_1' + f_8(t)\Phi_2' + f_9(t)\Phi_3'\big) + \sigma_{xx}^\infty(t) + \sigma_{yy}^\infty(t), \quad (29)$$

$$\begin{aligned}\sigma_{yy}(z;t) - \sigma_{xx}(z;t) + 2i\sigma_{xy}(z;t) &= 2\Big(\bar z\big(\tfrac{1}{2}f_\infty(t)\Phi_1'' + f_8(t)\Phi_2'' + f_9(t)\Phi_3''\big)\\ &\quad + \big(\tfrac{1}{2}f_\infty(t)\Psi_1' + f_8(t)\Psi_2' + f_9(t)\Psi_3'\big) + f_8(t)s^{-1}\Psi^{(p)\prime}\Big)\\ &\quad + \sigma_{yy}^\infty(t) - \sigma_{xx}^\infty(t) + 2i\sigma_{xy}^\infty(t), \end{aligned} \quad (30)$$

where $f_j(t)$ $(j = 1, \ldots, 9)$ are the analytical inverse Laplace transforms (1) of the s-functions, that is,

$$f_j(t) = \Gamma^{-1}\big[f_j^*(s)\big]. \quad (31)$$

It is observed from Equations (28) and (30) that to compute the displacements and stresses at multiple time instants, one need compute the potentials $\Phi^{(k)}$, $\Psi^{(k)}$, $\Psi^{(p)}$ and their derivatives only once (following the procedure described in Sections 5.1–5.3), and then successively multiply them by the time functions $f_j(t)$ $(j = 1, \ldots, 9)$ for each time instant. This procedure dramatically reduces the computational costs, as compared with time stepping approaches that use a nonconstant time step size.

Since the time dependence of the solutions is simply determined by the time functions $f_j(t)$ $(j = 1, \ldots, 9)$, the present approach provides the capability to adopt a variety of physical models and loading conditions. It is more flexible than the traditional time-stepping approach, in which the constitutive equation for the physical model is involved in the governing equations; see [Huang et al. 2005c; 2005b; 2005a].

In the solution procedure, the Fourier coefficients are not computed explicitly. The accuracy of the solution is nevertheless still dependent on the number of Fourier terms, as can be seen from the expressions of the potentials (12). We will perform the computation for given values M_k ($k = 1$ to N), and then increase the values of M_k until a specified degree of accuracy is achieved. Details about determining the number of terms in the Fourier expansion and the error estimation are given by [Mogilevskaya and Crouch 2001].

6. Examples

It is well known that for the class of problems considered in this paper the viscoelastic stresses are time-independent and are exactly same as the stresses in the corresponding elastic problems [Timoshenko and Goodier 1970]. In our approach, this conclusion can be rigorously proved for the case of one hole. For the case of multiple holes it has been verified numerically for all the examples in this paper. This fact provides the means to verify the solution for the stresses obtained with our approach. To do so we performed the computation and compared the results for the stresses to those for the elastic problems given in [Wang et al. 2003a] (the latter results have been verified with the benchmark results obtained earlier by [Ling 1948] and [Haddon 1967]). We achieved the same accuracy as reported in [Wang et al. 2003a].

Thus, below we only present the results for displacements. To demonstrate the versatility of our approach we present the examples for three different viscoelastic models.

6.1. ***Examples for viscoelastic model I.*** In this series of examples we assume that the viscoelastic material responds as a Boltzmann model in shear and elastically in dilatation (Figure 2). The constitutive equations for shear and dilatation are

$$\frac{G_1 + G_2}{G_1} s_{ij} + \frac{\eta}{G_1} \dot{s}_{ij} = 2G_2 \epsilon_{ij} + 2\eta \dot{\epsilon}_{ij}, \qquad \sigma_{kk} = 3K \varepsilon_{kk},$$

where the meanings of the elastic and viscous parameters G_1, G_2 and η are explained in Figure 2. The numbers s_{ij} (σ_{kk}) and ϵ_{ij} (ε_{kk}) are the deviatoric (volumetric) components of the stress and strain tensors σ_{ij} and ε_{ij}:

$$\sigma_{ij} = s_{ij} + \tfrac{1}{3}\delta_{ij}\sigma_{kk}, \qquad \varepsilon_{ij} = \epsilon_{ij} + \tfrac{1}{3}\delta_{ij}\varepsilon_{kk}.$$

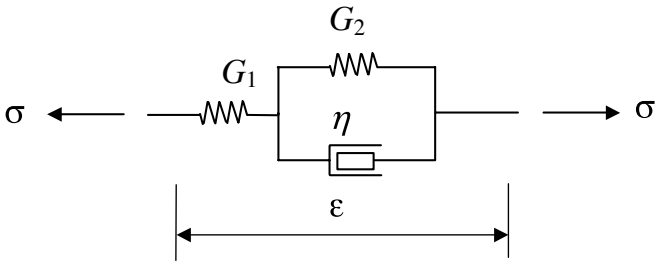

Figure 2. Boltzmann model.

Following the procedure described in [Wang and Crouch 1982], one can find the s-varying constants for this model as follows:

$$\begin{aligned} G^*(s) &= \frac{G_1(G_2+\eta s)}{G_1+G_2+\eta s}, \\ \kappa^*(s) &= 1+\frac{6G_1(G_2+\eta s)}{G_1(G_2+\eta s)+3(G_1+G_2+\eta s)K}. \end{aligned} \tag{32}$$

Assume that the stresses at infinity and the tractions on the boundaries of the holes are suddenly applied at $t=0$ and remain constant. Thus,

$$f_\infty(t)=1 \quad \text{and} \quad f_p(t)=1.$$

By Laplace transformation, this yields

$$f_\infty^*(s)=\frac{1}{s} \quad \text{and} \quad f_p^*(s)=\frac{1}{s}.$$

With the substitution of these equations and (32) into the expressions for f_i^* (see pages 483–484), and after an analytic inverse Laplace transformation, one obtains for the time functions the expressions

$$\begin{aligned} f_1(t) &= \tfrac{1}{4}\chi_1(t), & f_2(t) &= -\tfrac{1}{2}\chi_1(t)+\chi_2(t)-\chi_3(t), \\ f_3(t) &= \tfrac{1}{2}\big(\chi_2(t)-\chi_3(t)\big), & f_4(t) &= \tfrac{1}{4}\chi_2(t), \\ f_5(t) &= -\tfrac{1}{2}\chi_2(t)+\chi_3(t), & f_6(t) &= \tfrac{1}{2}\chi_3(t), \\ f_7(t) &= \tfrac{1}{4}\big(\chi_1(t)-\chi_2(t)\big) & f_8(t) &= -1+2\chi_4(t), \\ & & f_9(t) &= \chi_4(t), \end{aligned} \tag{33}$$

with

$$\chi_1(t) = \frac{(G_1+G_2)(C_2+3G_1G_2)}{G_1G_2C_1} - \frac{1}{G_2}e^{-\alpha t} - \frac{6G_1^2e^{-\beta t}}{(3K+G_1)C_1},$$

$$\chi_2(t) = \frac{1}{G_1} + \frac{1-e^{-\alpha t}}{G_2},$$

$$\chi_3(t) = \frac{(G_1+G_2)C_1}{2G_1G_2C_2} - \frac{1}{2G_2}e^{-\alpha t} + \frac{6G_1^2e^{-\gamma t}}{(3K+4G_1)C_2},$$

$$\chi_4(t) = \frac{1}{2} - \frac{3G_1G_2}{2C_2} - \frac{9KG_1^2e^{-\gamma t}}{2(3K+4G_1)C_2},$$

where the following abbreviations have been introduced:

$$\alpha = \frac{G_2}{\eta}, \tag{34}$$

$$\beta = \frac{1}{\eta}\Big(\frac{3KG_1}{3K+G_1} + G_2\Big), \qquad \gamma = \frac{1}{\eta}\Big(\frac{3KG_1}{3K+4G_1} + G_2\Big),$$

$$C_1 = 3KG_2 + G_1(3K+G_2), \qquad C_2 = 3KG_2 + G_1(3K+4G_2).$$

6.1.1. *An example with constant far-field stresses.* Consider two traction-free circular holes of different sizes in an infinite plane subjected to far-field stresses σ_{xx}^{∞}, σ_{yy}^{∞} and σ_{xy}^{∞}. As shown in Figure 3, two holes L_1 and L_2 with radii R_1 and R_2 are aligned with the x- axis and separated by a distance d.

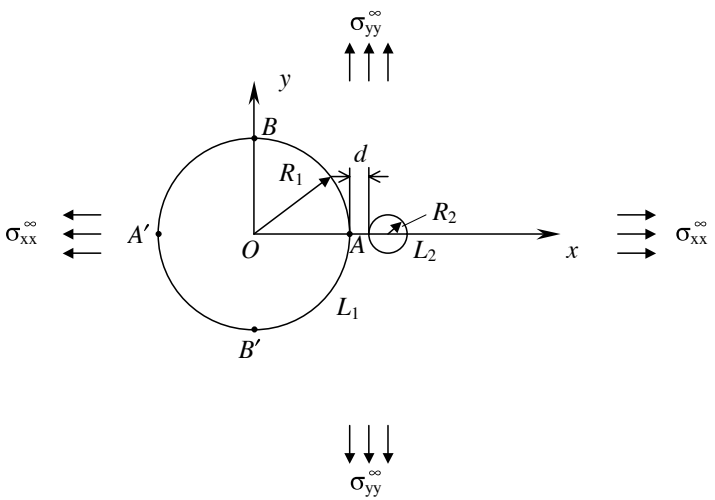

Figure 3. Two circular holes in an infinite plane.

The elastic problem with the same geometrical configuration under three loading conditions (longitudinal tension: $\sigma_{xx}^{\infty} = \sigma_0$, $\sigma_{yy}^{\infty} = \sigma_{xy}^{\infty} = 0$; transverse tension: $\sigma_{yy}^{\infty} = \sigma_0$, $\sigma_{xx}^{\infty} = \sigma_{xy}^{\infty} = 0$; and pure shear: $\sigma_{xy}^{\infty} = \sigma_0$, $\sigma_{xx}^{\infty} = \sigma_{yy}^{\infty} = 0$) was considered in [Wang et al. 2003a]. By using the method described in the present paper, we obtained the results for the corresponding viscoelastic problems. The parameters were adopted for the viscoelastic material were

$$G_1 = 8 \times 10^3 \sigma_0, \quad G_2 = 2 \times 10^3 \sigma_0, \quad \eta = 5 \times 10^3 \sigma_0 \cdot \text{sec}, \quad K = 17333.3\sigma_0,$$

To obtain the dimensionless time we used the viscosity coefficient $\gamma = \eta / G_2 = 2.5$ second.

To examine the numerical results for displacements, the relative elongations of the diameters of hole L_1 in the x and y directions

$$\delta_x = \frac{u_x(A) - u_x(A')}{2R_1} \quad \text{and} \quad \delta_y = \frac{u_y(B) - u_y(B')}{2R_1} \tag{35}$$

are computed for the case $R_1/R_2 = 5$; $d/R_2 = 1$ and $\sigma_{xx}^{\infty} = \sigma_0$, $\sigma_{yy}^{\infty} = 0.5\sigma_0$, $\sigma_{xy}^{\infty} = 0$ and the results were compared with those obtained with the commercial finite element software-ANSYS. Since ANSYS cannot directly model an infinite area, the infinite viscoelastic plane was modeled as a large plate ($200R_2 \times 200R_2$). Prony series were adopted to approximate the relaxation functions of the shear and bulk moduli and a time stepping algorithm was used to obtain the time domain solution in ANSYS. With ANSYS, 4839 finite elements were used and the computation took 2 hours 16 minutes on an IBM SP workstation (500 time steps). With the present approach, only 36 terms in the Fourier series were used to represent the boundary displacements for the two holes and the computation just took 19 seconds with a 900 MHz PC (500 time instants). It is seen from Figure 4 that the results given by the two approaches match very well.

6.1.2. *An example with constant pressure.* Consider the case of three holes shown in Figure 5. The boundaries of two smaller holes with the radii $R_2 = R_3 = R$ are assumed to be traction-free. The central hole with the radius R_1 ($R_1/R = 5$) is subjected to constant pressure $p_1 = -\sigma_0$. The three holes are separated by a distance $d = R$. The material properties for the viscoelastic plane are the same as those in the previous example.

The relative elongations of the diameters of the central hole L_1 in the x and y directions, given by (35), are computed and compared with the results provided by ANSYS. It is seen from Figure 6 that the results given by the two approaches agree very well. Due to the existence of holes L_2 and L_3 along the x axis, the change of diameter of the central hole in the x direction is larger than that in the y direction.

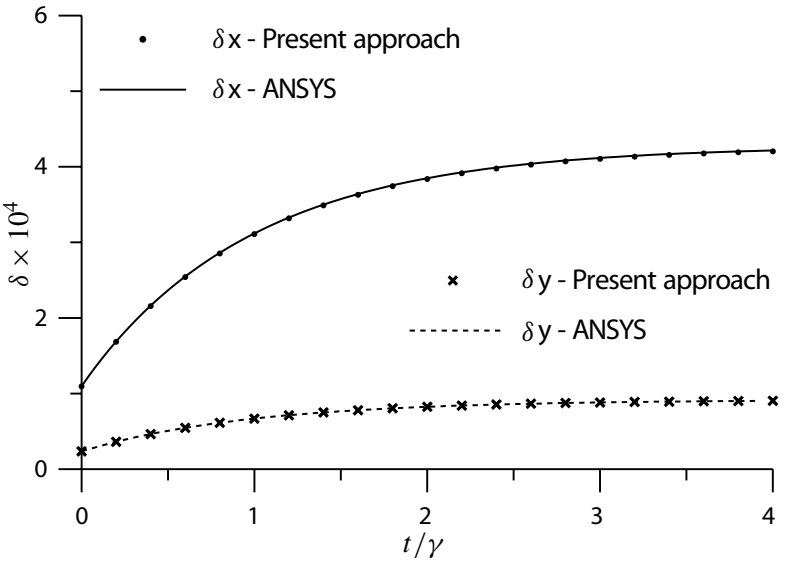

Figure 4. Change of diameter of the hole L_1 due to far-field stresses.

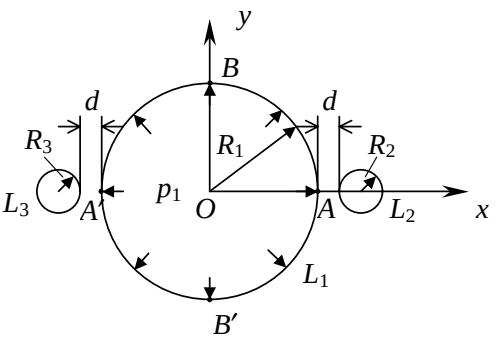

Figure 5. Three holes in an infinite plane with the central hole subjected to constant pore pressure.

6.2. ***Examples for viscoelastic model II.*** In this series of examples we assume that the viscoelastic material responds as a Boltzmann model in both shear and dilatation, and the Poisson's ratio ν is constant. As the result of these assumptions the viscoelastic properties of the material can be represented by the constants G_1, G_2, η (Figure 2) and ν.

Following the procedure described in [Wang and Crouch 1982], one can find the s-varying constants for this model using the equations

$$G^*(s) = \frac{G_1\,(G_2 + \eta s)}{G_1 + G_2 + \eta s}, \quad \kappa^*(s) = 3 - 4\nu.$$

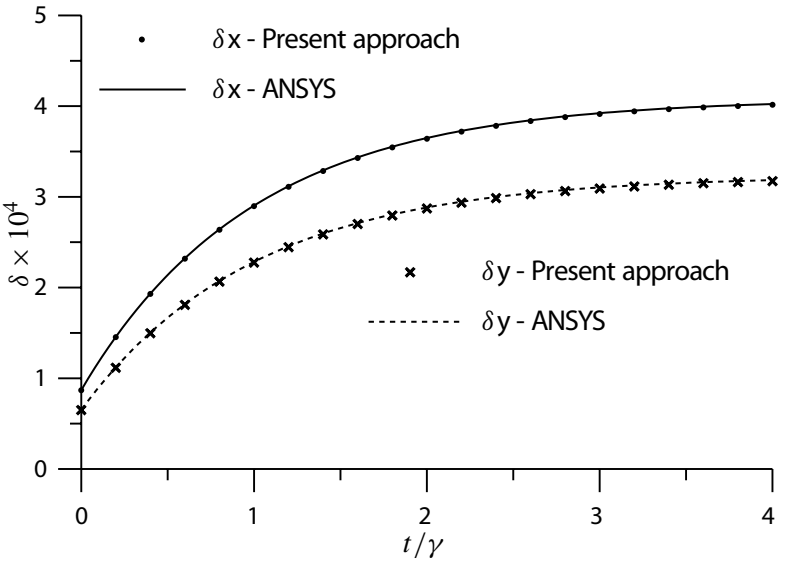

Figure 6. Change of diameter of the central hole due to a constant pressure.

In case that the stresses at infinity and the tractions on the boundaries of the holes are kept constant, the time functions $f_j(t)$ $(j = 1, \ldots, 9)$ can again be expressed by Equations (33) with the functions $\chi_k(t)$ $(k = 1, \ldots, 4)$ given by

$$\chi_1(t) = (3-4\nu)\left(\frac{1}{G_1} + \frac{1-e^{-\alpha t}}{G_2}\right), \qquad \chi_2(t) = \frac{1}{G_1} + \frac{1-e^{-\alpha t}}{G_2},$$

$$\chi_3(t) = \frac{1}{4-4\nu}\left(\frac{1}{G_1} + \frac{1-e^{-\alpha t}}{G_2}\right), \qquad \chi_4(t) = \frac{1}{4-4\nu},$$

where α is defined in Equation (34).

6.2.1. *An example with constant far-field stresses.* The geometry of this example is the same as that depicted in Figure 5. The boundaries of all three holes are assumed to be traction-free and the infinite plane is subjected to biaxial far-field stresses $\sigma_{xx}^{\infty} = \sigma_0$ and $\sigma_{yy}^{\infty} = 0.5\sigma_0$. The material properties adopted in computation were

$$G_1 = 8 \times 10^3 \sigma_0, \quad G_2 = 2 \times 10^3 \sigma_0, \quad \eta = 5 \times 10^3 \sigma_0 \cdot \text{sec}, \quad \nu = 0.25.$$

The viscosity coefficient $\gamma = \eta/G_2 = 2.5$ second was again employed. The relative elongations of the diameters of the central hole L_1 in the x and y directions, given by Equation (35), are computed and compared with the results provided by the time stepping approach described in [Huang et al. 2005b]. It is seen from Figure 7 that the results given by the two approaches are practically identical. To accomplish the computation of the same number (500) of time instants (or steps)

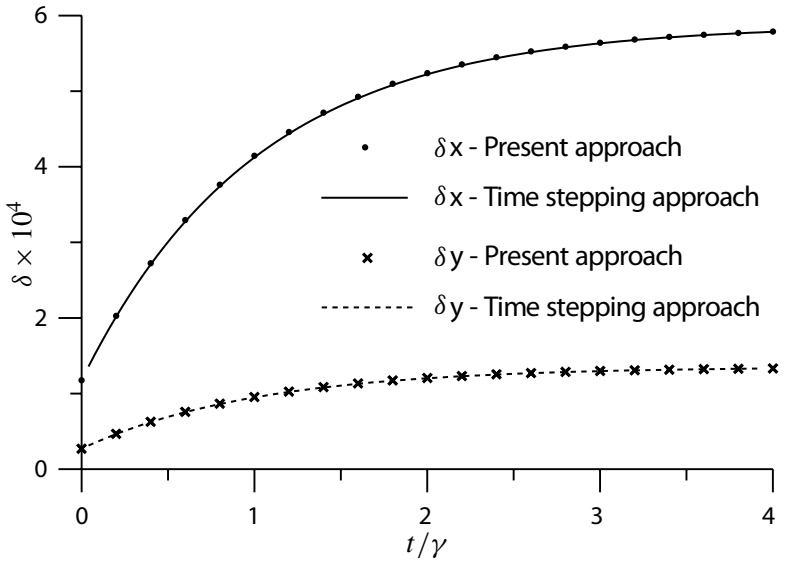

Figure 7. Change of diameter of the central hole due to constant far-field stresses.

and reach the same accuracy, the present approach used 35 terms of the Fourier series for each of the three circular holes and the computation took 42 seconds, while the time stepping approach used 45 terms of the Fourier series for the central hole and 12 terms of the Fourier series for the two smaller holes and the computation took about twice as long, 1 minute 38 seconds. The difference can be explained as follows: with the current approach, the algebraic equation systems are formulated and solved only once and the same potentials (and their derivatives) are used for the computation at every time instant; only the time functions $f_j(t)$ $(j = 1, \ldots, 9)$ need to be recomputed to obtain the stresses and displacements at different time instants. In the time stepping approach, since the solution for a typical time step relies on the results for the previous step, the system of algebraic equations needs to be solved for each time step [Huang et al. 2005b].

6.2.2. *An example with time-dependent pressure.* Now we modify the loading conditions in the previous example (Section 6.2.1) and assume that $\sigma_{xx}^{\infty} = \sigma_{yy}^{\infty} = \sigma_{xy}^{\infty} = 0$ and the central hole is subjected to time-dependent pressure given in sinusoidal form as

$$p_1(t) = -\sigma_0 (1 + c \sin \omega t).$$

The boundaries of the other two holes are traction-free.

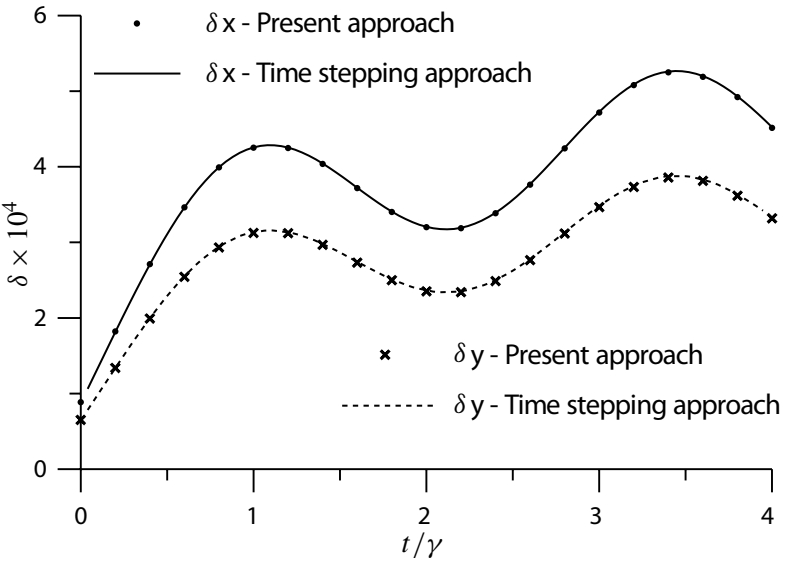

Figure 8. Change of diameter of the central hole due to a time-dependent pressure.

The time functions $f_j(t)$ $(j = 1, \ldots, 7, 9)$ can again be expressed by the corresponding equations in (33), with the functions $\chi_k(t)$ $(k = 1, \ldots, 4)$ given by

$$\chi_1(t) = \frac{3-4\nu}{G_1 G_2(\eta^2\omega^2 + G_2^2)}\Big(-G_1(\eta^2\omega^2 - c\eta\omega G_2 + G_2^2)e^{-(G_2/\eta)t} (1 + c\sin\omega t)G_2(\eta^2\omega^2 + G_2^2 + G_1 G_2) + G_1\eta\omega(\eta\omega - c\cos\omega t G_2)\Big),$$

$$\chi_2(t) = \frac{1}{3-4\nu}\chi_1(t), \quad \chi_3(t) = \frac{1}{(3-4\nu)(4-4\nu)}\chi_1(t), \quad \chi_4(t) = \frac{1}{4-4\nu}(1+c\sin\omega t),$$

while

$$f_8(t) = -(1 + c\sin\omega t) + 2\chi_4(t).$$

The material properties for this example are the same as those in the previous subsection. In the computation, the following values for the pressure are adopted: $c = 0.5$ and $\omega = 1\,\text{sec}^{-1}$. The relative elongations of the diameters of the central hole L_1 in the x and y directions, given by Equation (35), are computed and compared with the results provided by the time stepping approach in Figure 8. It is seen that the results given by the two approaches are practically identical. The behaviors of δx and δy are characterized by the combination of exponential and sinusoidal functions.

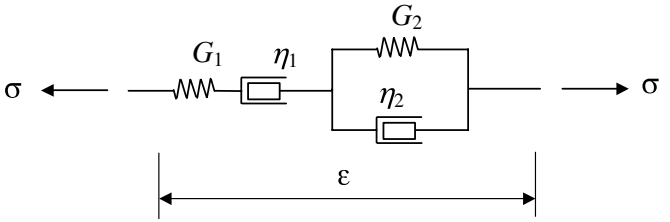

Figure 9. Burgers model.

6.3. ***Examples for viscoelastic model III.*** Here we take

$$\ddot{s}_{ij}+\Big(\frac{G_1}{\eta_1}+\frac{G_1}{\eta_2}+\frac{G_2}{\eta_2}\Big)\dot{s}_{ij}+\frac{G_1G_2}{\eta_1\eta_2}s_{ij}=2G_1\ddot{\epsilon}_{ij}+2\frac{G_1G_2}{\eta_2}\dot{\epsilon}_{ij},\qquad \sigma_{kk}=3K\varepsilon_{kk},$$

where the meanings of the elastic and viscous parameters G_1, G_2, η_1 and η_2 are explained in Figure 9.

Following the procedure described in [Wang and Crouch 1982], one can find the s-varying constants using the equations

$$G^*(s)=\frac{G_1s^2+\dfrac{G_1G_2}{\eta_2}s}{s^2+\Big(\dfrac{G_1}{\eta_1}+\dfrac{G_1}{\eta_2}+\dfrac{G_2}{\eta_2}\Big)s+\dfrac{G_1G_2}{\eta_1\eta_2}},$$

$$\kappa^*(s)=1+\frac{6G_1s^2+6\dfrac{G_1G_2}{\eta_2}s}{G_1s^2+\dfrac{G_1G_2}{\eta_2}s+3\left(s^2+\Big(\dfrac{G_1}{\eta_1}+\dfrac{G_1}{\eta_2}+\dfrac{G_2}{\eta_2}\Big)s+\dfrac{G_1G_2}{\eta_1\eta_2}\right)K}.$$

If the far-field stresses and the tractions on the boundaries of holes are both constant, one can obtain the time functions $f_j(t)$ $(j=1,\dots,9)$ expressed by (33), with the functions $\chi_k(t)$ $(k=1,\dots,4)$ given as

$$\chi_1(t)=\frac{1}{KG_1}\left(K-\frac{G_1^2}{3K+G_1}e^{-\alpha t}(1+e^{\beta t})+G_1\Big(2+\frac{K}{G_2}(1-e^{-\varrho t})+\frac{K}{\eta_1}t\Big)\right.$$
$$\left.+\frac{e^{-\alpha t}(-1+e^{\beta t})G_1^2\big((3KG_1-(3K+G_1)G_2)\eta_1+3KG_1\eta_2\big)}{(3K+G_1)C_3}\right),$$

$$\chi_2(t)=\frac{1}{G_1}+\frac{1-e^{-\varrho t}}{G_2}+\frac{1}{\eta_1}t,$$

$$\chi_3(t)=\frac{1}{2KG_1}\Bigg(K+\frac{G_1^2}{3K+4G_1}e^{-\alpha' t}(1+e^{\beta' t})+G_1\Big(-1+\frac{K}{G_2}(1-e^{-\varrho t})+\frac{K}{\eta_1}t\Big)$$
$$-\frac{2e^{-\alpha' t}(-1+e^{\beta' t})G_1^2\big(-3KG_2\eta_1+G_1((3K-4G_2)\eta_1+3K\eta_2)\big)}{(3K+4G_1)C_3'}\Bigg),$$

$$\chi_4(t)=\frac{1}{2}-\frac{3G_1}{4(3K+4G_1)C_3'}\Bigg(e^{\alpha' t}\Big(3KG_2\eta_1+G_1\big((-3K+4G_2)\eta_1-3K\eta_2\big)+C_3'\Big)$$
$$+e^{-\alpha'' t}\big(-3KG_2\eta_1+G_1((3K-4G_2)\eta_1+3K\eta_2)+C_3'\big)\Bigg),$$

where the constants that occur are

$$C_1=(3K+G_1)\eta_1\eta_2,$$
$$C_2=3KG_2\eta_1+G_1\big((3K+G_2)\eta_1+3K\eta_2\big),$$
$$C_3=\sqrt{-12KG_1G_2C_1+C_2^2},$$
$$C_1'=(3K+4G_1)\eta_1\eta_2,$$
$$C_2'=3KG_2\eta_1+G_1\big((3K+4G_2)\eta_1+3K\eta_2\big),$$
$$C_3'=\sqrt{-12KG_1G_2C_1'+C_2'^2},$$
$$\alpha=\frac{C_2+C_3}{2C_1},\quad \beta=\frac{C_3}{C_1},\quad \varrho=\frac{G_2}{\eta_2},\quad \alpha'=\frac{-C_2'+C_3'}{2C_1'},\quad \alpha''=\frac{C_2'+C_3'}{2C_1'}.$$

6.3.1. *An example with constant far-field stresses.* Consider the same example described in Section 6.1.1 (Figure 3). The geometric parameters are taken as follows: $R_1/R_2=5$, $d/R_2=1$. The holes are traction-free and the stresses at infinity are given as $\sigma_{xx}^{\infty}=\sigma_0$, $\sigma_{xx}^{\infty}=\sigma_{xy}^{\infty}=0$. The material properties adopted for the computations are

$$G_1=8\times10^3\sigma_0,\quad G_2=2\times10^3\sigma_0,\quad \eta_1=8\times10^3\sigma_0\cdot\text{sec},$$
$$\eta_2=5\times10^3\sigma_0\cdot\text{sec},\quad K=17333.3\sigma_0,$$

In this example the displacement u_x along the straight line between the two points $(5R_2,0)$ and $(6R_2,0)$ is computed for three time instants: $t=0$ sec, $t=1$ sec, and $t=10$ sec (Figure 10). The left end point $(5R_2,0)$ is fixed. It can be observed that the deformation keeps increasing with time. This can be explained by the linear term in t in the time-dependent expressions for χ_1, χ_2, χ_3, χ_4 starting at the bottom of the previous page.

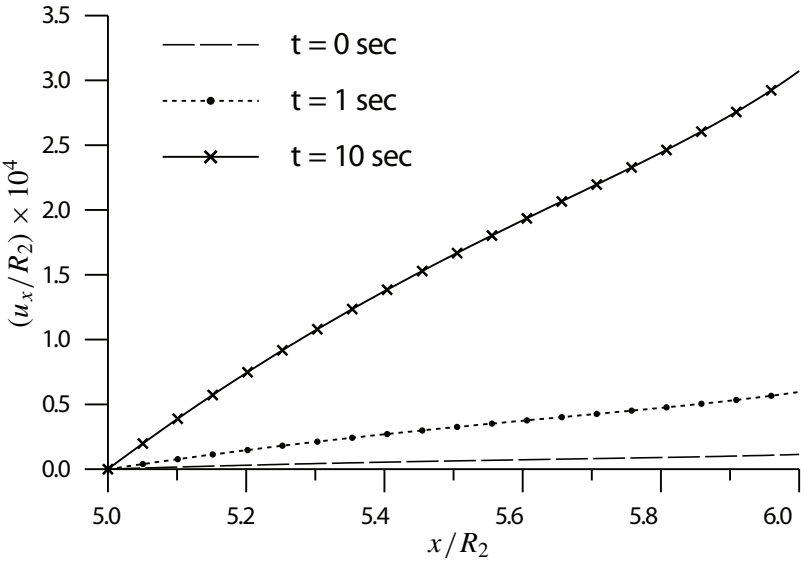

Figure 10. u_x along the line between the two holes.

6.3.2. *An example with constant far-field stresses and pressure.* In this example, we demonstrate the use of our method for solving problems involving multiple randomly distributed holes. The same material properties are adopted as in the previous subsection. The viscoelastic plane is subjected to constant far-field stresses $\sigma_{xx}^{\infty} = \sigma_0$, $\sigma_{xx}^{\infty} = \sigma_{xy}^{\infty} = 0$, and constant uniform pressure $p = -\sigma_0$ is applied to one of the holes. Figures 11–13 show contours of u_x in the plane at three time instants: $t = 0$ sec, $t = 0.5$ sec and $t = 10$ sec. It is shown that the plane is stretched and that the displacements are increasing with time. The solution to this problem took approximately 26 minutes on a 900 MHz PC.

Even though this problem only involves 12 holes, our approach can be used to solve more complicated problems involving a larger number of holes of arbitrary sizes and locations as long as none of the holes overlap, and with more complicated loading conditions.

6.4. ***Special case of one hole.*** For the particular case of a single hole in an elastic plane, the displacements on the boundary of the hole are exactly represented by a two-term complex Fourier series [Muskhelishvili 1963]. This fact is retained for the viscoelastic plane and the only nonzero 'coefficients' are

$$\begin{aligned} \langle D_{-1}^{(1)} \rangle &= -R(\tilde{\sigma}_{yy}^{\infty} - \tilde{\sigma}_{xx}^{\infty} - 2i\tilde{\sigma}_{xy}^{\infty}), \\ \langle D_{1}^{(1)} \rangle &= \tfrac{1}{2} R(\tilde{\sigma}_{xx}^{\infty,*} + \tilde{\sigma}_{yy}^{\infty}), \\ \langle D_{1}^{(3)} \rangle &= -\tilde{p}R. \end{aligned} \tag{36}$$

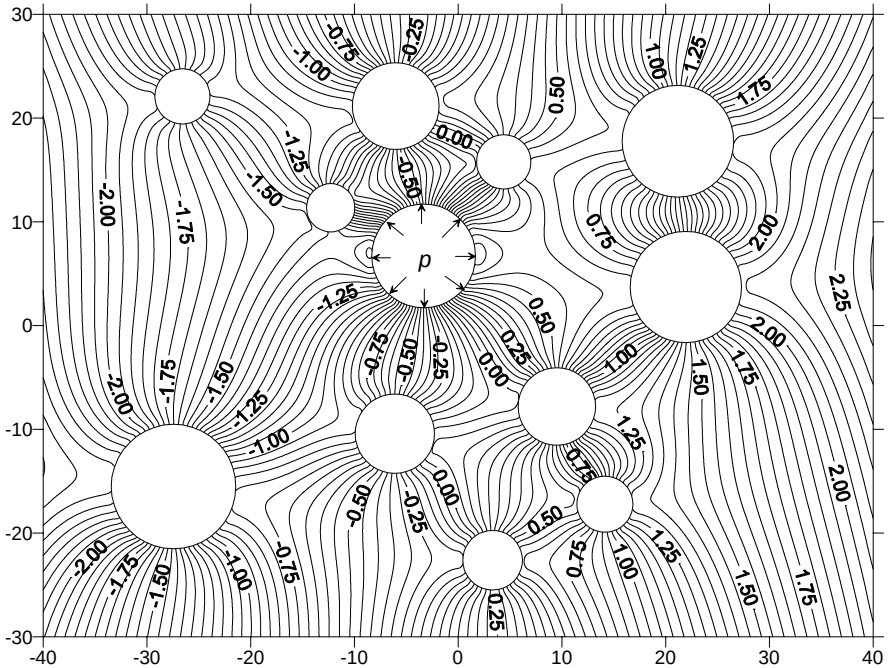

Figure 11. Contour of u_x at $t = 0$ sec.

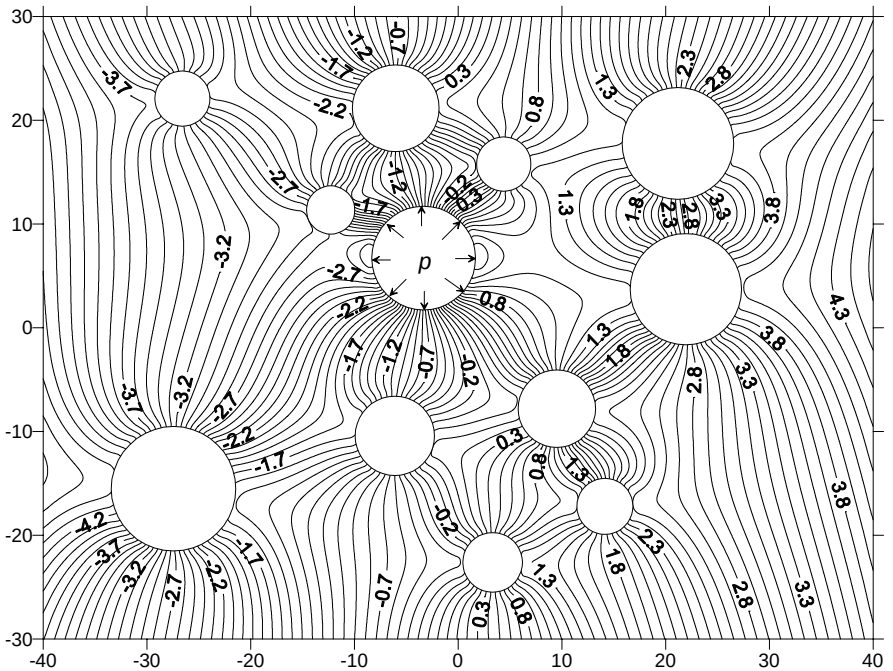

Figure 12. Contour of u_x at $t = 0.5$ sec.

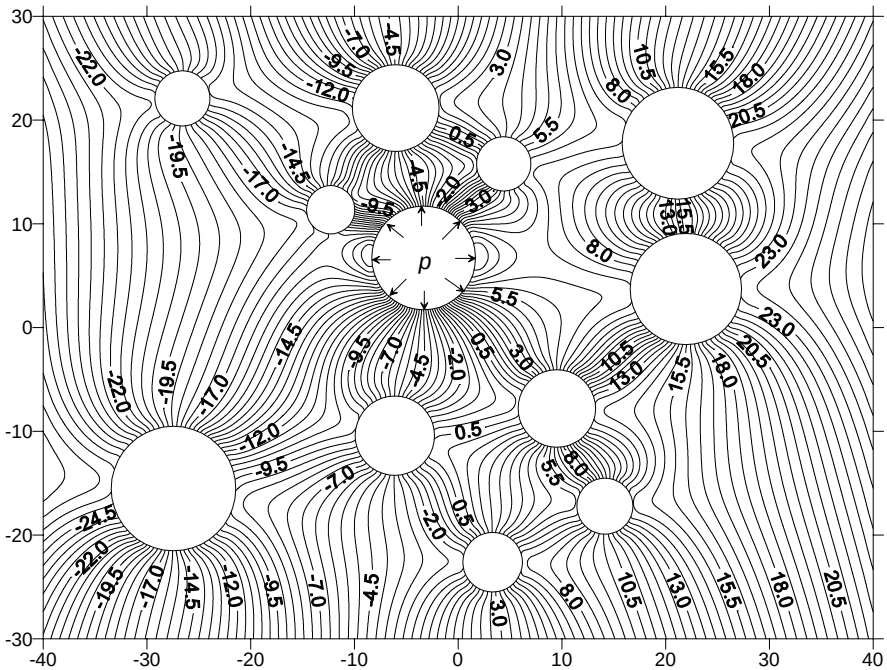

Figure 13. Contour of u_x at $t = 10$ sec.

The time functions $f_j(t)$ $(j = 1, \ldots, 9)$ can be obtained for the specific viscoelastic model and loading condition, as explained in the examples above. Using (36) and the time functions $f_j(t)$ and performing some algebraic manipulations one can obtain the analytical solution for the special case of a single circular hole within an infinite viscoelastic plane.

7. Concluding remarks

A complex variable boundary integral method combined with analytical Laplace transform and its inversion is presented to obtain a semi-analytical solution for the problem of an infinite viscoelastic plane containing multiple circular holes. The method is based on the use of the correspondence principle and a complex variable hypersingular integral equation for a corresponding elastic problem. A significant feature of the governing integral equation is that the transformed material parameters are not involved in the integral terms for the transformed boundary displacements.

The main features of the solution for an analogous elastic problem are preserved in the current method [Wang et al. 2003a]. The unknown displacements on the circular boundaries of the holes in Laplace domain are approximated by truncated

complex Fourier series with the coefficients dependent on the transform parameter. A system of linear algebraic equations is formed by using the Taylor series expansion. Solutions of stresses and displacements in Laplace domain are written in terms of viscoelastic analogs of Kolosov–Muskhelishvili potentials, which are defined through integrals of displacements on the boundaries of the holes. The time domain solution for stresses and displacements are obtained using the analytical inverse Laplace transform.

The present method has the following advantages:

(1) The time dependence of the viscoelastic solution is expressed through several simple time functions. Thus, the method can easily incorporate a variety of physical models and loading conditions.

(2) All the mathematical operations (space integration, direct and inverse Laplace transforms) are performed analytically. The accuracy of the problem is only dependent on the number of terms in the complex Fourier series and the only error (apart from round-off) comes from the truncation of the Fourier series. This method provides an analytical solution for the problem involving only one hole, where the boundary displacements can be exactly expressed through finite terms in the Fourier series.

(3) The matrix of the resulting system of linear algebraic equations is inverted only once and the results are used for the calculation of the viscoelastic responses at any time instants. Thus, the method produces significant computational savings as compared with the numerical methods based on time stepping. The latter methods permit the use of a one-time inversion of the matrix only if the time step size is constant. Our method has no such limitation.

(4) The number of degrees of freedom is much less than in finite element-based methods.

The present approach allows a straightforward extension to the case where the displacements are prescribed on the boundaries of the holes if the Poisson's ratio of the viscoelastic matrix is constant. The case with a time-dependent Poisson's ratio for the matrix and the displacements prescribed at the boundaries is more complicated and needs more investigation.

Future developments of the approach might include the extension to problems of multiple circular holes within a finite circular viscoelastic domain as well as the extension to problems involving a half-plane containing multiple holes (by using the viscoelastic analog of the equation (21) in [Mogilevskaya 2000]). Another possibility is to extend the approach to problems of multiple holes of arbitrary shape. The governing Equation (2) remains valid for this case. Thus, the problem can be solved using the boundary element technique where the boundary of each hole is

divided into elements and the unknowns on each of the elements are approximated by piecewise polynomials with time-dependent coefficients. Problems involving multiple curvilinear cracks could be also considered. This class of problems is governed by Equation (2), with unknown displacement discontinuities rather than displacements [Linkov and Mogilevskaya 1994].

Acknowledgments

The authors would like to acknowledge the University of Minnesota Supercomputing Institute for providing access to the finite element software ANSYS.

References

[Bird 1992] M. D. Bird, *A Fourier series method for determining the interaction of circular inhomogeneities in harmonic and biharmonic problems*, Ph.D. thesis, Stanford University, 1992.

[Bird and Steele 1991] M. D. Bird and C. R. Steele, "A separated solution procedure for bending of circular plates with circular holes", *Appl. Mech. Rev.* **44**:11, part 2 (1991), 27–35.

[Bird and Steele 1992] M. D. Bird and C. R. Steele, "Solution procedure for Laplace's equation on multiply connected circular domains", *J. Appl. Mech.* (*ASME*) **59** (1992), 398–404.

[Carini and Gioda 1986] A. Carini and G. Gioda, "A boundary integral equation technique for viscoelastic stress analysis", *Int. J. Numer. Anal. Methods Geomech.* **10**:6 (1986), 585–608.

[Chen et al. 2006a] J. T. Chen, C. C. Hsiao, and S. Y. Leu, "Null-field integral equation approach for plate problems with circular holes", *J. Appl. Mech.* (*ASME*) **73**:4 (2006), 679–693.

[Chen et al. 2006b] J. T. Chen, W. C. Shen, and P. Y. Chen, "Analysis of circular torsion bar with circular holes using null-field approach", *Comput. Model. Eng. Sci.* **12**:2 (2006), 109–119.

[Chen et al. 2006c] J. T. Chen, W. C. Shen, and A. C. Wu, "Null-field integral equations for stress field around circular holes under antiplane shear", *Eng. Anal. Bound. Elem.* **30**:3 (2006), 205–217.

[Crouch and Mogilevskaya 2003] S. L. Crouch and S. G. Mogilevskaya, "On the use of Somigliana's formula and Fourier series for elasticity problems with circular boundaries", *Int. J. Numer. Methods Eng.* **58**:4 (2003), 537–578.

[Findly et al. 1989] W. N. Findly, J. S. Lai, and K. Onaran, *Creep and relaxation of nonlinear viscoelastic materials*, Dover, New York, 1989.

[Haberman 1998] R. Haberman, *Elementary applied partial differential equations with Fourier series and boundary value problems*, 3rd ed., Prentice-Hall, Upper Saddle River, NJ, 1998. MR 84a:35001

[Haddon 1967] R. A. Haddon, "Stresses in an infinite plate with two unequal circular holes", *Q. J. Mech. Appl. Math.* **20**:3 (1967), 277–291.

[Huang et al. 2005a] Y. Huang, S. L. Crouch, and S. G. Mogilevskaya, "A direct boundary integral method for viscoelastic-elastic composite materials", pp. 264–267 in *Computational fluid and solid mechanics 2005*, edited by K. J. Bathe, Elsevier, Amsterdam, 2005.

[Huang et al. 2005b] Y. Huang, S. L. Crouch, and S. G. Mogilevskaya, "Direct boundary integral procedure for a Boltzmann viscoelastic plane with circular holes and elastic inclusions", *Comput. Mech.* **37**:1 (2005), 110–118.

[Huang et al. 2005c] Y. Huang, S. L. Crouch, and S. G. Mogilevskaya, "A time domain direct boundary integral method for a viscoelastic plane with circular holes and inclusions", *Eng. Anal. Bound. Elem.* **29**:7 (2005), 725–737.

[Kusama and Mitsui 1982] T. Kusama and Y. Mitsui, "Boundary element method applied to linear viscoelastic analysis", *Appl. Math. Model.* **6**:4 (1982), 285–290.

[Lee 1955] E. H. Lee, "Stress analysis in visco-elastic bodies", *Quart. Appl. Math.* **13** (1955), 183–190. MR 16,1073e

[Lee and Kim 1995] S. S. Lee and Y. J. Kim, "Time-domain boundary element analysis of cracked linear viscoelastic solids", *Eng. Frac. Mech.* **51**:4 (1995), 585–590.

[Lee et al. 1994] S. S. Lee, Y. S. Sohn, and S. H. Park, "On fundamental solutions in time-domain boundary element analysis of linear viscoelasticity", *Eng. Anal. Bound. Elem.* **13**:3 (1994), 211–217.

[Legros et al. 2004] B. Legros, S. G. Mogilevskaya, and S. L. Crouch, "A boundary integral method for multiple circular inclusions in an elastic half-plane", *Eng. Anal. Bound. Elem.* **28**:9 (2004), 1083–1098.

[Ling 1948] C. B. Ling, "On the stresses in a plate containing two circular holes", *J. Appl. Phys.* **19**:1 (1948), 77–82. MR 9,395k

[Linkov 2002] A. M. Linkov, *Boundary integral equations in elasticity theory*, Kluwer, Dordrecht, 2002.

[Linkov and Mogilevskaya 1994] A. M. Linkov and S. G. Mogilevskaya, "Complex hypersingular integrals and integral equations in plane elasticity", *Acta Mech.* **105**:1–4 (1994), 189–205. MR 95c:73096

[Linkov and Mogilevskaya 1998] A. M. Linkov and S. G. Mogilevskaya, "Complex hypersingular BEM in plane elasticity problems", pp. 299–364 in *Singular integrals in boundary element methods*, edited by V. Sladek and J. Sladek, Computational Mechanics Publications, Southampton, 1998.

[Mesquita and Coda 2001] A. D. Mesquita and H. B. Coda, "An alternative time integration procedure for Boltzmann viscoelasticity: a BEM approach", *Comput. Struct.* **79**:16 (2001), 1487–1496. MR 2002f:74079

[Mesquita and Coda 2002a] A. D. Mesquita and H. B. Coda, "Alternative Kelvin viscoelastic procedure for finite elements", *Appl. Math. Model.* **26**:4 (2002), 501–516.

[Mesquita and Coda 2002b] A. D. Mesquita and H. B. Coda, "Boundary integral equation method for general viscoelastic analysis", *Int. J. Solids Struct.* **39**:9 (2002), 2643–2664.

[Mesquita and Coda 2003] A. D. Mesquita and H. B. Coda, "New methodology for the treatment of two dimensional viscoelastic coupling problems", *Comput. Methods Appl. Mech. Eng.* **192**:16–18 (2003), 1911–1927.

[Mogilevskaya 2000] S. G. Mogilevskaya, "Complex hypersingular integral equation for the piecewise homogeneous half-plane with cracks", *Intl. J. Frac.* **102**:2 (2000), 177–204.

[Mogilevskaya and Crouch 2001] S. G. Mogilevskaya and S. L. Crouch, "A Galerkin boundary integral method for multiple circular elastic inclusions", *Int. J. Numer. Methods Eng.* **52**:10 (2001), 1069–1106.

[Mogilevskaya and Crouch 2002] S. G. Mogilevskaya and S. L. Crouch, "A Galerkin boundary integral method for multiple circular elastic inclusions with homogeneously imperfect interfaces", *Int. J. Solids Struct.* **39**:18 (2002), 4723–4746. Erratum in *ibid*. **40**, 1335.

[Mogilevskaya and Crouch 2004] S. G. Mogilevskaya and S. L. Crouch, "A Galerkin boundary integral method for multiple circular elastic inclusions with uniform interphase layers", *Int. J. Solids Struct.* **41**:5–6 (2004), 1285–1311.

[Mogilevskaya and Linkov 1998] S. G. Mogilevskaya and A. M. Linkov, "Complex fundamental solutions and complex variables boundary element method in elasticity", *Comput. Mech.* **22**:1 (1998), 88–92. MR 99f:73089

[Muskhelishvili 1963] N. I. Muskhelishvili, *Some basic problems of the mathematical theory of elasticity*, Noordhoff, Groningen, 1963.

[Rizzo and Shippy 1971] F. J. Rizzo and D. J. Shippy, "An application of the correspondence principle of linear viscoelasticity theory", *SIAM J. Appl. Math.* **21**:2 (1971), 321–330. Zbl 0211.28303

[Schapery 1962] R. A. Schapery, "Approximate methods of transform inversion for viscoelastic stress analysis", pp. 1075–1085 in *Proc. 4th U.S. Nat. Congr. Appl. Mech.* (Berkeley), vol. 2, Amer. Soc. Mech. Engrs., New York, 1962. MR 27 #3144

[Shinokawa et al. 1985] T. Shinokawa, N. Kaneko, and N. Yoshida, "Application of viscoelastic combined finite and boundary element analysis to geotechnical engineering", Chapter 10, pp. 37–46 in *Boundary elements VII* (Lake Como, Italy, 1985), vol. 2, edited by C. A. Brebbia and G. Maier, Springer, Berlin, 1985.

[Sim and Kwak 1988] W. J. Sim and B. M. Kwak, "Linear viscoelastic analysis in time domain by boundary element method", *Comput. Struct.* **29**:4 (1988), 531–539.

[Sun and Hsiao 1985] B. N. Sun and C. C. Hsiao, "Viscoelastic boundary element method for analyzing polymer crazing as quasifracture", Chapter 3, pp. 69–86 in *Boundary elements VII* (Lake Como, Italy, 1985), vol. 1, edited by C. A. Brebbia and G. Maier, Springer, Berlin, 1985.

[Timoshenko and Goodier 1970] S. P. Timoshenko and J. N. Goodier, *Theory of elasticity*, 3rd ed., McGraw-Hill, New York, 1970.

[Wang and Crouch 1982] Y. Wang and S. L. Crouch, "Boundary element methods for viscoelastic media", pp. 705–711 in *Issues in rock mechanics* (Berkeley), edited by R. E. Goodman and F. E. Heuze, The Society of Mining Engineers of the American Institute of Mining, Metallurgical and Petroleum Engineers, New York, 1982.

[Wang et al. 2003a] J. Wang, S. L. Crouch, and S. G. Mogilevskaya, "A complex boundary integral method for multiple circular holes in an infinite plane", *Eng. Anal. Bound. Elem.* **27**:8 (2003), 789–802.

[Wang et al. 2003b] J. Wang, S. G. Mogilevskaya, and S. L. Crouch, "A numerical procedure for multiple circular holes and elastic inclusions in a finite domain with a circular boundary", *Comput. Mech.* **32**:4–6 (2003), 250–258.

Received 11 Nov 2005.

YUN HUANG: huan0238@umn.edu
Department of Civil Engineering, University of Minnesota, 500 Pillsbury Drive SE, Minneapolis, MN 55455, United States

SOFIA G. MOGILEVSKAYA: mogil003@umn.edu
Department of Civil Engineering, University of Minnesota, 500 Pillsbury Drive SE, Minneapolis, MN 55455, United States
http://www.ce.umn.edu/people/faculty/mogilevs/

STEVEN L. CROUCH: crouch@itdean.umn.edu
Department of Civil Engineering, University of Minnesota, 500 Pillsbury Drive SE, Minneapolis, MN 55455, United States
http://www.ce.umn.edu/people/faculty/crouch/

JOURNAL OF MECHANICS OF MATERIALS AND STRUCTURES
Vol. 1, No. 3, 2006

A NEW CLASS OF EQUILIBRATED STRESS FIELDS FOR NO-TENSION BODIES

MASSIMILIANO LUCCHESI, MIROSLAV ŠILHAVÝ AND NICOLA ZANI

We study the equilibrium problem for bodies made of a no-tension material, subjected to distributed or concentrated loads on their boundary. Admissible and equilibrated stress fields are interpreted as tensor-valued measures with distributional divergence represented by a vector-valued measure, as outlined in two 2005 papers by Lucchesi et al. Such stress fields are generalizations of ordinary functions, which allows us to consider stress concentrations on surfaces and lines. The general framework for this approach is presented first and then illustrated on examples of two-dimensional panels under different loads. In the general framework we determine weak divergences and the surface tractions of several stress field measures via the (surface) divergence theorem. Combinations of these stress fields are shown to give the solutions for the panels, which we assume to be clamped at the bottom, and subjected to various loads on the top and possibly on the sides of the panel. The shapes of the singular lines and stresses are explicitly determined in these cases.

1. Introduction

In studying the equilibrium problem of bodies made of a no-tension (or masonry-like) material [Del Piero 1989; Di Pasquale 1984], it is very hard to find an explicit solution of the corresponding boundary value problem [Lucchesi and Zani 2003a]. Therefore, in applications we often limit ourselves to looking for stress fields that are equilibrated with the applied loads and compatible with the incapability of the material to withstand traction. These admissible equilibrium stress fields can be used in the context of limit analysis [Del Piero 1998] to determine the collapse load, or at least some of its lower bounds. The solution to this problem is considerably simplified by allowing the stress to be singular in some regions of the body. In [Lucchesi and Zani 2002; 2003b], solutions for two-dimensional panels are examined which are regular except on a finite number of singularity curves where the stress field is unbounded. The method of solving the equilibrium equations is based on the fact that if horizontal and vertical loads are distributed only on the panel's top and the stress determinant is null, the equilibrium equations constitute a system of

Keywords: masonry panels, equilibrium, divergence measures.

conservation laws, formally identical to the nonlinear system ruling the dynamics of the one-dimensional isentropic flow of a pressureless compressible gas. Under appropriate hypotheses, this system is equivalent to a single scalar conservation law [Brenier and Grenier 1998; Bouchut and James 1999]. Then the singularity curves are determined by means of the Rankine–Hugoniot jump condition corresponding to this scalar equation. This method is not directly applicable if distributed loads are present on the lateral sides of the panel or if the determinant of the stress does not vanish.

Following [Lucchesi et al. 2004; 2005a], the present paper uses tensor-valued measures to describe the stress fields in no-tension bodies. On the common range of applicability, the language of measures is essentially equivalent to the method of the conservation law mentioned above. However, the approach via measures is conceptually more direct in accounting for the singularities of the stress field and in the way the balance of forces is taken into account. The former means that we consider generally measures that are not absolutely continuous with respect to the Lebesgue measure (= volume); the latter means that the balance of forces is interpreted in the weak sense. This in turn means that the distributional divergence of the stress measure is equal to the body force in the interior of the body, and that the boundary trace of the measure equals the external boundary loads, given by a prescribed measure.

Using the divergence theorem, we first calculate the weak divergence and the trace of some elementary stress fields:

(i) those distributed over volumes or concentrated on surfaces and lines, and

(ii) stress fields given by some specific expression (see Equation (3–8)) that is encountered in some solutions for panels given below.

The stress fields encountered in the applications to panels are linear combinations of the elementary stress fields in items (i) and (ii) of Proposition 1. We then consider briefly the general balance equation, and show, among other things, that for the stress field consisting of the bulk stress and of the stress concentrated on a surface, one obtains the classical form of the balance equations.

The rest of the paper illustrates the general notions on the rectangular panels made of a no-tension material. We assume that the panel is free from body forces, clamped at its bottom and subjected to loads prescribed on the boundary; applications to three-dimensional bodies under gravity will be treated in a future work. The stress field in our solutions is plane and negative semidefinite and characterized by the presence of one or more curves of concentrated stress. This feature, which is allowed by supposing the material to have infinite compressive strength, seems to be paradoxical at first sight. On the other hand, this simplifying hypothesis is frequently used in the study of masonry structures, at least when the collapse is

believed to take place for small values of the compressive stress [Heyman 1966]. Moreover, these singular equilibrated stress fields look like a formalization of the rough idea that a masonry building is 'safe' if its interior contains an equilibrated (and compressed) structure, an idea that was probably already in the mind of Leonardo da Vinci [Benvenuto 1991].

Even though the present paper makes no mention of the displacement fields, our use of measures to describe the stresses raises the question of the appropriate duality between the stresses and strains. We are especially interested in the expression

$$\mathsf{T} \cdot \boldsymbol{\epsilon}(\boldsymbol{u}) \tag{1–1}$$

for the virtual work of the stress field T against the virtual displacement $\boldsymbol{u}$ with the small strain tensor $\boldsymbol{\epsilon}(\boldsymbol{u}) = \frac{1}{2}(\nabla \boldsymbol{u} + \nabla \boldsymbol{u}^{\mathsf{T}})$. Generally, the 'wilder' T is, the smoother $\boldsymbol{u}$ must be, and vice versa. The issues are well understood in Hencky's plasticity, where $\boldsymbol{u}$ is generally a vector field with bounded deformation. The papers [Témam and Strang 1980; 1980; Anzellotti 1983] and [Kohn and Témam 1983] provide a variety of results pertaining to that case. Roughly, T must be a Lebesgue measurable function with divergence measure and with some natural integrability properties. Thus no concentrations in T are allowed. Our situation is the opposite: the stress has concentrations and the strain must be 'tamer.' The results of Whitney's theory of flat chains [Whitney 1957; Federer 1969] apply here (see [Šilhavý 2005c]). For symmetric tensor-valued stress measures T with divergence measure, the expression in Equation (1–1) is a well defined measure provided the displacement $\boldsymbol{u}$ is Lipschitz continuous (for stress measures with additional properties the class of displacements may be wider). The result is not immediate because $\boldsymbol{\epsilon}(\boldsymbol{u})$ may be undefined on the surface of concentration of T; a substantial use has been made of the fact that the divergence of T is a measure. We will return to these issues in a separate paper.

2. Vector-valued measures

This section introduces measures with values in a finite-dimensional inner product space V. Such measures can be identified with an m-tuple of (scalar-valued) signed measures where $m := \dim V$ is the dimension of V. We refer to [Rudin 1974, Chapters 1 and 6] for the details of scalar-valued signed measures. The notation in Equations (2–2) and (2–3), below, will be used systematically throughout the paper.

Throughout the paper, Lin denotes the space of all linear transformations from $\mathbb{R}^n$ into $\mathbb{R}^n$ with the scalar product $\boldsymbol{A} \cdot \boldsymbol{B} = \operatorname{tr}(\boldsymbol{A}\boldsymbol{B}^{\mathsf{T}})$, $\boldsymbol{A}, \boldsymbol{B} \in \mathrm{Lin}$, and Sym is a subspace of Lin consisting of all symmetric transformations. We interpret Lin

as the space of all second order tensors, and use vector and tensor notations and conventions from [Gurtin 1981] and [Šilhavý 1997].

If V is a finite-dimensional real inner product space then a function $\boldsymbol{\mu}$, defined on the system of all Borel subsets of $\mathbb{R}^n$, is said to be a *V-valued measure* on $\mathbb{R}^n$ if

$$\boldsymbol{\mu}\Big(\bigcup_{i=1}^{\infty} A_i\Big) = \sum_{i=1}^{\infty} \boldsymbol{\mu}(A_i), \tag{2–1}$$

for every pairwise disjoint sequence A_i of Borel sets. We recall that the system of all Borel sets is the smallest σ algebra of subsets of $\mathbb{R}^n$ that contains all open subsets of $\mathbb{R}^n$. The application of Equation (2–1) to the sequence $A_i = \varnothing$, $i = 1, \dots,$ gives $\boldsymbol{\mu}(\varnothing) = \mathbf{0}$. If $U \subset \mathbb{R}^n$ is a Borel set, we say that a V-valued measure $\boldsymbol{\mu}$ is *supported* on U if $\boldsymbol{\mu}(B) = \mathbf{0}$ for every Borel set $B \subset \mathbb{R}^n$ such that $U \cap B = \varnothing$. We denote by $\mathcal{M}(U, V)$ the set of all V-valued measures supported on U. We call the elements of $\mathcal{M}(U, \mathbb{R})$ *signed measures* on U and the elements of $\mathcal{M}(U, \mathrm{Lin})$ *tensor measures.* In the special case $V = \mathbb{R}^m$ one has

$$\boldsymbol{\mu}(A) = (\mu^1(A), \dots, \mu^m(A)),$$

for each Borel set $A \subset \mathbb{R}^n$ where μ^i, $1 \le i \le m$, are signed measures. A similar reduction of $\boldsymbol{\mu}$ applies to any V equipped with a basis.

If $\boldsymbol{\mu}$ is a V-valued measure, we say that a Borel set $A \subset \mathbb{R}^n$ is a $\boldsymbol{\mu}$ null set if $\boldsymbol{\mu}(B) = \mathbf{0}$ for each Borel set $B \subset A$. We say that a map $\boldsymbol{f}$ is defined as $\boldsymbol{\mu}$ *almost everywhere* (a.e.) on a set M if the set of all $\boldsymbol{x} \in M$ for which $\boldsymbol{f}(\boldsymbol{x})$ is not defined forms a $\boldsymbol{\mu}$ null set. Similarly, we say that a given property holds a.e. on M if the set of all $\boldsymbol{x}$ for which the property is violated forms a $\boldsymbol{\mu}$ null set.

If $\boldsymbol{\alpha} : U \to V$ is a bounded Borel function and $\boldsymbol{\nu} \in \mathcal{M}(U, V)$, then

$$\int_U \boldsymbol{\alpha} \cdot d\boldsymbol{\nu}$$

is a well defined number. If $\boldsymbol{a} \in U$, we denote by $\delta_{\boldsymbol{a}} \in \mathcal{M}(U, \mathbb{R})$ the *Dirac measure* at $\boldsymbol{a}$, defined by

$$\delta_{\boldsymbol{a}(B)} = \begin{cases} 1 & \text{if} \quad \boldsymbol{a} \in B, \\ 0 & \text{if} \quad \boldsymbol{a} \notin B, \end{cases}$$

for any Borel set $B \subset \mathbb{R}^n$, and note that if $f : U \to \mathbb{R}$ is a (bounded) Borel function then

$$\int_U f \, d\delta_{\boldsymbol{a}} = f(\boldsymbol{a}).$$

We denote by $\mathscr{L}^n$ the Lebesgue measure in $\mathbb{R}^n$ [Federer 1969, Subsection 2.6.5] and if k is an integer, $0 \le k \le n$, we denote by $\mathscr{H}^k$ the k-dimensional Hausdorff measure in $\mathbb{R}^n$ [Federer 1969, Subsections 2.10.2–2.10.6]; recall that $\mathscr{H}^n = \mathscr{L}^n$. If

A is a Borel set, we denote by $\mathcal{H}^k \llcorner A$ the *restriction* of $\mathcal{H}^k$ to A, which is the measure defined by

$$(\mathcal{H}^k \llcorner A)(B) = \mathcal{H}^k(A \cap B), \tag{2–2}$$

for each Borel set $B \subset \mathbb{R}^n$. If $A \subset U$ is a Borel set and $\boldsymbol{f}$ is a V-valued Borel map defined a.e. on A, integrable with respect to $\mathcal{H}^k$ on A, then $\boldsymbol{f}\mathcal{H}^k \llcorner A$ denotes the V-valued measure on $\mathbb{R}^n$ defined by

$$(\boldsymbol{f}\mathcal{H}^k \llcorner A)(B) = \int_{A\cap B} \boldsymbol{f}\, d\mathcal{H}^k, \tag{2–3}$$

for each Borel set $B \subset \mathbb{R}^n$. The definitions (2–2) and (2–3) also apply to $k = n$, that is, to $\mathcal{L}^n \equiv \mathcal{H}^n$, resulting in $\mathcal{L}^n \llcorner A$ and $\boldsymbol{f}\mathcal{L}^n \llcorner A$. If $\boldsymbol{\alpha} : A \to V$ is a bounded Borel function then

$$\int_A \boldsymbol{\alpha} \cdot d(\boldsymbol{f}\mathcal{H}^k \llcorner A) = \int_A \boldsymbol{\alpha} \cdot \boldsymbol{f}\, d\mathcal{H}^k.$$

The construction (2–3) will be used to introduce stresses concentrated on surfaces. In that case $A \equiv \mathcal{S}$ is a k-dimensional surface with boundary (see the Appendix for the summary of differential-geometric notions), $\boldsymbol{f} \equiv \boldsymbol{T}_s$ is a $\mathcal{H}^k$ integrable map on $\mathcal{S}$ with values in Lin and

$$\mathbf{T}_s := \boldsymbol{T}_s \mathcal{H}^k \llcorner \mathcal{S} \tag{2–4}$$

is a stress field concentrated on $\mathcal{S}$. Similarly, if $A = U$ is an open subset of $\mathbb{R}^n$ and $\boldsymbol{T}_r$ is an $\mathcal{L}^n$ integrable map on U with values in Lin then

$$\mathbf{T}_r := \boldsymbol{T}_r \mathcal{L}^n \llcorner U \tag{2–5}$$

is a distributed stress field on U. Only combinations of measures of type (2–4) and (2–5) are of real use in Sections 5–7. The corresponding equilibrium equations are considered in Sections 3 and 4.

3. Divergence measure tensor fields

If V is a finite-dimensional real inner product space and if U is an open subset of $\mathbb{R}^n$, we denote by $C_0^\infty(U, V)$ the set of all infinitely differentiable functions

$$\boldsymbol{\alpha} : \mathbb{R}^n \to V$$

whose support $\operatorname{spt}\boldsymbol{\alpha}$ is contained in U. We say that a tensor-valued measure

$$\mathbf{T} \in \mathcal{M}(U, \mathrm{Lin})$$

is a *divergence measure tensor field* if there exists a measure

$$\mathbf{div}\, \mathbf{T} \in \mathcal{M}(U, \mathbb{R}^n),$$

called the *divergence* of T, such that

$$\int_U \nabla \boldsymbol{v} \cdot d\mathsf{T} = -\int_U \boldsymbol{v} \cdot d\ \mathbf{div}\ \mathsf{T}, \tag{3–1}$$

for each $\boldsymbol{v} \in C_0^\infty(U, \mathbb{R}^n)$. We note that vector-valued measures with divergence measure have been introduced in [Chen and Frid 2001; 2003]; vector or tensor-valued functions with divergence measure have been considered in [Anzellotti 1983; Kohn and Témam 1983; Chen and Frid 1999; Degiovanni et al. 1999; Marzocchi and Musesti 2001; Šilhavý 2005a; Chen and Torres 2005]. (For the application of divergence measure tensor fields to masonry structures, see [Lucchesi et al. 2005a].) A measure $\mathsf{T} \in \mathcal{M}(U, \mathrm{Lin})$ is said to be an *equilibrated tensor field* if there exist measures $\mathbf{b} \in \mathcal{M}(U, \mathbb{R}^n)$ and $\mathbf{t} \in \mathcal{M}(\partial U, \mathbb{R}^n)$ such that

$$\int_U \nabla \boldsymbol{v} \cdot d\mathsf{T} = \int_U \boldsymbol{v} \cdot d\mathbf{b} + \int_{\partial U} \boldsymbol{v} \cdot d\mathbf{t}, \tag{3–2}$$

for each $\boldsymbol{v} \in C_0^\infty(\mathbb{R}^n, \mathbb{R}^n)$ [Podio-Guidugli 2005; Šilhavý 2005a; 2005b; 2005c]. Here ∂U denotes the topological boundary of U. Since the measures $\mathbf{b}$ and $\mathbf{t}$ are supported on the disjoint sets U and ∂U, respectively, they are uniquely determined (provided they exist). We call the pair $(\mathbf{b}, \mathbf{t})$ the *load* corresponding to T and the measure $\mathbf{t}$ the *normal trace* of T; we use the notation $\mathrm{N}(\mathsf{T}) := \mathbf{t}$ for the normal trace. Equation (3–2) then reads

$$\int_U \nabla \boldsymbol{v} \cdot d\mathsf{T} = -\int_U \boldsymbol{v} \cdot d\ \mathbf{div}\ \mathsf{T} + \int_{\partial U} \boldsymbol{v} \cdot d\mathrm{N}(\mathsf{T}), \tag{3–3}$$

for each $\boldsymbol{v} \in C_0^\infty(\mathbb{R}^n, \mathbb{R}^n)$. Clearly, any equilibrated tensor field T is a divergence measure tensor field, and if $(\mathbf{b}, \mathbf{t})$ is the load, then $\mathbf{div}\mathsf{T} = -\mathbf{b}$. There are divergence measure tensor fields that are not equilibrated [Šilhavý 2005b, Chapter 9; Šilhavý 2005c, Example 9.1], that is, for which the measure $\mathbf{t}$ does not exist.

The integration by parts shows that if $\boldsymbol{T} : U \to \mathrm{Lin}$ is a continuously differentiable tensor field with integrable gradient on an open set $U \subset \mathbb{R}^n$, then the tensor-valued measure

$$\mathsf{T} = \boldsymbol{T}\mathscr{L}^n \llcorner U$$

is a divergence measure tensor field and

$$\mathbf{div}\ \mathsf{T} = \mathrm{div}\, \boldsymbol{T}\mathscr{L}^n \llcorner U.$$

Here div is the classical divergence given by the usual differential expression; a particular case of the surface divergence introduced in the Appendix, while **div** denotes the divergence as a measure, defined above. The reader is also referred to the Appendix for the differential-geometric concepts employed in the subsequent discussion. If, additionally, U is an open region with Lipschitz boundary, and $\boldsymbol{T}$

has a continuous extension to the closure $\operatorname{cl} U$ of U, again denoted by $\boldsymbol{T}$, that is $\mathscr{H}^{n-1}$ integrable on ∂U, then the divergence theorem shows that T is an equilibrated tensor field and

$$\mathrm{N}(\mathsf{T}) = \boldsymbol{T}\boldsymbol{m}\,\mathscr{H}^{n-1} \llcorner \partial U,$$

where $\boldsymbol{m}$ is the outer normal to U. This justifies the term 'normal trace' for $\mathrm{N}(\mathsf{T})$.

The following proposition generalizes the above considerations to singular tensor fields concentrated on k-dimensional surfaces, $1 \le k \le n$. If $\boldsymbol{T} : \mathscr{S} \to \mathrm{Lin}$ is a tensor field on a k-dimensional surface $\mathscr{S}$ with boundary, we say that $\boldsymbol{T}$ is *superficial* [Gurtin 2000, p. 94] if $\boldsymbol{T}(\boldsymbol{x})\boldsymbol{v} = \boldsymbol{0}$ for every $\boldsymbol{x} \in S$ and every $\boldsymbol{v} \in \mathbb{R}^n$ perpendicular to $\mathbf{T}_{\boldsymbol{x}}(\mathscr{S})$. This is equivalent to each of the following two statements:

(a) $\mathbf{T}_{\boldsymbol{x}}(\mathscr{S})^{\perp} \subset \ker \boldsymbol{T}(\boldsymbol{x})$ for every $\boldsymbol{x} \in S$;

(b) $\operatorname{ran} \boldsymbol{T}^{\mathsf{T}}(\boldsymbol{x}) \subset \mathbf{T}_{\boldsymbol{x}}(\mathscr{S})$.

Here ker and ran denote the kernel and range of a linear transformation.

Proposition 1. *Let U be an open subset of $\mathbb{R}^n$, let $k \ge 1$ be an integer, let $\mathscr{S}$ be a compact orientable k-dimensional surface with boundary such that $\operatorname{int} \mathscr{S} \subset U$, let $\boldsymbol{T} : \mathscr{S} \to \mathrm{Lin}$ be a continuous map with a continuous and $\mathscr{H}^k$ integrable derivative in $\operatorname{int} \mathscr{S}$, and put*

$$\mathsf{T} := \boldsymbol{T}\mathscr{H}^k \llcorner \mathscr{S}.$$

Then

(i) *T is equilibrated $\Leftrightarrow$ T is a divergence measure tensor field $\Leftrightarrow$ $\boldsymbol{T}$ is superficial;*

(ii) *if $\boldsymbol{T}$ is superficial then*

$$\mathbf{div}\,\mathsf{T} = \operatorname{div} \boldsymbol{T}\mathscr{H}^k \llcorner (\mathscr{S} \cap U) - \boldsymbol{T}\boldsymbol{m}\mathscr{H}^{k-1} \llcorner (\partial\mathscr{S} \cap U) \tag{3–4}$$

and

$$\mathrm{N}(\mathsf{T}) = \boldsymbol{T}\boldsymbol{m}\,\mathscr{H}^{k-1} \llcorner (\partial\mathscr{S} \cap \partial U), \tag{3–5}$$

where $\boldsymbol{m}$ is the outer normal to $\mathscr{S}$.

Item (1) says that a measure concentrated on a k-dimensional surface is a divergence measure tensor field only if it is superficial. If this is the case then the divergence of T consists of the (surface) divergence of $\boldsymbol{T}$ concentrated on $\mathscr{S} \cap U$ and of the normal component of $\boldsymbol{T}$ concentrated on $\partial\mathscr{S} \cap U$ while the normal trace of T is the remaining part of the normal component of $\boldsymbol{T}$, that is, the part concentrated on $\partial\mathscr{S} \cap \partial U$. We emphasize that $k \ge 1$ is arbitrary. If $k = 1$, that is, if $\mathscr{S}$ is a curve, then the measure

$$\boldsymbol{T}\boldsymbol{m}\,\mathscr{H}^{k-1} \llcorner (\partial\mathscr{S} \cap U)$$

reduces to

$$\sum_{\boldsymbol{a}\in\partial\mathcal{S}\cap U} \boldsymbol{T}(\boldsymbol{a})\boldsymbol{m}(\boldsymbol{a})\delta_{\boldsymbol{a}},$$

where the set $\partial\mathcal{S}\cap U$ is the set of all endpoints of $\mathcal{S}$ in U and $\boldsymbol{m}(\boldsymbol{a})$ are outward tangents to $\mathcal{S}$ at the endpoints. A similar interpretation applies to the right side of Equation (3–5). We note that the argument used below to prove Item (i) can also be applied to show that there are no nontrivial divergence measure tensor fields concentrated at points, that is, surfaces of dimension 0.

Proof. (ii): Assume that $\boldsymbol{T}$ is superficial and prove Equations (3–4) and (3–5). Let $\boldsymbol{v}\in C_0^\infty(\mathbb{R}^n,\mathbb{R}^n)$; since $\boldsymbol{T}$ is superficial, $\boldsymbol{T}^{\mathsf{T}}\boldsymbol{v}$ is tangential and thus the surface divergence theorem 1, the identity (A–7), and the hypothesis $\operatorname{int}\mathcal{S}\subset U$ give

$$\int_{\mathcal{S}\cap U}(\boldsymbol{v}\cdot\operatorname{div}\boldsymbol{T}+\boldsymbol{T}\cdot\nabla\boldsymbol{v})\,d\mathcal{H}^k=\int_{\partial\mathcal{S}}\boldsymbol{T}\boldsymbol{m}\cdot\boldsymbol{v}\,d\mathcal{H}^{k-1}.$$

Rearranging, we obtain

$$\int_{\mathcal{S}\cap U}\boldsymbol{T}\cdot\nabla\boldsymbol{v}\,d\mathcal{H}^k=-\int_{\mathcal{S}\cap U}\boldsymbol{v}\cdot\operatorname{div}\boldsymbol{T}\,d\mathcal{H}^k + \int_{\partial\mathcal{S}\cap U}\boldsymbol{T}\boldsymbol{m}\cdot\boldsymbol{v}\,d\mathcal{H}^{k-1}+\int_{\partial\mathcal{S}\cap\partial U}\boldsymbol{T}\boldsymbol{m}\cdot\boldsymbol{v}\,d\mathcal{H}^{k-1};$$

comparing this with Equation (3–3) and invoking the uniqueness of $\mathbf{div}\,\mathsf{T}$ and $\mathrm{N}(\mathsf{T})$ we see that Equation (3–4) and Equation (3–5) hold.

(i): We shall prove the cycle of implications: T is equilibrated $\Rightarrow$ T is a divergence measure tensor field $\Rightarrow$ $\boldsymbol{T}$ is superficial $\Rightarrow$ T is equilibrated. The first of these implications is automatic, as mentioned above, while the last implication has been proved in (ii). Thus it remains to be proved that if T is a divergence measure tensor field then $\boldsymbol{T}$ is superficial. Let T be a divergence measure tensor field, let $\boldsymbol{x}\in\mathcal{S}\cap U$ and assume first additionally that $\boldsymbol{x}\notin\partial\mathcal{S}$. Let Z and $\boldsymbol{\omega}$ be as in Condition (ii) of Subsection A.1, and assume, as we can, that $Z\subset U$. Let $\lambda\in C_0^\infty(\mathbb{R}^n,\mathbb{R})$ be such that $\operatorname{spt}\lambda\subset Z$. Let $\boldsymbol{b}\in\mathbb{R}^{n-k}$ and $\boldsymbol{a}\in\mathbb{R}^n$. If $\epsilon>0$ then there exists $h\in C^\infty(\mathbb{R}^{n-k},\mathbb{R})$ such that

$$h(\mathbf{0})=0,\qquad \nabla h(\mathbf{0})=\boldsymbol{b} \tag{3–6}$$

and $|h|_\infty<\epsilon$. Here $|\cdot|_\infty$ is the maximum norm; that is, if M is a set and $f:M\to V$ then

$$|f|_\infty:=\sup\{|f(\boldsymbol{x})|:\boldsymbol{x}\in M\}.$$

Let $\boldsymbol{v}\in C_0^\infty(U,\mathbb{R}^n)$ be defined by

$$\boldsymbol{v}=\begin{cases}\boldsymbol{a}\lambda\,(h\circ\boldsymbol{\omega}) & \text{on } Z,\\ 0 & \text{on } \mathbb{R}^n\setminus Z.\end{cases} \tag{3–7}$$

Using $|h \circ \boldsymbol{\omega}|_\infty = |h|_\infty < \epsilon$ one finds that $|\boldsymbol{v}|_\infty \le |\boldsymbol{a}||\lambda|_\infty \epsilon$. Applying the product rule to calculate $\nabla \boldsymbol{v}$ from Equation (3–7), using Equation (3–6), and noting that $h \circ \boldsymbol{\omega} = 0$ on $\mathcal{S}$, one finds that

$$\nabla \boldsymbol{v} = \begin{cases} \lambda \boldsymbol{a} \otimes \nabla \boldsymbol{\omega}^{\mathsf{T}} \boldsymbol{b} & \text{on } \mathcal{S} \cap Z, \\ 0 & \text{on } \mathcal{S} \setminus Z. \end{cases}$$

Equation (3–1) thus reads

$$\int_{\mathcal{S} \cap Z} \lambda \, \nabla \boldsymbol{\omega} \, \boldsymbol{T}^{\mathsf{T}} \boldsymbol{a} \cdot \boldsymbol{b} \, d\mathcal{H}^k = - \int_U \boldsymbol{v} \cdot d\mathbf{div}\, \mathbf{T}.$$

Denoting by $\mathbf{M}(\boldsymbol{\mu})$ the total variation of a vector-valued measure $\boldsymbol{\mu} \in \mathcal{M}(U, V)$,

$$\mathbf{M}(\boldsymbol{\mu}) := \sup\{ \int_U \boldsymbol{\alpha} \cdot d\boldsymbol{\mu} : \boldsymbol{\alpha} \in C_0^\infty(U, V), |\boldsymbol{\alpha}|_\infty \le 1\},$$

we note that the inequality $|\boldsymbol{v}|_\infty \le |\boldsymbol{a}||\lambda|_\infty \epsilon$ gives

$$\Big| \int_U \boldsymbol{v} \cdot d \ \mathbf{div}\ \mathbf{T} \Big| \le \mathbf{M}(\ \mathbf{div}\ \mathbf{T}) |\boldsymbol{a}||\lambda|_\infty \epsilon,$$

and hence

$$\Big| \int_{\mathcal{S} \cap Z} \lambda \, \nabla \boldsymbol{\omega} \, \boldsymbol{T}^{\mathsf{T}} \boldsymbol{a} \cdot \boldsymbol{b} \, d\mathcal{H}^k \Big| \le \mathbf{M}(\mathbf{div}\ \mathbf{T}) |\boldsymbol{a}||\lambda|_\infty \epsilon.$$

As $\epsilon > 0$ is arbitrary, we have

$$\int_{\mathcal{S} \cap Z} \lambda \, \nabla \boldsymbol{\omega} \, \boldsymbol{T}^{\mathsf{T}} \boldsymbol{a} \cdot \boldsymbol{b} \, d\mathcal{H}^k = 0.$$

As this must hold for any λ, $\boldsymbol{a}$, $\boldsymbol{b}$ subject to the conditions above, we have

$$\nabla \boldsymbol{\omega} \, \boldsymbol{T}^{\mathsf{T}} = \mathbf{0}$$

on $\mathcal{S} \cap Z$, and since $\ker \nabla \boldsymbol{\omega}(\boldsymbol{x}) = \mathbf{T}_{\boldsymbol{x}}(\mathcal{S})$, we deduce that $\operatorname{ran} \boldsymbol{T}^{\mathsf{T}}(\boldsymbol{x}) \subset \mathbf{T}_{\boldsymbol{x}}(\mathcal{S})$. Thus the restriction of $\boldsymbol{T}$ to $\mathcal{S} \cap (U \setminus \partial \mathcal{S})$ is superficial. Since the closure of the last set is $\mathcal{S}$, the continuity of $\boldsymbol{T}$ implies that $\boldsymbol{T}$ is superficial on $\mathcal{S}$. □

A subset C of $\mathbb{R}^n$ is said to be a *cone* if $r\boldsymbol{v} \in C$ for every $r > 0$ and $\boldsymbol{v} \in C$. For each $\boldsymbol{x} \in \mathbb{R}^n$ and $r > 0$, let $\mathbf{B}(\boldsymbol{x}, r)$ denote the open ball in $\mathbb{R}^n$ of center $\boldsymbol{x}$ and radius r, and let $\mathbb{S}^{n-1}$ denote the unit sphere in $\mathbb{R}^n$.

Proposition 2. *Let $U \subset \mathbb{R}^n$ be an open region with Lipschitz boundary containing the origin, and let C be an open cone such that $\partial C \setminus \{\mathbf{0}\}$ is an $(n-1)$-dimensional surface. Let $\alpha : \operatorname{cl} C \cap \mathbb{S}^{n-1} \to \mathbb{R}$ be a continuous function which is continuously differentiable in $C \cap \mathbb{S}^{n-1}$, and let $\boldsymbol{T} : (U \cap \operatorname{cl} C) \setminus \{\mathbf{0}\} \to \mathrm{Lin}$ be given by*

$$\boldsymbol{T}(\boldsymbol{x}) = |\boldsymbol{x}|^{-n-1} \alpha\Big(\frac{\boldsymbol{x}}{|\boldsymbol{x}|}\Big) \boldsymbol{x} \otimes \boldsymbol{x}, \quad \boldsymbol{x} \in (U \cap \operatorname{cl} C) \setminus \{\mathbf{0}\}. \tag{3–8}$$

Then $\boldsymbol{T}$ *is continuous in* $(U \cap \operatorname{cl} C) \setminus \{\mathbf{0}\}$ *and continuously differentiable in* $C \cap U$ *and we have*

$$\operatorname{div} \boldsymbol{T} = \mathbf{0} \quad \text{in} \quad C \cap U. \tag{3–9}$$

Moreover, if we put

$$\mathsf{T} = \boldsymbol{T}\mathscr{L}^n \llcorner (C \cap U),$$

then T *is an equilibrated tensor field and*

$$\mathbf{div}\, \mathsf{T} = \boldsymbol{c}\, \delta_{\mathbf{0}}, \tag{3–10}$$

$$\mathrm{N}(\mathsf{T}) = \boldsymbol{T}\boldsymbol{m}\, \mathscr{H}^{n-1} \llcorner (\partial U \cap C), \tag{3–11}$$

where

$$\boldsymbol{c} = \int_{C \cap \mathbb{S}^{n-1}} \alpha(\boldsymbol{e}) \boldsymbol{e}\, d\mathscr{H}^{n-1}(\boldsymbol{e}), \tag{3–12}$$

and $\boldsymbol{m}$ *is the outer normal to* $\partial U \cap C$.

For $n = 2$, the stress field $\boldsymbol{T}$ as in Equation (3–8) falls within the class studied in [Podio-Guidugli 2005, Section 4], from where also (3–9) can be deduced. In (3–12) we denote by $\boldsymbol{e} \in C \cap \mathbb{S}^{n-1}$ the integration variable. Using the divergence theorem and (3–9) as in the proof below, one also finds that

$$\boldsymbol{c} = \int_{C \cap \partial U} \boldsymbol{T}\boldsymbol{m}\, d\mathscr{H}^{n-1}. \tag{3–13}$$

Proof. The continuity and differentiability of $\boldsymbol{T}$ follows directly from the assumptions on α and (3–9) is a straightforward calculation which we omit. To prove (3–10) and (3–11), we denote by B_r the closed ball with center $\mathbf{0}$ and radius $r > 0$ and consider the set $(C \setminus B_r) \cap U$. This is an open set and if $r > 0$ is small enough to satisfy $B_r \subset U$ (recall that $\mathbf{0} \in U$), then

$$\partial[(C \setminus B_r) \cap U] = (C \cap \partial U) \cup (C \cap \partial B_r) \cup [(\partial C \setminus B_r) \cap U] \cup T \tag{3–14}$$

to within a set of $\mathscr{H}^{n-1}$ measure 0 where

$$T := \{\boldsymbol{x} \in (\partial C \setminus \{\mathbf{0}\}) \cap \partial U : \boldsymbol{n}_{\partial C \setminus \{\mathbf{0}\}}(\boldsymbol{x}) = \boldsymbol{m}(\boldsymbol{x})\}, \tag{3–15}$$

where $\boldsymbol{n}_{\partial C \setminus \{\mathbf{0}\}}$ is the outer normal to $C \setminus \{\mathbf{0}\}$ and $\boldsymbol{m}$ is the outer normal to U. Equation (3–14) can be deduced from the general formula in [Marzocchi and Musesti 2001, Proposition 2.2]. We note that $(C \setminus B_r) \cap U$ is an open region with Lipschitz boundary with the outer normal given by

$$\boldsymbol{n}(\boldsymbol{x}) = \begin{cases} \boldsymbol{m}(\boldsymbol{x}) & \text{if } \boldsymbol{x} \in C \cap \partial U, \\ -\boldsymbol{x}/r & \text{if } \boldsymbol{x} \in C \cap \partial B_r\ , \\ \boldsymbol{n}_{\partial C \setminus \{\mathbf{0}\}}(\boldsymbol{x}) & \text{if } \boldsymbol{x} \in [(\partial C \setminus B_r) \cap U] \cup T, \end{cases} \tag{3–16}$$

to within a change on a $\mathcal{H}^{n-1}$ null set. Furthermore, we note that

$$\boldsymbol{T}\boldsymbol{n}_{\partial C\setminus\{\mathbf{0}\}} = \mathbf{0} \quad \text{on} \quad \partial C \setminus \{\mathbf{0}\} \tag{3–17}$$

because $\boldsymbol{x}\cdot\boldsymbol{n}_{\partial C\setminus\{\mathbf{0}\}} = 0$ since C is a cone with vertex $\mathbf{0}$. If $\boldsymbol{v} \in C_0^\infty(\mathbb{R}^n, \mathbb{R}^n)$ is a vector field, then

$$\int_U \nabla\boldsymbol{v}\cdot d\mathsf{T} = \int_C \nabla\boldsymbol{v}\cdot\boldsymbol{T}\, d\mathscr{L}^n = \lim_{r\to 0}\int_{C\setminus B_r} \nabla\boldsymbol{v}\cdot\boldsymbol{T}\, d\mathscr{L}^n.$$

Theorem 1 and formula (A–7) yield

$$\int_{C\setminus B_r} \nabla\boldsymbol{v}\cdot\boldsymbol{T}\, d\mathscr{L}^n = -\int_{C\setminus B_r} \boldsymbol{v}\cdot\operatorname{div}\boldsymbol{T}\, d\mathscr{L}^n + \int_{\partial[(C\setminus B_r)\cap U]} \boldsymbol{v}\cdot\boldsymbol{T}\boldsymbol{n}\, d\mathscr{H}^{n-1}.$$

Combining with Equations (3–14)–(3–16) we obtain

$$\begin{aligned}\int_{C\setminus B_r} \nabla\boldsymbol{v}\cdot\boldsymbol{T}\, d\mathscr{L}^n = &-\int_{C\setminus B_r} \boldsymbol{v}\cdot\operatorname{div}\boldsymbol{T}\, d\mathscr{L}^n \\ &-\int_{C\cap\partial B_r} \boldsymbol{v}(\boldsymbol{x})\cdot\boldsymbol{T}(\boldsymbol{x})\frac{\boldsymbol{x}}{r}\, d\mathscr{H}^{n-1}(\boldsymbol{x}) \\ &+\int_{C\cap\partial U} \boldsymbol{v}\cdot\boldsymbol{T}\boldsymbol{m}\, d\mathscr{H}^{n-1},\end{aligned} \tag{3–18}$$

where we have used

$$\int_{[(\partial C\setminus B_r)\cap U]\cup T} \boldsymbol{v}\cdot\boldsymbol{T}\boldsymbol{n}_{\partial C\setminus\{\mathbf{0}\}}\, d\mathscr{H}^{n-1} = 0,$$

which follows from Equation (3–17). A combination of (3–18) with (3–9) provides

$$\int_U \nabla\boldsymbol{v}\cdot d\mathsf{T} = -\lim_{r\to 0}\int_{C\cap\partial B_r} \boldsymbol{v}(\boldsymbol{x})\cdot\boldsymbol{T}(\boldsymbol{x})\frac{\boldsymbol{x}}{r}\, d\mathscr{H}^{n-1}(\boldsymbol{x}) + \int_{C\cap\partial U} \boldsymbol{v}\cdot\boldsymbol{T}\boldsymbol{m}\, d\mathscr{H}^{n-1}. \tag{3–19}$$

Moreover, the continuity of $\boldsymbol{v}$ gives

$$\lim_{r\to 0}\int_{C\cap\partial B_r} \boldsymbol{v}(\boldsymbol{x})\cdot\boldsymbol{T}(\boldsymbol{x})\frac{\boldsymbol{x}}{r}\, d\mathscr{H}^{n-1}(\boldsymbol{x}) = \boldsymbol{v}(\mathbf{0})\cdot\lim_{r\to 0}\int_{C\cap\partial B_r} \boldsymbol{T}(\boldsymbol{x})\frac{\boldsymbol{x}}{r}\, d\mathscr{H}^{n-1}(\boldsymbol{x}), \tag{3–20}$$

provided the limit on the right side exists. On the other hand, we have

$$\int_{C\cap\partial B_r} \boldsymbol{T}(\boldsymbol{x})\frac{\boldsymbol{x}}{r}\, d\mathscr{H}^{n-1}(\boldsymbol{x}) = \int_{C\cap\mathbb{S}^{n-1}} \alpha(\boldsymbol{e})\boldsymbol{e}\, d\mathscr{H}^{n-1}(\boldsymbol{e}), \tag{3–21}$$

for scaling reasons, because C is a cone. Therefore, in view of Equations (3–19), (3–20), (3–21) and (3–12),

$$\int_U \nabla \boldsymbol{v} \cdot d\mathsf{T} = -\boldsymbol{v}(\mathbf{0}) \cdot \boldsymbol{c} + \int_{C \cap \partial U} \boldsymbol{v} \cdot \boldsymbol{T}\boldsymbol{m}\, d\mathscr{H}^{n-1}.$$

A comparison with Equation (3–2) gives (3–10) and (3–11). □

4. Balance equations

If an equilibrated tensor field $\mathsf{T} \in \mathcal{M}(U, \mathrm{Lin})$ is interpreted as the stress field in a continuous body under the action of a body force given by a prescribed measure $\mathsf{b}_0 \in \mathcal{M}(U, \mathbb{R}^n)$ and the boundary traction given by a prescribed measure

$$\mathsf{t}_0 \in \mathcal{M}(\partial U, \mathbb{R}^n),$$

then the equations of equilibrium read

$$\mathbf{div}\, \mathsf{T} + \mathsf{b}_0 = \mathbf{0}, \tag{4–1}$$

$\mathrm{N}(\mathsf{T}) = \mathsf{t}_0$. In particular, if b_0 is absolutely continuous with respect to the Lebesgue measure (e.g., the gravity), that is,

$$\mathsf{b}_0 = \boldsymbol{b}_0 \mathscr{L}^n \llcorner U, \tag{4–2}$$

where $\boldsymbol{b}_0 : U \to \mathbb{R}^n$ is an $\mathscr{L}^n$ integrable function, then $\mathbf{div}\, \mathsf{T}$ must be absolutely continuous with respect to $\mathscr{L}^n$ as well.

We now illustrate these balance equations on various linear combinations of the fields described in Propositions 1 and 2. Let $U \subset \mathbb{R}^n$ be an open set.

(i) Let K^+ and K^- be two regions with Lipschitz boundary contained in $\mathrm{cl}\, U$, which are complementary in the sense that the following relations hold:

$$\mathrm{int}\, K^+ \cap \mathrm{int}\, K^- = \varnothing, \quad K^+ \cup K^- = \mathrm{cl}\, U, \quad \partial K^\pm \cap U = K^+ \cap K^- \cap U.$$

Let furthermore $\boldsymbol{T}^\pm : K^\pm \to \mathrm{Lin}$ be continuous maps which have a continuous and $\mathscr{L}^n$ integrable derivative in $\mathrm{int}\, K^\pm$. Denoting by $\mathscr{S} := \partial K^\pm \cap U$ the common interface in U we see that the exterior normals $\boldsymbol{n}^\pm$ to $K^\pm$ satisfy $\boldsymbol{n}^+ = -\boldsymbol{n}^-$ on $\mathscr{S}$ and we denote this common value by $\boldsymbol{n} : \mathscr{S} \to \mathbb{S}^{n-1}$. Denoting further by $\boldsymbol{T} : \mathrm{int}\, K^+ \cup \mathrm{int}\, K^- \to \mathrm{Lin}$ the field given by $\boldsymbol{T}^\pm$ on $\mathrm{int}\, K^\pm$ and noting that $\boldsymbol{T}$ is defined $\mathscr{L}^n$ a.e. on U, we define the measure T by

$$\mathsf{T} = \boldsymbol{T} \mathscr{L}^n \llcorner U.$$

Applying Proposition 1 to $\boldsymbol{T} \equiv \boldsymbol{T}^\pm$, $\mathscr{S} \equiv K^\pm$, we see that $\boldsymbol{T}^\pm \mathscr{L}^n \llcorner K^\pm$ is an equilibrated tensor field and

$$\mathrm{div}(\boldsymbol{T}^\pm \mathscr{L}^n \llcorner K^\pm) = \mathrm{div}\, \boldsymbol{T}^\pm \mathscr{L}^n \llcorner K^\pm - \boldsymbol{T}^\pm \boldsymbol{n}^\pm \mathscr{H}^{n-1} \llcorner \mathscr{S},$$

$$\mathrm{N}(\boldsymbol{T}^{\pm}\mathscr{L}^n \llcorner K^{\pm}) = \boldsymbol{T}^{\pm}\boldsymbol{m}\,\mathscr{H}^{n-1} \llcorner (\partial K^{\pm} \cap \partial U),$$

where $\boldsymbol{m}$ is the outer normal to U. Adding the results, we conclude that T is an equilibrated tensor field and

$$\mathbf{div}\,\mathsf{T} = \operatorname{div}\boldsymbol{T}\mathscr{L}^n \llcorner U - [\boldsymbol{T}]\boldsymbol{n}\mathscr{H}^{n-1} \llcorner \mathscr{J},$$

$$\mathrm{N}(\mathsf{T}) = \boldsymbol{T}\boldsymbol{m}\mathscr{H}^{n-1} \llcorner \partial U,$$

where $\operatorname{div}\boldsymbol{T}$ is the divergence of $\boldsymbol{T}$ on $U \setminus \mathscr{J}$ and for every $\boldsymbol{x} \in \mathscr{J}$,

$$[\boldsymbol{T}](\boldsymbol{x}) := \boldsymbol{T}^{+}(\boldsymbol{x}) - \boldsymbol{T}^{-}(\boldsymbol{x})$$

is the jump of $\boldsymbol{T}$ across $\mathscr{J}$. Any map $\boldsymbol{T}$ which arises in the above way is called a *piecewise smooth tensor field*. If T is a stress field under the action of the body force as in Equation (4–2), then the equilibrium equation (4–1) is equivalent to the following two equations:

$$\operatorname{div}\boldsymbol{T} + \boldsymbol{b}_0 = \mathbf{0} \text{ in } U \setminus \mathscr{J}, \quad [\boldsymbol{T}]\boldsymbol{n} = \mathbf{0} \text{ on } \mathscr{J}.$$

(ii) If $\boldsymbol{T}_r$ is a piecewise smooth tensor field with the interface $\mathscr{J}$ as in (i) above and $\boldsymbol{T}_s : \mathscr{J} \to \mathrm{Lin}$ is a superficial tensor field satisfying the hypothesis of Proposition 1 (ii) with $k = n-1$ and $\mathscr{S} := \mathscr{J}$, then the tensor field

$$\mathsf{T} := \boldsymbol{T}_r\mathscr{L}^n \llcorner U + \boldsymbol{T}_s\mathscr{H}^{n-1} \llcorner \mathscr{J}$$

is equilibrated and

$$\mathbf{div}\,\mathsf{T} = \operatorname{div}\boldsymbol{T}_r\mathscr{L}^n \llcorner U + \big(\operatorname{div}\boldsymbol{T}_s - [\boldsymbol{T}_r]\boldsymbol{n}\big)\mathscr{H}^{n-1} \llcorner \mathscr{J},$$

$$\mathrm{N}(\mathsf{T}) = \boldsymbol{T}_r\boldsymbol{m}\mathscr{H}^{n-1} \llcorner \partial U + \boldsymbol{T}_s\boldsymbol{p}\mathscr{H}^{n-2} \llcorner (\partial U \cap \partial\mathscr{J}),$$

where $\boldsymbol{p}$ is the outer normal to $\mathscr{J}$. With the body force as in Equation (4–2) the equilibrium equation (4–1) is equivalent to the pair of standard equations

$$\operatorname{div}\boldsymbol{T}_r + \boldsymbol{b}_0 = \mathbf{0} \text{ in } U \setminus \mathscr{J}, \quad [\boldsymbol{T}_r]\boldsymbol{n} - \operatorname{div}\boldsymbol{T}_s = \mathbf{0} \text{ on } \mathscr{J}; \tag{4–3}$$

see, for example, [Gurtin and Murdoch 1975; Podio-Guidugli and Caffarelli 1990; Gurtin 2000].

(iii) Let $\mathscr{S}_j$, $j = 1, \ldots, p$, be curves with endpoints such that $\operatorname{int}\mathscr{S}_j \subset U$. Assume that $\operatorname{int}\mathscr{S}_i \cap \operatorname{int}\mathscr{S}_j = \varnothing$, $\partial\mathscr{S}_i \cap \partial\mathscr{S}_j = \{\boldsymbol{a}\}$ for all $i \neq j$ and some $\boldsymbol{a} \in U$, and that $\partial\mathscr{S}_i \cap \partial U \neq \varnothing$ for all i. Let the measure T be defined by

$$\mathsf{T} := \sum_{j=1}^{p} \boldsymbol{T}_j\mathscr{H}^1 \llcorner \mathscr{S}_j,$$

where $\boldsymbol{T}_j$ is a superficial tensor field on $\mathcal{S}$ which satisfies the hypotheses of Proposition 1. Then T is an equilibrated tensor field and

$$\mathbf{div}\,\mathsf{T} = \sum_{j=1}^{p} \operatorname{div} \boldsymbol{T}_j \mathcal{H}^1 \llcorner \mathcal{S}_j + \Big[\sum_{j=1}^{p} \boldsymbol{T}_j(\boldsymbol{a})\boldsymbol{m}_j(\boldsymbol{a})\Big]\delta_{\boldsymbol{a}},$$

$$\mathrm{N}(\mathsf{T}) = \Big[\sum_{j=1}^{p} \boldsymbol{T}_j(\boldsymbol{a}_j)\boldsymbol{m}_j(\boldsymbol{a}_j)\Big]\delta_{\boldsymbol{a}_j},$$

where the points $\boldsymbol{a}_j$ are defined by $\partial\mathcal{S}_j \cap \partial U = \{\boldsymbol{a}_j\}$ and for any $\boldsymbol{b} \in \partial\mathcal{S}_i$ the symbol $\boldsymbol{m}_i(\boldsymbol{b})$ denotes the outer tangent to $\mathcal{S}_i$ at $\boldsymbol{b}$. If $n \geq 2$, the equilibrium equation (4–1) with b_0 as in (4–2) reads

$$\operatorname{div} \boldsymbol{T}_j = \boldsymbol{0} \ \text{ on } \mathcal{S}_j \ \text{ for } j = 1, \dots, p, \qquad \sum_{j=1}^{p} \boldsymbol{T}_j(\boldsymbol{a})\boldsymbol{m}_j(\boldsymbol{a}) = \boldsymbol{0}, \tag{4–4}$$

while if $n = 1$ then the first equation of (4–4) must be replaced by $\operatorname{div} \boldsymbol{T}_j + \boldsymbol{b}_0 = \boldsymbol{0}$.

(iv) Let $\boldsymbol{T}_r : (U \cap \operatorname{cl} C) \setminus \{\boldsymbol{0}\} \to \mathrm{Lin}$ be a tensor field of the form described in Proposition 2, let $\mathcal{S}$ be a curve with endpoints such that one endpoint is in ∂U and another coincides with $\boldsymbol{0}$, and let $\boldsymbol{T}_s : \mathcal{S} \to \mathrm{Lin}$ be a continuous superficial tensor field that is continuously differentiable in $\operatorname{int}\mathcal{S}$. Let T be given by

$$\mathsf{T} = \boldsymbol{T}_r \mathcal{L}^n \llcorner (C \cap U) + \boldsymbol{T}_s \mathcal{H}^1 \llcorner \mathcal{S};$$

then T is an equilibrated tensor field and

$$\mathbf{div}\,\mathsf{T} = \operatorname{div} \boldsymbol{T}_s \mathcal{H}^1 \llcorner \mathcal{S} + [\boldsymbol{c} + \boldsymbol{T}_s(\boldsymbol{0})\boldsymbol{m}(\boldsymbol{0})]\delta_{\boldsymbol{0}},$$

$$\mathrm{N}(\mathsf{T}) = \boldsymbol{T}_s(\boldsymbol{a})\boldsymbol{m}(\boldsymbol{a})\delta_{\boldsymbol{a}} + \boldsymbol{T}_r \boldsymbol{n}\, \mathcal{H}^{n-1} \llcorner (C \cap \partial U),$$

where $\boldsymbol{c}$ is given by Equation (3–12), $\boldsymbol{a}$ is defined by $\partial U \cap \partial\mathcal{S} = \{\boldsymbol{a}\}$, the symbols $\boldsymbol{m}(\boldsymbol{0})$, $\boldsymbol{m}(\boldsymbol{a})$ denote the outer tangents to $\mathcal{S}$ at $\boldsymbol{0}$, $\boldsymbol{a}$, respectively, and $\boldsymbol{n}$ is the outer normal to U. If $n \geq 2$, the equilibrium equation (4–1) with b_0 as in (4–2) can be satisfied only if $\boldsymbol{b}_0 = \boldsymbol{0}$ (see (3–9)) and if this is the case, it is equivalent to the following pair of equations:

$$\operatorname{div} \boldsymbol{T}_s = \boldsymbol{0}, \quad \boldsymbol{c} + \boldsymbol{T}_s(\boldsymbol{0})\boldsymbol{m}(\boldsymbol{0}) = \boldsymbol{0}.$$

5. Dimension two

Let $U \subset \mathbb{R}^2$ be an open set and $\mathcal{S} \subset \operatorname{cl} U$ be a smooth curve, let s be the natural (arc) parameter of $\mathcal{S}$ and let $\boldsymbol{t}(s)$, $\boldsymbol{n}(s)$, and $\kappa(s)$ be the unit tangent, the unit normal, and

the curvature, respectively. If $\boldsymbol{T}_s : \mathcal{S} \to \mathrm{Lin}$ is a symmetric tensor field on $\mathcal{S}$ then $\boldsymbol{T}_s$ is superficial if and only if we have

$$\boldsymbol{T}_s(s) = \sigma(s)\, \boldsymbol{t}(s) \otimes \boldsymbol{t}(s), \tag{5–1}$$

with σ a scalar field on $\mathcal{S}$. Then

$$\operatorname{div} \boldsymbol{T}_s = \frac{d}{ds}(\sigma \boldsymbol{t}) = \frac{d\sigma}{ds}\boldsymbol{t} + \kappa\sigma \boldsymbol{n}, \tag{5–2}$$

where the first equality follows from Equation (A–9) by noting that the natural parameterization of $\mathcal{S}$ has unit Jacobian, and the second equality follows from Frenet's formula. Alternatively, if we suppose that the curve $\mathcal{S}$ is the graph of a function $y = \omega(x)$, with $x \in [x_0, x_1]$, that is, $\mathcal{S} = \{(x, \omega(x)) \in U : x \in [x_0, x_1]\}$, then

$$\operatorname{div} \boldsymbol{T}_s = J^{-1} \frac{d}{dx}\left(\frac{\sigma}{J}\, \boldsymbol{e}_1 + \frac{\sigma}{J}\, \omega' \boldsymbol{e}_2\right), \tag{5–3}$$

where the prime denotes the differentiation with respect to x,

$$J = \frac{ds}{dx} = \sqrt{1 + (\omega')^2}, \tag{5–4}$$

and $\boldsymbol{e}_1, \boldsymbol{e}_2$ is the standard basis of $\mathbb{R}^2$. This follows from the application of Equation (A–9) to $\boldsymbol{\phi} : (x_0, x_1) \to \mathbb{R}^2$ given by $\boldsymbol{\phi}(x) = (x, \omega(x))$. Note also that the unit tangent $\boldsymbol{t}$ and the unit normal $\boldsymbol{n}$ of $\mathcal{S}$ are given by

$$\boldsymbol{t} = J^{-1}(\boldsymbol{e}_1 + \omega' \boldsymbol{e}_2), \quad \boldsymbol{n} = J^{-1}(-\omega' \boldsymbol{e}_1 + \boldsymbol{e}_2). \tag{5–5}$$

Remark 1. Let $[\boldsymbol{T}_r]\boldsymbol{n}$ be the jump of the normal component of $\boldsymbol{T}_r$ across $\mathcal{S}$. Equations (5–2) and (4–3) yield

$$[\boldsymbol{T}_r]\boldsymbol{n} - \frac{d\sigma}{ds}\boldsymbol{t} - \kappa\sigma \boldsymbol{n} = \boldsymbol{0}. \tag{5–6}$$

If we multiply this relation by $\boldsymbol{t}$ and $\boldsymbol{n}$ and put $\boldsymbol{t} \cdot [\boldsymbol{T}_r]\boldsymbol{n} = -q$ and $\boldsymbol{n} \cdot [\boldsymbol{T}_r]\boldsymbol{n} = -p$, we obtain, respectively,

$$\frac{d\sigma}{ds} + q = 0, \qquad \kappa\sigma + p = 0.$$

These equations coincide with the equilibrium equations of a planar curved beam when the bending moment and the shear force are null, if we interpret q and p as the tangential and normal component of the load, respectively, and $\sigma \boldsymbol{t} = \boldsymbol{T}_s \boldsymbol{t}$ as the axial force [Love 1944].

From (5–1) and the first equation in (5–5) we get

$$\boldsymbol{T}_s = \sigma J^{-2}\left\{\boldsymbol{e}_1 \otimes \boldsymbol{e}_1 + 2\omega' \boldsymbol{e}_1 \odot \boldsymbol{e}_2 + (\omega')^2 \boldsymbol{e}_2 \otimes \boldsymbol{e}_2\right\}, \tag{5–7}$$

where

$$\boldsymbol{e}_1 \odot \boldsymbol{e}_2 = \tfrac{1}{2}(\boldsymbol{e}_1 \otimes \boldsymbol{e}_2 + \boldsymbol{e}_2 \otimes \boldsymbol{e}_1).$$

Defining $\delta_{11}, \delta_{12}, \delta_{22}$ by

$$[\boldsymbol{T}_r] = \delta_{11}\boldsymbol{e}_1 \otimes \boldsymbol{e}_1 + 2\delta_{12}\boldsymbol{e}_1 \odot \boldsymbol{e}_2 + \delta_{22}\,\boldsymbol{e}_2 \otimes \boldsymbol{e}_2, \tag{5–8}$$

we obtain from the second equation in (5–5)

$$[\boldsymbol{T}_r]\boldsymbol{n} = J^{-1}\big\{(\delta_{12} - \omega'\delta_{11})\boldsymbol{e}_1 + (\delta_{22} - \omega'\delta_{12})\boldsymbol{e}_2\big\}. \tag{5–9}$$

With

$$\beta := \frac{\sigma}{J}, \tag{5–10}$$

we deduce from Equations (4–3), (5–9) and (5–3) the system of ordinary differential equations

$$\beta' + \omega'\delta_{11} - \delta_{12} = 0, \tag{5–11}$$

$$(\beta\omega')' + \omega'\delta_{12} - \delta_{22} = 0, \tag{5–12}$$

some applications of which are illustrated in the following sections. We observe that, in view of Equations (5–1), the first equation in (5–5) and (5–10), we have

$$\beta = \sigma(\boldsymbol{t}\cdot\boldsymbol{e}_1) \quad \text{and} \quad \beta\omega' = \sigma(\boldsymbol{t}\cdot\boldsymbol{e}_2), \tag{5–13}$$

which are the horizontal and vertical components of the axial force, respectively.

6. Panels: vertical top loads

In the rest of the paper we apply the considerations of Sections 3–5 to study the statics of rectangular panels in two dimensions made of a no-tension material, with infinite compressive strength [Del Piero 1989]. The panel is free from body forces, clamped at its bottom and subjected to loads prescribed on the boundary. The stress is supposed to be symmetric, plane and negative semidefinite, with singularities along a finite number of curves in the interior $U \subset \mathbb{R}^2$ of the panel; we use equilibrated tensor fields to describe the stress. If $\mathcal{S}$ is the union of these curves, the stress field T is the sum of a measure absolutely continuous with respect to Lebesgue's measure with a smooth density $\boldsymbol{T}_r$ in $U \setminus \mathcal{S}$, and a measure concentrated on $\mathcal{S}$, whose density is a smooth superficial tensor field $\boldsymbol{T}_s$. The equilibrium requires that $\boldsymbol{T}_r$ has null divergence outside $\mathcal{S}$, and that the surface divergence of $\boldsymbol{T}_s$ be balanced by the jump of the normal component of $\boldsymbol{T}_r$ across $\mathcal{S}$, as required by Equation (4–3). In the examples presented in this paper, the form of the singularity curves and the superficial stress field $\boldsymbol{T}_s$ are obtained by means of this relation, once $\boldsymbol{T}_r$ has been determined.

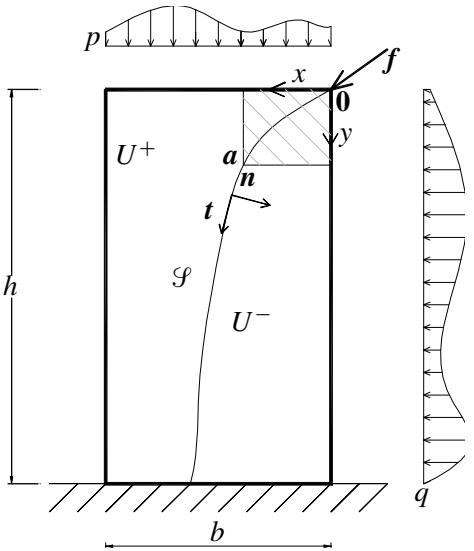

Figure 1. The panel under general load conditions.

We shall deal with either solid rectangular panels or rectangular panels with an opening. In all cases we place the origin of the coordinate system (x, y) in the upper right corner of the panel, with the axis x along the upper side of the panel pointing to left and the y axis along the right side pointing downwards, see Figure 1.

Consider first a solid rectangular panel of width b and height h, clamped at its base $y = h$ and subjected to a vertical load, p, distributed on its top, $y = 0$, a horizontal load, q, distributed along its right side, $x = 0$, and a force,

$$\boldsymbol{f} = f_1 \boldsymbol{e}_1 + f_2 \boldsymbol{e}_2,$$

concentrated at the upper right corner (Figure 1). Denoting by U the inner part of the panel,

$$U = \{(x, y) \in \mathbb{R}^2 : 0 < x < b,\ 0 < y < h\},$$

we aim to determine a curve $\mathcal{S}$ in U

$$y = \omega(x), \quad \text{with} \quad \omega(0) = 0, \tag{6–1}$$

and a continuously differentiable, negative-semidefinite superficial stress field $\boldsymbol{T}_s$ on $\mathcal{S}$, such that the tensor field $\mathbf{T}$, defined by

$$\mathbf{T} := \boldsymbol{T}_r \mathscr{L}^2 \llcorner U + \boldsymbol{T}_s \mathscr{H}^1 \llcorner \mathcal{S},$$

is balanced and in equilibrium with the external loads, where $\boldsymbol{T}_r$ is given by

$$\boldsymbol{T}_r = \begin{cases} -p(x)\boldsymbol{e}_2 \otimes \boldsymbol{e}_2, & \text{in } U^+, \\ -q(y)\boldsymbol{e}_1 \otimes \boldsymbol{e}_1 & \text{in } U^-, \end{cases} \tag{6–2}$$

with $U^- = \{(x, y) \in U : 0 < x < \omega^{-1}(y)\}$ and $U^+ = \{(x, y) \in U : \omega^{-1}(y) < x < b\}$ denoting the two regions into which U is divided by $\mathcal{S}$. Since, according to (6–2), $\boldsymbol{T}_r$ is equilibrated with the distributed loads p and q and satisfies the first equation in (4–3), it is sufficient to determine $\mathcal{S}$ and $\boldsymbol{T}_s$ to satisfy the second equation in (4–3) and the equilibrium boundary condition

$$\boldsymbol{T}_s(\boldsymbol{0})\boldsymbol{t}(\boldsymbol{0}) = -\boldsymbol{f}. \tag{6–3}$$

To this end, note that in this case Equations (5–8) and (6–2) give

$$\delta_{11} = q(\omega(x)), \quad \delta_{22} = -p(x), \quad \delta_{12} = 0$$

and therefore from Equations (5–11) and (5–12) we deduce

$$\beta' + q(\omega(x))\omega' = 0 \tag{6–4}$$

and

$$(\beta\omega')' + p(x) = 0. \tag{6–5}$$

Denoting by P and Q the respective primitives of p and q with $P(0) = 0$ and $Q(0) = 0$, we get

$$\beta(x) = \beta(0) - Q(\omega(x)), \tag{6–6}$$

$$\beta(x)\omega'(x) = \beta(0)\omega'(0) - P(x). \tag{6–7}$$

With the help of (6–6), (6–7) becomes

$$(Q(\omega(x)) - \beta(0))\,\omega'(x) = P(x) - \beta(0)\omega'(0), \tag{6–8}$$

and, in view of Equation (5–13), the equilibrium boundary condition (6–3) becomes

$$\beta(0) = -f_1, \quad \beta(0)\omega'(0) = -f_2. \tag{6–9}$$

Then, (6–8) implies

$$(Q(\omega(x)) + f_1)\,\omega'(x) = P(x) + f_2, \tag{6–10}$$

which can be integrated under the boundary condition in the second equation of (6–1). This is equivalent to the requirement for equilibrium of all rectangular regions, like the one shaded in Figure 1, with respect to the rotation about the point $\boldsymbol{a}$ [Lucchesi and Zani 2002]. Since $\boldsymbol{T}_s$ is negative-semidefinite, we can see that $\sigma(0) \leq 0$ in view of Equation (5–1), and from Equations (5–4) and (5–10) we

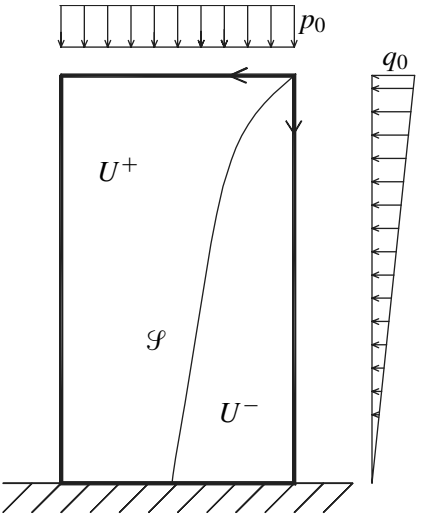

Figure 2. Load-distribution laws on the boundary of the panel; Example 1.

obtain $\beta \leq 0$. Moreover, since the curve $\mathcal{S}$ (except for its ends) is wholly contained within U, we have $\omega'(0) \geq 0$. From Equation (6–9), it follows that both f_1 and f_2 must be non-negative, that is to say, the force $\boldsymbol{f}$ must be directed towards the inside of the panel [Di Pasquale 1984].

Example 1. In this example, we suppose that the vertical distributed load is uniform, the horizontal one is linear and the concentrated force is zero (Figure 2), that is,

$$p(x) = p_0, \quad q(y) = q_0\left(1 - \frac{y}{h}\right), \quad \boldsymbol{f} = \boldsymbol{0}.$$

Under such conditions

$$Q(\omega) = q_0\omega\left(1 - \frac{\omega}{2h}\right), \quad P(x) = p_0 x \tag{6–11}$$

and from Equations (6–10) and the second equation in (6–1) we obtain for $\mathcal{S}$ the implicit equation

$$q_0\omega^2\left(1 - \frac{\omega}{3h}\right) = p_0 x^2. \tag{6–12}$$

It can be seen that $\mathcal{S}$ intersects the panel base at

$$x = h\sqrt{\frac{2q_0}{3p_0}}.$$

In order for such a solution to be valid, the intersection point must be within the panel's base, that is to say,

$$b \geq h\sqrt{\frac{2q_0}{3p_0}},$$

and this requires that q_0 does not exceed the value

$$q_m = \frac{3}{2}p_0\left(\frac{b}{h}\right)^2.$$

The attainment of this value would cause the panel to overturn around the corner at coordinates $x = b$, $y = h$. From (6–12) we deduce

$$x = \omega\sqrt{\frac{q_0}{p_0}\left(1 - \frac{\omega}{3h}\right)},$$

and then

$$\omega' = \left(\frac{2h}{2h-\omega}\right)\sqrt{\frac{p_0}{q_0}\left(1 - \frac{\omega}{3h}\right)}$$

by Equations (6–10) and (6–11). The expression for σ can be obtained from Equations (5–10), (6–6), the first equation of (6–11), and (5–4), and it is easy to verify that σ is an increasing function of x. In particular, at the panel bottom we have $\omega = h$ and therefore, taking Equations (5–4) and (6–6) into account, we obtain

$$\omega' = 2\sqrt{\frac{2p_0}{3q_0}}, \qquad J = \sqrt{1 + \frac{8p_0}{3q_0}}, \qquad \beta = -\frac{1}{2}q_0 h,$$

from which we obtain the reaction $\boldsymbol{T}_s\boldsymbol{t} = \sigma\boldsymbol{t}$ at the end of $\mathcal{S}$ of magnitude

$$\frac{1}{2}q_0 h\sqrt{1 + \frac{8p_0}{3q_0}}$$

by Equations (6–4) and (6–9).

Example 2. In this example, we again suppose that the vertical load is uniform, while the horizontal one is zero. Moreover, we assume a concentrated force to be acting (Figure 3),

$$p = p_0, \quad q = 0, \quad \boldsymbol{f} = f_1\boldsymbol{e}_1 + f_2\boldsymbol{e}_2,$$

so that $P(x) = p_0 x$ and $Q(\omega) = 0$. Therefore, we assume $\boldsymbol{T}_r$ as in Equation (6–2) with $p(x) = p_0$ and $q(x) = 0$, and from Equations (6–10) and the second equation in (6–1) we deduce

$$\omega(x) = \frac{p_0 x^2}{2f_1} + \nu x, \tag{6–13}$$

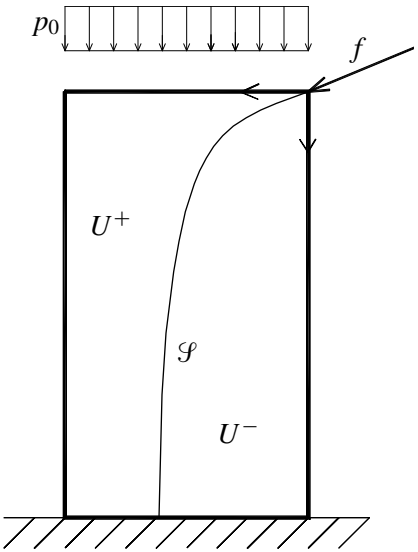

Figure 3. Load-distribution laws on the boundary of the panel; Example 2.

with $\nu = f_2/f_1$. Thus, in view of Equations (5–4), (6–6), the first equation in (6–9) and (5–10) we obtain

$$J = \sqrt{1 + \left(\frac{p_0 x}{f_1} + \nu\right)^2}, \quad \beta = -f_1, \quad \sigma = -f_1\sqrt{1 + \left(\frac{p_0 x}{f_1} + \nu\right)^2}, \tag{6–14}$$

from which we can determine $\boldsymbol{T}_s$ with the help of Equation (5–7).

From (6–13), for $x = b$, $\omega = h$ and $\nu < h/b$, we get the maximum magnitude of force $\boldsymbol{f}$ compatible with the equilibrium,

$$|\boldsymbol{f}_m| = \frac{p_0 b^2}{2(h - \nu b)}\sqrt{1 + \nu^2}.$$

Moreover, in view of Equations (6–13) and the third equation in (6–14) the intensity of the concentrated reaction at the panel's base is

$$f_1\sqrt{1 + \frac{2p_0 h}{f_1} + \nu^2}.$$

This result can be generalized to the situation where, besides the vertical load p_0, there are two forces, $\boldsymbol{f}$ and $\boldsymbol{g}$, applied to the panel's corners. For simplicity, we limit ourselves to the case in which $\boldsymbol{f}$ and $\boldsymbol{g}$ are horizontal, as shown in Figure 4. Let us suppose $f \leq g$. Proceeding as in the previous case it can be verified that,

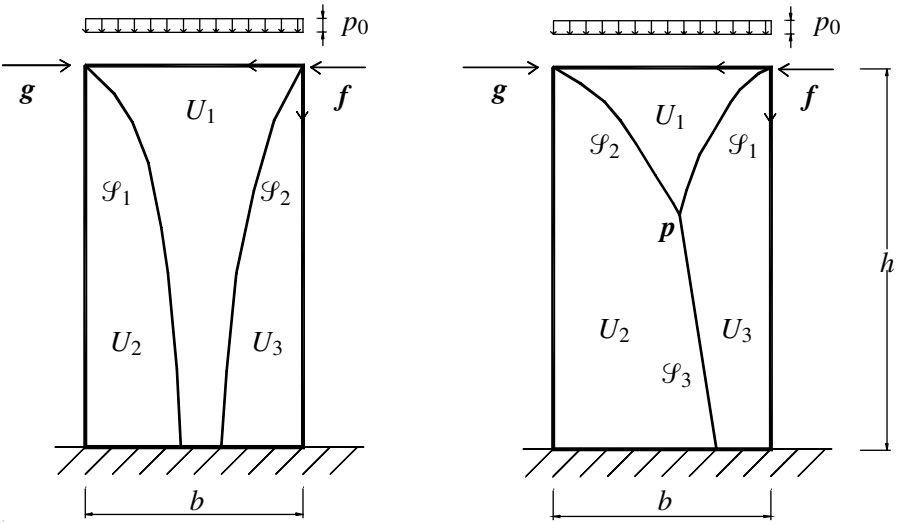

Figure 4. Stress states.

for

$$\sqrt{f}+\sqrt{g}\le\frac{1}{2}b\sqrt{\frac{2p_0}{h}},$$

the panel is subdivided into three regions, U_1, U_2 and U_3, by parabolas $\mathcal{S}_1$ and $\mathcal{S}_2$ with equations

$$\omega_1(x)=\frac{p_0x^2}{2f}\quad\text{with}\quad\sigma_1=-f\sqrt{1+\left(\frac{p_0x}{f}\right)^2}\tag{6–15}$$

and

$$\omega_2(x)=\frac{p_0(b-x)^2}{2g}\quad\text{with}\quad\sigma_2=-g\sqrt{1+\left(\frac{p_0(b-x)}{g}\right)^2},\tag{6–16}$$

and, moreover,

$$\boldsymbol{T}_r=\begin{cases}-p_0\boldsymbol{e}_2\otimes\boldsymbol{e}_2 & \text{in } U_1\\ & \text{in } U_2\cup U_3.\end{cases}\tag{6–17}$$

For

$$\sqrt{f}+\sqrt{g}>\frac{1}{2}b\sqrt{\frac{2p_0}{h}}$$

and

$$g-f\le\frac{p_0b^2}{2h},$$

the curves $\mathcal{S}_1$ and $\mathcal{S}_2$ intersect at a point $\boldsymbol{p}$ in the interior of U. In this case, an equilibrated tensor field is determined by supposing that the the panel is further

subdivided by the curve $\mathcal{S}_3$ (Figure 4 (b)). For $\boldsymbol{T}_r$ defined by Equation (6–17), we have $[\boldsymbol{T}_r] = \boldsymbol{0}$ across $\mathcal{S}_3$ and, in view of (5–6), this implies the vanishing of both the curvature κ and $d\sigma/ds$. Thus, $\mathcal{S}_3$ is a straight line whose equation can be determined with the help of (6–15) and (6–16), by observing that at the point $\boldsymbol{p}$ we have

$$\sigma_1 \boldsymbol{t}_1 + \sigma_2 \boldsymbol{t}_2 - \sigma_3 \boldsymbol{t}_3 = \boldsymbol{0},$$

in view of the second equation in Equation (4–4), which expresses the "equilibrium of the node $\boldsymbol{p}$". Finally, we obtain

$$\omega_3(x) = \frac{p_0 b(b-2x)}{2(g-f)} \quad \text{with} \quad \sigma_3 = -(g-f)\sqrt{1+\left(\frac{p_0 b}{g-f}\right)^2}.$$

For

$$g - f = \frac{p_0 b^2}{2h},$$

the panel is free to rotate around the point with coordinates $(0, h)$.

Example 3. Consider the case in which the panel is subjected only to the sole action of the uniform distributed vertical load $p = p_0$. Using the results of the previous example, we wish to verify that, beyond the regular stress state, $\boldsymbol{T} = -p_0 \boldsymbol{e}_2 \otimes \boldsymbol{e}_2$, defined throughout U, it is possible to determine infinitely many equilibrated and compatible stress fields, each of which characterized by

(i) a superficial stress $\boldsymbol{T}_s$ defined on a curve $\mathcal{S}$ with equation $y = \omega(x)$ that is symmetric with respect to the axis $x = b/2$ (Figure 5), which intersects this axis for $y = \lambda$, $(0 \le \lambda < h)$ and that also intersects the panel bottom for $|x - b/2| = \mu$, $(0 < \mu \le b/2)$,

$$\omega(b/2) = \lambda, \quad \omega(b/2 \pm \mu) = h, \quad \omega'(b/2) = 0; \tag{6–18}$$

(ii) a stress field

$$\boldsymbol{T}_r = \begin{cases} -p_0 \boldsymbol{e}_2 \otimes \boldsymbol{e}_2, & \text{in } U^+, \\ & \text{in } U^-, \end{cases} \tag{6–19}$$

where $U^- = \{(x, y) \in U : |x - b/2| < \mu,\ \omega(x) < y < h\}$ is the region below $\mathcal{S}$ and U^+ is the interior of its complement in U.

In fact, using Equations (6–4) and (6–5) with $p = p_0$, $q = 0$, and combining with (6–18), we see that $\mathcal{S}$ is a parabola given by

$$\omega(x) = \lambda + \frac{h-\lambda}{\mu^2}(x - b/2)^2 \tag{6–20}$$

and that β is given by

$$\beta = -\frac{p_0 \mu^2}{2(h-\lambda)},$$

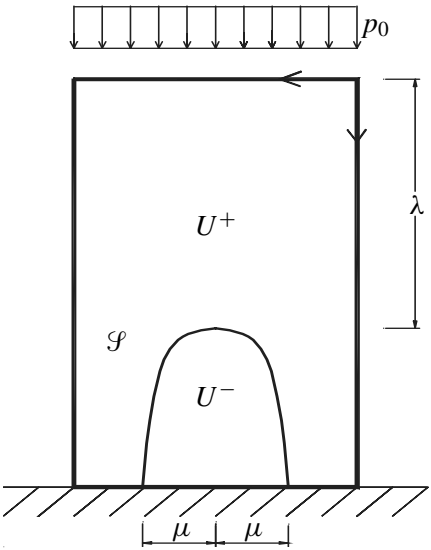

Figure 5. Stress field; Example 3.

from which we can calculate J, σ and $\boldsymbol{T}_s$ by Equations (5–4), (5–10) and (5–7). It can be seen that the interaction between the two parts of the panel, separated by the symmetry axis, $x = b/2$, consists solely of a horizontal force concentrated at the apex of $\mathcal{S}$, whose intensity $-\beta$ is an increasing function of λ which becomes unbounded when λ tends to h.

Example 4 (panels with openings). Let us consider a rectangular panel with base $b = b_1 + 2b_2$ and height $h = h_1 + h_2$, with a symmetric opening with dimensions b_1 and h_1 (Figure 6), clamped at its base and subjected to a vertical load p_0, uniformly distributed on its top. Clearly, the stress field from the preceding example is appropriate here also provided that the parabola in Equation (6–20) is entirely contained inside the panel. It is easy to see that the most favorable situation is attained when the apex of the parabola belongs to the top of the panel (Figure 6). Then $\boldsymbol{T}_r$ is as in (6–19), where regions U^- and U^+ are divided by parabola $\mathcal{S}$

$$\omega(x) = \frac{p_0(b/2 - x)^2}{2g},$$

with

$$\sigma = -g\sqrt{1 + \left(\frac{p_0(b/2 - x)}{g}\right)^2},$$

where

$$g = -\beta$$

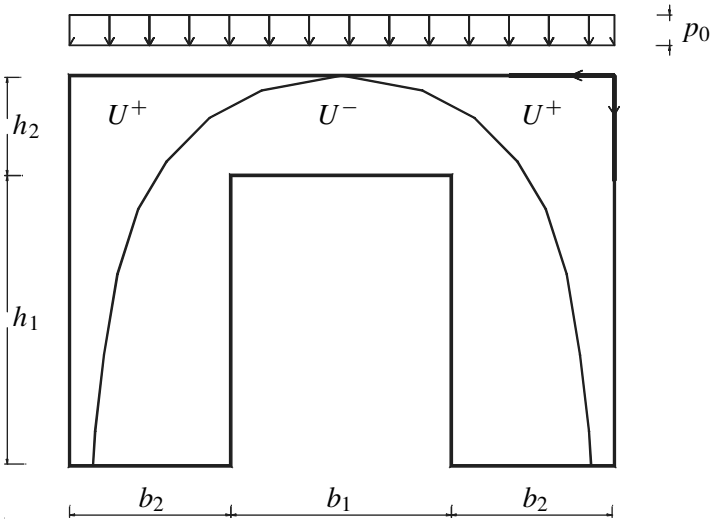

Figure 6. Panel with a symmetric opening.

is the interaction between the two parts of the panel across the symmetry axis. For $g = p_0 b_1^2/(8h_2)$ the parabola $\mathcal{S}$ contains the points (b_2, h_2) and $(b_1 + b_2, h_2)$, whereas for $g = p_0 b^2/(8h)$, $\mathcal{S}$ meets the corners of the panel with coordinates $(0, h)$ and (b, h); hence the equilibrium is possible only for $p_0 b^2/(8h) \geq p_0 b_1^2/(8h_2)$, that is, for

$$\zeta \leq 4\xi(\xi + 1), \tag{6–21}$$

with $\xi = b_2/b_1$ and $\zeta = h_1/h_2$. We observe that when the equality holds in Equation (6–21), $\mathcal{S}$ meets the four points $(0, h)$, (b_2, h_2), $(b_1 + b_2, h_2)$, and (b, h) and thus, apart from the value of p_0, the panel can be considered to be a kinematically indeterminate structure, made of four hinged bodies.

Assuming that $\zeta < 4\xi(\xi + 1)$, we now want to determine an equilibrated stress field when the panel is subjected to a horizontal force $\boldsymbol{f}$ applied to the upper right corner $\mathbf{0}$ in addition to the vertical load p_0. First, let us consider the case in which parabola $\mathcal{S}_1$ with equation $\omega(x) = p_0 x^2/(2f)$ is contained inside the panel as shown in Figure 7 (see also Example 2). For this, f has to satisfy the inequality

$$\frac{p_0(b_1 + b_2)^2}{2h_2} \leq f \leq \frac{p_0 b^2}{2h}, \tag{6–22}$$

because for

$$f = p_0(b_1 + b_2)^2/(2h_2),$$

ω meets the point $\boldsymbol{b}$, whereas for

$$f = p_0 b^2/(2h),$$

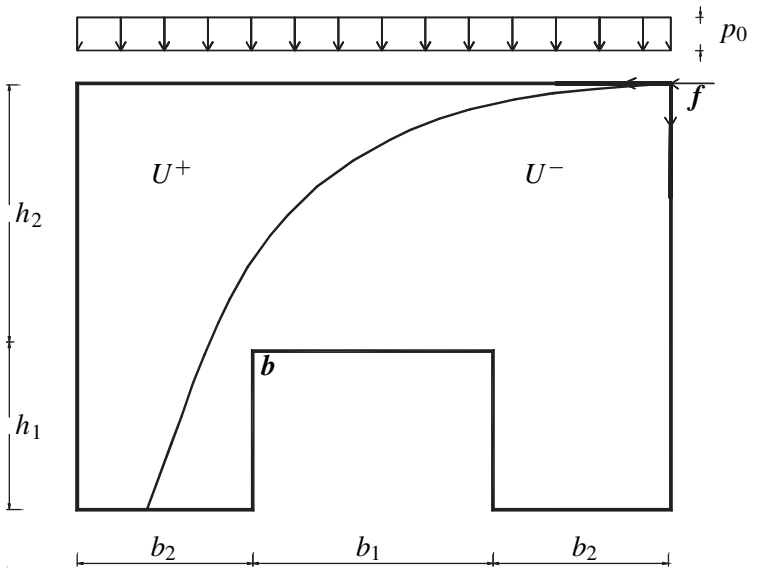

Figure 7. Stress field with a horizontal force $\boldsymbol{f}$, for $\zeta \leq \frac{\xi(3\xi+2)}{(\xi+1)^2}$.

ω meets the point $\boldsymbol{c}$. Inequalities (6–22) are verified only if

$$p_0 b^2/(2h) \geq p_0(b_1+b_2)^2/(2h_2),$$

that is, if

$$\zeta \leq \frac{\xi(3\xi+2)}{(\xi+1)^2}. \tag{6–23}$$

When Equations (6–23) and (6–22) are satisfied, we can assume that $\boldsymbol{T}_r$ and $\boldsymbol{T}_s$ are given in the same way as in the first part of Example 2 and then we see that the maximum value of f compatible with the equilibrium is

$$f_m = \frac{p_0 b^2}{2h}. \tag{6–24}$$

Let us now consider the case

$$\frac{\xi(3\xi+2)}{(\xi+1)^2} < \zeta < 4\xi(\xi+1). \tag{6–25}$$

In view of the previous discussion (see the second part of Example 2 and Figure 4 (b), the equilibrated tensor field can be obtained with the following three singularity curves:

(i) an arc of parabola $\mathcal{P}_1$, with equation

$$\omega_1(x) = \frac{p_0(x-a)^2}{2g}$$

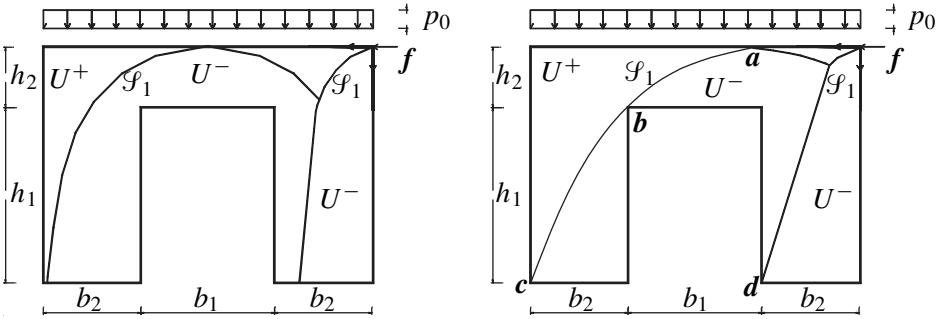

Figure 8. Stress field in the panel. (a) Apex of S_1 on the symmetry axis. (b) The collapse state.

and apex in $\boldsymbol{a} \equiv (a, 0)$ with $a \in (b/2, 0)$;

(ii) an arc of parabola $\mathcal{S}_2$ with the equation

$$\omega_2(x) = \frac{p_0 x^2}{2f},$$

and apex in $(0, 0)$;

(iii) a line $\mathcal{S}_3$, starting from the intersection point of $\mathcal{S}_1$ and $\mathcal{S}_2$ (Figure 8).

These curves subdivide the panel into three regions, where $\boldsymbol{T}_r$ is defined as in (6–17).

With the aim to obtain the maximum admissible intensity of f, we first determine the values of g and a so that the parabola $\mathcal{S}_1$ meet the points $\boldsymbol{b} \equiv (b_1 + b_2, h_2)$ and $\boldsymbol{c} \equiv (b, h)$ (Figure 8 (b)); this is always possible in view of Equation (6–25). In this way we obtain

$$g = \frac{p_0 b_1^2 \xi^2 \left(2 + \zeta + 2\sqrt{1+\zeta}\right)}{2\zeta^2 h_2}, \qquad a = b_1 \left(1 + \frac{\xi}{\zeta}\left(\zeta - 1 - \sqrt{1+\zeta}\right)\right). \quad (6\text{–}26)$$

Once g and a are determined, we impose the requirement that the segment $\mathcal{S}_3$ meets the point $\boldsymbol{d} \equiv (b_2, h)$ and then we get

$$f_m = \frac{p_0 b_1^2}{2h_2} \cdot \frac{2\xi\,(\xi+1)\,\sqrt{\zeta+1} + 2\xi^2\,(\zeta+1) + 2\xi - \zeta}{\zeta(\zeta+1)}. \quad (6\text{–}27)$$

When this value of f is reached, the panel behaves as a kinematically indeterminate structure made of three bodies, hinged at points $\boldsymbol{a}$, $\boldsymbol{b}$, $\boldsymbol{c}$ and $\boldsymbol{d}$.

We observe that a, as given by the second equation in (6–26), is positive in view of the first inequality of (6–25), and vanishes for

$$\zeta = \frac{\xi(3\xi+2)}{(\xi+1)^2}.$$

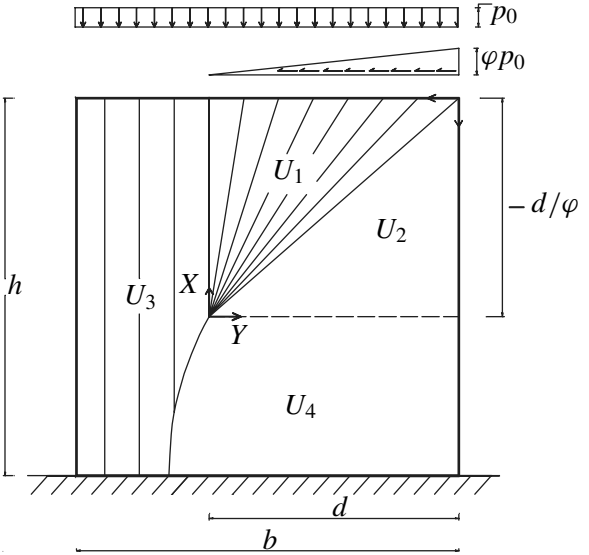

Figure 9. Load-distribution laws on the top of the rectangular panel and corresponding stress field.

In this particular circumstance, the value of f_m given by (6–27) coincides with the value of f_m given by (6–24) and with the value of g given by the first equation in (6–26).

7. Panels: oblique top loads

Let us consider a rectangular panel of width b and height h, clamped at its bottom and subjected to horizontal and vertical loads distributed on the top of the panel. Assume that the vertical load p_0 is uniform, whereas the horizontal load q has a linear distribution (Figure 9),

$$p(x) = p_0, \quad 0 \le x \le b;$$

$$q(x) = \begin{cases} \frac{\varphi p_0 (d-x)}{d}, & 0 \le x \le d, \\ 0, & d \le x \le b. \end{cases}$$

Let U be the interior of the panel. As proved in [Lucchesi and Zani 2003a], the stress field $\boldsymbol{T}_0$ in the region $0 \le x \le d$ and $0 \le y \le d/\varphi$ is given by

$$\boldsymbol{T}_0 = \begin{cases} \frac{p_0 \varphi^2 d (x-d)^2}{(\varphi y - d)^3} \boldsymbol{e}_1 \otimes \boldsymbol{e}_1 + \frac{2 p_0 \varphi d (x-d)}{(\varphi y - d)^2} \boldsymbol{e}_1 \odot \boldsymbol{e}_2 + \frac{p_0 d}{\varphi y - d} \boldsymbol{e}_2 \otimes \boldsymbol{e}_2 & \text{in } U_1 \\ & \text{in } U_2, \end{cases}$$

where U_1, U_2 are cones, both with vertex $\boldsymbol{p} = (d, d\varphi)$, given by

$$U_1 = \{(x, y) \in U : 0 \le x \le d,\ 0 \le \varphi y \le x\},$$

$$U_2 = \{(x, y) \in U : 0 \le x \le d,\ x \le \varphi y \le d\}.$$

The stress field $\boldsymbol{T}_0$ is discontinuous along the line $x = \varphi y$ but it is an easy matter to verify that the jump of the normal component of $\boldsymbol{T}_0$ across the discontinuity line is zero. Therefore $x = \varphi y$ differs from the singularity curves considered in the previous examples in that its corresponding superficial stress field vanishes.

In the coordinate system with origin in $\boldsymbol{p}$, $X = d - x$, $Y = d/\varphi - y$, shown in Figure 9, with corresponding unit normal base $\hat{\boldsymbol{e}}_1 = -\boldsymbol{e}_1$ and $\hat{\boldsymbol{e}}_2 = -\boldsymbol{e}_2$, we have

$$\boldsymbol{T}_0(\boldsymbol{x}) = \begin{cases} -\frac{p_0 d}{\varphi}(\boldsymbol{x} \cdot \hat{\boldsymbol{e}}_2)^{-3}\, \boldsymbol{x} \otimes \boldsymbol{x} & \text{in } U_1, \\ \boldsymbol{0} & \text{in } U_2, \end{cases}$$

where we put $\boldsymbol{x} = (X, Y)$. Recalling Proposition 2, we note that in U_1 we have

$$\boldsymbol{T}_0(\boldsymbol{x}) = |\boldsymbol{x}|^{-3}\, \alpha\left(\frac{\boldsymbol{x}}{|\boldsymbol{x}|}\right) \boldsymbol{x} \otimes \boldsymbol{x},$$

with the function α given by

$$\alpha(\boldsymbol{e}) = -\frac{p_0 d}{\varphi}(\boldsymbol{e} \cdot \hat{\boldsymbol{e}}_2)^{-3}, \tag{7–1}$$

$\boldsymbol{e} \in \mathbb{S}^1$. Therefore, writing $\boldsymbol{e} = \hat{\boldsymbol{e}}_1 \cos\theta + \hat{\boldsymbol{e}}_2 \sin\theta$ and $\psi = \tan^{-1}(1/\varphi)$, from Equation (7–1) we obtain the following value of the vector constant $\boldsymbol{c}$ as in (3–12):

$$\begin{aligned} \boldsymbol{c} &= -\frac{p_0 d}{\varphi} \int_{\psi}^{\pi/2} (\boldsymbol{e} \cdot \hat{\boldsymbol{e}}_2)^{-3}\, \boldsymbol{e}\ d\mathcal{H}^1(\boldsymbol{e}), \\ &= -\frac{p_0 d}{\varphi} \int_{\psi}^{\pi/2} (\sin\theta)^{-3} (\hat{\boldsymbol{e}}_1 \cos\theta + \hat{\boldsymbol{e}}_2 \sin\theta)\, d\theta, \\ &= -p_0 d(\varphi \hat{\boldsymbol{e}}_1/2 + \hat{\boldsymbol{e}}_2), \\ &= p_0 d(\varphi \boldsymbol{e}_1/2 + \boldsymbol{e}_2), \end{aligned} \tag{7–2}$$

which equals the resultant of the load applied to the top of the panel on the interval $[0, d]$; see Equation (3–13).

To determine the stress field in the remaining parts of the panel, we assume the existence of a singularity curve $\mathcal{S}$ with equation $y = \omega(x)$, starting from the point

$\boldsymbol{p}$, and we proceed as in Example 2, assuming

$$\boldsymbol{T}_r = \begin{cases} \boldsymbol{T}_0 & \text{in } U_1 \cup U_2, \\ -p_0 \boldsymbol{e}_2 \otimes \boldsymbol{e}_2 & \text{in } U_3, \\ \boldsymbol{0} & \text{in } U_4. \end{cases}$$

The form of the curve $y = \omega(x)$ is obtained similarly to that in Equation (6–13): one identifies $\boldsymbol{f} = \boldsymbol{c}$ and hence $f_1 = p_0 d\varphi/2$ and $\nu = 2/\varphi$ [see (7–2)] to obtain

$$\omega(x) = \frac{(x-d)^2}{\varphi d} + \frac{2(x-d)}{\varphi} + \frac{d}{\varphi} = \frac{x^2}{\varphi d}.$$

The maximun value of φ compatible with equilibrium is $b^2/(hd)$ and is attained when $\mathcal{S}$ meets the corner (b, h) of the panel.

8. Conclusions

The divergence measure tensor fields presented above constitute a new class of singular stress fields equilibrated with the loads and compatible with the incapability of the material to withstand traction. They appear to be a powerful tool that can be helpful in many applications to assess the safe magnitude of the applied load.

Although the examples presented in this work deal only with the plane problem in the absence of the body forces, the general part of this paper is meant to be applicable to more general situations [Lucchesi et al. 2004; 2005b].

Appendix A. Appendix: surfaces and surface divergence theorem

This appendix gathers the differential geometric notions used above. These are mainly the k-dimensional surfaces in $\mathbb{R}^n$, which we denote generically by $\mathcal{U}$, the k-dimensional surfaces with boundary, which we denote by $\mathcal{S}$, the surface divergence of vector fields and tensor fields on $\mathcal{U}$ or $\mathcal{S}$, and the surface divergence theorem 1. Most of the notions discussed below can be used in their intuitive sense but we prefer to give explicit definitions to avoid misunderstandings.

We start with the notion of surface. We give a definition that is convenient for the proof of Proposition 1. We refer to [Federer 1969, Subsection 3.1.19] for the discussion of surfaces without boundary of arbitrary class C^s and to [Lee 2003] for manifolds with boundary of class C^∞.

A.1. ***Surfaces.*** If $\mathcal{U}$ is a subset of $\mathbb{R}^n$, k an integer with $0 \le k \le n$, and s a positive integer, then the following conditions are equivalent [Federer 1969, Subsection 3.1.19]:

(i) for each $\boldsymbol{x} \in \mathcal{U}$ there exists a neighborhood Z of $\boldsymbol{x}$ in $\mathbb{R}^n$ and a class C^s injective map $\boldsymbol{\phi}$ from an open set in $\mathbb{R}^k$ into $\mathbb{R}^n$ with continuous inverse such

that

$$\mathcal{U} \cap Z = \operatorname{ran} \boldsymbol{\phi}, \quad \operatorname{rank} \nabla \boldsymbol{\phi}(\boldsymbol{p}) = k \quad \text{whenever } \boldsymbol{p} \in \operatorname{dom} \boldsymbol{\phi};$$

(ii) for each $\boldsymbol{x} \in \mathcal{U}$ there exists a neighborhood Z of $\boldsymbol{x}$ in $\mathbb{R}^n$ and a class C^s map $\boldsymbol{\omega} : Z \to \mathbb{R}^{n-k}$ such that

$$\mathcal{U} \cap Z = \boldsymbol{\omega}^{-1}(\mathbf{0}), \quad \operatorname{rank} \nabla \boldsymbol{\omega}(\boldsymbol{y}) = n - k \quad \text{whenever } \boldsymbol{y} \in Z.$$

If these equivalent conditions are satisfied, we say that $\mathcal{U}$ is a *k-dimensional surface* of class C^s. It is not assumed that surfaces are connected. We shall always assume that $s \geq 2$, and omit the qualification "of class C^2" in our terminology. It is easy to see that $\mathcal{U}$ is an n-dimensional surface in $\mathbb{R}^n$ if and only if $\mathcal{U}$ is an open subset of $\mathbb{R}^n$ and $\mathcal{U}$ is a 0-dimensional surface if and only if $\mathcal{U}$ is a set of isolated points. We call one-dimensional surfaces *curves*. We shall encounter zero-dimensional surfaces as boundaries of curves.

If $\boldsymbol{x} \in \mathcal{U}$ we denote by $\mathbf{T}_{\boldsymbol{x}}(\mathcal{U}) \subset \mathbb{R}^n$ the *tangent space* to $\mathcal{U}$ at $\boldsymbol{x}$, defined by

$$\mathbf{T}_{\boldsymbol{x}}(\mathcal{U}) = \operatorname{ran} \nabla \boldsymbol{\phi}(\boldsymbol{\phi}^{-1}(\boldsymbol{x})) = \ker \nabla \boldsymbol{\omega}(\boldsymbol{x}), \tag{A–1}$$

where $\boldsymbol{\phi}$ and $\boldsymbol{\omega}$ are as in (i) and (ii) above; we note that the two expressions in (A–1) are independent of the choices of these two objects. Clearly, $\mathbf{T}_{\boldsymbol{x}}(\mathcal{U})$ is a k-dimensional subspace of $\mathbb{R}^n$.

Next we discuss surfaces with boundary. These occur in the surface divergence theorem, below, and are defined as closed parts $\mathcal{S}$ of surfaces $\mathcal{U}$ without boundary such that the boundary $\partial\mathcal{S}$ is regular enough to have a well defined tangent space for $\mathcal{H}^{k-1}$ a.e. point.

A.2. ***Surfaces with boundary.*** We say that a subset $\mathcal{S}$ of $\mathbb{R}^n$ is a *k-dimensional surface with boundary* if the following three conditions are satisfied:

(i) $\mathcal{S}$ is closed;

(ii) there exists a k-dimensional surface $\mathcal{U}$ such that $\mathcal{S} \subset \mathcal{U}$;

(iii) for every $\boldsymbol{x}$ in the relative boundary $\partial\mathcal{S}$ of $\mathcal{S}$ in $\mathcal{U}$ there exist a set Z and a map $\boldsymbol{\phi}$ as in Item 1 of Section A.1, an $\epsilon > 0$, and a Lipschitz function $f : \operatorname{dom} f \to \mathbb{R}$ on an open subset of $\mathbb{R}^{k-1}$ such that

$$\boldsymbol{\phi}(D_-) \subset Z \cap (\mathcal{S} \setminus \partial\mathcal{S}), \quad \boldsymbol{\phi}(D_+) \subset Z \cap (\mathcal{U} \setminus \mathcal{S}),$$

where $D_\pm$ are the "$\pm\epsilon$ layers along the graph of f," given by

$$D_\pm = \{(\boldsymbol{y}, a) \in \mathbb{R}^k : \boldsymbol{y} \in \operatorname{dom} f, a = f(\boldsymbol{y}) \pm t, \text{ where } 0 < t < \epsilon\}.$$

We set $\operatorname{int}\mathcal{S} := \mathcal{S} \setminus \partial\mathcal{S}$ and note that $\operatorname{int}\mathcal{S}$ is a surface (without boundary) as defined in Section A.1. If $\boldsymbol{x} \in \mathcal{S}$, we define the *tangent space* $\mathbf{T}_{\boldsymbol{x}}(\mathcal{S})$ to $\mathcal{S}$ at $\boldsymbol{x}$

by $\mathbf{T}_{\boldsymbol{x}}(\mathcal{S}) = \mathbf{T}_{\boldsymbol{x}}(\mathcal{U})$; this definition is independent of the choice of $\mathcal{U}$. Note that if $\boldsymbol{x}$, Z, $\boldsymbol{\phi}$, and f are as in Item (iii) above then

$$Z \cap \partial\mathcal{S} = \boldsymbol{\phi}(\text{graph } f),$$

that is, $\boldsymbol{\phi}$ carries the graph of f into $\partial\mathcal{S}$; in particular $\boldsymbol{x} = \boldsymbol{\phi}(\boldsymbol{y}, f(\boldsymbol{y}))$ for some $\boldsymbol{y} \in \text{dom } f$. Motivated by this, we define the *tangent space* $\mathbf{T}_{\boldsymbol{x}}(\partial\mathcal{S})$ of $\partial\mathcal{S}$ at $\boldsymbol{x}$ for $\mathcal{H}^{k-1}$ a.e. $\boldsymbol{x} \in \partial\mathcal{S}$ as the image of the tangent space $\mathcal{T}$ at $(\boldsymbol{y}, f(\boldsymbol{y}))$ to graph f under $\nabla\boldsymbol{\phi}$ whenever $\mathcal{T}$ exists. By definition, $\mathcal{T}$ exists if and only if f is differentiable at $\boldsymbol{y}$; we then set

$$\mathcal{T} := \text{span}\big\{\nabla_i \boldsymbol{h}(\boldsymbol{y}) : i = 1, \dots, k-1\big\},$$

where $\boldsymbol{h} : \text{dom } f \to \mathbb{R}^k$ is defined by $\boldsymbol{h}(\boldsymbol{z}) = (\boldsymbol{z}, f(\boldsymbol{z}))$, $\boldsymbol{z} \in \text{dom } f$, and

$$\nabla_i,\ i \le i \le k-1,$$

denotes the partial differentiation in $\mathbb{R}^{k-1}$. We then set

$$\mathbf{T}_{\boldsymbol{x}}(\partial\mathcal{S}) := \text{span}\{\nabla\boldsymbol{\phi}(\boldsymbol{y}, f(\boldsymbol{y}))\nabla_i \boldsymbol{h}(\boldsymbol{y}) : i = 1, \dots, k-1\}$$

where $\boldsymbol{y}$ is defined by $\boldsymbol{x} = \boldsymbol{\phi}(\boldsymbol{y}, f(\boldsymbol{y}))$. Since f is differentiable at $\mathcal{L}^{k-1}$ a.e. point of dom f by Rademacher's theorem, $\mathbf{T}_{\boldsymbol{x}}(\partial\mathcal{S})$ is defined for $\mathcal{H}^{k-1}$ a.e. $\boldsymbol{x} \in \partial\mathcal{S}$.

The tangent space to $\partial\mathcal{S}$ is now used to define an exterior normal to $\partial\mathcal{S}$ as follows. If $\mathcal{S}$ is a k-dimensional surface with boundary then there exists a function $\boldsymbol{m}$, defined on $\mathcal{H}^{k-1}$ almost all of $\partial\mathcal{S}$ and with values in $\mathbb{S}^{n-1}$, which we write $\boldsymbol{m} : \partial\mathcal{S} \to \mathbb{S}^{n-1}$, such that we have the following conditions satisfied for $\mathcal{H}^{k-1}$ a.e. $\boldsymbol{x} \in \partial\mathcal{S}$:

(i) $\boldsymbol{m}(\boldsymbol{x}) \in \mathbf{T}_{\boldsymbol{x}}(\mathcal{S})$;

(ii) $\boldsymbol{m}(\boldsymbol{x})$ is perpendicular to $\mathbf{T}_{\boldsymbol{x}}(\partial\mathcal{S})$;

(iii) $\boldsymbol{m}$ points out of $\mathcal{S}$ in the sense that there exists a continuously differentiable map $\mathcal{S} : (-1, 1) \to \mathbb{R}^n$ with $\mathcal{S}((-1, 0]) \subset \mathcal{S}$, $\mathcal{S}(0) = \boldsymbol{x}$ and $d\mathcal{S}/dt\,(0) = \boldsymbol{m}(\boldsymbol{x})$.

Any two functions satisfying (i)–(iii) differ at most on a set of $\mathcal{H}^{k-1}$ measure 0; we call any such an $\boldsymbol{m}$ the *exterior normal* of $\mathcal{S}$, and refer to [Lee 2003, Proposition 13.26] for the proof in the case of C^∞ manifolds with C^∞ boundary. If $\mathcal{S}$ is a curve with endpoints and hence $\partial\mathcal{S}$ is a collection of the initial and final endpoints (see below for the definition), then the outer normal coincides with the outer tangents to $\mathcal{S}$ at the endpoints.

In the special case $k = n$, we call the n-dimensional surfaces with boundary in $\mathbb{R}^n$ *regions with Lipschitz boundary;* recall that, contrary to the common terminology, we assume that $\mathcal{S}$ is closed; since in this case $\partial\mathcal{S}$ coincides with the topological boundary of $\mathcal{S}$, it follows that int $\mathcal{S}$ is a region with Lipschitz boundary in the standard sense [Nečas 1967], which we call *open regions with Lipschitz boundary.*

For the special case $k = 1$ we call surfaces of dimension 1 with boundary *curves with endpoints.*

Referring to [Lee 2003, Chapter 13] for the standard notion of an orientation of a vector space, we say that a k-dimensional surface in $\mathbb{R}^n$ with boundary is *orientable* if there exists a continuous map on $\mathcal{S}$ giving the orientation of each tangent space of $\mathcal{S}$. Each such a map is called an *orientation* of the surface. An *oriented* k-dimensional surface with boundary is a surface $\mathcal{S}$ with boundary together with an orientation of $\mathcal{S}$.

A.3. ***Fields on surfaces, surface gradient and surface divergence.*** With the aim to define the surface divergence of a vector or tensor field defined on a surface, we first introduce a surface derivative via 'theoretical' formulas (A–2) and (A–3), below, and give 'practical' formulas (A–4) and (A–5).

If $\mathcal{S}$ is a k-dimensional surface with boundary, $S \subset \mathcal{S}$, $f : S \to V$ where V is a finite-dimensional inner product space, and $\boldsymbol{x} \in S \setminus \partial\mathcal{S}$, we say that f is *differentiable* at $\boldsymbol{x}$ if $N \cap \mathcal{S} \subset S$ for some neighborhood N of $\boldsymbol{x}$ in $\mathbb{R}^n$ and if there exists a linear transformation $\nabla f(\boldsymbol{x})$ from $\mathbb{R}^n$ to V, called the *surface derivative* of f at $\boldsymbol{x}$, such that

$$\nabla f(\boldsymbol{x})\boldsymbol{P} = \nabla f(\boldsymbol{x}) \tag{A–2}$$

and

$$\lim_{\substack{\boldsymbol{y}\to\boldsymbol{x} \\ \boldsymbol{y}\in S,\, \boldsymbol{y}\neq\boldsymbol{x}}} |f(\boldsymbol{y}) - f(\boldsymbol{x}) - \nabla f(\boldsymbol{x})(\boldsymbol{y}-\boldsymbol{x})|/|\boldsymbol{y}-\boldsymbol{x}| = 0, \tag{A–3}$$

where $\boldsymbol{P}$ is the orthogonal projection from $\mathbb{R}^n$ onto $\mathbf{T}_{\boldsymbol{x}}(\mathcal{S})$. Note that for $k = n$ this coincides with the usual definition of the (Fréchet) derivative interpreted as a linear transformation [Dieudonné 1960, Chapter VIII]; for $k = n - 1$ this reduces to the surface gradient defined in [Gurtin and Murdoch 1975; Gurtin 2000]. For a general k, we interpret $\nabla f(\boldsymbol{x})$ as a linear transformation from $\mathbb{R}^n$ to V and not as a linear transformation from $\mathbf{T}_{\boldsymbol{x}}(\mathcal{S})$ to V. However Equation (A–2) shows that $\nabla f(\boldsymbol{x}) = \boldsymbol{0}$ on the orthogonal complement $\mathbf{T}_{\boldsymbol{x}}(\mathcal{S})^{\perp}$. If $V = \mathbb{R}$, we identify the linear transformation $\nabla f(\boldsymbol{x})$ from $\mathbb{R}^n$ to $\mathbb{R}$ with a vector in $\mathbb{R}^n$, equally denoted, via $\nabla f(\boldsymbol{x})\boldsymbol{a} = \nabla f(\boldsymbol{x}) \cdot \boldsymbol{a}$ for any $\boldsymbol{a} \in \mathbb{R}^n$. It is easy to see that if $\boldsymbol{\phi}$ is as in Section A.1 (i) then f is differentiable at $\boldsymbol{x}$ if and only if $f \circ \boldsymbol{\phi}$ is differentiable in the classical sense at $\boldsymbol{p} := \boldsymbol{\phi}^{-1}(\boldsymbol{x})$ and then

$$\nabla f(\boldsymbol{x}) = \nabla(f \circ \boldsymbol{\phi})(\boldsymbol{p})[\nabla\boldsymbol{\phi}(\boldsymbol{p})]^{-1}\boldsymbol{P}, \tag{A–4}$$

where $[\nabla\boldsymbol{\phi}(\boldsymbol{p})]^{-1} : \mathbf{T}_{\boldsymbol{x}}(\mathcal{S}) \to \mathbb{R}^k$ is the inverse of $\nabla\boldsymbol{\phi}(\boldsymbol{p}) : \mathbb{R}^k \to \mathbf{T}_{\boldsymbol{x}}(\mathcal{S})$. Also, if N is a neighborhood of $\boldsymbol{x}$ in $\mathbb{R}^n$ and $g : N \to V$ is an extension of f that is differentiable in the classical sense at $\boldsymbol{x}$ then

$$\nabla f(\boldsymbol{x}) = \nabla g(\boldsymbol{x})\boldsymbol{P}, \tag{A–5}$$

where $\nabla g(\boldsymbol{x})$ is the derivative of g at $\boldsymbol{x}$ in the classical sense. If $T \subset S$, we say that $f : S \to V$ is *continuously differentiable* on T if $\nabla f(\boldsymbol{x})$ exists for every $\boldsymbol{x} \in T$ and the mapping ∇f is continuous on T.

If $\boldsymbol{q} : S \to \mathbb{R}^n$ is differentiable at $\boldsymbol{x} \in S$, we define the *surface divergence* $\operatorname{div} \boldsymbol{q}(\boldsymbol{x}) \in \mathbb{R}$ of $\boldsymbol{q}$ at $\boldsymbol{x}$ by

$$\operatorname{div} \boldsymbol{q}(\boldsymbol{x}) := \operatorname{tr}[\nabla \boldsymbol{q}(\boldsymbol{x})].$$

For $k = n$ this coincides with the standard divergence, while for $k = n - 1$ this reduces to the surface divergence defined in [Gurtin and Murdoch 1975] and [Gurtin 2000].

If $S \subset \mathcal{S}$ and $\boldsymbol{q} : S \to \mathbb{R}^n$, we say that $\boldsymbol{q}$ is *tangential* [Gurtin 2000] if $\boldsymbol{q}(\boldsymbol{x}) \in \mathbf{T}_{\boldsymbol{x}}(\mathcal{S})$ for every $\boldsymbol{x} \in S$. If $\boldsymbol{T} : S \to \operatorname{Lin}$ is differentiable at $\boldsymbol{x} \in S$, we define the *surface divergence* $\operatorname{div} \boldsymbol{T}(\boldsymbol{x}) \in \mathbb{R}^n$ of $\boldsymbol{T}$ at $\boldsymbol{x}$ to be the unique element of $\mathbb{R}^n$ such that

$$\boldsymbol{a} \cdot \operatorname{div} \boldsymbol{T}(\boldsymbol{x}) = \operatorname{div}[\boldsymbol{T}^{\mathsf{T}} \boldsymbol{a}](\boldsymbol{x}), \tag{A–6}$$

for every $\boldsymbol{a} \in \mathbb{R}^n$; see [Gurtin and Murdoch 1975] and [Gurtin 2000]. We note the following standard identity for a smooth tensor field $\boldsymbol{T}$ and a smooth vector field $\boldsymbol{v}$ on an open subset of a surface:

$$\operatorname{div}(\boldsymbol{T}^{\mathsf{T}} \boldsymbol{v}) = \nabla \boldsymbol{v} \cdot \boldsymbol{T} + \boldsymbol{v} \cdot \operatorname{div} \boldsymbol{T}. \tag{A–7}$$

To give formulas for the surface divergence, we assume that $\mathcal{U} \subset \mathbb{R}^n$ is a surface of dimension k, that $\boldsymbol{\phi} : P \to \mathcal{U}$ is a local parameterization of $\mathcal{U}$ on an open set $P \subset \mathbb{R}^k$ of class C^2, (that is, $\boldsymbol{\phi}$ satisfies Item (i) of Section A.1), and that $\boldsymbol{q} : \operatorname{ran} \boldsymbol{\phi} \to \mathbb{R}^n$ is a continuously differentiable tangential vector field on $\operatorname{ran} \boldsymbol{\phi} \subset \mathcal{U}$. We write

$$\boldsymbol{q} \circ \boldsymbol{\phi} = \sum_{i=1}^{k} q^i \boldsymbol{g}_i,$$

where $\boldsymbol{g}_i : P \to \mathbb{R}^n$ are the coordinate vectors of $\boldsymbol{\phi}$, given by $\boldsymbol{g}_i = \nabla \boldsymbol{\phi}\, \boldsymbol{e}_i$, where $\boldsymbol{e}_i$, $i = 1, \ldots, k$, is the standard basis in $\mathbb{R}^k$. Then q^i are continuously differentiable functions on P and one has

$$(\operatorname{div} \boldsymbol{q}) \circ \boldsymbol{\phi} = J_{\boldsymbol{\phi}}{}^{-1} \sum_{i=1}^{k} \nabla_i (J_{\boldsymbol{\phi}} q^i), \tag{A–8}$$

where $J_{\boldsymbol{\phi}: P \to (0,\infty)}$ is the Jacobian of $\boldsymbol{\phi}$, defined by

$$J_{\boldsymbol{\phi}}{}^2 = \det(\nabla \boldsymbol{\phi}^{\mathsf{T}} \nabla \boldsymbol{\phi}),$$

and ∇_i denotes the partial differentiation in $\mathbb{R}^k$. This can be deduced from [Lee 2003, Problem 14-11 (a)] in the case of class C^∞ objects and the generalization to the above smoothness assumptions is straightforward; nevertheless we note that $\boldsymbol{\phi}$

must be of class C^2 to make the right side of Equation (A–8) meaningful. One finds similarly that a continuously differentiable symmetric tensor field $\boldsymbol{T} : \operatorname{ran} \boldsymbol{\phi} \to \operatorname{Lin}$ is superficial if and only if it can be written in the form

$$\boldsymbol{T} \circ \boldsymbol{\phi} = \sum_{i,j=1}^{k} T^{ij} \boldsymbol{g}_i \otimes \boldsymbol{g}_j,$$

where T^{ij} are continuously differentiable functions on P. From Equations (A–6) and (A–8) we can deduce that

$$(\operatorname{div} \boldsymbol{T}) \circ \boldsymbol{\phi} = J_{\boldsymbol{\phi}^{-1}} \sum_{i,j=1}^{k} \nabla_j (J_{\boldsymbol{\phi}} T^{ij} \boldsymbol{g}_i). \tag{A–9}$$

Theorem 1 (Surface divergence theorem). *If $\mathcal{S}$ is an oriented k-dimensional surface with boundary and if $\boldsymbol{q} : \mathcal{S} \to \operatorname{Lin}$ is a continuous tangential vector field with compact support and with a continuous and $\mathcal{H}^k$ integrable derivative in* $\operatorname{int} \mathcal{S}$ *then*

$$\int_{\mathcal{S}} \operatorname{div} \boldsymbol{q} \, d\mathcal{H}^k = \int_{\partial \mathcal{S}} \boldsymbol{q} \cdot \boldsymbol{m} \, d\mathcal{H}^{k-1} \tag{A–10}$$

where $\boldsymbol{m}$ is the exterior normal to $\mathcal{S}$.

We refer to [Lee 2003, Theorem 14.23] for the proof for C^∞ objects. The proof under the present generality follows by noting that the maps $\boldsymbol{\phi}$ as in Section A.2 item (iii) carry (parts) of $\mathcal{S}$ into (parts) of regions with Lipschitz boundary in $\mathbb{R}^k$ for which the divergence theorem is known to hold [Nečas 1967] for functions from the Sobolev class $W^{1,1}$. In the proof one invokes Equation (A–8) to transform the surface integral of the surface divergence into the volume integral of the 'volume' divergence, invoking the divergence theorem and transforming the resulting integral to the right side of Equation (A–10). The proof is then completed with the help of a partition of unity, see [Šilhavý 2005b, Chapter 5] for details. The use of formula (A–8) requires a class C^2 smoothness of $\mathcal{S}$.

Acknowledgments

The research of M. Šilhavý has been supported by a MIUR grant, "Variational theory of microstructure, semiconvexity, and complex materials." The support is gratefully acknowledged.

References

[Anzellotti 1983] G. Anzellotti, "Pairings between measures and bounded functions and compensated compactness", *Ann. Mat. Pur. Appl.* **135**:1 (1983), 293–318.

[Benvenuto 1991] E. Benvenuto, *An introduction to the history of structural mechanics, II: Vaulted structures and elastic systems*, Springer, Berlin, 1991.

[Bouchut and James 1999] F. Bouchut and F. James, "Duality solutions for pressureless gases, monotone scalar conservation laws, and uniqueness", *Commun. Part. Diff. Eq.* **24** (1999), 2173–2190.

[Brenier and Grenier 1998] Y. Brenier and E. Grenier, "Sticky particles and scalar conservation laws", *SIAM J. Numer. Anal.* **35**:6 (1998), 2317–2328.

[Chen and Frid 1999] G.-Q. Chen and H. Frid, "Divergence-measure fields and hyperbolic conservation laws", *Arch. Ration. Mech. An.* **147**:2 (1999), 89–118.

[Chen and Frid 2001] G.-Q. Chen and H. Frid, "On the theory of divergence-measure fields and its applications", *Bol. Soc. Bras. Mat.* **32** (2001), 1–33.

[Chen and Frid 2003] G.-Q. Chen and H. Frid, "Extended divergence-measure fields and the Euler equations for gas dynamics", *Commun. Math. Phys.* **236**:2 (2003), 251–280.

[Chen and Torres 2005] G.-Q. Chen and M. Torres, "Divergence-measure fields, sets of finite perimeter, and conservation laws", *Arch. Ration. Mech. An.* **175**:2 (2005), 245–267.

[Degiovanni et al. 1999] M. Degiovanni, A. Marzocchi, and A. Musesti, "Cauchy fluxes associated with tensor fields having divergence measure", *Arch. Ration. Mech. An.* **147**:3 (1999), 197–223.

[Del Piero 1989] G. Del Piero, "Constitutive equation and compatibility of the external loads for linear elastic masonry-like materials", *Meccanica* **24**:3 (1989), 150–162.

[Del Piero 1998] G. Del Piero, "Limit analysis and no-tension materials", *Int. J. Plasticity* **14**:1-3 (1998), 259–271.

[Di Pasquale 1984] S. Di Pasquale, "Statica dei solidi murari teorie ed esperienze", Pubblicazione 27, Dipartimento di Costruzioni, Università di Firenze, 1984.

[Dieudonné 1960] J. Dieudonné, *Foundations of modern analysis*, Academic Press, New York and London, 1960.

[Federer 1969] H. Federer, *Geometric measure theory*, Springer, New York, 1969.

[Gurtin 1981] M. E. Gurtin, *An introduction to continuum mechanics*, Academic Press, Boston, 1981.

[Gurtin 2000] M. E. Gurtin, *Configurational forces as basic concepts of continuum physics*, Springer, New York, 2000.

[Gurtin and Murdoch 1975] M. E. Gurtin and A. I. Murdoch, "A continuum theory of elastic material surfaces", *Arch. Ration. Mech. An.* **57**:4 (1975), 291–323.

[Heyman 1966] J. Heyman, "The stone skeleton", *Int. J. Solids Struct.* **2**:2 (1966), 249–256.

[Kohn and Témam 1983] R. Kohn and R. Témam, "Dual spaces of stresses and strains, with applications to Hencky plasticity", *Appl. Math. Opt.* **10**:1 (1983), 1–35.

[Lee 2003] J. M. Lee, *Introduction to smooth manifolds*, Springer, New York, 2003.

[Love 1944] A. E. H. Love, *A treatise on the mathematical theory of elasticity*, Dover, New York, 1944.

[Lucchesi and Zani 2002] M. Lucchesi and N. Zani, "On the collapse of masonry panel", in *Proceedings of 7th International Seminar on Structural Masonry for Developing Countries*, Belo Horizonte, Brazil, 2002, 2002.

[Lucchesi and Zani 2003a] M. Lucchesi and N. Zani, "Some explicit solutions to plane equilibrium problem for no-tension bodies", *Struct. Eng. Mech.* **16**:3 (2003), 295–316.

[Lucchesi and Zani 2003b] M. Lucchesi and N. Zani, "Stati di sforzo per pannelli costituiti da materiale non resistente a trazione", in *Proceedings of XVI AIMETA Congress*, Ferrara, 2003.

[Lucchesi et al. 2004] M. Lucchesi, M. Šilhavý, and N. Zani, "Stress state for heavy masonry panels", Paper presented at the Colloquium Lagrangianum, Venice, 2004.

[Lucchesi et al. 2005a] M. Lucchesi, M. Šilhavý, and N. Zani, "Singular equilibrated stress fields for no-tension panels", pp. 255–265 in *Mechanical modelling and computational issues in civil engineering*, edited by M. Frémond and F. Maceri, Lecture Notes Appl. Comput. Mech. **23**, Springer, 2005.

[Lucchesi et al. 2005b] M. Lucchesi, M. Šilhavý, and N. Zani, "Stress fields for axisymmetric no-tension bodies", in *Proceedings of XVII AIMETA Congress*, Florence, 2005.

[Marzocchi and Musesti 2001] A. Marzocchi and A. Musesti, "Decomposition and integral representation of Cauchy interactions associated with measures", *Continuum Mech. Therm.* **13**:3 (2001), 149–169.

[Nečas 1967] J. Nečas, *Les méthodes directes en théorie des equations elliptiques*, Masson, Paris, 1967.

[Podio-Guidugli 2005] P. Podio-Guidugli, "Examples of concentrated contact interactions in simple bodies", *J. Elasticity* **75**:2 (2005), 167–186.

[Podio-Guidugli and Caffarelli 1990] P. Podio-Guidugli and G. V. Caffarelli, "Surface interaction potentials in elasticity", *Arch. Ration. Mech. An.* **109**:4 (1990), 343–383.

[Rudin 1974] W. Rudin, *Real and complex analysis*, McGraw-Hill, New York, 1974.

[Strang and Témam 1980] G. Strang and R. Témam, "Duality and relaxation in the variational problems in plasticity", *J. Mécanique* **19** (1980), 493–527.

[Témam and Strang 1980] R. Témam and G. Strang, "Functions of bounded deformation", *Arch. Ration. Mech. An.* **75**:1 (1980), 7–21.

[Šilhavý 1997] M. Šilhavý, *The mechanics and thermodynamics of continuous media*, Springer, Berlin, 1997.

[Šilhavý 2005a] M. Šilhavý, "Divergence measure fields and Cauchy's stress theorem", *Rend. Sem. Mat. Padova* **113** (Februrary 2005), 15–45.

[Šilhavý 2005b] M. Šilhavý, "Geometric integration theory and Cauchy's stress theorem", Lecture notes, 2005.

[Šilhavý 2005c] M. Šilhavý, "Normal traces of divergence measure vectorfields on fractal boundaries", Preprint, Dipartimento di Matematica, University of Pisa, 2005.

[Whitney 1957] H. Whitney, *Geometric integration theory*, Princeton University Press, Princeton, 1957.

Received 4 Dec 2005.

MASSIMILIANO LUCCHESI: massimiliano.lucchesi@unifi.it
Dipartimento di Costruzioni, Università di Firenze, Piazza Brunelleschi 6, 50121 Florence, Italy

MIROSLAV ŠILHAVÝ: Silhavy@math.cas.cz
Dipartimento di Matematica, Università di Pisa, Largo Bruno Pontecorvo 5, 56127 Pisa, Italy

and

Mathematical Institute of the AV ČR, Žitna 25, 115 67, Prague 1, Czech Republic

NICOLA ZANI: nicola.zani@unifi.it
Dipartimento di Costruzioni, Università di Firenze, Piazza Brunelleschi 6, 50121 Florence, Italy

JOURNAL OF MECHANICS OF MATERIALS AND STRUCTURES
Vol. 1, No. 3, 2006

ELASTIC INDENTATION PROBLEMS IN THIN FILMS ON SUBSTRATE SYSTEMS

ROBERTA SBURLATI

In this paper an analytical solution of an elastic isotropic thin-film on an elastic substrate under an axisymmetric loading on the plane surface is presented. The analysis is intended to model the micronanoindentation tests to evaluate some of the relevant properties of thin films and provide information about the influence of interface conditions between the film and the substrate.

The theoretical solution of the equations of three-dimensional elasticity is obtained by using Dini and Fourier–Bessel expansions for the displacement field. To describe the elastic mechanical interaction between the indenter and the film for low load, we make use of the pressure distribution for contact between two homogeneous bodies, and the corresponding displacement field is solved in explicit form. The contact law is obtained with two different ideal interface conditions between the film and the substrate: perfectly bonded and frictionless contact.

This form of the elastic solution may be utilized for different axisymmetric pressure distributions performed to model the interaction between the indenter and the film, thus obtaining an analytical framework for comparing experimental and numerical results.

1. Introduction

The growing importance of nanomicroscale materials has recently rekindled the interest in thin-film technology and the mechanical properties of a thin solid film deposited on a substrate. The interaction between a rigid indenter and an elastic half-space is a classical problem of contact mechanics that was studied by Sneddon [1966] by using the integral transforms technique. When a solid thin film is deposited over the substrate, the problem becomes more complex and the elastic response of the film subjected to indentation can be categorized according to the film/substrate material properties. In the first case, the film is soft in comparison with the substrate stiffness (soft-film); in the second case, the elastic properties of the film and the substrate are comparable; and in the third case the thin film is stiffer (hard film). For the first case, some investigators assume a mathematical artifice that simplifies the analysis: the substrate is approximated as rigid [Matthewson

Keywords: elasticity, contact mechanics, thin film, nanoindentation.

1981]. However, for the other cases, a correct evaluation of the mechanical behavior of the indentation problem requires knowledge of the effects of elastic properties of both the film and the substrate.

Experimental indentation tests are frequently used to measure the elastic properties of materials and to investigate the role of adhesion forces. In order to experimentally measure "film-only" properties, a commonly used rule of thumb for the substrate influences is to limit the indentation depth to less than 10% of the film thickness. Actually, some studies have shown that the critical parameter to take into account in the experimental indentation tests is the ratio between the thickness of the film and the contact area radius a; also in this case, it is proposed that the limit is less than 10% in order to use the monolithic theory. While using this rule is experimentally feasible for films that are greater than about a micrometer in thickness, this approach cannot be used for very thin films. Hence these assumptions, frequently accepted in the experimental tests for a large class of materials, are not applicable at the nanoscale [VanLandingham 2003; Fischer-Cripps 2004].

Intense studies have taken into account the adhesion forces which arise between the indenter and the film and on the interface film/substrate, and which give rise to an increasing of the contact area with respect to the contact without adhesion case [Maugis 1999].

In this work, we consider an isotropic film coating an isotropic elastic substrate subjected to an axisymmetric loading condition which simulates the presence of an indenter of assigned form in a quasi-static indentation test. We make two main assumptions. First, in view of the local character of the indentation problem, we introduce a suitable parameter b representing the radius in which the contact phenomenon is contained. In such a way, we write the components of the displacement field by means of Dini and Fourier–Bessel expansions, so avoiding the use of the Hankel integral transforms and, consequently, the problem of their inversions [Yu et al. 1990]. We shall subsequently show that, under suitable conditions, the specific value assumed for the parameter b is not relevant. Second, since the original mixed boundary value indentation problem leads to dual integral equations that, due to their complexity, can only be solved numerically by means of the Fredholm integral technique, we have changed the boundary conditions by assuming a preassigned distribution of traction on the free surface; this assumption is also introduced in the paper of Li and Chou [1997] within the framework of the Hankel integral transform technique.

In so doing, we solve the elastic problem of a thin film coating/substrate system under a prescribed axisymmetric load by using a Dini and a Fourier–Bessel expansion for the radial and the vertical component of the displacement field respectively. The elastic response of the film is analyzed with two different interface conditions between the substrate and the film to bound the real case: frictionless contact

and perfectly bonded. We also analyze the case in which the elastic properties of the film are very different from the substrate ones (soft-film/hard substrate). We get an explicit analytical form for the displacement and stress fields in terms of Fourier–Bessel expansions depending on some coefficients related to the form of the indenter and to the preassigned pressure distribution suitable to model the interaction film-indenter.

Although we do not assume specific restrictions on the thickness of the film, we consider the film "thin" for two reasons: first, because of its experimental relevance in micro and nanoindentation tests; and second, because we are interested in evaluating substrate effects that are not relevant for thick films (see the classical half-space theory [Sneddon 1966]).

Finally, we remark that the indentation test involves plastic deformation; indeed if we consider the loading of an initially flat specimen with a spherical indenter, after an initial elastic response at low loads, there is an elastic-plastic deformation. However, the elastic three-dimensional solution presented in this paper may be used to describe the low load elastic film response when the classical half-space solution is no longer true due to the presence of the film thickness.

The elastic solution may also be used to describe the unloading curve by adopting the Oliver and Pharr method; of course, one has to take into account the residual depth at complete unload [Oliver and Pharr 1992; Field and Swain 1993].

2. Problem formulation

In this section we study the indentation problem of a rigid, frictionless axisymmetric indenter on a circular thin-film/substrate system of radius b. The film is assumed to be either in frictionless contact or perfectly bonded to an elastic substrate. The thickness of the finite film overlaying the substrate is denoted as h. We choose a cylindrical coordinate system $(0, r, \vartheta, z)$ such that z is parallel to the generator of the indenter and the origin 0 is placed at the first contact point between the indenter and the film.

Due to the local character of the effect, we limit our study to the volume of a cylinder of radius b (the centre is the origin); by assuming that b is sufficiently large with respect to the radius a of the contact area, we can suppose that, for $r \geq b$, the vertical displacement does not change in the presence of the indenter; in other words, we assume $w(b, z) = 0$.

By considering an axisymmetric loading condition on the plane surface, we limit our attention to the radial and the transversal displacement fields $u^{(i)} = u^{(i)}(r, z)$ and $w^{(i)} = w^{(i)}(r, z)$ for the film and the substrate respectively (with $i = f, s$); by using a Dini expansion in r for $u^{(i)}(r, z)$ and a Fourier–Bessel expansion in r for $w^{(i)}(r, z)$ (see [Watson 1944], p. 576–577, equation (5) with $\nu = 1$, $H = 1$ in

equation (1), respectively), we write

$$u^{(f)}(r,z) = -\sum_{j=1}^{\infty} g_j^{(f)}(z)\phi_j J_1(\phi_j r), \quad w^{(f)}(r,z) = \sum_{j=1}^{\infty} f_j^{(f)}(z) J_0(\phi_j r), \tag{1}$$

$$u^{(s)}(r,z) = -\sum_{j=1}^{\infty} g_j^{(s)}(z)\phi_j J_1(\phi_j r), \quad w^{(s)}(r,z) = \sum_{j=1}^{\infty} f_j^{(s)}(z) J_0(\phi_j r). \tag{2}$$

The functions $g_j^{(s)}(z)$ and $f_j^{(s)}(z)$ denote the variations of the displacements through the thickness of the film and of the substrate; we have put

$$\phi_j = \frac{Z_j^{(0)}}{b},$$

where $Z_j^{(0)}$ denote, for $j = 1, 2, 3, \ldots$, the positive zeros of the zero-order Bessel function $J_0(r)$.

In this paper we assume that the film and the substrate are both isotropic; the linear elasticity equations therefore assume the form

$$(\lambda_i+2\mu_i)\left(\frac{\partial^2}{\partial r^2}u^{(i)}+\frac{1}{r}\frac{\partial}{\partial r}u^{(i)}-\frac{1}{r^2}u^{(i)}+\frac{\partial^2}{\partial z\partial r}w^{(i)}\right)+\mu_i\left(\frac{\partial^2}{\partial z^2}u^{(i)}-\frac{\partial^2}{\partial z\partial r}w^{(i)}\right) = 0,$$

$$(\lambda_i+2\mu_i)\left(\frac{\partial^2}{\partial z^2}w^{(i)}+\frac{1}{r}\frac{\partial}{\partial z}u^{(i)}+\frac{\partial^2}{\partial z\partial r}u^{(i)}\right)+\mu_i\left(\frac{\partial^2}{\partial r^2}w^{(i)}-\frac{\partial^2}{\partial z\partial r}u^{(i)}\right) - \mu_i\frac{1}{r}\left(\frac{\partial}{\partial z}u^{(i)}-\frac{\partial}{\partial r}w^{(i)}\right) = 0,$$

where λ_i and μ_i are the Lamé moduli.

By substituting the displacement field (1), (2) into these equations, we get the differential equations

$$(\lambda_i + 2\mu_i)\frac{d^2}{dz^2}f_j^{(i)} + \phi_j^2\left((\lambda_i+\mu_i)\frac{d}{dz}g_j^{(i)} - \mu_i f_j^{(i)}\right) = 0, \tag{3}$$

$$\mu_i\frac{d^2}{dz^2}g_j^{(i)} - (\lambda_i+\mu_i)\frac{d}{dz}f_j^{(i)} - \phi_j^2(2\mu_i+\lambda_i)g_j^{(i)} = 0, \tag{4}$$

whose solution has the form

$$f_j^{(f)}(z) = C_1^{(j)}\cosh(\phi_j z) + C_2^{(j)}\sinh(\phi_j z) + C_3^{(j)} z\cosh(\phi_j z) + C_4^{(j)} z\sinh(\phi_j z),$$

$$g_j^{(f)}(z) = -\frac{1}{\phi_j}C_1^{(j)}\sinh(\phi_j z) - \frac{1}{\phi_j}C_2^{(j)}\cosh(\phi_j z)$$

$$- \frac{1}{\phi_j} C_3^{(j)} \left(\frac{1}{\phi_j} \frac{\lambda_f + 3\mu_f}{\lambda_f + \mu_f} \cosh(\phi_j z) + z \sinh(\phi_j z) \right)$$
$$- \frac{1}{\phi_j} C_4^{(j)} \left(\frac{1}{\phi_j} \frac{\lambda_f + 3\mu_f}{\lambda_f + \mu_f} \sinh(\phi_j z) + z \cosh(\phi_j z) \right),$$

$$f_j^{(s)}(z) = Q_1^{(j)} \cosh(\phi_j z) + Q_2^{(j)} \sinh(\phi_j z) + Q_3^{(j)} z \cosh(\phi_j z) + Q_4^{(j)} z \sinh(\phi_j z),$$

$$g_j^{(s)}(z) = -\frac{1}{\phi_j} Q_1^{(j)} \sinh(\phi_j z) - \frac{1}{\phi_j} Q_2^{(j)} \cosh(\phi_j z)$$
$$- \frac{1}{\phi_j} Q_3^{(j)} \left(\frac{1}{\phi_j} \frac{\lambda_s + 3\mu_s}{\lambda_s + \mu_s} \cosh(\phi_j z) + z \sinh(\phi_j z) \right)$$
$$- \frac{1}{\phi_j} Q_4^{(j)} \left(\frac{1}{\phi_j} \frac{\lambda_s + 3\mu_s}{\lambda_s + \mu_s} \sinh(\phi_j z) + z \cosh(\phi_j z) \right).$$

in the film and in the substrate, respectively. The coefficients $C_1^{(j)}$, $C_2^{(j)}$, $C_3^{(j)}$, $C_4^{(j)}$ and $Q_1^{(j)}$, $Q_2^{(j)}$, $Q_3^{(j)}$, $Q_4^{(j)}$ will be uniquely determined by imposing the boundary and interface conditions that will be introduced in the next section.

The displacement field is obtained by considering the sum over all values of j; thus

$$u^{(f)}(r, z) = \sum_{j=1}^{\infty} \Bigg(C_1^{(j)} \sinh(\phi_j z) + C_2^{(j)} \cosh(\phi_j z)$$
$$+ C_3^{(j)} \Big(\frac{1}{\phi_j} \frac{\lambda_f + 3\mu_f}{\lambda_f + \mu_f} \cosh(\phi_j z) + z \sinh(\phi_j z) \Big)$$
$$+ C_4^{(j)} \Big(\frac{1}{\phi_j} \frac{\lambda_f + 3\mu_f}{\lambda_f + \mu_f} \sinh(\phi_j z) + z \cosh(\phi_j z) \Big) \Bigg) J_1(\phi_j r), \quad (5)$$

$$w^{(f)}(r, z) = \sum_{j=1}^{\infty} \big(C_1^{(j)} \cosh(\phi_j z) + C_2^{(j)} \sinh(\phi_j z)$$
$$+ C_3^{(j)} z \cosh(\phi_j z) + C_4^{(j)} z \sinh(\phi_j z) \big) J_0(\phi_j r). \quad (6)$$

$$u^{(s)}(r, z) = \sum_{j=1}^{\infty} \Bigg(Q_1^{(j)} \sinh(\phi_j z) + Q_2^{(j)} \cosh(\phi_j z)$$
$$+ Q_3^{(j)} \Big(\frac{1}{\phi_j} \frac{\lambda_s + 3\mu_s}{\lambda_s + \mu_s} \cosh(\phi_j z) + z \sinh(\phi_j z) \Big)$$
$$+ Q_4^{(j)} \Big(\frac{1}{\phi_j} \frac{\lambda_s + 3\mu_s}{\lambda_s + \mu_s} \sinh(\phi_j z) + z \cosh(\phi_j z) \Big) \Bigg) J_1(\phi_j r), \quad (7)$$

$$w^{(s)}(r,z)=\sum_{j=1}^{\infty}\big(Q_1^{(j)}\cosh(\phi_j z)+Q_2^{(j)}\sinh(\phi_j z) + Q_3^{(j)} z\cosh(\phi_j z)+Q_4^{(j)} z\sinh(\phi_j z)\big)J_0(\phi_j r). \quad (8)$$

3. Boundary and interface conditions

In order to explicitly find the form of the elastic solution (5)–(8), we investigate the boundary condition on the free surface of the film and on the interface film/substrate.

Due to the complexity of the indentation problem, an axisymmetric normal pressure and vanishing shear stress components are assumed on the free surface, in $z=0$, as follows

$$\sigma_{zz}^{(f)}(r,0)=p(r) \qquad \text{and} \qquad \sigma_{rz}^{(f)}(r,0)=0. \quad (9)$$

It is convenient to write the normal pressure distribution $p(r)$ with a Fourier–Bessel expansion in the form

$$p(r)=\sum_{j=1}^{\infty}A_j J_0(\phi_j r), \qquad \text{where} \qquad A_j=\frac{2\int_0^a rp(r)J_0(\phi_j r)dr}{b^2 J_1(b\phi_j)^2}. \quad (10)$$

A detailed discussion on the expansion convergence can be found in [Watson 1944]. On the other hand, in the substrate, for large z, we assume

$$\lim_{z\to\infty}u^{(s)}(r,z)=0 \qquad \text{and} \qquad \lim_{z\to\infty}w^{(s)}(r,z)=0. \quad (11)$$

These conditions give the following equations: $Q_1^{(j)}=-Q_2^{(j)}$ and $Q_3^{(j)}=-Q_4^{(j)}$.

Now we introduce two different conditions in the interface zone; the film is assumed to be in frictionless contact or perfectly bonded to a substrate. The solutions obtained for both these ideal cases are introduced to bound the real cases where the contact between the film and the substrate is neither frictionless nor perfectly bonded.

3.1. ***Perfectly bonded case.*** On the interface surface $z=h$, we require the continuity of displacement and traction components as follow

$$[w(r,h)]=0, \qquad [u(r,h)]=0, \quad (12)$$

$$[\sigma_{zz}(r,h)]=0, \qquad [\sigma_{rz}(r,h)]=0. \quad (13)$$

The conditions in (12), (13) together with (9) allow us to get the explicit form of the remaining unknown coefficients $C_\alpha^{(j)}$, $\alpha=1,\dots,4$ and $Q_\alpha^{(j)}$, $\alpha=2$, in terms of the A_j coefficients.

In the case of a *rigid substrate*, by putting $\lambda^{(f)} = \lambda$ and $\mu^{(f)} = \mu$, the interface conditions

$$w(r,h) = 0 \quad \text{and} \quad u(r,h) = 0 \tag{14}$$

give rise to the following simplified forms for the coefficients:

$$C_1^{(j)} = -\frac{(\lambda+2\mu)\big((\lambda+3\mu)\sinh(2\phi_j h) - 2\phi_j h(\lambda+\mu)\big)}{4\mu\phi_j\big((\lambda+\mu)(\lambda+3\mu)\sinh^2(\phi_j h) + \phi_j^2 h^2(\lambda+\mu)^2 + (2\mu+\lambda)^2\big)} A_j,$$

$$C_2^{(j)} = \frac{(\lambda+2\mu)(\lambda+3\mu)\cosh(2\phi_j h) + 2\phi_j^2 h^2(\lambda+\mu)^2 + (\lambda+2\mu)(\lambda+3\mu)}{4\mu\phi_j\big((\lambda+\mu)(\lambda+3\mu)\sinh^2(\phi_j h) + \phi_j^2 h^2(\lambda+\mu)^2 + (2\mu+\lambda)^2\big)} A_j,$$

$$C_3^{(j)} = -\frac{(\lambda+\mu)\big((\lambda+3\mu)\cosh(2\phi_j h) + (\lambda+\mu)\big)}{4\mu\big((\lambda+\mu)(\lambda+3\mu)\sinh^2(\phi_j h) + \phi_j^2 h^2(\lambda+\mu)^2 + (2\mu+\lambda)^2\big)} A_j,$$

$$C_4^{(j)} = \frac{(\lambda+\mu)\big((\lambda+3\mu)\sinh(2\phi_j h) - 2h\phi_j(\lambda+\mu)^2\big)}{4\mu\big((\lambda+\mu)(\lambda+3\mu)\sinh^2(\phi_j h) + \phi_j^2 h^2(\lambda+\mu)^2 + (2\mu+\lambda)^2\big)} A_j.$$

The coefficients A_j can be found by using the expression in (10) for the pressure on the free film surface.

3.2. ***Frictionless contact.*** On the interface surface $z = h$, we require the continuity of transversal displacement components, traction components, and null shear traction, as follows:

$$[w(r,h)] = 0, \qquad \sigma_{rz}^{(i)}(r,h) = 0,$$
$$[\sigma_{zz}(r,h)] = 0, \quad [\sigma_{rz}(r,h)] = 0.$$

Together with (9), these conditions allow us to get the coefficients $C_\alpha^{(j)}$, $\alpha = 1,\ldots,4$ and $Q_\alpha^{(j)}$, $\alpha = 2, 3$, in terms of the A_j.

For a *rigid substrate* the coefficient expressions assume the simplified form

$$C_1^{(j)} = -\frac{(\lambda+2\mu)(\cosh(2\phi_j h) - 1)}{2\mu\phi_j(\lambda+\mu)(\sinh(2\phi_j h) + 2\phi_j h)} A_j,$$

$$C_2^{(j)} = \frac{(\lambda+2\mu)\sinh(2\phi_j h) + (\lambda+\mu)2\phi_j h}{2\mu\phi_j(\lambda+\mu)(\sinh(2\phi_j h) + 2\phi_j h)} A_j,$$

$$C_3^{(j)} = -\frac{\sinh(2\phi_j h)}{2\mu(\sinh(2\phi_j h) + 2\phi_j h)} A_j,$$

$$C_4^{(j)} = \frac{\cosh(2\phi_j h) - 1}{2\mu(\sinh(2\phi_j h) + 2\phi_j h)} A_j.$$

The displacement field is obtained in explicit form from Equations (5)–(8), by taking into account the coefficients expression A_j for detailed preassigned pressure form (10) and the coefficients $C_\alpha^{(j)}, \alpha = 1, \dots, 4$ and $Q_\alpha^{(j)}, \alpha = 2$, for different interface conditions (Sections 3.1, 3.2).

Now we specify the form of the indenter since it is related to the pressure field on the free surface. Specifically, in the following we assume that the pressure distribution is given by the classical solutions for the indentation on an elastic half-space.

We remark that it is also possible to introduce different pressure distributions to simulate different effects between the indenter and the film (adhesion forces, approximate pressure distribution taking into account the thickness of the films; see [Yang 2003; Chadwick 2002]).

3.2.1. *Rigid flat-ended cylindrical punch.* We consider the case in which the film is deformed by a flat-ended rigid cylinder with radius a. In this case the pressure distribution for the homogeneous half-space is:

$$p(r) = -p_0\left(1 - \frac{r^2}{a^2}\right)^{-\frac{1}{2}}, \qquad p_0 = \frac{P}{2\pi a^2},$$

where P is the resultant applied load. By using equation (10) the coefficients A_j assume the following form

$$A_j = \frac{2ap_0 \sin(a\phi_j)}{b^2\phi_j J_1(b\phi_j)^2}.$$

3.2.2. *Rigid spherical punch with shallow indentation.* We consider a spherical punch by assuming that the radius a of the contact area is much smaller than the radius R of the sphere, that is, $a \ll R$. The pressure distribution, for $r < a$, has the form

$$p(r) = -p_0\left(1 - \frac{r^2}{a^2}\right)^{\frac{1}{2}} \quad \text{with} \quad p_0 = \frac{3P}{2\pi a^2} \quad \text{and} \quad a^3 = \frac{3PR(1-\nu^2)}{4E}.$$

In this case the coefficients A_j are

$$A_j = \frac{2p_0\big(\sin(a\phi_j) - a\phi_j \cos(a\phi_j)\big)}{ab^2\phi_j^3 J_1(b\phi_j)^2}.$$

3.2.3. *Rigid conical punch.* We consider a right circular cone with semi-vertical angle α whose axis coincides with the z-axis and the vertex points downward into the interior of the layer. The pressure distribution under the punch is

$$p(r) = -p_0 \cosh^{-1}\left(\frac{a}{r}\right) \text{ with } p_0 = \frac{P}{\pi a^2}, \quad a^2 = \frac{2P(1-\nu^2)}{\pi E \tan\beta} \text{ with } \beta = \frac{\pi}{2} - \alpha.$$

The j-th coefficient has the form

$$A_j = \frac{p_0 a^2\left(1 - \frac{1}{12}a^2\phi_j^2 + \frac{1}{360}a^4\phi_j^4 - \cdots\right)}{b^2 J_1(b\phi_j)^2}.$$

This expression was obtained by using an expansion of the $J_0(r)$ Bessel function.

4. Contact law and stress distribution in thin film

The contact law is obtained by using the explicit form of the transversal displacement (6) in $z = 0$ and $r = 0$ and can be written in the following compact form

$$\delta_{\text{film}} = \sum_{j=1}^{\infty} K_j A_j \tag{15}$$

Now, by using the explicit form of the coefficients $C_\alpha^{(j)}$, $\alpha = 1, \ldots, 4$ and $Q_\alpha^{(j)}$, $\alpha = 2$, we get the terms K_j in which we take into account the interface conditions; the pressure distribution form allows us to determine the terms A_j.

In the case of a *thin film on a rigid substrate*, the terms K_j are

$$K_j^{\text{bonded}} = \frac{(\nu^2 - 1)\left((4\nu - 3)\sinh(2\phi_j h) + 2\phi_j h\right)}{E\phi_j\left((4\nu - 3)\cosh(\phi_j h)^2 - (2\nu - 1)^2 - \phi_j^2 h^2\right)},$$

$$K_j^{\text{contact}} = \frac{2(\nu^2 - 1)(\cosh(2\phi_j h) - 1)}{E\phi_j(\sinh(2\phi_j h) + 2\phi_j h)},$$

where ν is the Poisson's ratio and E the Young's modulus.

The knowledge of the stress field is relevant for the understanding of the failure mechanism of the coating/substrate system. The j-th term of the stress components for the case of a rigid substrate can be written as follows:

$$\begin{aligned}\sigma_{zz}^{(j)} = 2\mu J_0(\phi_j r)\Bigg(& C_1^{(j)}\phi_j \sinh(\phi_j z) + C_2^{(j)}\phi_j \cosh(\phi_j z) \\ & + C_3^{(j)}\left(\frac{\mu}{\lambda + \mu}\cosh(\phi_j z) + \phi_j z \sinh(\phi_j z)\right) \\ & + C_4^{(j)}\left(\frac{\mu}{\lambda + \mu}\sinh(\phi_j z) + \phi_j z \cosh(\phi_j z)\right)\Bigg),\end{aligned}$$

$$\sigma_{rz}^{(j)} = 2\mu J_1(\phi_j r)\Big(C_1^{(j)}\phi_j \cosh(\phi_j z) + C_2^{(j)}\phi_j \sinh(\phi_j z) + C_3^{(j)}\Big(\frac{\lambda+2\mu}{\lambda+\mu}\sinh(\phi_j z) + \phi_j z\cosh(\phi_j z)\Big) + C_4^{(j)}\Big(\frac{\lambda+2\mu}{\lambda+\mu}\cosh(\phi_j z) + \phi_j z\cosh(\phi_j z)\Big)\Big),$$

$$\sigma_{rr}^{(j)} = \frac{2\mu}{r}\Big(C_1^{(j)}\sinh(\phi_j z) + C_2^{(j)}\cosh(\phi_j z)\Big)\big(-\phi_j r J_0(\phi_j r) + J_1(\phi_j r)\big) + \frac{2\mu C_3^{(j)}}{r\phi_j}\Big(\Big(\frac{\lambda+3\mu}{\lambda+\mu}\cosh(\phi_j z) + \phi_j z\sinh(\phi_j z)\Big)J_1(\phi_j r) - \Big(\phi_j r\frac{2\lambda+3\mu}{\lambda+\mu}\cosh(\phi_j z) + \phi_j^2 r z\sinh(\phi_j z)\Big)J_0(\phi_j r)\Big) + \frac{2\mu C_4^{(j)}}{r\phi_j}\Big(\Big(\frac{\lambda+3\mu}{\lambda+\mu}\sinh(\phi_j z) + \phi_j z\cosh(\phi_j z)\Big)J_1(\phi_j r) - \Big(\phi_j r\frac{2\lambda+3\mu}{\lambda+\mu}\sinh(\phi_j z) + \phi_j^2 r z\cosh(\phi_j z)\Big)J_0(\phi_j r)\Big),$$

$$\sigma_{\vartheta\vartheta}^{(j)} = -\frac{2\mu}{r}\big(C_1^{(j)}\sinh(\phi_j z)J_1(\phi_j r) + C_2^{(j)}\cosh(\phi_j z)J_0(\phi_j r)\big) - \frac{2\mu C_3^{(j)}}{r\phi_j}\Big(\Big(\frac{\lambda+3\mu}{\lambda+\mu}\cosh(\phi_j z) + \phi_j z\sinh(\phi_j z)\Big)J_1(\phi_j r) + \phi_j r\frac{\lambda}{\lambda+\mu}\cosh(\phi_j z)J_0(\phi_j r)\Big) - \frac{2\mu C_4^{(j)}}{r\phi_j}\Big(\Big(\frac{\lambda+3\mu}{\lambda+\mu}\sinh(\phi_j z) + \phi_j z\cosh(\phi_j z)\Big)J_1(\phi_j r) + \phi_j r\frac{\lambda}{\lambda+\mu}\sinh(\phi_j z)J_0(\phi_j r)\Big).$$

The explicit expressions for the case in which the film and the substrate are both elastic are obtained in an analogous way.

5. Numerical results

In this section we present two numerical examples useful to analyze the behavior of the contact law and the stress distribution in terms of the film thickness and the elastic properties of the substrate and the film.

Consider therefore a thin isotropic film ($E = 2\,\text{MPa}$ and $\nu = 0.25$) coated on a rigid substrate and in contact with a rigid sphere of radius $R = 10\,\mu\text{m}$. In Figure 1 we show the contact law, for different thickness of the film ($h = 5\,\mu\text{m}$ and $10\,\mu\text{m}$),

obtained by using the solutions presented in Section 4 with Hertzian pressure distributions.

We remark that, when the thickness of the film is very large with respect to the contact area radius a (i.e. $h \gg a$), we obtain numerical results in agreement with the theory of an elastic half-space with the properties of the film. On the other hand, when the thickness of the film is within the range between a and $10a$, the elastic response of the film changes for the presence of the rigid substrate [Yu et al. 1990; Li and Chou 1997]. Moreover, when the contact area radius is very large with respect to the film thickness (i.e. $h \ll a$), or in the case of a very soft material, the pressure distribution on the free surface of the film, and therefore the terms A_j of the expansion (10), must be assigned by using models suitable to take into account the adhesion forces or the different pressure distribution [Maugis 1999].

Figure 2 shows the radial displacement in two ideal interface cases when the film thickness is $h = 5\,\mu$m. The radial displacement, near the edge of the contact area, has a change of sign in the thickness; in particular, for $r = a$ and $z = 0$ the radial displacement is negative (for both the interface cases) while it is positive in the interface for the frictionless case and zero for the perfectly bonded case.

Figures 3 and 4 show the normal, radial and tangential stress components for $P = 2\,\mu$N; the maximum value of the normal compression stress is present on the

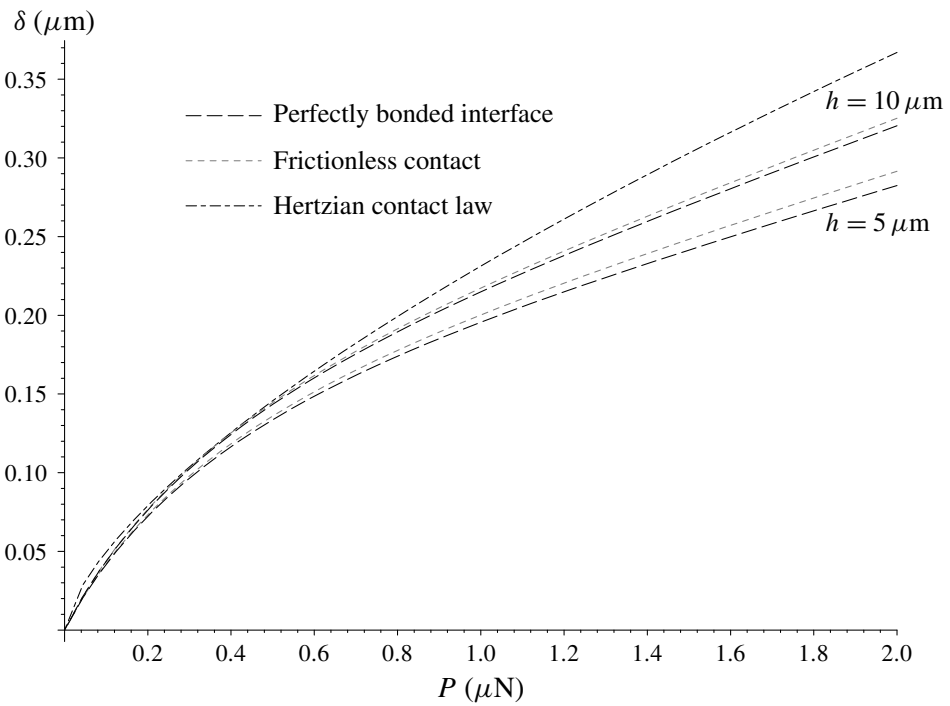

Figure 1. Contact laws for different film thicknesses.

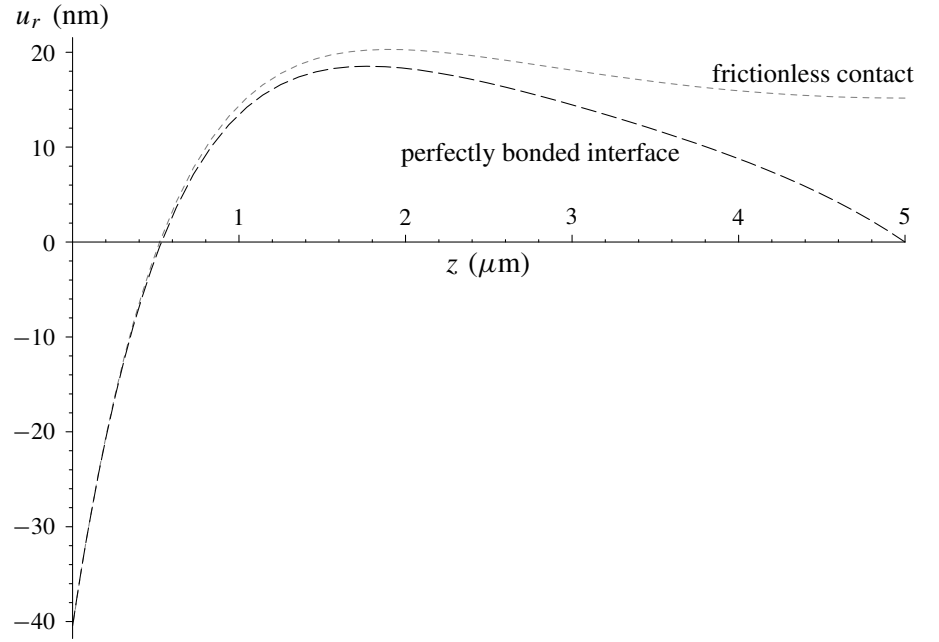

Figure 2. Radial displacement along the z-axis ($P = 2\,\mu$N, $r = a$).

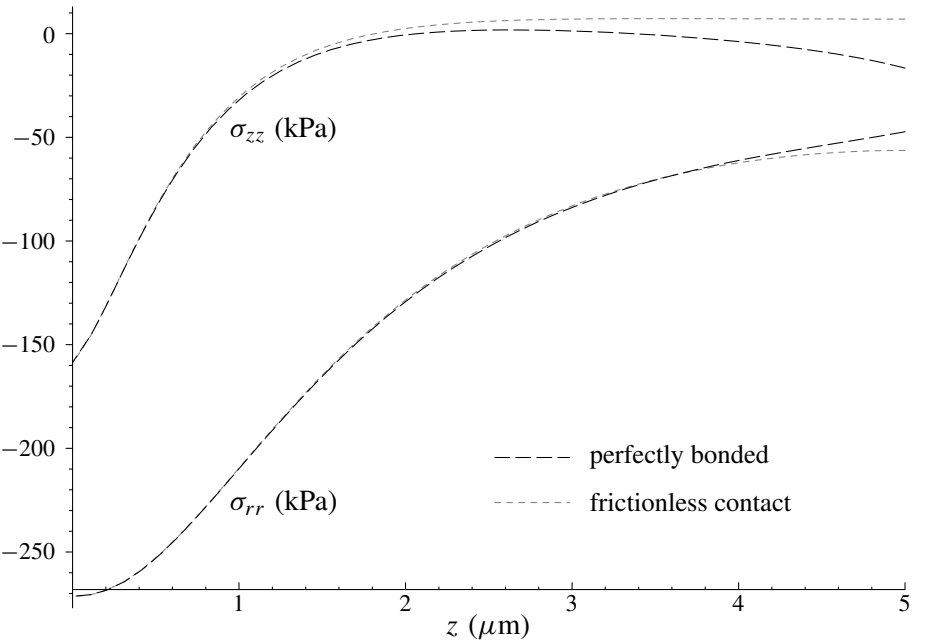

Figure 3. Radial and normal stress along the z-axis ($P = 2\,\mu$N, $r = 0$).

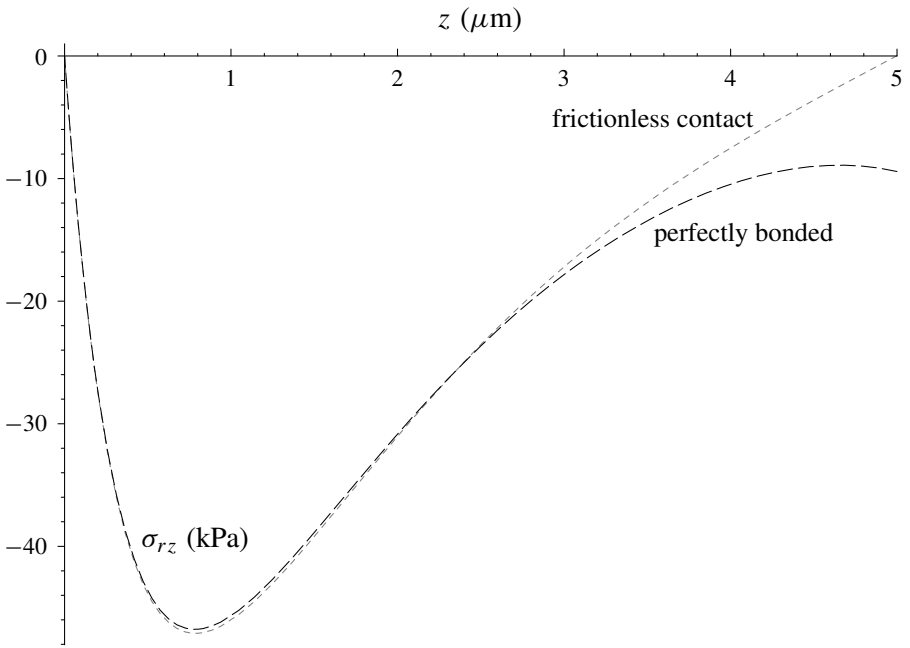

Figure 4. Shear stress along the z-axis ($P = 2\,\mu$N, $r = a$).

free surface and it is equal, for $r = 0$, to the value of load pressure distribution p_o (see Section 3.2.2). An analysis for different film thickness values shows that the component stress σ_{zz} in the interface zone increases as the thickness of the film decreases.

The second example deals with different films on an elastic substrate. We have considered thin films (oxide SiO_2 and tungsten W) coated on a silicon substrate ($E = 165$ GPa and $\nu = 0.27$) and we have compared the numerical analytical results with the experimental data obtained in Chudoba et al. [2000].

Figure 5 shows the results for the oxide film ($E = 72$ GPa and $\nu = 0.17$) with different thicknesses; the analytical model with Hertzian pressure distributions is suitable to describe the load-displacement behavior for elastic indentations with a spherical indenter for small values of the contact area radius a. In a first range, the contact law is in agreement with the elastic homogeneous half-space solution for oxide bulk material; in a second range, the contact law is different from the Hertzian contact law due to the substrate effects. Finally, for large contact area radius, the analytical results underestimate the experimental results to the order of 20%; the reason for this fact is that the present analysis is limited to the idealized static problem in which other effects encountered in indentation problems are neglected (the different pressure distribution taking into account the substrate, adhesion forces, large deformation, and dynamic effects). In this case the Hertzian

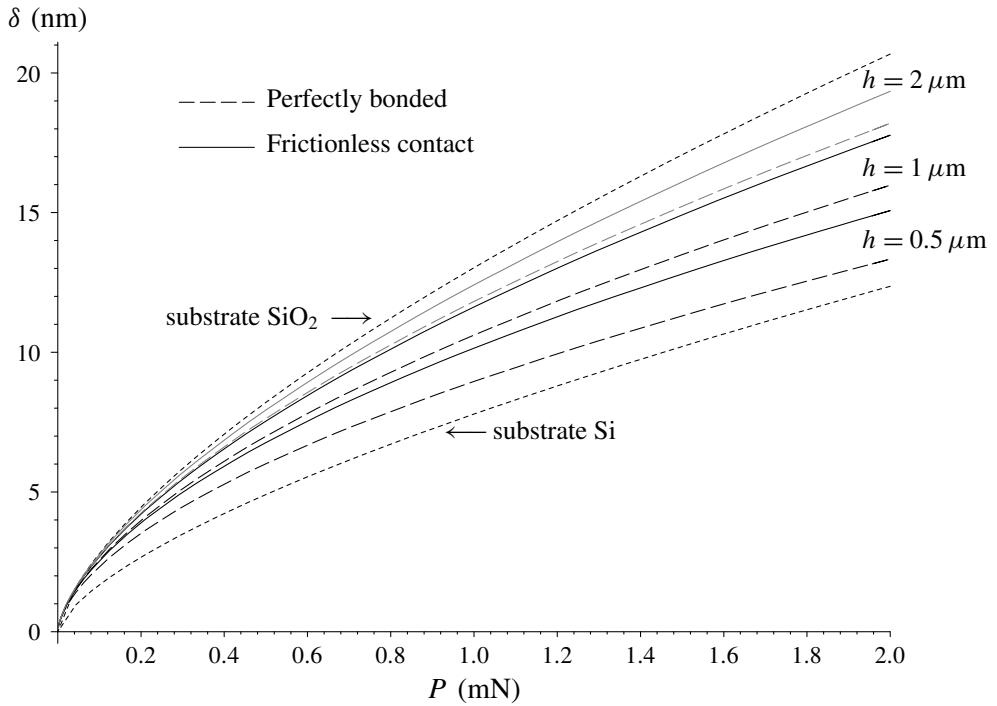

Figure 5. Contact law for SiO_2 films on Si for different interface conditions.

contact law for a half-space with the film constitutive properties overestimate the experimental results.

The results for a tungsten film ($E = 409$ GPa and $\nu = 0.28$) are shown in Figure 6; the analytical model with a Hertzian pressure is suitable to describe the load-displacement behaviour for small values of the contact area radius; for large values of a, the results obtained overestimate the experimental results since the Hertzian pressure distribution of the half-space is inaccurate to simulate the action of the indenter on the film for the soft substrate effect and a more appropriate pressure distribution needs to be assigned [Yang 2003; Chadwick 2002]. In this case the Hertzian contact law underestimates the experimental results.

More explicitly, the analytical results obtained for large a show that the Hertzian overestimation for soft films on hard substrates and the underestimation for hard films on soft substrates are significant when the indentation depth is less than one-tenth of the film thickness. This behaviour of over and underestimation by the Hertzian theory for soft and rigid films is in agreement with the results recently obtained by Wang et al. [2004], where a finite element analysis devoted to finding substrate effects at the nanoscale is presented.

Finally we remark that, for the cases discussed in this paper, we have numerically checked that, for value of b greater than $10a$, the values obtained become

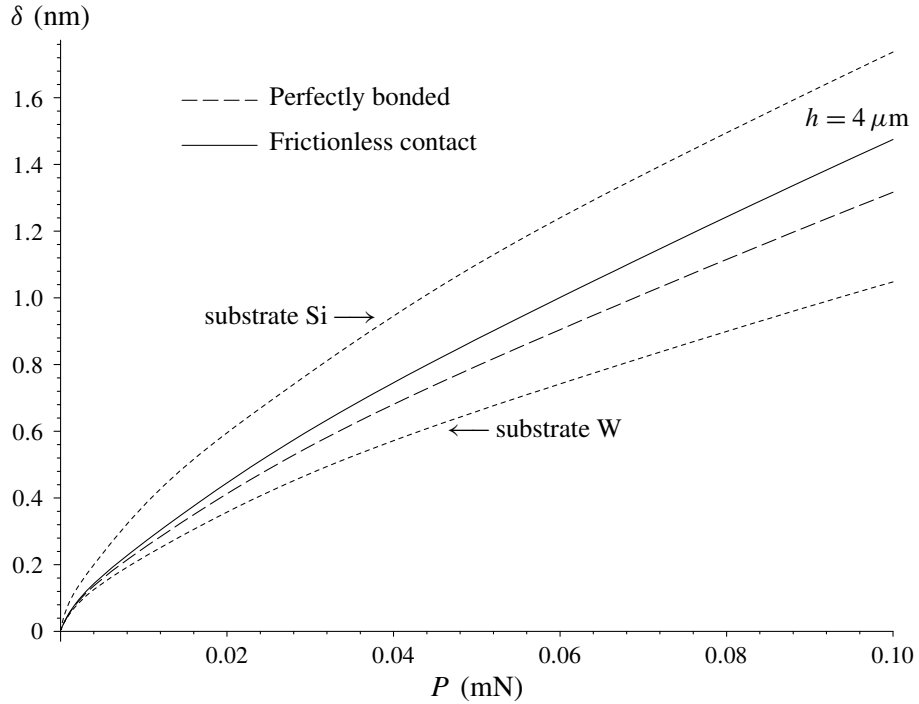

Figure 6. Contact law for tungsten film (W) on Si for different interface conditions.

numerically stable (by further increasing b) and so the specific choice assumed for b becomes irrelevant. On the other hand, assuming a large b requires considering Fourier–Bessel and Dini expansions up to very high terms, whose evaluation is unfruitful and very time-consuming. In our examples we assumed $b = 10a$ and we truncated the series when the data stabilized: typically with about 300 terms.

6. Conclusions

An elastic analysis has been performed to determine the displacement and the stress fields of thin-film coating/substrate system subjected to an axisymmetrical contact loading. The contact law presented in Section 4 approaches the half-space one when the film thickness is sufficiently large with respect to the contact area radius. If the film thickness is not large compared to the contact radius area, the response of the film is different because of the influence of the substrate. On the other hand, if the film thickness is very small compared to the contact radius, the classical pressure distribution in the half-space simulates inaccurately the action of the indenter on the film and a more appropriate pressure distribution has to be preassigned. Not only the classical pressure distributions under the indenter are

potentially inaccurate, but so are the classical relations between contact area and load.

The solutions presented in Section 3, for different indenter shapes, furnish good suggestions for the study of the effect of adhesive forces that become more relevant when the coating bodies are small or compliant in nature. Finally, we remark that it is possible to extend the analysis of [Johnson and Sridhar 2001] adhesion theory for a thin elastic film on an elastic substrate by using the solution obtained in Section 4 [Maugis 1999].

Acknowledgements

The author thanks the reviewers for their contributions and particularly for the FE analysis which has given further support to the results presented in the paper.

This work was supported by MIUR Cofin Prin 2003: *Interfacial damage failure in structural systems: applications to civil engineering and emerging research fields*; and Cofin Prin 2005: *Interfacial resistance and failure in materials and structural systems.*

References

[Chadwick 2002] R. S. Chadwick, "Axisymmetric indentation of a thin incompressible elastic layer", *SIAM J. Appl. Math.* **62**:5 (2002), 1520–1530. MR 2003d:74067

[Chudoba et al. 2000] T. Chudoba, N. Schwarzer, and F. Richter, "Determination of elastic properties of thin films by indentation measurements with a spherical indenter", *Surf. Coat. Technol.* **127**:1 (2000), 9–17.

[Field and Swain 1993] J. S. Field and M. V. Swain, "A simple predictive model for spherical indentation", *J. Mater. Res.* **8**:2 (1993), 297–306.

[Fischer-Cripps 2004] A. C. Fischer-Cripps, *Nanoindentation*, Springer, New York, 2004.

[Johnson and Sridhar 2001] K. L. Johnson and I. Sridhar, "Adhesion between a spherical indenter and an elastic solid with a compliant elastic coating", *J. Phys. D, Appl. Phys.* **34** (2001), 683–689.

[Li and Chou 1997] J. Li and T. W. Chou, "Elastic field of a thin-film/substrate system under an axysimmetric loading", *Int. J. Solids Struct.* **34**:35-36 (1997), 4463–4478.

[Matthewson 1981] M. J. Matthewson, "Axi-symmetric contact on thin compliant coatings", *J. Mech. Phys. Solids* **29**:2 (1981), 89–113.

[Maugis 1999] D. Maugis, *Contact, adhesion and rupture of elastic solids*, Springer, New York, 1999.

[Oliver and Pharr 1992] W. C. Oliver and G. M. Pharr, "An improved technique for determining hardness and elastic modulus using load and displacement sensing indentation experiments", *J. Mater. Res.* **7**:6 (1992), 1564–1583.

[Sneddon 1966] I. N. Sneddon, *Mixed boundary value problems in potential theory*, North-Holland, Amsterdam, 1966. MR 35 #6853

[VanLandingham 2003] M. R. VanLandingham, "Review of instrumented indentation", *J. Res. Natl. Inst. Stand. Technol.* **108**:4 (2003), 249–265.

[Wang et al. 2004] M. Wang, K. M. Liechti, J. M. White, and R. M. Winter, "Nanoindentation of polymeric thin films with an interfacial force microscope", *J. Mech. Phys. Solids* **52**:10 (2004), 2329–2354.

[Watson 1944] G. N. Watson, *A treatise on the theory of Bessel functions*, Cambridge University Press, Cambridge, 1944. MR 6,64a

[Yang 2003] F. Yang, "Axisymmetric indentation of an incompressible elastic thin film", *J. Phys. D, Appl. Phys.* **36**:1 (2003), 50–55.

[Yu et al. 1990] H. Y. Yu, S. C. Sanday, and B. B. Rath, "The effect of substrate on the elastic properties of films determined by the indentation test-axisymmetric Boussinesq problem", *J. Mech. Phys. Solids* **38**:6 (1990), 745–764.

Received 8 Dec 2005.

ROBERTA SBURLATI: sburlati@diseg.unige.it
Dipartimento di Ingegneria Strutturale e Geotecnica, Facoltà di Ingegneria, Università di Genova, Via Montallegro 1, I-16145 Genova, Italy
http://www.diseg.unige.it/staff/sburlati/rsburlati

JOURNAL OF MECHANICS OF MATERIALS AND STRUCTURES
Vol. 1, No. 3, 2006

MICROCRACK INITIATION AT THE TIP OF A FINITE RIGID CONDUCTING LINE IN PIEZOELECTRIC MEDIA

ZHONGMIN XIAO, HONGXIA ZHANG AND BINGJIN CHEN

In this paper is proposed a dislocation emission mechanism for microcrack initiation at the tip of a finite rigid conducting line in a piezoelectric solid. When a finite rigid conducting line is embedded in a piezoelectric matrix, because of the highly concentrated stress and electric displacement fields at its tips, dislocations of one sign are driven away from the tip, while the stationary dislocations of the opposite sign are left behind. As a result, a micro Zener–Stroh crack is initiated at each tip for the in-plane case, and two microcracks at each tip for the anti-plane case. We obtain analytical solutions of both in-plane and anti-plane extension forces for microcracks initiated at the tip of a finite rigid conducting line. By obtaining the stress and electric displacement fields at the tip under nonzero net Burgers vectors, we observe two critical crack lengths. We find that the in-plane and anti-plane critical extension forces for a finite rigid conducting line are related to those for a conventional crack in the same piezoelectric materials.

1. Introduction

Because of the intrinsic electromechanical coupling behavior, piezoelectric ceramics are used as actuators in adaptive structures. However, piezoelectric ceramics are very brittle and susceptible to fracture. The propagation of defects such as dislocations, cracks and inclusions would degenerate the performance of devices. It is important to understand the fracture behavior of piezoelectric ceramics.

There have been some efforts in establishing the fracture criterion for piezoelectric materials in the presence of cracks. The J integral, equal to the total potential energy release rate, has been proposed as a fracture criterion by; for example, Suo, Kuo, Barnett and Willis [Suo et al. 1992], while Pak [1990; 1992] used it to predict Mode III and Mode I fracture. However, so far there is no experimental support for this criterion. Park [1993; 1995] proposed using mechanical strain energy release

Keywords: Zener–Stroh crack, rigid line, mechanical strain energy release rate, stress and electric displacement (SED) intensity factors, piezoelectric material.

rate — the mechanical part of the total potential energy release rate — as the fracture criterion, and found that this criterion agrees qualitatively with the existing experimental observations.

Rigid line inclusions (or, for brevity, rigid lines) have been used to model certain materials or flat defects, such as metal precipitates in a piezoelectric solid. For the past decades, many researchers addressed rigid lines by solving the whole field solutions for various configurations; see, for example, [Wang et al. 1985, 1986; Li and Ting 1989; Ballarini 1990; Fan and Keer 1993; Asundi and Deng 1995]. Recently, rigid lines embedded in piezoelectric solids have been studied in [Shi 1997; Deng and Meguid 1998; Gao and Fan 2001]. All that the research work has identified is a square root singularity at the rigid line tip, and led to a stress intensity factor similar to that for a crack.

Based on those analyses, Xiao and Fan [1990] proposed a mechanism for Mode I microcrack initiation at the tip of a semi-infinite rigid line in a purely elastic solid. As a result, the fracture toughness for a rigid line was related to that for a crack in the same solid. Xiao et al. [2003] proposed a model of two Mode III microcrack initiations at the tip of a semi-infinite rigid line in a piezoelectric solid, and found the relation between the fracture toughness for a rigid line and that for a crack in the same solid. Here, the criteria of microcrack initiation at the tip of a finite rigid line in a piezoelectric solid, both for in-plane and anti-plane cases, are formally set, in analogy to crack propagation, as

$$G_{+}^{*} = G_{+\mathrm{cr}}^{*} \qquad \text{and} \qquad G_{-}^{*} = G_{-\mathrm{cr}}^{*}, \tag{1-1}$$

respectively, where G denotes the mechanical strain energy release rate when the rigid line extends, and is termed as "the rigid line extension force"; the superscript $*$ is used for a rigid line in order to distinguish it from the crack extension force; and the subscripts $+$ and $-$ represent in-plane and anti-plane cases, respectively. The two critical values $G_{+\mathrm{cr}}^{*}$ and $G_{-\mathrm{cr}}^{*}$ at the right-hand sides of Equations (1-1) are deemed to be material constants that can be determined from tests. Based on the authors' knowledge, however, there are no such experimental results in the open literature so far. It is our conjecture that the two critical values for a rigid line can be correspondingly related to those for a crack in the same solid, since both cases associate with the square root singularity in terms of the stress and electric displacement (SED) intensity factors.

We denote by $G_{+\mathrm{cr}}$ and $G_{-\mathrm{cr}}$ the mechanical strain energy release rates of a Mode I and Mode III crack in the same piezoelectric material, respectively. Our research objective is to search for possible relations between $G_{+\mathrm{cr}}^{*}$ and $G_{+\mathrm{cr}}$, as well as between $G_{-\mathrm{cr}}^{*}$ and $G_{-\mathrm{cr}}$; for example

$$G_{+\mathrm{cr}}^{*} = C_1\, G_{+\mathrm{cr}} \qquad \text{and} \qquad G_{-\mathrm{cr}}^{*} = C_2\, G_{-\mathrm{cr}}, \tag{1-2}$$

in which C_1 and C_2 are constants to be determined. To perform our investigation, models of microcrack initiation at a rigid line tip proposed by Xiao [1990; 2003] are extended to the current problems.

For the anti-plane case, a finite rigid conducting line is loaded around its two tips with the SED intensity fields $\mathbf{K}_-^* = \left\{K_{III}^* \quad K_{D2}^*\right\}^T$, where K_{III}^* and K_{D2}^* are the anti-plane shear stress and electric displacement intensity factors; see Figure 1.

For the in-plane case, a finite rigid conducting line of length $2a$, perpendicular to the poling axis, is loaded at the tips by the SED intensity fields $\mathbf{K}_+^* = \left\{K_{II}^* \quad K_I^* \quad K_{D1}^*\right\}^T$, where K_{II}^*, K_I^* and K_{D1}^* are the in-plane shear stress, tensile stress and electric displacement intensity factors; see Figure 2.

Based on the dislocation emission mechanism at the rigid line tip proposed in [Xiao and Fan 1990; Xiao et al. 2003], dislocations of one sign are driven away from the tip of the rigid conducting line because of the concentrated fields along certain slip planes, while the dislocations with the opposite sign pile up at the tip of the rigid conducting line. As a result, Zener–Stroh cracks are initiated at both tips, as shown in Figure 3 for the anti-plane and in Figure 4 for the in-plane case.

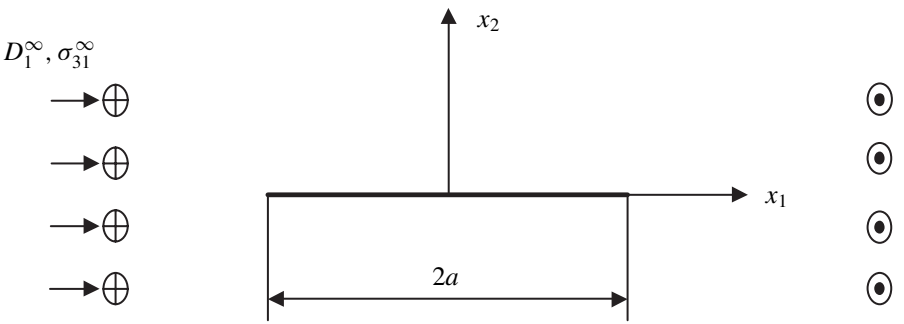

Figure 1. A finite conducting rigid line loaded around its tip with the anti-plane concentrated fields.

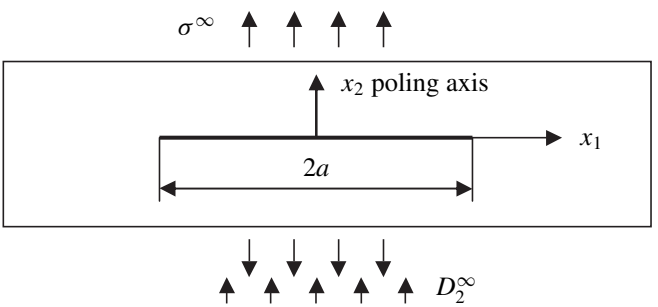

Figure 2. A finite conducting rigid line loaded around its tip with the in-plane concentrated fields.

This microcrack initiation mechanism is considered as a possible way to release the high strain energy. It is worth mentioning that this mechanism was first observed in [Kikuchi et al. 1981] and that the resulting crack was named an "anti-Zener–Stroh crack" in [Weertman 1986].

2. Formulation

2.1. ***Anti-plane case.*** In this case, because of the concentrated SED fields [Shi 1997], a pair of microcracks is initiated (see Figure 3) at both tips of the finite rigid conducting line loaded with the anti-plane SED fields $\mathbf{K}_{\text{III}}^*$ (see Figure 1). We assume that the microcracks are still loaded with the tip SED fields $\mathbf{K}_{\text{III}}^*$. The pair of microcracks at one tip has the same field variables as those at the other tip, and the deformations of the two microcracks at each tip are anti-symmetric in the x_3 direction.

Here, we will analyze only the upper-right crack. The SED distributions near the right tip are approximated by $\mathbf{K}_{\text{III}}^*/\sqrt{2\pi y}$, with $y > 0$. We will study how a microcrack of length $2c$ is affected by the tip SED fields $\mathbf{K}_{\text{III}}^*$ and by the net Burgers vectors of dislocations $\mathbf{d}_T$ inside the microcrack.

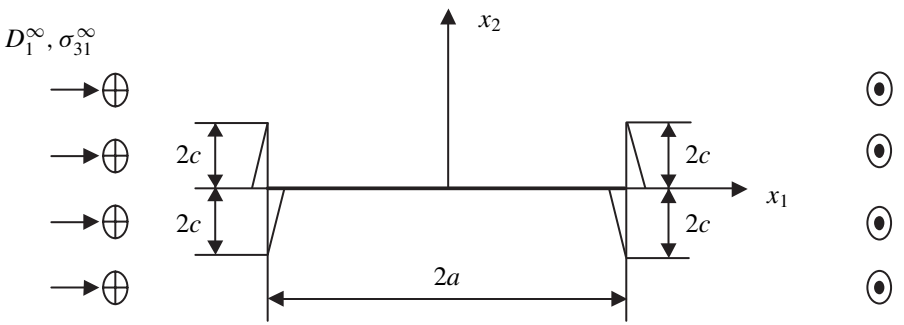

Figure 3. Microcracks initiated at the tip for the anti-plane case.

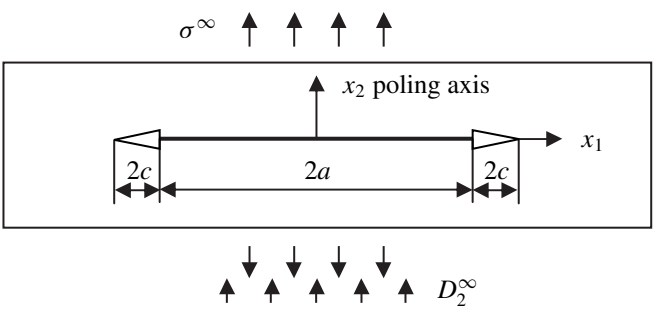

Figure 4. Microcrack initiated at the tip for the in-plane case.

The interaction between the rigid conducting line and the dislocations at both the upper and lower half-planes causes the SED fields at the upper half-plane. We first consider the two dislocations with Burgers vector $\tilde{\mathbf{d}}$, one located at the point (a, ζ) and another at $(a, -\zeta)$, $\zeta > 0$. The SED fields induced at the point (a, y), $y > 0$, by the two dislocations interacting with the rigid conducting line [Chen et al. 2005b] take the form

$$\left\{\sigma_{13}(y,\zeta) \;\; D_1(y,\zeta)\right\}^T\big|_{x=a} = \frac{1}{4\pi}\mathbf{C}\left(-\frac{1}{y-\zeta} - \frac{1}{y-\zeta}\sqrt{\frac{\zeta}{y}}\,h_1(y,\zeta,a) + h_5(y,\zeta,a)\right)\tilde{\mathbf{d}}(\zeta),$$

where $h_1(y, \zeta, a)$ and $h_5(y, \zeta, a)$ are given in Appendix B, and where the material property matrix $\mathbf{C}$ is

$$\mathbf{C} = \begin{bmatrix} c_{44} & e_{15} \\ e_{15} & -\varepsilon_{11} \end{bmatrix},$$

with c_{44}, e_{15} and ε_{11} being the elastic, piezoelectric and dielectric constants.

Because of a continuous distribution of dislocations, the SED fields along the upper-right crack line are given by

$$\left\{\sigma_{13}(a,y) \;\; D_1(a,y)\right\}^T = \frac{1}{4\pi}\mathbf{C}\int_0^{2c}\left(-\frac{1}{y-\zeta} - \frac{1}{y-\zeta}\sqrt{\frac{\zeta}{y}}\,h_1(y,\zeta,a) + h_5(y,\zeta,a)\right)\tilde{\mathbf{D}}(\zeta)\,d\zeta,$$

where the density vector of the charged screw dislocations along the crack line is $\tilde{\mathbf{D}}(\zeta) = \left\{\tilde{D}_3(\zeta) \quad \tilde{D}_4(\zeta)\right\}^T$, with $\tilde{D}_4(\zeta) = \tilde{D}_\varphi(\zeta)$.

With the assumption that the microcrack faces are free from surface traction and charge, we have

$$\left\{\sigma_{13}(a,y) \;\; D_1(a,y)\right\}^T = -\frac{\mathbf{K}_-^*}{\sqrt{2\pi y}}, \quad 0 \le y \le 2c. \tag{2-1}$$

Moreover, the charged screw dislocation densities along the crack line must satisfy

$$\int_0^{2c} \tilde{D}_i(\zeta)\,d\zeta = d_{x_i}^T, \quad i = 3, 4, \tag{2-2}$$

with the net Burgers vector inside the microcrack $\mathbf{d}_T = \left\{d_{x_3}^T \;\; d_{x_4}^T\right\}^T$ and $d_{x_4}^T = d_\varphi^T$.

Introduce the substitutions

$$u = \frac{y}{c} - 1, \qquad r = \frac{\zeta}{c} - 1.$$

Equations (2-1) and (2-2) are then rewritten as

$$\frac{1}{4\pi}\sum_{j=3}^{4} C_{(i-2)(j-2)}\int_{-1}^{1}\tilde{D}_j(r)\left(-\frac{1}{u-r}-\frac{1}{u-r}\tilde{h}_1\Big(u,r,\frac{c}{a}\Big)+\tilde{h}_5\Big(u,r,\frac{c}{a}\Big)\right)dr$$
$$=-\frac{\hat{K}_i^*}{\sqrt{2\pi c}}\frac{1}{\sqrt{u+1}},\quad -1\le u,r\le 1,\ i=3,4, \tag{2-3}$$

and

$$\int_{-1}^{1}\tilde{D}_i(r)\,dr \;=\; \frac{d_{x_i}^T}{c};\quad i=3,4, \tag{2-4}$$

where $\tilde{h}_1(u,r,c/a)$ and $\tilde{h}_5(u,r,c/a)$ are given in Appendix B, and

$$\hat{K}_3^*=K_{III}^*,\qquad \hat{K}_4^*=K_{D2}^*.$$

2.2. ***In-plane case.*** The physical problem that we examine is shown in Figure 2: a finite rigid conducting line of length $2a$, loaded with the in-plane SED fields $\mathbf{K}_+^*$ in a piezoelectric solid. As discussed in Section 1, because of the concentrated SED fields that we mentioned and were obtained by Deng and Meguid [1998], dislocations of one sign move away from the rigid line tips, and the left-behind dislocations form a microcrack at each tip, as shown in Figure 4. We assume that the microcracks are still controlled by the tip fields $\mathbf{K}_+^*$. Since the physical properties of the two microcracks are the same, we only study the one on the right. The SED distributions near the right tip are approximated by $\mathbf{K}_+^*/\sqrt{2\pi(x-a)}$, with $x>a$. We study how a microcrack of length $2c$ is affected by the tip fields $\mathbf{K}_+^*$ and the net Burgers vectors of the dislocations $\mathbf{b}_T$ inside the microcrack.

Based on [Chen et al. 2005a], the SED fields, arising along the crack line because of the interaction between a single charged edge dislocation located at the point $(2a+\xi,\ 0)$ with the Burgers vector $\tilde{\mathbf{b}}$ and with the finite rigid conducting line, are given by

$$\mathbf{II}_2(x,\xi)|_{y=0} \;=\; \frac{1}{4\pi}\frac{\tilde{\mathbf{b}}(\xi)}{x-\xi}\left(\widehat{\boldsymbol{W}}\;-\;\breve{\boldsymbol{W}}\sqrt{\frac{\xi^2-a^2}{x^2-a^2}}\right)\;-\;\frac{1}{4\pi}\frac{\breve{\boldsymbol{W}}\tilde{\mathbf{b}}(\xi)}{\sqrt{x^2-a^2}},$$

where $\mathbf{II}_2=\{\sigma_{21}\ \ \sigma_{22}\ \ D_2\}^T$. The real 3×3 matrices $\widehat{\boldsymbol{W}}$ and $\breve{\boldsymbol{W}}$ are given by

$$\widehat{\boldsymbol{W}}=\tilde{\mathbf{H}}^{-1}-\tilde{\mathbf{H}}^{-1}\tilde{\mathbf{S}}^2+\tilde{\mathbf{L}},\qquad \breve{\boldsymbol{W}}=\tilde{\mathbf{H}}^{-1}-\tilde{\mathbf{H}}^{-1}\tilde{\mathbf{S}}^2-\tilde{\mathbf{L}},$$

while the real 3×3 matrices $\tilde{\mathbf{H}}$, $\tilde{\mathbf{S}}$, $\tilde{\mathbf{L}}$ can be obtained by removing the third column and the third row of the real 4×4 matrices $\mathbf{H}$, $\mathbf{S}$, $\mathbf{L}$ (see Appendix A). Because of a continuous distribution of dislocations along the crack line, the SED fields are

given by

$$\mathbf{II}_2(x,0) \;=\; \frac{1}{4\pi}\left(\int_a^{a+2c}\frac{\tilde{\mathbf{B}}(\xi)}{x-\xi}\left(\widehat{\boldsymbol{W}}-\breve{\boldsymbol{W}}\sqrt{\frac{\xi^2-a^2}{x^2-a^2}}\right)d\xi \;-\; \int_a^{a+2c}\frac{\breve{\boldsymbol{W}}\tilde{\mathbf{B}}(\xi)}{\sqrt{x^2-a^2}}\,d\xi\right), \tag{2-5}$$

where the density vector of the charged edge dislocations along the microcrack line is $\tilde{\mathbf{B}}(\xi)=\left\{B_{x_1}(\xi)\;\; B_{x_2}(\xi)\;\; B_{\varphi}(\xi)\right\}^T$, with $B_{x_3}(\xi)=B_{\varphi}(\xi)$.

The boundary conditions on the crack faces in piezoelectric solids are assumed to be free of surface traction and charge [Deeg 1980; Pak 1990]. Therefore, one has

$$\mathbf{II}_2(x,0) \;=\; -\frac{\mathbf{K}_+^*}{\sqrt{2\pi\,(x-a)}}, \qquad a\le x\le a+2c. \tag{2-6}$$

The charged edge dislocation densities must satisfy

$$\int_a^{a+2c}\tilde{\mathbf{B}}(\xi)\,d\xi \;=\; \mathbf{b}_T, \tag{2-7}$$

where the net Burgers vector inside the crack are $\mathbf{b}_T=\left\{b_{x_1}^T\;\; b_{x_2}^T\;\; b_{\varphi}^T\right\}^T$, with $b_{x_3}^T=b_{\varphi}^T$.

The integral over $[a,\ a+2c]$ is normalized to $[-1,\ 1]$ by the substitutions

$$t=\frac{x-a}{c}-1, \qquad s=\frac{\xi-a}{c}-1.$$

Equations (2-6) and (2-7) now read

$$\sum_{i=1}^{3}\left(\widehat{W}_{mi}\int_{-1}^{1}\frac{\tilde{B}_{x_i}(s)}{t-s}\,ds - \breve{W}_{mi}\int_{-1}^{1}\frac{G_1(t,c/a)\,\tilde{B}_{x_i}(s)}{G_3(s,c/a)\,(t-s)}\,ds - \breve{W}_{mi}\int_{-1}^{1}G_1(t,c/a)\,\tilde{B}_{x_i}(s)\,ds\right)$$
$$=-\sqrt{\frac{8\pi}{c}}\,G_2(t)\,\tilde{K}_m^*, \quad -1\le s,t\le 1,\ m=1,2,3 \tag{2-8}$$

and

$$\int_{-1}^{1}\tilde{B}_{x_i}(s)\,ds \;=\; \frac{b_{x_i}^T}{c}, \quad i=1,2,3, \tag{2-9}$$

where

$$\tilde{K}_1^*=K_{II}^*, \qquad \tilde{K}_2^*=K_I^*, \qquad \tilde{K}_3^*=K_{D1}^*,$$

$$G_1(t,c/a)=\frac{1}{\sqrt{1+t}\sqrt{1+t+2a/c}},$$

$$G_2(t) = \frac{1}{\sqrt{1+t}}, \qquad G_3(s, c/a) = \frac{1}{\sqrt{1+s}\sqrt{1+s+2a/c}}.$$

3. Numerical Procedure

Let $\boldsymbol{\Psi}(s)$ and $\boldsymbol{\Xi}(r)$ be bounded functions in $[-1, 1]$, and the charged edge and screw dislocation density vectors can be written as

$$\begin{aligned} \tilde{\mathbf{B}}(s) &= \boldsymbol{\Psi}(s)\,(1+s)^{\alpha}(1-s)^{\beta}, \\ \tilde{\mathbf{D}}(r) &= \boldsymbol{\Xi}(r)\,(1+r)^{\lambda}(1-r)^{\gamma}, \end{aligned}$$

with

$$\begin{aligned} \boldsymbol{\Psi}(s) &= \left\{\Psi_1(s) \;\; \Psi_2(s) \;\; \Psi_\varphi(s)\right\}^T, \qquad \Psi_3(s) = \Psi_\varphi(s), \\ \boldsymbol{\Xi}(r) &= \left\{\Xi_3(r) \;\; \Xi_4(r)\right\}^T, \qquad \Xi_4(r) = \Xi_\varphi(r). \end{aligned}$$

3.1. ***Anti-plane case.*** The discretized forms of Equations (2-3) and (2-4) are written

$$\frac{1}{4\pi}\sum_{j=1}^{n}\tilde{W}_j(r_j)\sum_{k=3}^{4}C_{(r-2)(k-2)}\,\Xi_k(r_j)\left(-\frac{1+\tilde{h}_1(u_i, r_j, c/a)}{u_i - r_j} + \tilde{h}_5(u_i, r_j, c/a)\right)$$
$$= -\frac{\hat{K}_r^*}{\sqrt{2\pi c}}\frac{1}{\sqrt{1+u_i}}, \quad -1 \le u, r \le 1, \; r = 3, 4, \quad (3\text{-}1)$$

and

$$\sum_{j=1}^{n}\tilde{W}_j(r_j)\Xi_r(r_j) = \frac{d_{x_r}^T}{c}, \quad r = 3, 4, \quad (3\text{-}2)$$

where r_j and u_i are the roots of the Jacobi polynomials,

$$P_n^{(\lambda,\gamma)}(r_j) = 0, \qquad P_{n+\lambda+\gamma}^{(-\gamma,-\lambda)}(u_i) = 0, \quad j = 1, \ldots, n, \; i = 1, \ldots, n-1, \quad (3\text{-}3)$$

and $\tilde{W}_j(r_j)$ can be obtained from the right-hand side of Equation (3-15) by replacing s_r, α, β with r_j, λ, γ, respectively.

Equations (3-1) and (3-2) provide a system of $2n$ linear algebraic equations to solve the $2n$ unknowns $\Xi_i(r_j)$, $i = 3, 4$, $j = 1, 2, \ldots, n$. If $\Xi_i^{(1)}(r)$ and $\Xi_i^{(2)}(r)$ are the solutions of the system

$$\begin{cases} \displaystyle\sum_{j=1}^{n}\tilde{W}_j(r_j)\,\Xi_m^{(\gamma)}(r_j)\left(-\frac{1+\tilde{h}_1(u_i, r_j, c/a)}{u_i - r_j} + \tilde{h}_5(u_i, r_j, c/a)\right) = \frac{1}{\sqrt{1+u_i}}\delta_{1\gamma} \\ \displaystyle\sum_{j=1}^{n}\tilde{W}_j(r_j)\,\Xi_m^{(\gamma)}(r_j) = \delta_{2\gamma}, \qquad m = 3, 4 \end{cases}$$

we obtain

$$\Xi_3^{(1)}(r) = \Xi_4^{(1)}(r) \quad \text{and} \quad \Xi_3^{(2)}(r) = \Xi_4^{(2)}(r), \tag{3-4}$$

$$\Xi_3(r) = -\sqrt{\frac{8\pi}{c}}\,\frac{\varepsilon_{11}K_{III}^* + e_{15}K_{D2}^*}{c_{44}\varepsilon_{11} + e_{15}^2}\,\Xi_3^{(1)}(r) + \frac{d_{x_3}^T}{c}\,\Xi_3^{(2)}(r), \tag{3-5}$$

$$\Xi_4(r) = -\sqrt{\frac{8\pi}{c}}\,\frac{e_{15}K_{III}^* - c_{44}K_{D2}^*}{c_{44}\varepsilon_{11} + e_{15}^2}\,\Xi_4^{(1)}(r) + \frac{d_{\varphi}^T}{c}\,\Xi_4^{(2)}(r). \tag{3-6}$$

Since there is a square root singularity at the upper tip of the upper-right microcrack, we take $\gamma = -1/2$. As the deformations of the rigid line tip at the upper and lower half-planes are antisymmetric along the x_3 axis, we take $\lambda = -1/2$. The effect of this approximation on the upper tip is reasonably negligible [He et al. 1991].

The anti-plane SED intensity factors $\mathbf{K}_- = \{K_{III} \;\; K_{D2}\}^T$ at the upper tip of the upper-right microcrack are obtained as

$$\mathbf{K}_- = \lim_{y\to 2c^+} \sqrt{2\pi(y-2c)}\,\{\sigma_{13}(y) \;\; D_1(y)\}^T = -\sqrt{\frac{\pi c}{4}}\,\mathbf{C}\,\boldsymbol{\Xi}(1), \tag{3-7}$$

where K_{III} and K_{D2} are the anti-plane shear stress and electric displacement intensity factors. Combining (3-7) with (3-4), (3-5), and (3-6) leads to

$$K_{III} = \sqrt{2}\pi\,\Xi_3^{(1)}(1)\,K_{III}^* - \frac{\sqrt{\pi}}{2\sqrt{c}}\left(c_{44}\,\Xi_3^{(2)}(1)\,d_{x_3}^T + e_{15}\,\Xi_4^{(2)}(1)\,d_{\varphi}^T\right), \tag{3-8}$$

$$K_{D2} = \sqrt{2}\pi\,\Xi_4^{(1)}(1)\,K_{D2}^* - \frac{\sqrt{\pi}}{2\sqrt{c}}\left(e_{15}\,\Xi_3^{(2)}(1)\,d_{x_3}^T - \varepsilon_{11}\,\Xi_4^{(2)}(1)\,d_{\varphi}^T\right). \tag{3-9}$$

According to [Park and Sun 1995], the anti-plane crack extension force can be defined as

$$G_{M-} = \lim_{\delta\to 0}\frac{1}{\delta}\int_0^{\delta}\sigma_{13}(y)\,u_3(\delta - y)\,dy.$$

Thus, the anti-plane microcrack extension force is obtained, in terms of the SED intensity factors, as

$$G_{M-} = \frac{\varepsilon_{11}\left(K_{III}\right)^2 + e_{15}K_{III}K_{D2}}{2\left(c_{44}\varepsilon_{11} + e_{15}^2\right)}. \tag{3-10}$$

The anti-plane extension force for the finite rigid conducting line loaded with the SED intensity fields $\mathbf{K}_-^*$, is obtained as

$$G_{M-}^* = -\frac{\varepsilon_{11}\left(K_{III}^*\right)^2 + e_{15}K_{III}^*K_{D2}^*}{2\left(c_{44}\varepsilon_{11} + e_{15}^2\right)}. \tag{3-11}$$

Combined with (3-8), (3-9), and (3-11), Equation (3-10) is rewritten as

$$G_{M-} = -\left(\sqrt{2}\pi\,\Xi_3^{(1)}(1)\right)^2 G^*_{M-} - \frac{\pi\sqrt{\pi}}{\sqrt{2c}}\,\Xi_3^{(1)}(1)\,\Xi_3^{(2)}(1)\left(K^*_{III}d^T_{x_3} + \frac{\left(c_{44}\,d^T_{x_3} + e_{15}\,d^T_{\varphi}\right)\left(\varepsilon_{11}K^*_{III} + e_{15}K^*_{D2}\right)}{2\left(c_{44}\varepsilon_{11} + e_{15}^2\right)}\right) + \frac{\pi\left(\Xi_3^{(2)}(1)\right)^2}{8c}\left(c_{44}\left(d^T_{x_3}\right)^2 + e_{15}d^T_{x_3}d^T_{\varphi}\right). \tag{3-12}$$

Note that $\Xi_j^{(u)}(1) \approx \Xi_j^{(u)}(r_1)$ for large n. In our calculation, we took $n = 100$. It is observed from Equation (3-4) that the coefficients $\Xi_3^{(1)}(1)$, $\Xi_4^{(1)}(1)$, $\Xi_3^{(2)}(1)$ and $\Xi_4^{(2)}(1)$ depend on the ratio of the microcrack's length of $2c$ to the rigid line's length of $2a$, but are independent of the material's property constants. This makes it possible to find the constant C_2 from Equation (3-12) that exhibits the relationship among the microcrack extension force G_{M-}, the rigid line extension force G^*_{M-}, the SED intensity factors $\mathbf{K}^*_-$, the net Burgers vectors $\mathbf{d}_T$, and the microcrack length $2c$. Here are the anti-plane coefficients corresponding to the ratio $c/a = 10^{-4}$:

$$\Xi_3^{(1)}(1) = \Xi_4^{(1)}(1) = 0.117764,$$
$$\Xi_3^{(2)}(1) = \Xi_4^{(2)}(1) = 0.415922.$$

Since these coefficients depend on the ratio c/a, the constant C_2 could be a function of it.

3.2. ***In-plane case.*** Following the method in [Erdogan et al. 1973], we write the discretized forms of Equations (2-8) and (2-9) as

$$\frac{1}{4\pi}\sum_{r=1}^{n}\sum_{i=1}^{3}\tilde{W}_r(s_r)\left(\frac{\widehat{W}_{mi}}{t_u - s_r} - \frac{\breve{W}_{mi}}{t_u - s_r}\frac{G_1(t_u, c/a)}{G_3(s_r, c/a)} - \breve{W}_{mi}\,G_1(t_u, c/a)\right)\Psi_i(s_r) = -\frac{\tilde{K}^*_m}{\sqrt{2\pi c}}\,G_2(t_u), \quad -1 \le s, t \le 1, \quad m = 1, 2, 3, \tag{3-13}$$

and

$$\sum_{r=1}^{n}\tilde{W}_r(s_r)\,\Psi_i(s_r) = \frac{b^T_{x_i}}{c}, \quad i = 1, 2, 3, \tag{3-14}$$

where s_r and t_u are the roots of the Jacobi polynomials,

$$P_n^{(\alpha,\beta)}(s_r) = 0, \qquad P_{n+\alpha+\beta}^{(-\beta,-\alpha)}(t_u) = 0, \quad r = 1, \ldots, n, \quad u = 1, \ldots, n-1,$$

and

$$\tilde{W}_r(s_r) = -\frac{(2n+\alpha+\beta+2)\,\Gamma(n+\alpha+1)\,\Gamma(n+\beta+1)}{(n+1)!\,(n+\alpha+\beta+1)\,\Gamma(n+\alpha+\beta+1)}\,\frac{2^{\alpha+\beta}}{P_n'^{(\alpha,\beta)}(s_r)\,P_{n+1}^{(\alpha,\beta)}(s_r)}, \tag{3-15}$$

with $\Gamma(z)$ being the well known Gamma function.

Equations (3-13) and (3-14) provide a system of $3n$ linear algebraic equations in the $3n$ unknowns $\Psi_i(s_r)$ with $i = 1, 2, 3$ and $r = 1, 2, \ldots, n$. Denote by $\Psi_m^{(\gamma)}(s_r)$ the solutions of the set of system

$$\begin{cases} \displaystyle\sum_{r=1}^{n}\sum_{i=1}^{3}\tilde{W}_r(s_r)\left(\frac{\widehat{W}_{mi}G_1(s_r,c/a)-\breve{W}_{mi}G_1(t_u,c/a)}{(t_u-s_r)\,G_3(s_r,c/a)}-\breve{W}_{mi}\,G_1\left(t_u,\frac{c}{a}\right)\right)\Psi_i^{(\gamma)}(s_r) \\ \qquad\qquad = -G_2(t_u)\,\delta_{m\gamma} \qquad (3\text{-}16) \\ \displaystyle\sum_{r=1}^{n}\tilde{W}_r(s_r)\,\Psi_m^{(\gamma)}(s_r) = \delta_{(m+4)\gamma}, \end{cases}$$

where $m = 1, 2, 3$ and $\gamma = 1, 2, \ldots, 6$, while δ_{ij} is Kronecker's delta.

We have

$$\Psi_1(s) = \sqrt{\frac{8\pi}{c}}\,K_{II}^*\,\Psi_1^{(1)}(s) + \frac{b_{x_1}^T}{c}\,\Psi_1^{(4)}(s), \tag{3-17}$$

$$\Psi_2(s) = \sqrt{\frac{8\pi}{c}}\left(K_I^*\Psi_2^{(2)}(s)+K_{D1}^*\Psi_2^{(3)}(s)\right)+\frac{b_{x_2}^T}{c}\Psi_2^{(5)}(s)+\frac{b_{\varphi}^T}{c}\Psi_2^{(6)}(s), \tag{3-18}$$

$$\Psi_3(s) = \sqrt{\frac{8\pi}{c}}\left(K_I^*\Psi_3^{(2)}(s)+K_{D1}^*\Psi_3^{(3)}(s)\right)+\frac{b_{x_2}^T}{c}\Psi_3^{(5)}(s)+\frac{b_{\varphi}^T}{c}\Psi_3^{(6)}(s). \tag{3-19}$$

Since a square root singularity exists at the right tip of the right microcrack, we take $\beta = -1/2$. An oscillatory singularity at the left tip can be induced because of the incompatibility of the piezoelectric material and the rigid line. Since the oscillatory singularity leads to the penetration of the crack surfaces, it is physically unfeasible. Fortunately, a pure square root singularity is restored by allowing crack surfaces to have contact, as in [Comninou 1977]. Therefore we can take $\alpha = -1/2$ in our calculations. This assumption may cause some approximation at the left tip, but the effect on the right tip is negligible [He et al. 1991]. After all, the result from the right tip is responsible for the crack propagation.

The in-plane SED intensity factors at the right tip of the microcrack are

$$\mathbf{K}_+ = \left\{K_{II} \quad K_I \quad K_{D1}\right\}^T = \lim_{x\to a+2c^+}\sqrt{2\pi(x-2a-c)}\,\mathbf{II}_2(x,0), \tag{3-20}$$

where K_{II}, K_I, and K_{D1} are the in-plane shear stress, the tensile stress and the electric displacement intensity factors. Substituting (2-5) into (3-20) and following

	c_{11} GPa	c_{12} GPa	c_{13} GPa	c_{33} GPa	c_{44} GPa	e_{31} C/m^2	e_{33} C/m^2	e_{15} C/m^2	ε_{11} nC/V·m	ε_{33} nC/V·m
PZT-5H	126	55	53	117	35.3	−6.5	23.3	17	15.1	13.0
PZT-5	121	75.4	75.2	111	21.1	−5.4	15.8	12.3	8.11	7.35
PZT-4	139	77.8	74.3	115	25.6	−5.2	15.1	12.7	6.46	5.62
PZT-7A	148	76.8	74.2	131	25.4	−2.1	9.5	12.7	4.07	2.08

Table 1. Material properties for piezoelectric ceramics (the poling direction is along the x_3 axis).

the procedure in [Muskhelishvili 1977], one obtains

$$\mathbf{K}_+ = \frac{\sqrt{\pi c}}{4}(\widehat{\boldsymbol{W}} - \breve{\boldsymbol{W}})\,\boldsymbol{\Psi}(1). \tag{3-21}$$

Substituting (3-17)–(3-19) into (3-21), one finds

$$K_{II} = \sqrt{2\pi}\, f_{11}\, K_{II}^* + \frac{\sqrt{\pi}}{2\sqrt{c}}\, f_{12}\, b_{x_1}^T, \tag{3-22}$$

$$K_I = \sqrt{2\pi}\, f_{21}\, K_I^* + \sqrt{2\pi}\, f_{22}\, K_{D1}^* + \frac{\sqrt{\pi}}{2\sqrt{c}}\left(f_{23}\, b_{x_2}^T + f_{24}\, b_{\varphi}^T\right), \tag{3-23}$$

$$K_{D1} = \sqrt{2\pi}\, f_{31}\, K_I^* + \sqrt{2\pi}\, f_{32}\, K_{D1}^* + \frac{\sqrt{\pi}}{2\sqrt{c}}\left(f_{33}\, b_{x_2}^T + f_{34}\, b_{\varphi}^T\right), \tag{3-24}$$

where

$$\begin{aligned} f_{1i} &= \tilde{L}_{11}\, \Psi_1^{(i^2)}(1), \quad i = 1, 2, \\ f_{ki} &= \tilde{L}_{k2}\, \Psi_2^{(i+1)}(1) + \tilde{L}_{k3}\, \Psi_3^{(i+1)}(1), \quad k = 2, 3, \quad i = 1, 2, \\ f_{ki} &= \tilde{L}_{k2}\, \Psi_2^{(i+2)}(1) + \tilde{L}_{k3}\, \Psi_3^{(i+2)}(1), \quad k = 2, 3, \quad i = 3, 4. \end{aligned}$$

The coefficients f_{1i}, f_{2i} and f_{3i} can be determined, since $\Psi_i^{(k)}(1) \approx \Psi_i^{(k)}(s_1)$ exists for large n. Also, it is observed from Equations (3-16)–(3-19) that these coefficients depend on the ratio of the microcrack length of $2c$ to the rigid line length of $2a$. We take $n = 100$ in the following calculations, and select PZT-5H, PZT-5, PZT-4 and PZT-7A ceramics for our numerical examples, with the material constants listed in Table 1, taken from [Dunn and Taya 1994; Pak 1992].

According to [Park and Sun 1993], the crack extension force can then be calculated as the mechanical strain energy released when propagating the crack an infinitesimal distance, that is,

$$G_{M+} = \lim_{\delta \to 0} \frac{1}{\delta} \int_0^{\delta} \sigma_{2i}(x)\, u_i(\delta - x)\, dx, \quad i = 1, 2,$$

where δ is the assumed crack extension. Thus, the extension force for the microcrack, in terms of the SED intensity factors, is $G_{M+} = \frac{1}{2}(\mathbf{K}_+)^T \mathbf{L}' \mathbf{K}_+$, where the real 2×3 matrix $\mathbf{L}'$ is obtained by removing the third row of the inverse of $\tilde{\mathbf{L}}$. Substituting into this equation the values given by (3-22)–(3-24), we get

$$G_{M+} = \frac{1}{2} 2\pi^2 (\mathbf{K}_+^*)^T \mathbf{X} \mathbf{K}_+^* + \frac{\pi\sqrt{\pi}}{\sqrt{2c}} (\mathbf{K}_+^*)^T \mathbf{Y} \mathbf{b_T} + \frac{\pi}{8c} (\mathbf{b_T})^T \mathbf{Z} \mathbf{b_T}, \quad (3\text{-}25)$$

where $\mathbf{X}$, $\mathbf{Y}$ and $\mathbf{Z}$ are the 3×3 matrices from Appendix C.

The extension force for the rigid conducting line loaded with the tip SED intensity fields $\mathbf{K}_+^*$ is obtained as

$$G_{M+}^* = -\tfrac{1}{2} (\mathbf{k}^*)^{\mathbf{T}} \mathbf{H}' \mathbf{k}^*,$$

where $\mathbf{k}^* = \{k_1^* \;\; k_2^* \;\; k_3^*\}^T$ is the tip strain intensity factors and $\mathbf{K}_+^* = \tilde{\mathbf{S}}^T \tilde{\mathbf{H}}^{-1} \mathbf{k}^*$.

Equation (3-25) can be rewritten in terms of G_{M+}^* as

$$G_{M+} = -\frac{2\pi^2 \mathbf{s}^T \tilde{\mathbf{X}} \mathbf{s}}{\mathbf{H'}_{11}} G_{M+}^* + \pi^2 \mathbf{X}_{11} \left(K_{II}^*\right)^2 + \frac{\pi\sqrt{\pi}}{\sqrt{2c}} \left(\mathbf{K}_+^*\right)^T \mathbf{Y} \mathbf{b_T} + \frac{\pi}{8c} (\mathbf{b_T})^T \mathbf{Z} \mathbf{b_T}, \quad (3\text{-}26)$$

where the 2×2 matrix $\tilde{\mathbf{X}}$ is obtained by removing the first row and the first column of the matrix $\mathbf{X}$, and we have $\mathbf{s}^T = \{\hat{\mathbf{S}}_{21} \;\; \hat{\mathbf{S}}_{31}\}^T$ with $\hat{\mathbf{S}} = \tilde{\mathbf{S}}^T \tilde{\mathbf{H}}^{-1}$.

Equation (3-26) gives the relationship among the microcrack extension force G_{M+}, the rigid line extension force G_{M+}^*, the tip SED intensity factors $\mathbf{K}_+^*$, the net Burgers vectors of dislocations $\mathbf{b_T}$ inside the microcrack, and the microcrack length $2c$. The elements of $\mathbf{X}$, $\mathbf{Y}$ and $\mathbf{Z}$ for the ratio $c/a = 10^{-4}$ are listed in Table 2.

4. Discussion

4.1. *Critical crack length.*

Anti-plane case. Equation (3-12) suggests that the upper-right microcrack tends to reach its critical value at

$$G_{-\mathrm{cr}} = -\left(\sqrt{2}\pi \; \Xi_3^{(1)}(1)\right)^2 G_{M-}^* - \frac{\pi\sqrt{\pi}}{\sqrt{2c_{\mathrm{cr}}}} \Xi_3^{(1)}(1) \Xi_3^{(2)}(1) \left(K_{III}^* d_{x_3}^T + \frac{\left(c_{44} d_{x_3}^T + e_{15} d_\varphi^T\right)\left(\varepsilon_{11} K_{III}^* + e_{15} K_{D2}^*\right)}{2\left(c_{44}\varepsilon_{11} + e_{15}^2\right)} \right) + \frac{\pi \left(\Xi_3^{(2)}(1)\right)^2}{8 c_{\mathrm{cr}}} \left(c_{44} \left(d_{x_3}^T\right)^2 + e_{15} d_{x_3}^T d_\varphi^T \right). \quad (4\text{-}1)$$

	PZT-5H	PZT-5	PZT-4	PZT-7A
$\mathbf{X}_{11}$	1.448×10^{-12}	1.931×10^{-12}	1.586×10^{-12}	1.514×10^{-12}
$\mathbf{X}_{22}$	1.256×10^{-12}	1.667×10^{-12}	1.405×10^{-12}	1.352×10^{-12}
$\mathbf{X}_{23}(\mathbf{X}_{32})$	5.511×10^{-4}	9.200×10^{-4}	9.570×10^{-4}	1.145×10^{-3}
$\mathbf{X}_{33}$	2.172×10^{4}	2.313×10^{4}	3.753×10^{4}	8.592×10^{4}
$\mathbf{Y}_{11}$	0.182	0.172	0.174	0.174
$\mathbf{Y}_{22}$	0.169	0.161	0.161	0.169
$\mathbf{Y}_{23}$	2.730×10^{-11}	2.589×10^{-11}	2.189×10^{-11}	1.278×10^{-11}
$\mathbf{Y}_{32}$	6.608×10^{7}	7.593×10^{7}	9.368×10^{7}	1.287×10^{8}
$\mathbf{Y}_{33}$	0.020	0.024	0.024	0.017
$\mathbf{Z}_{11}$	2.275×10^{10}	1.540×10^{10}	1.901×10^{10}	2.006×10^{10}
$\mathbf{Z}_{22}$	2.246×10^{10}	1.516×10^{10}	1.805×10^{10}	2.078×10^{10}
$\mathbf{Z}_{23}(\mathbf{Z}_{32})$	3.955	2.747	20757	1.698
$\mathbf{Z}_{33}$	3.323×10^{-10}	2.156×10^{-10}	1.940×10^{-10}	7.054×10^{-11}

Table 2. Matrices $\mathbf{X}$, $\mathbf{Y}$ and $\mathbf{Z}$ under the ratio $c/a = 10^{-4}$.

The two critical crack lengths can be obtained from (4-1). The anti-plane tip SED fields $\mathbf{K}^*_{-}$ and the net Burgers vector $\mathbf{d_T}$ determine the two critical crack lengths.

In the absence of the electric field K^*_{D2}, of the electric displacement loading d^T_φ, and of the piezoelectric constant e_{15}, Equation (4-1) can be reduced to that for isotropic elastic media, as

$$G_{-\mathrm{cr}|\mathrm{iso}} = -\left(\sqrt{2}\pi\ \Xi_3^{(1)}(1)\right)^2 G^*_{-|\mathrm{iso}} - \frac{\pi\sqrt{\pi}\ \Xi_3^{(1)}(1)\ \Xi_3^{(2)}(1)}{\sqrt{2c_{\mathrm{cr}}}}\ K^*_{III}\ d^T_{x_3} + \frac{\pi\left(\Xi_3^{(2)}(1)\right)^2}{8c_{\mathrm{cr}}}\ \mu\left(d^T_{x_3}\right)^2, \quad (4\text{-}2)$$

where $G^*_{-|\mathrm{iso}} = -\left(K^*_{III}\right)^2/(2\mu)$.

In-plane case. Equation (3-26) suggests that the right microcrack tends to reach its critical value at

$$G_{\mathrm{cr}} = -\frac{2\pi^2\,\mathbf{s}^T\tilde{\mathbf{X}}\,s}{\mathbf{H}'_{11}}\,G^*_{M+} + \pi^2\,\mathbf{X}_{11}\left(K^*_{II}\right)^2 + \frac{\pi\sqrt{\pi}}{\sqrt{2c_{\mathrm{cr}}}}\left(\mathbf{K}^*_{+}\right)^T\mathbf{Y}\mathbf{b_T} + \frac{\pi}{8c_{\mathrm{cr}}}(\mathbf{b_T})^T\mathbf{Z}\mathbf{b_T}. \quad (4\text{-}3)$$

For a general Zener–Stroh crack, loaded with external stress and nonzero net dislocations, there are two critical crack lengths: one is stable, the other unstable [Fan 1994]. This particular physical phenomenon is also seen in Equation (4-3). The smaller critical crack length is a stable one under the Zener–Stroh mechanism.

The crack propagates until it reaches its second critical crack length, which is under the Griffith crack mechanism. Obviously, the applied SED fields $\mathbf{K}_+^*$ at the tip and the net Burgers vectors $\mathbf{b_T}$ inside the microcrack determine the two critical crack lengths.

The shear stress intensity factor K_{II}^* does not exist at the tip of the rigid line embedded in isotropic elastic materials subjected to remote loading. By using the solutions from [Wang et al. 1985; Li and Ting 1989], combined with the matrices $\mathbf{S}$, $\mathbf{L}$ and $\mathbf{H}$ for isotropic elastic materials given in [Li and Ting 1989], we can reduce (4-3) to

$$G_{+\mathrm{cr}|\mathrm{iso}} = -\big(\sqrt{2}\pi\, F_1(1)\big)^2 \frac{(1-2\upsilon)^2}{3-4\upsilon}\, G^*_{+|\mathrm{iso}} + \frac{\pi\sqrt{\pi}}{\sqrt{2c_{\mathrm{cr}}}}\, F_1(1)\, \Psi_2^{(5)}(1)\, K_I^*\, b^T_{x_2} + \frac{\pi}{8c_{\mathrm{cr}}}\, \frac{\mu}{1-\upsilon}\big(\Psi_2^{(5)}(1)\big)^2 (b^T_{x_2})^2,$$

where

$$F_1(1) = \Psi_2^{(2)}(1)\, \frac{\mu}{1-\upsilon},$$

$$G^*_{+|\mathrm{iso}} = -\,\frac{1-\upsilon}{2\mu}\, \frac{3-4\upsilon}{(1-2\upsilon)^2}\, (K_I^*)^2, \quad 1 < 3-4\upsilon < 3.$$

Here are the numerical values of $F_1(1)$ for different values of Poisson's υ, showing that effect of υ on $F_1(1)$ is quite small.

υ	$F_1(1)$	$\Psi_2^{(5)}(1)$
1/4	0.140453	0.337617
1/3	0.141730	0.328747
1/2	0.143271	0.318310

4.2. ***Connection constants.*** Consider a very brittle piezoelectric material, and assume that no dislocations are emitted from the rigid line tip and electric dislocations can be negligible, so that $b^T_{x_2} = b^T_{x_1} = b^T_{\varphi} = 0$ for the in-plane case and $d^T_{x_3} = d^T_{\varphi} = 0$ for the anti-plane case.

Anti-plane case. Equations (4-1) and (4-2) can be reduced to $G^*_{-\mathrm{cr}} = C_2\, G_{-\mathrm{cr}}$, with

$$C_2 = -\,\frac{1}{\big(\sqrt{2}\pi\, \Xi_3^{(1)}(1)\big)^2}. \tag{4-4}$$

Equation (4-4) partially confirmed our initial conjecture in the second equation in (1-2), both for brittle piezoelectric and for purely elastic materials. Since the coefficient $\Xi_3^{(1)}(1)$ is a result of the ratio c/a, the coefficient C_2 is a function of the ratio c/a. The numerical values of the coefficient C_2 for different ratio c/a are listed in Table 3. It shows that the absolute value of the coefficient C_2 decreases

with the increasing c/a, or with the microcrack propagation. It is observed that the C_2 value is almost constant when the microcrack is at the very initial stage ($c/a < 10^{-3}$). The variation of C_2 value for different ratio c/a is so small that we can consider the coefficient C_2 a constant. The C_2 value also indicated that the crack initiation will be catastrophic.

c/a	C_1	C_2
10^{-8}	−5.93064	−3.653
10^{-7}	−5.93064	−3.653
10^{-6}	−5.93064	−3.653
10^{-5}	−5.93064	−3.653
10^{-4}	−5.93064	−3.65299
$5\cdot 10^{-4}$	−5.93064	−3.65295
10^{-3}	−5.93065	−3.6529
$5\cdot 10^{-3}$	−5.93068	−3.65247
10^{-2}	−5.93073	−3.65193
$5\cdot 10^{-2}$	−5.93108	−3.64749
10^{-1}	−5.9315	−3.64158
$5\cdot 10^{-1}$	−5.93443	−3.58969
1	−5.93721	−3.56074

Table 3. The connection constants C_1 for PZT-5H and C_2.

For ductile piezoelectric solids, the net Burgers vector $\mathbf{b}_T$ inside the mixed mode microcrack and the net Burgers vector $\mathbf{d}_T$ inside the Mode III microcrack are nonzero. In this case, $G^*_{+\mathrm{cr}}$ relies on the net Burgers vectors of shear dislocations $b^T_{x_1}$, on the net Burgers vectors of climbing dislocations $b^T_{x_2}$, and on the net Burgers vectors of electric dislocations b^T_φ inside the microcrack as shown in (4-3); while $G^*_{-\mathrm{cr}}$ relies on the net Burgers vectors of shear dislocations $d^T_{x_3}$ and on the net Burgers vectors of electric dislocations d^T_φ inside the microcrack as shown in Equation (4-1). We would like to assume that $b^T_{x_1}$, $b^T_{x_2}$, b^T_φ, $d^T_{x_3}$ and d^T_φ are material-dependent constants, which measure the magnitudes of the ductility and dielectricity of the matrix material. Also, it is very likely that after a microcrack is initiated, no more dislocations enter the crack, because the concentrated stress ahead of the rigid line tip has been released. Nonetheless, all these assumptions and conjectures need experimental support before pursuing further theoretical investigations.

In-plane case. If the rigid line isn't loaded with the tip shear stress field K^*_{II}, Equation (4-3) is reduced to

$$G^*_{+\mathrm{cr}} = C_1\, G_{+\mathrm{cr}},$$

with

$$C_1 = -\frac{1}{2\pi^2}\frac{\mathbf{H}'_{11}}{\mathbf{s}^T\tilde{\mathbf{X}}\,\mathbf{s}}. \tag{4-5}$$

Equation (4-5) partially confirmed our initial conjecture in the first equation in (1-2), though only for very brittle materials under tensile stress and electric displacement fields. The numerical values of the coefficient C_1 for PZT-5H, PZT-4, PZT-5 and PZT-7A ceramics under the ratio $c/a = 10^{-4}$ are as follows:

PZT-5H	PZT-5	PZT-4	PZT-7A
5.931	17.651	12.158	10.355

The numerical values of the coefficient C_1 for PZT-5H for the ratio c/a are listed in Table 3. It is observed that, when the micro crack is at the very initial stage ($c/a < 10^{-3}$), the coefficient C_1 is constant. When the micro crack propagates further, the absolute value of the coefficient C_1 increases so slightly that we can still consider it a constant in the same solid. The C_1 value also indicates that the microcrack initiation is catastrophic.

For isotropic elastic materials, one finds

$$G^*_{+\mathrm{cr|iso}} = C_{1|\mathrm{iso}}\, G_{+\mathrm{cr|iso}},$$

in which

$$C_{1|\mathrm{iso}} = -\frac{3-4\upsilon}{\left(\sqrt{2}\pi F_1(1)\right)^2(1-2\upsilon)^2}.$$

It is worth mentioning that for the incompressible solid, $\upsilon = 0.5$, the numerical value of $C_{1|\mathrm{iso}}$ approaches infinity, which indicates that the crack initiation is catastrophic.

It is noted that microcrack initiation at other angles may occur at the rigid line tip under some mixed loadings for the anti-plane and in-plane cases. The current approach can also be employed to analyze such cases, if the rigid line extension force is calculated as the mechanical strain energy released per infinitesimal translation in the inclined direction. However, the constants C_1 and C_2 may be different and need to be further investigated for different angles.

Appendix A

In a Cartesian coordinate system (x_1, x_2, x_3), for a linear piezoelectric medium without body forces and with free charges at constant temperature, the constitutive and equilibrium equations given in [Tiersten 1969] are

$$\sigma_{ij} = c_{ijkl}\, u_{k,l} + e_{kji}\, \phi_{,k}, \qquad D_i = e_{ikl}\, u_{k,l} - \varepsilon_{ik}\, \phi_{,k}, \qquad i,j,k,l = 1,2,3, \tag{A-1}$$

$$\sigma_{ij,j} = 0, \qquad D_{i,i} = 0, \qquad i,j = 1,2,3, \tag{A-2}$$

where σ_{ij}, D_i, u_i, ϕ are the mechanical stress, electric displacement, elastic displacement and electric potential, while c_{ijkl}, e_{kij}, ε_{ij} are the elastic, piezoelectric and dielectric constants.

For a two-dimensional problem in which the variables depend on x_1, x_2 only, a general solution to Equation (A-2), given in [Barnett and Lothe 1975], is

$$\mathbf{u} = \mathbf{a} f(z), \qquad z = x_1 + p x_2. \tag{A-3}$$

Here f is an arbitrary function of z, while p and $\mathbf{a}$ are determined by inserting (A-3) into (A-2). We have

$$\left[\mathbf{Q} + p(\mathbf{R} + \mathbf{R}^T) + p^2 \mathbf{T}\right] \mathbf{a} = \mathbf{0}, \tag{A-4}$$

where the matrices $\mathbf{Q}$, $\mathbf{R}$ and $\mathbf{T}$ are

$$\mathbf{Q} = \begin{bmatrix} c_{i1k1} & e_{1i1} \\ e^T_{1k1} & -\varepsilon_{11} \end{bmatrix}, \quad \mathbf{R} = \begin{bmatrix} c_{i1k2} & e_{2i1} \\ e^T_{1k2} & -\varepsilon_{12} \end{bmatrix}, \quad \mathbf{T} = \begin{bmatrix} c_{i2k2} & e_{2i2} \\ e^T_{2k2} & -\varepsilon_{22} \end{bmatrix}.$$

The generalized stresses obtained by substituting (A-3) into (A-1) can be written in terms of the stress function $\mathbf{\Phi}$ as

$$\begin{Bmatrix} \sigma_{1j} & D_1 \end{Bmatrix}^T = -\mathbf{\Phi}_{,2}, \qquad \begin{Bmatrix} \sigma_{2j} & D_2 \end{Bmatrix}^T = -\mathbf{\Phi}_{,1},$$

in which

$$\mathbf{\Phi} = \mathbf{b} f(z), \qquad \mathbf{b} = (\mathbf{R}^T + p\mathbf{R})\,\mathbf{a} = -p^{-1}(\mathbf{Q} + p\mathbf{R})\,\mathbf{a}.$$

From (A-4) we see that eight eigenvalues p consist of four pairs of complex conjugates. If p_α, $\mathbf{a}_a$ are the eigenvalues and the associated eigenvectors, we let

$$\begin{aligned} &\mathrm{Im}(p_\alpha) > 0, \qquad p_{\alpha+4} = \bar{p}_\alpha, \\ &\mathbf{a}_{\alpha+4} = \bar{\mathbf{a}}_\alpha, \qquad \mathbf{b}_{\alpha+4} = \bar{\mathbf{b}}_\alpha, \quad \alpha = 1, 2, 3, 4, \end{aligned}$$

where Im stands for the imaginary part and the overbar denotes complex conjugation.

Assuming that p_α are distinct, the general solutions are obtained by

$$\mathbf{u} = 2\,\mathrm{Re}\left(\sum_{\alpha=1}^{4} \mathbf{a}_\alpha\, f_\alpha(z_\alpha) \right), \qquad \mathbf{\Phi} = 2\,\mathrm{Re}\left(\sum_{\alpha=1}^{4} \mathbf{b}_\alpha\, f_\alpha(z_\alpha) \right),$$

where Re stands for the real part, and

$$f_{\alpha+4} = \bar{f}_\alpha.$$

The 4×4 complex matrices $\mathbf{A}$ and $\mathbf{B}$ defined by

$$\mathbf{A} = \begin{bmatrix} \mathbf{a}_1 & \mathbf{a}_2 & \mathbf{a}_3 & \mathbf{a}_4 \end{bmatrix}, \qquad \mathbf{B} = \begin{bmatrix} \mathbf{b}_1 & \mathbf{b}_2 & \mathbf{b}_3 & \mathbf{b}_4 \end{bmatrix},$$

satisfy, when properly normalized, the orthogonality relation

$$\begin{bmatrix} \mathbf{B}^T & \mathbf{A}^T \\ \bar{\mathbf{B}}^T & \bar{\mathbf{A}}^T \end{bmatrix} \begin{bmatrix} \mathbf{A} & \bar{\mathbf{A}} \\ \mathbf{B} & \bar{\mathbf{B}} \end{bmatrix} = \begin{bmatrix} \mathbf{I} & \mathbf{O} \\ \mathbf{O} & \mathbf{I} \end{bmatrix}.$$

The matrices $\mathbf{H}$, $\mathbf{L}$ and $\mathbf{S}$ defined by

$$\begin{aligned} \mathbf{H} &= i2\,\mathbf{A}\mathbf{A}^T, \\ \mathbf{L} &= i2\,\mathbf{B}\mathbf{B}^T, \\ \mathbf{S} &= i\left(\mathbf{A}\mathbf{B}^T - \mathbf{I}\right) \end{aligned}$$

can be shown to be real. The matrices $\mathbf{H}$ and $\mathbf{L}$ are symmetric.

Appendix B

$$h_1(y,\zeta,a) = \sqrt{\frac{1}{y^2+4a^2}}\sqrt{\frac{\zeta y+4a^2}{2} + \frac{1}{2}P(y,\zeta,a)}$$

$$h_2(y,\zeta,a) = -\sqrt{\frac{1}{y^2+4a^2}}\sqrt{\frac{\zeta y-4a^2}{2} + \frac{1}{2}P(y,\zeta,a)}$$

$$h_3(y,\zeta,a) = \sqrt{\frac{\zeta}{y+\zeta}}\sqrt{\frac{1}{(y+\zeta)^2+4a^2}}\cdot\sqrt{\frac{\zeta(y+\zeta)+4a^2}{2} + \frac{1}{2}Q(y,\zeta,a)}$$

$$h_4(y,\zeta,a) = -\sqrt{\frac{\zeta}{y+\zeta}}\sqrt{\frac{1}{(y+\zeta)^2+4a^2}}\cdot\sqrt{\frac{\zeta(y+\zeta)-4a^2}{2} + \frac{1}{2}Q(y,\zeta,a)}$$

$$P(y,\zeta,a) = \sqrt{16a^4 + \zeta^2y^2 + 4a^2(y^2+\zeta^2)}$$

$$Q(y,\zeta,a) = \sqrt{16a^4 + \zeta^2(y+\zeta)^2 + 4a^2(y^2+2\zeta^2+2y\zeta)}$$

$$h_5(y,\zeta,a) = -\frac{1}{y}(1 - h_3(y,\zeta,a)) - \frac{1}{y+\zeta}\left(1 - \sqrt{\frac{\zeta}{y}}h_2(y,\zeta,a)\right) - \frac{1}{y+2\zeta}\left(1 + h_4(y,\zeta,a)\right)$$

$$\tilde{h}_1(u,r,c/a) = \sqrt{\frac{r+1}{u+1}}\,h_1(u+1,\,r+1,\,a/c)$$

$$\tilde{h}_5(u,r,c/a) = \frac{1}{c}\,h_5(u+1,\,r+1,\,a/c).$$

Appendix C

$$
\begin{aligned}
\mathbf{X}_{11} &= \mathbf{L}'_{11}(f_{11})^2 \\
\mathbf{X}_{22} &= \mathbf{L}'_{22}(f_{21})^2 + \mathbf{L}'_{23}\, f_{21}\, f_{31} \\
\mathbf{X}_{23} &= \mathbf{X}_{32} = \mathbf{L}'_{22}\, f_{21}\, f_{22} + \tfrac{1}{2}\mathbf{L}'_{23}\big(f_{22}\, f_{31} + f_{21}\, f_{32}\big) \\
\mathbf{X}_{33} &= \mathbf{L}'_{22}(f_{22})^2 + \mathbf{L}'_{23}\, f_{22}\, f_{32} \\
\mathbf{Y}_{11} &= \mathbf{L}'_{11}\, f_{11}\, f_{12} \\
\mathbf{Y}_{22} &= \mathbf{L}'_{22}\, f_{21}\, f_{23} + \tfrac{1}{2}\mathbf{L}'_{23}\big(f_{21}\, f_{33} + f_{31}\, f_{23}\big) \\
\mathbf{Y}_{23} &= \mathbf{L}'_{22} f_{21} f_{24} + \tfrac{1}{2}\mathbf{L}'_{23}\big(f_{21}\, f_{34} + f_{31}\, f_{24}\big) \\
\mathbf{Y}_{32} &= \mathbf{L}'_{22}\, f_{22}\, f_{23} + \tfrac{1}{2}\mathbf{L}'_{23}\big(f_{22}\, f_{33} + f_{32}\, f_{23}\big) \\
\mathbf{Y}_{33} &= \mathbf{L}'_{22} f_{22} f_{24} + \tfrac{1}{2}\mathbf{L}'_{23}\big(f_{22}\, f_{34} + f_{32}\, f_{24}\big) \\
\mathbf{Z}_{11} &= \mathbf{L}'_{11}(f_{12})^2 \\
\mathbf{Z}_{22} &= \mathbf{L}'_{22}(f_{23})^2 + \mathbf{L}'_{23}\, f_{23}\, f_{33} \\
\mathbf{Z}_{23} &= \mathbf{Z}_{32} = \mathbf{L}'_{22}\, f_{23}\, f_{24} + \tfrac{1}{2}\mathbf{L}'_{23}\big(f_{23}\, f_{34} + f_{24}\, f_{33}\big) \\
\mathbf{Z}_{33} &= \mathbf{L}'_{22}(f_{24})^2 + \big(\tilde{\mathbf{L}}^{-1}\big)_{33}(f_{34})^2 + \mathbf{L}'_{23}\, f_{24}\, f_{34}.
\end{aligned}
$$

References

[Asundi and Deng 1995] A. Asundi and W. Deng, "Rigid inclusions on the interface between two bonded anisotropic media", *J. Mech. Phys. Solids* **43**:7 (1995), 1045–1058.

[Ballarini 1990] R. Ballarini, "A rigid line inclusion at a bimaterial interface", *Eng. Fract. Mech.* **37**:1 (1990), 1–5.

[Barnett and Lothe 1975] D. M. Barnett and J. Lothe, "Dislocations and line charges in anisotropic piezoelectric insulators", *Phys. Status Solidi B* **67**:1 (1975), 105–111.

[Chen et al. 2005a] B. J. Chen, D. W. Shu, and Z. M. Xiao, "Dislocation interacting with collinear rigid lines in piezoelectric media", 2005. Submitted to JoMMS.

[Chen et al. 2005b] B. J. Chen, D. W. Shu, and Z. M. Xiao, "Electro-elastic interaction between a piezoelectric screw dislocation and collinear rigid lines", *Int. J. Eng. Sci.* **44**:7 (2005), 422–435.

[Comninou 1977] M. Comninou, "The interface crack", *J. Appl. Mech.* (*ASME*) **44**:4 (1977), 631–636.

[Deeg 1980] W. F. Deeg, *The analysis of dislocation, crack, and inclusion problems in piezoelectric solids*, Ph.D. thesis, Stanford University, 1980.

[Deng and Meguid 1998] W. Deng and S. A. Meguid, "Analysis of conducting rigid inclusion at the interface of two dissimilar piezoelectric materials", *J. Appl. Mech.* (*ASME*) **65**:1 (1998), 76–84.

[Dunn and Taya 1994] M. L. Dunn and M. Taya, "Electroelastic field concentrations in and around inhomogeneities in piezoelectric solids", *J. Appl. Mech.* (*ASME*) **61**:2 (1994), 474–475.

[Erdogan et al. 1973] F. Erdogan, G. D. Gupta, and T. S. Cook, "Numerical solution of singular integral equations", pp. 368–425 in *Methods of Analysis and Solutions of Crack Problems*, edited by G. C. Sih, Noordhoff, Leyden, 1973.

[Fan 1994] H. Fan, "Interfacial Zener-Stroh crack", *J. Appl. Mech.* (*ASME*) **61**:4 (1994), 829–834.

[Fan and Keer 1993] H. Fan and L. M. Keer, "Two-dimensional line defects in anisotropic elastic solids", *Int. J. Fract.* **62**:1 (1993), 25–42.

[Gao and Fan 2001] C. F. Gao and W. X. Fan, "An interface inclusion between two dissimilar piezoelectric materials", *Appl. Math. Mech.* **22**:1 (2001), 96–104. English edition.

[He et al. 1991] M. Y. He, A. Bartlett, and A. G. Evans, "Kinking of a crack out of an interface: Role of in-plane stress", *J. Am. Ceram. Soc.* **74**:4 (1991), 767–771.

[Kikuchi et al. 1981] M. Kikuchi, K. Shiozawa, and J. Weertman, "Void nucleation in astroloy: Theory and experiments", *Acta Metall.* **29**:10 (1981), 1747–1758.

[Li and Ting 1989] Q. Li and T. C. T. Ting, "Line inclusions in anisotropic elastic solids", *J. Appl. Mech.* (*ASME*) **56**:3 (1989), 556–563.

[Muskhelishvili 1977] N. I. Muskhelishvili, *Some basic problems of the mathematical theory of elasticity*, Noordhoff, Leyden, 1977.

[Pak 1990] Y. E. Pak, "Crack extension force in a piezoelectric material", *J. Appl. Mech.* (*ASME*) **57**:3 (1990), 647–653.

[Pak 1992] Y. E. Pak, "Linear electro-elastic fracture mechanics of piezoelectric materials", *Int. J. Fract.* **54**:1 (1992), 79–100.

[Park and Sun 1993] S. B. Park and C. T. Sun, "Effect of electric field on fracture of piezoelectric ceramics", *Int. J. Fract.* **70**:3 (1993), 203–216.

[Park and Sun 1995] S. B. Park and C. T. Sun, "Fracture criteria for piezoelectric ceramics", *J. Am. Ceram. Soc.* **78**:6 (1995), 1475–1480.

[Shi 1997] W. C. Shi, "Rigid line inclusions under anti-plane deformation and in-plane electric field in piezoelectric materials", *Eng. Fract. Mech.* **56**:2 (1997), 265–274.

[Suo et al. 1992] Z. Suo, C. M. Kuo, D. M. Barnett, and J. R. Willis, "Fracture mechanics for piezoelectric ceramics", *J. Mech. Phys. Solids* **40**:4 (1992), 739–765.

[Tieresten 1969] H. F. Tieresten, *Linear piezoelectric plate vibration*, Plenum, New York, 1969.

[Wang et al. 1985] Z. Y. Wang, H. T. Zhang, and Y. T. Chou, "Characteristics of the elastic field of a rigid line inhomogeneity", *J. Appl. Mech.* (*ASME*) **52**:4 (1985), 818–822.

[Wang et al. 1986] Z. Y. Wang, H. T. Zhang, and Y. T. Chou, "Stress singularity at the tip of a rigid line inhomogeneity under antiplane shear loading", *J. Appl. Mech.* (*ASME*) **53**:2 (1986), 459–461.

[Weertman 1986] J. Weertman, "Zener-Stroh crack, Zener-Hollomon parameter, and other topics", *J. Appl. Phys.* **60**:6 (1986), 1877–1887.

[Xiao and Fan 1990] Z. M. Xiao and H. Fan, "Microcrack initiation at tip of a rigid line inhomogeneity", *Int. J. Fract.* **82**:1 (1990), 1–9.

[Xiao et al. 2003] Z. M. Xiao, Y. Dai, and B. J. Chen, "Micro-crack initiation at tip of a rigid line inhomogeneity in piezoelectric materials", *Int. J. Eng. Sci.* **41**:2 (2003), 137–147.

Received 8 Dec 2005.

ZHONGMIN XIAO: mzxiao@ntu.edu.sg
School of Mechanical & Aerospace Engineering, Nanyang Technological University, Nanyang Avenue, Singapore 639798

HONGXIA ZHANG: zh0001ia@ntu.edu.sg
School of Mechanical & Aerospace Engineering, Nanyang Technological University, Nanyang Avenue, Singapore 639798

BINGJIN CHEN: mbjchen@ntu.edu.sg
School of Mechanical & Aerospace Engineering, Nanyang Technological University, Nanyang Avenue, Singapore 639798

JOURNAL OF MECHANICS OF MATERIALS AND STRUCTURES
Vol. 1, No. 3, 2006

QUASI-STATIC PUNCH INDENTATION OF A HONEYCOMB SANDWICH PLATE: EXPERIMENTS AND MODELLING

DIRK MOHR, ZHENYU XUE AND ASHKAN VAZIRI

Punching experiments on wide honeycomb sandwich beams were performed to evaluate the predictive capabilities of a newly developed constitutive model in structural applications. The employed constitutive model for plastically compressible orthotropic materials accounts for both non-uniform hardening and softening associated with stressing in different directions. This feature is vital when assessing the structural performance of metal sandwich plates with low density cellular cores. Pure shear and uniaxial compression tests have been carried out to identify the input stress-strain data for the constitutive model. The sandwich beam has been modeled with shell/beam elements for the face sheets and only one continuum element through-the-thickness for the honeycomb core material. Comparison of the numerical results with experimental observations validates the capability of the proposed approach based on continuum modeling of the core in capturing the main features of sandwich beam response under punch loading.

1. Introduction

Metallic sandwich structures have been used for decades in lightweight aerospace vehicles due to their high flexural stiffness-to-weight ratio. More recently, sandwich constructions are also considered in naval architecture. The general idea is to enhance the structural performance of ships under high intensity pressure loading through the use of outer hulls made in sandwich construction. Hutchinson and Xue [2005] have demonstrated that optimized all-metal sandwich plates may have distinct structural advantages over comparable weight monolithic plates under high intensity pulse. The virtual design of large-scale sandwich structures requires reliable computational models capable of predicting the mechanical response of sandwich structures for a wide spectrum of loading scenarios and geometries. The core layer of all-metal sandwich structures may consist of either random or periodic shell, plate and beam assemblies. Prominent examples are metallic foams,

Keywords: sandwich structures, finite element modeling, constitutive modeling, metallic honeycomb, plasticity.

honeycombs and truss lattice structures [Gibson and Ashby 1997]. Using state-of-the art finite element software, the exact geometry of both the core layer and the face sheets may be modeled in detail and estimates of the overall structural behavior may be obtained with great accuracy [Mohr and Doyoyo 2004a; Xue and Hutchinson 2004a; Vaziri et al. 2006]. However, it is recognized that the computational costs associated with detailed models comprised of millions of finite elements are too high for use in an industrial environment. As an alternative to detailed modeling, various researchers have dealt with the development of constitutive models which describe the so-called macroscopic behavior of the sandwich core layer [Deshpande and Fleck 2000; Mohr and Doyoyo 2004c; Xue and Hutchinson 2004b; Rabczuk et al. 2004; Xue et al. 2005; Mohr 2005; Zok et al. 2005]. In other words, the discrete core layer structure is considered as a homogenous solid which allows for its discretization with solid elements, thereby drastically reducing the computational costs of simulating the response of large scale sandwich structures.

We emphasize here that this macroscopic modeling approach is of great value for practical engineers, even though it may not be satisfactory from a mathematical point of view. With respect to rigorous homogenization (for example, [Ponte Castañeda and Suquet 1998]), there are two important conditions which are frequently violated when developing macroscopic constitutive models for sandwich core materials. First, the condition of separation of length scales is seldom satisfied. This may lead to scale effects due to the dominance of boundary effects. Furthermore, the constitutive model predictions will be poor under the presence of large macroscopic stress and strain gradients. Second, the deformation in conventional sandwich core materials usually localizes at the macroscopic length scale when subject to compression (crushing), which rules out the applicability of established homogenization procedures.

The aim of this work is to assess the accuracy of a newly developed macroscopic model [Xue et al. 2005] in predicting the response of a wide honeycomb sandwich beam subject to punch loading. The model by Xue et al. [2005] invokes an ellipsoidal anisotropic yield surface in the six-dimensional stress space, an associated flow rule and a fully-coupled differential hardening/softening model. This specific model has been chosen since it can also account for strain-rate dependency, an important feature which is expected to become relevant in future studies on the blast resistance of sandwich structures. Here, we will evaluate the model performance for quasi-static loading. The experimental results of Mohr and Doyoyo [2004b], Wang and McDowell [2005] and Hong et al. [2006] have shown that the initial out-of-plane yield surface of honeycombs is of elliptical shape (Figure 1). This important feature has been incorporated into the constitutive model of Xue et al. [2005], thereby improving the poor performance of frequently used heuristic constitutive

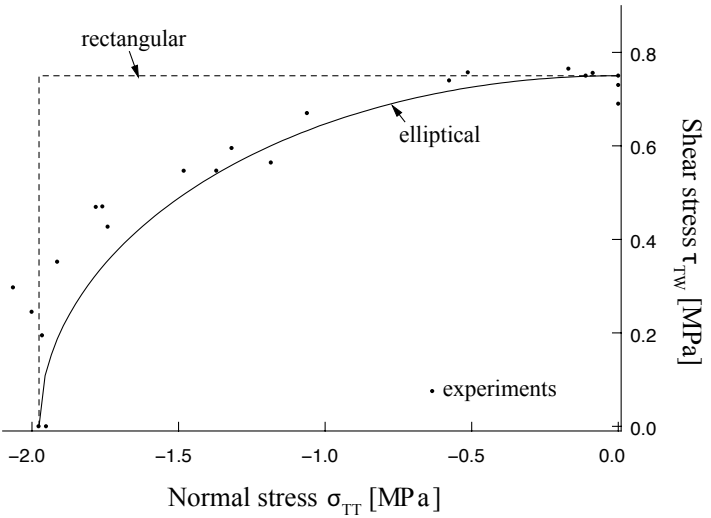

Figure 1. Initial yield surface of a metallic honeycomb core under combined compression and out-of-plane shear (σ_{TT},τ_{TW}). The open dots represent experimental data points [Mohr and Doyoyo 2004b]. The solid line corresponds to the prediction from the ellipsoidal surface invoked in the present constitutive model of [Xue et al. 2005] when all the plastic Poisson ratios are zero. The dashed curve presents the 'rectangular yield surface' of the heuristic honeycomb models in LS-DYNA [LSTC 2000] and PamCrash [ESI 1999].

models for honeycombs [LSTC 2000; ESI 1999]. Observe from Figure 1 that the elliptical yield surface closely follows the experimental points while simple uncoupled models cannot represent the interaction of shear and normal stresses.

In this work, wide sandwich beams with hexagonal aluminum honeycomb core have been manufactured and subjected to punch loading. A newly developed two-actuator system is used to perform pure shear tests on a 1.8% relative density aluminum honeycomb in order to identify the associated input stress-strain data. Subsequently, the constitutive model of Xue et al. [2005] is calibrated and used to simulate the punch tests. From the comparison of experiments and simulations, we find that this computationally-efficient macroscopic model provides accurate predictions of the overall response for a rather complex loading scenario which includes both local and global deformation.

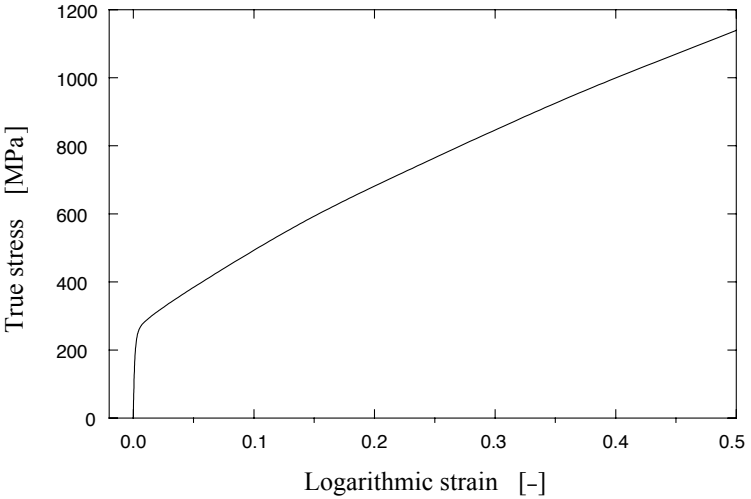

Figure 2. True stress versus logarithmic strain curve for the stainless steel 304 face sheets as obtained from uniaxial tensile testing of flat dogbone specimens.

2. Material

A custom-made sandwich material is used in this study. It is composed of an aluminum honeycomb core which is adhesively bonded to stainless steel face sheets. This lightweight core layer is $C = 15.9$ mm thick and contributes about 20% to the mass of the sandwich cross-section. The face sheets on the other hand have the thickness of $t_f = 0.2$ mm, which makes up for the remaining 80% of the cross-sectional mass. The weight contribution of the 0.1 mm thick adhesive layers (Lord 310A/B, Lord Corporation, Cary, NC) may be neglected.

2.1. ***Mechanical properties of the face sheets.*** The mechanical behavior of the stainless steel face sheets (Type 304, AlvestaPolarit, Sweden) has been determined from standard uniaxial tensile tests on dogbone-shaped specimens. The measured stress-strain curve, in terms of true stresses and logarithmic plastic strains, is shown in Figure 2. The face sheet material has the Young's modulus of $E = 200$ GPa and the initial yield strength of about $\sigma_f = 250$ MPa; it exhibits a pronounced strain hardening before the specimens fail at a strain of about $\varepsilon_f = 0.5$.

2.2. ***Honeycomb core.*** The honeycomb core material manufactured by Hexcel (Dublin, CA) is made from $t = 34\mu m$ thick aluminum 5056 foil; the single- and double-thickness cell walls of the hexagonal cells are respectively about $l = 3.1$ mm

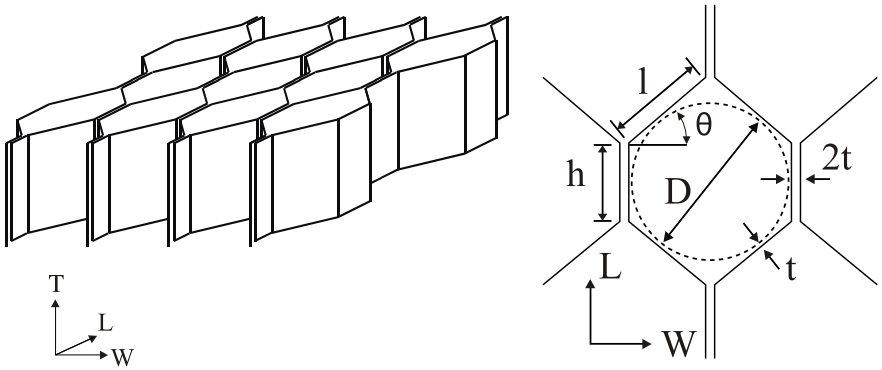

(a)

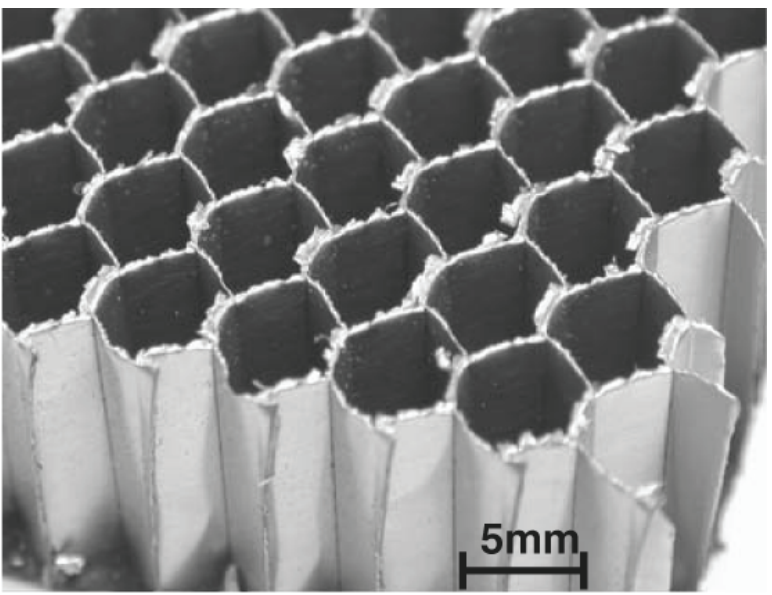

(b)

Figure 3. (a) Schematic of the hexagonal honeycomb core geometry; (b) photograph of the 1.8% relative density aluminum honeycomb.

in-plane			out-of-plane		
E_{WW}	E_{LL}	G_{WL}	E_{TT}	G_{TW}	G_{TL}
[MPa]	[MPa]	[MPa]	[MPa]	[MPa]	[MPa]
0.11	0.27	0.02	1252.76	155.77	315.19

Table 1. Elastic constants of the 1.8% relative density hexagonal honeycomb.

and $h = 2.4$ mm wide (Figure 3). The relative core density $\rho^\star$ of the honeycomb core can be obtained from

$$\rho^\star = \frac{1 + \frac{h}{l}}{\cos\theta(\sin\theta + \frac{h}{l})}, \tag{1}$$

where θ is the cell wall opening angle, Figure 3 (a). This leads to the core density of $\rho^\star \cong 1.8\%$ for the honeycomb core material study ($\theta = 40°$). Table 1 summarizes the corresponding elastic constants of the honeycomb core. These have been evaluated from the classical formulas summarized in the textbook by Gibson and Ashby [1997] for a base material of $E_s = 72$ GPa. We note that the core material is highly orthotropic with a very small stiffness and strength in the WL-plane, where W and L denote the so-called in-plane directions of the honeycomb microstructure as shown in Figure 3. Conversely, the material is strong in the T-direction. Figure 4 shows a representative macroscopic stress-strain curve as obtained from uniaxial compression tests in the T-direction [Mohr and Doyoyo 2004b]. It is a well known characteristic of metallic honeycombs that the response curve for out-of-plane loading exhibits an initial peak stress which is significantly higher than the stress level in the so-called crushing regime. Densification starts at a logarithmic strain of about $\varepsilon^d_{TT} \cong -1.0$. In addition to the uniaxial compression tests, we designed a new experiment to determine the material response under pure shear loading in the WT-plane, which will be described in the following section.

3. Pure shear experiments

Sandwich structures are designed such that face sheets carry the bending and in-plane loads. The core layer on the other hand must sustain the shear loads. The shear lap test proposed in ASTM C273 may be suitable to determine the elastic shear modulus and the strength of brittle honeycombs, but it yields inconclusive results in the large deformation regime of low-density metallic honeycombs. This is due to the localization of deformation within the honeycomb microstructure which may cause the rotation of the grip plates. Consequently, the macroscopic strain field becomes non-uniform as well. Doyoyo and Mohr [2003] proposed a modified Arcan apparatus to overcome this problem, but their equipment has been limited to

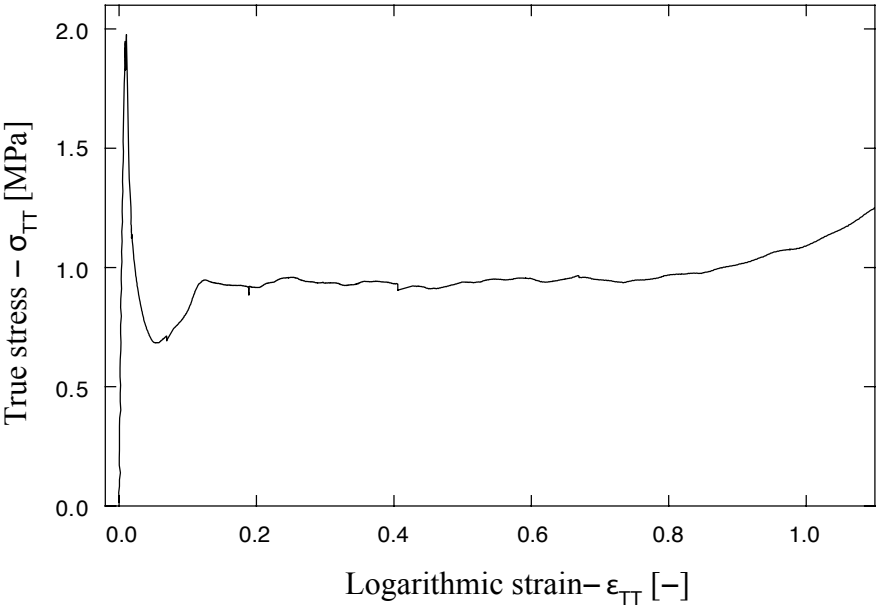

Figure 4. Experimental true stress-logarithmic strain relationships for the hexagonal aluminum honeycomb core under uniaxial compression along the *T*-direction.

relatively small butterfly specimens. Here, we make use of a hydraulic two-actuator system (custom made by Instron, Canton, MA) to characterize the macroscopic stress-strain curve for pure shear loading in the *T W*-plane. (Here, the term 'pure shear' is used to emphasize that the stress state is free from normal stresses which would be present in the case of 'simple shear'.)

3.1. ***Experimental procedure.*** Figures 5 (a) and 5 (b) display a schematic and a photograph of the experimental setup, respectively. The specimen (part 8 as labeled in Figure 5 (b) is composed of a 17 mm thick honeycomb core layer sandwiched between two 8 mm thick aluminum plates. A relatively thick adhesive layer is applied which imposes locally clamped boundary conditions on the honeycomb cell walls. This sandwich specimen is clamped between two nonrotating grip plates (parts 6 and 7). The top grip plate (part 7) is rigidly connected to the vertical actuator (part 1), which can only move along the vertical direction. The bottom grip plate (part 6) is attached to the horizontal actuator system (part 4). The same grip is mounted on a low friction slide table (part 5), which allows for the horizontal motion while preventing rotations. Since the rotation of both the top and the bottom

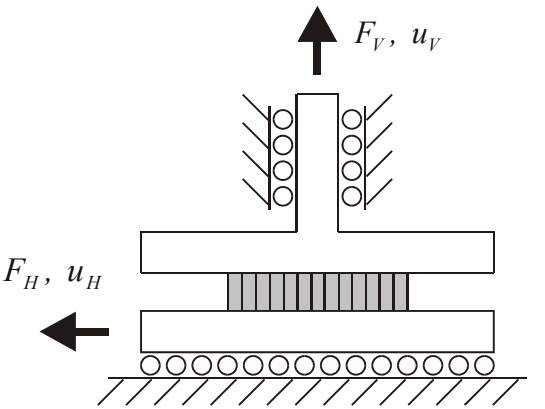

(a)

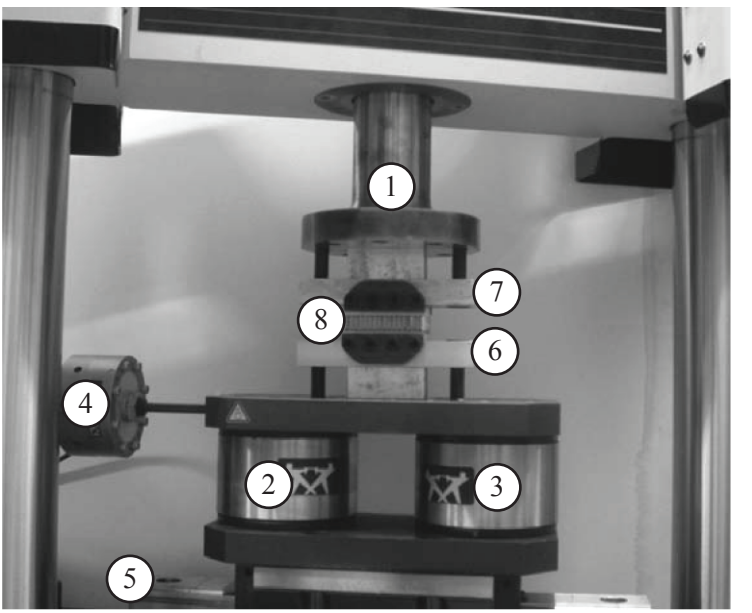

(b)

Figure 5. The experimental setup used for pure shear testing. (a) Schematic of the mechanical system. (b) Photograph of the biaxial testing system: (1) piston of the vertical actuator; (2) and (3) vertical load cells; (4) horizontal piston with load cell; (5) low friction slide table; (6) bottom grip plate; (7) top grip plate; (8) specimen.

grips are suppressed by the system, a bending moment builds up when a horizontal force is applied to the specimen. Thus, two parallel uniaxial load cells (parts 2 and 3) are used to measure the vertical force.

The experiments are performed in a combined load- and displacement-controlled mode. Unlike the simple shear test in which the vertical displacement must be kept constant ($u_V = 0$), the pure shear experiments must be performed under force control in order to keep the vertical force zero, that is, $F_V = 0$ while $u_V \neq 0$ (Figure 5 (a)). Using the hydraulic system control software (Fast Track, Instron, Canton, MA), the sum of the two vertical force measurements is defined as single virtual channel and consequently used to control the vertical actuator such that $F_V = 0$. The horizontal actuator has been controlled by the built-in LVDT for the horizontal position measurement.

The sandwich specimens are $l = 80mm$ long (along the W-direction) and $C =$ 17 mm thick (in the T-direction) which corresponds to a length-to-thickness ratio of about 4.7. The specimen width in the L-direction is $w = 50$ mm. Based on measurements of the horizontal force and the horizontal and vertical displacements, we define the engineering shear stress as

$$S_{TW} = \frac{F_H}{wl}, \tag{2}$$

and the engineering shear and normal strains as

$$E_{TW} = \frac{u_H}{C} \quad \text{and} \quad E_{TT} = \frac{u_V}{C}, \tag{3}$$

respectively. All tests have been carried out at a constant horizontal velocity of 3 mm/min.

3.2. ***The core response to pure shear loading.*** The measured shear stress versus shear strain curves are shown in Figure 6 (a). Selected photographs taken throughout the experiment are depicted in Figure 7. The material response is linear up to a shear stress of about 0.5 MPa. Beyond this point, the slope of this curve decreases slightly as shear buckles become visible within the honeycomb microstructure (Figure 7 (b)). The shear stress-strain curve reaches its maximum at about $\tau_{max} = 0.7$ MPa (point of shear failure) before it approaches a considerably lower plateau stress level of about 0.45 MPa. The stress level drops further as the honeycomb cell walls fracture at a shear strain of about 0.9. It is noteworthy that the high frequency fluctuations in the stress-strain curve are due to the immediate response of the two-actuator control system as macroscopic softening occurs throughout the combined vertical force/ horizontal displacement controlled experiments.

Both the photographs and the plot of the normal strain history (Figure 6 (b)) show the shear-induced compaction of the honeycomb material. In order to meet

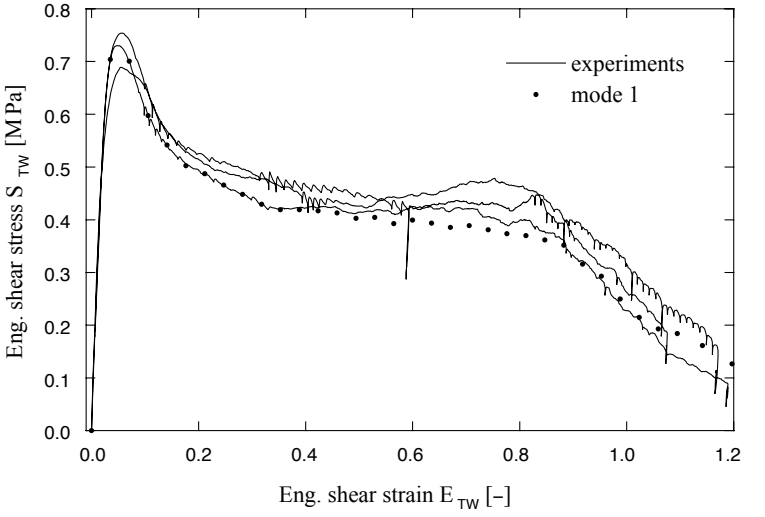

(a)

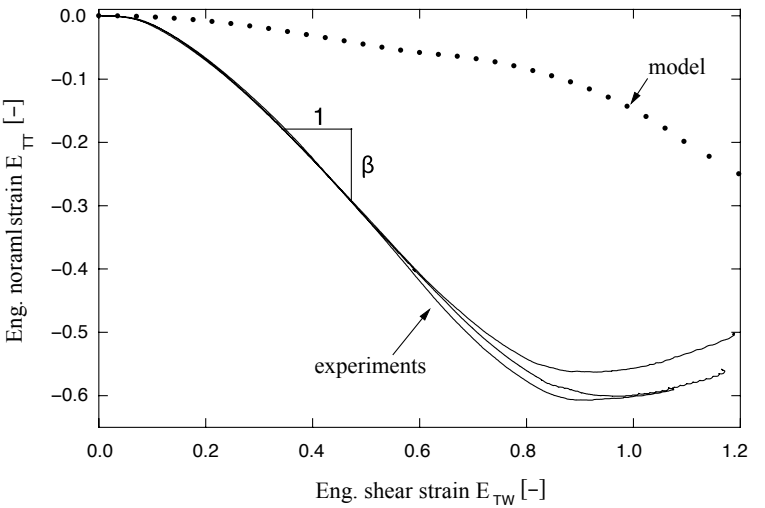

(b)

Figure 6. Experiments and model calibration for pure shear: (a) engineering stress-strain curve; (b) shear-induced compaction. The model assumptions of associated plastic flow and zero plastic Poisson ratios are suitable for predicting the behavior at small strains, whereas nonassociated flow dominates for large shear strains.

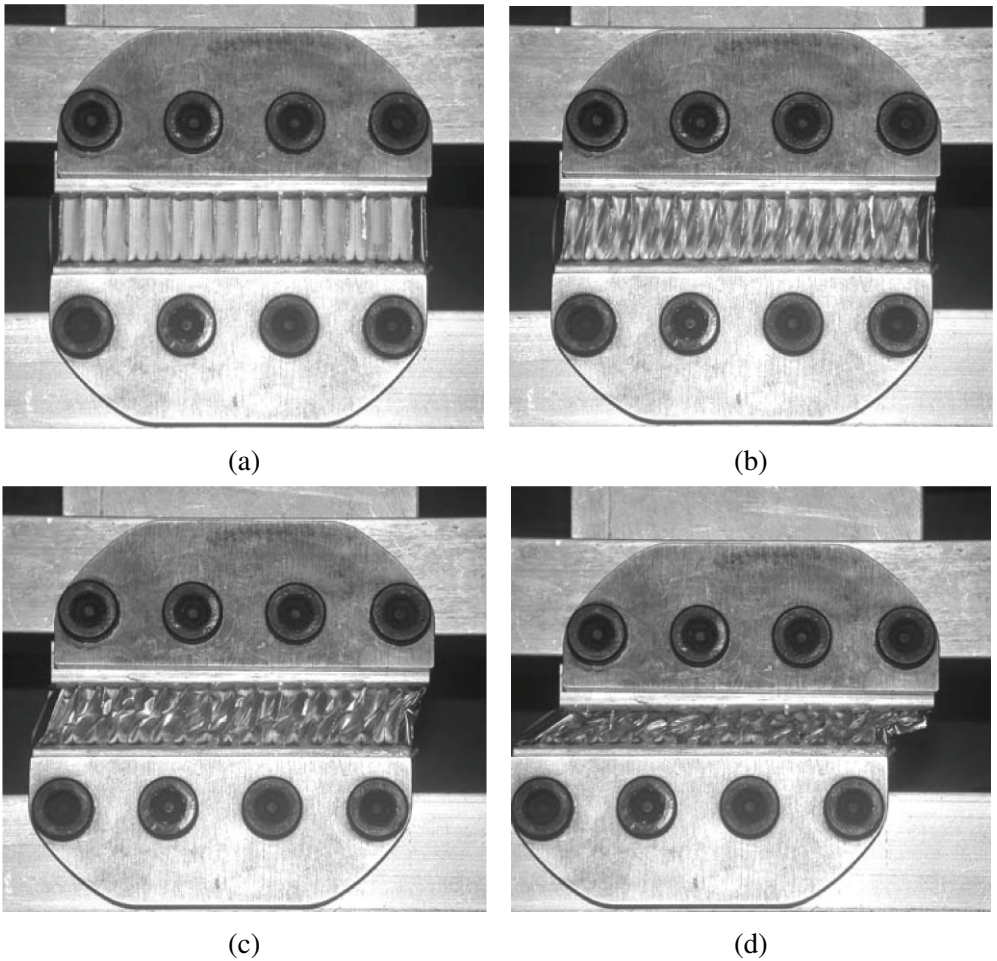

Figure 7. Deformed configuration of the honeycomb core specimen throughout pure shear testing at various stages of deformation: (a) $E_{TW} = 0$, (b) $E_{TW} = 0.04$, (c) $E_{TW} = 0.21$, and (d) $E_{TW} = 0.58$.

the pure shear condition of $F_V = 0$, the sandwich specimen reduces its thickness, that is, the strain increment is $dE_{TT} < 0$. The shear-induced normal strains are very small for shear strains below 0.1. However, for shear strains above 0.1, the deformation in the T-direction becomes considerable. For large shear strains, the shear compaction factor is approximately constant,

$$\frac{dE_{TT}}{dE_{TW}} \cong -\beta, \tag{4}$$

where $\beta = 0.88$ for the current experiment (Figure 6 (b)).

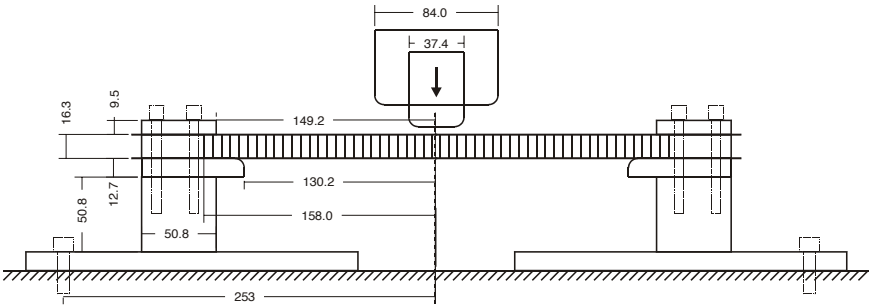

(a)

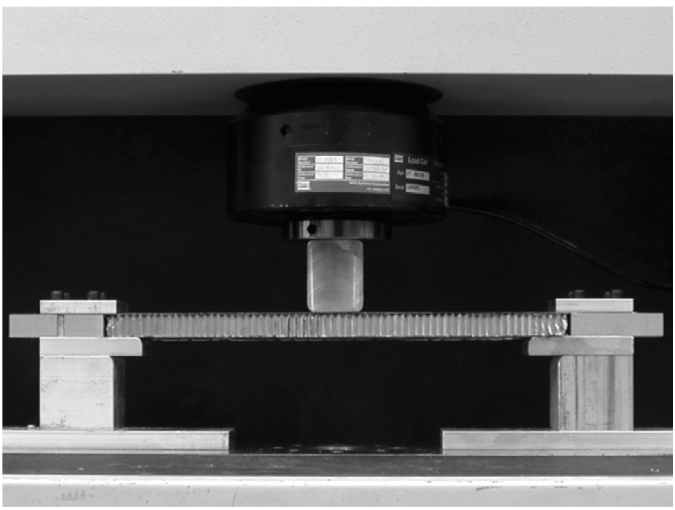

(b)

Figure 8. (a) Schematic of the experimental setup of the punch test. All dimensions are given in mm. (b) Photograph of the fixture with the custom made honeycomb sandwich beam. The width of all tested sandwich beams was W=45.7 mm.

4. Punching experiments

4.1. ***Experimental setup.*** Figure 8 shows a photograph and schematic of the experimental setup. A special fixture has been designed to clamp the $W = 45.7$ mm wide sandwich beams. The maximum unsupported length of the sandwich beam is $L = 260.4$ mm. The 15.9 mm thick sandwich core of the 16.3 mm thick sandwich plate has been replaced by equally thick aluminum blocks in the clamping

area. Four M6-12.8 cap screws are used at each end of the specimen to apply the clamping pressure to the 9.5 mm thick aluminum plates (Figure 8 (a)). The entire fixture is mounted on the base table of a screw-driven universal testing machine. Two punches of different sizes are used: a small punch of width 37.4 mm (Figure 8) and a large punch of 84 mm width. All corner radii of the punch and fixture are 6.35 mm. The punches are connected to a 200kN load cell which measures the vertical reaction force, P, exerted to the punch. Since the sandwich beam structure is considerably more compliant than the testing frame and fixture, we assume that the cross-head and punch displacement, u_p, are identical. The experiments are carried out at constant cross-head velocity of 5 mm/min.

4.2. ***The sandwich response to quasistatic punch indentation.*** A series of photographs is shown in the left column of Figures 9 and 10 for the small and large punch experiments, respectively. The measured force-displacement curves are shown by solid lines in Figure 11 (a). Figure 11 (b) shows the same curves again with an abscissa axis shift of 10 mm for punch displacements smaller than the sandwich beam thickness, $u_p \leq 16.3$ mm. Both force-displacement curves exhibit a peak at about $P_s \cong 1150$ N followed by a drop of about 200 N. Subsequently, the force-displacement curve increases in a nonlinear manner before it becomes approximately linear for punch displacements that are considerably larger than the sandwich beam thickness. In this regime, face sheet stretching dominates the response of the sandwich beam; the force-displacement curve for the small punch has a slope of 132 N/mm, whereas the slope of the large punch curve is about 157 N/mm. It may be seen from the photographs taken at a cross-head position of about 3 mm (Figures 9 (a) and 10 (a)) that the initial nonlinear response of the sandwich beam is dominated by the shear deformation of the core material. As for the pure shear tests (Figure 7), shear buckles become visible in the honeycomb cell walls of the unsupported beam cross-section. It appears that the initial peak of the force-displacement curve is due to the shear failure of the core material. Recall that the shear stress-strain curves exhibited a similar peak. This argument may be supported by the observation that this peak is approximately the same irrespective of the punch width. Denoting the maximum shear resistance of the core material by τ_{max}, the punch force P_s associated with the initial shear failure of the sandwich beam can be obtained using a simple beam analysis:

$$P_s = 2\tau_{max} C W. \tag{5}$$

According to the pure shear tests, we have

$$\tau_{max} = 0.75 \text{ MPa},$$

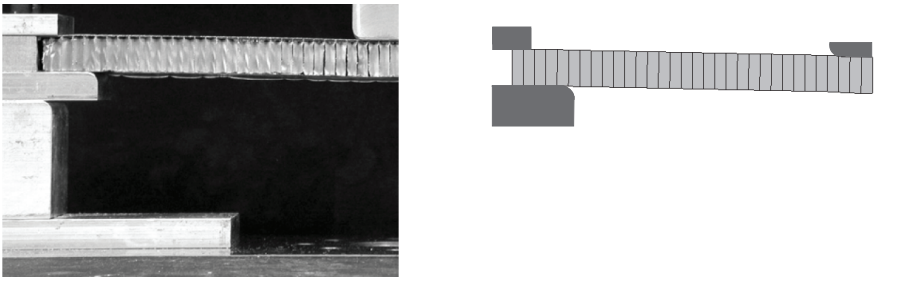

(a) $u_P = 3.1\,\text{mm}$

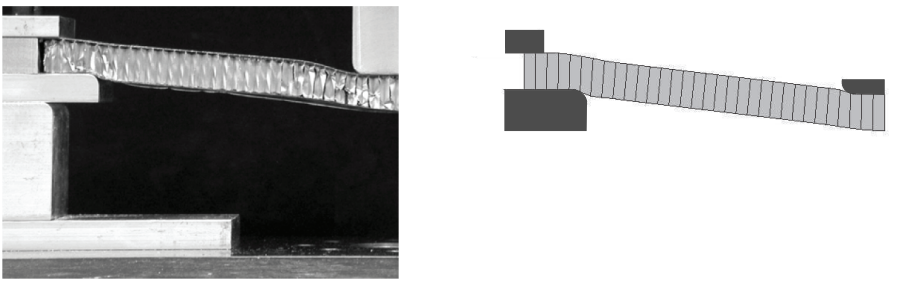

(b) $u_P = 17.5\,\text{mm}$

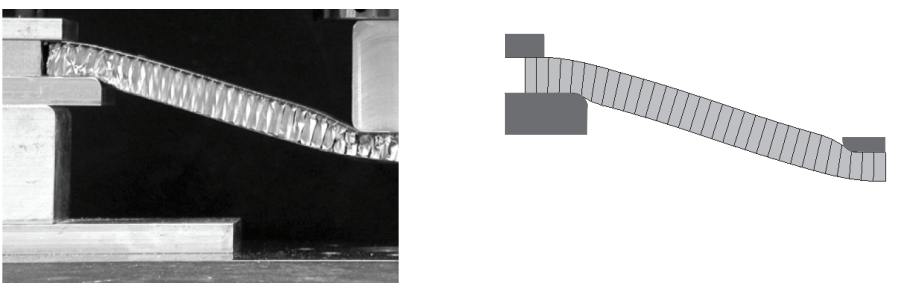

(c) $u_P = 41.5\,\text{mm}$

Figure 9. Comparison of the experiments and simulations for the small punch (width=37.4 mm). The left column shows the photographs taken throughout the experiment and the right column depicts the corresponding deformed configurations of the sandwich beams as predicted from simulations.

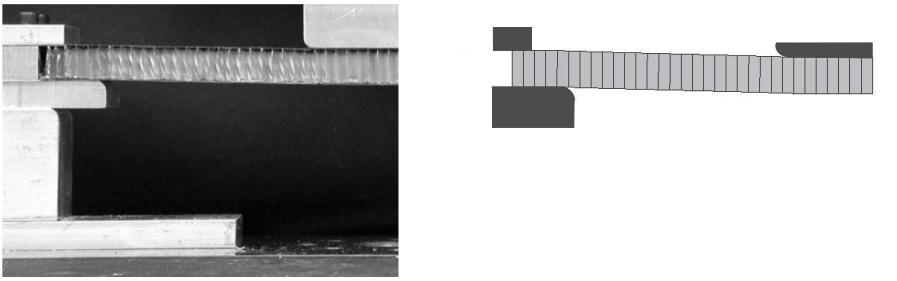

(a) $u_P = 2.8\,\text{mm}$

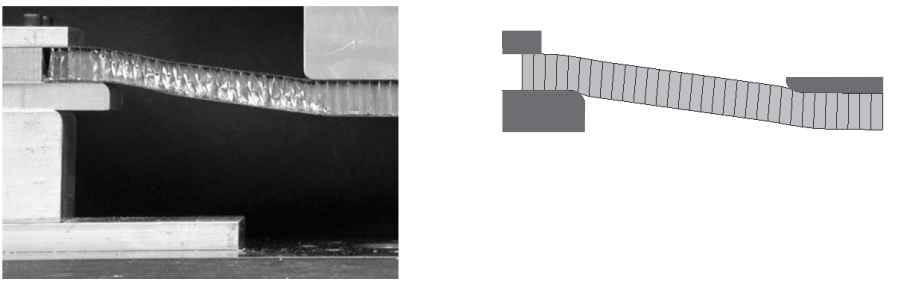

(b) $u_P = 16.5\,\text{mm}$

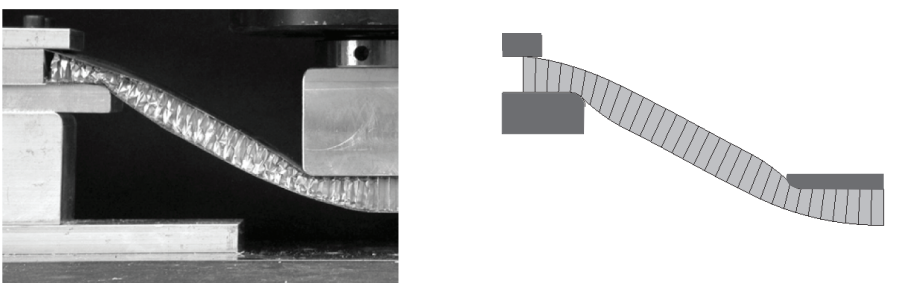

(c) $u_P = 58.5\,\text{mm}$

Figure 10. Comparison of the experiments and simulations for the large punch. The left column show the photographs taken throughout experiments while the right column depicts the corresponding configurations as predicted from simulations.

resulting in $P_s = 1090\,\mathrm{N}$, which is in a good agreement with our experimental observations. After the shear failure of the core material, the small punch locally indents the sandwich beam (Figure 9 (b)). Local indentation is also observed in the vicinity of the clamped beam boundary. The pressure under the wide punch is smaller and it can be seen from Figure 10 (b) that the core material underneath the punch remains intact for displacements smaller than 16.5 mm. For large deflections, the shear deformation of the core material increases only slightly. Instead, both the top and bottom face sheets are substantially stretched which leads to a stiffening response. Since the distance between the punch and the support is smaller for the wide punch, the stretching of the face sheet is more intense for the same punch displacement, which explains the larger slope of the large punch force-displacement curve at large deflections.

5. Modeling

5.1. ***Constitutive modeling of the honeycomb core layer.*** A special version of the constitutive model proposed by Xue et al. [2005] for plastically compressible orthotropic materials is employed in this study to represent the core layer. Denoting the six independent components of the Cauchy stress tensor by the vector

$$\boldsymbol{\sigma} = (\sigma_1, \sigma_2, \sigma_3, \sigma_4, \sigma_5, \sigma_6)^T \equiv (\sigma_{TT}, \sigma_{WW}, \sigma_{LL}, \sigma_{TL}, \sigma_{WL}, \sigma_{TW})^T$$

(where the initial coordinate frame is aligned with the orthotropy axes of the honeycomb core), the characteristic ellipsoidal yield surface is written in the form

$$f(\boldsymbol{\sigma}, \boldsymbol{s}) = \sum_{i=1}^{6} \left(\frac{\sigma_i}{s_i}\right)^2 - 1 = 0, \tag{6}$$

where $\boldsymbol{s}$ denotes the corresponding vector of deformation resistances. (In the proposed constitutive model, an ellipsoidal yield surface is invoked that generalizes Hill's surface for orthotropic plastically incompressible materials. The general formulation of this constitutive model is able to incorporate nonconstant plastic Poisson ratios in the axes of anisotropy—that is, the plastic Poisson ratios can be a function of plastic strains. However, for the current study the plastic deformation of the core is approximated by taking all plastic Poisson ratios as zero.) Within the framework of associated incremental plasticity, strain hardening/softening is taken into account by the evolution of the deformation resistance. More specifically, we take the independent hardening/softening approach where the evolution of individual components of the vector of deformation resistance, s_i, depends only on the corresponding true plastic strain components, ε_i^P, where

$$\boldsymbol{\varepsilon^P} = (\varepsilon_1^P, \varepsilon_2^P, \varepsilon_3^P, \varepsilon_4^P, \varepsilon_5^P, \varepsilon_6^P)^T \equiv (\varepsilon_{TT}^P, \varepsilon_{WW}^P, \varepsilon_{LL}^P, 2\varepsilon_{TL}^P, 2\varepsilon_{WL}^P, 2\varepsilon_{TW}^P)^T.$$

In other words, we have $s_i = s_i(\varepsilon_i^P)$.

In the present punching experiment, the core material is predominantly loaded in the TW-plane. Therefore, the strain hardening/softening functions for uniaxial loading along the T-axis, $s_{TT}(\varepsilon_{TT}^P)$, and for shear loading in the TW-plane, $s_{TW}(2\varepsilon_{TW}^P)$, must be calibrated with fidelity. The in-plane functions $s_{WW}(\varepsilon_{WW}^P)$ and $s_{LL}(\varepsilon_{LL}^P)$ are also important from a theoretical point of view, but due to the strong orthotropy of the hexagonal aluminum honeycomb, the contribution of the in-plane stresses to the overall response of the sandwich beam may be neglected. Table 1 shows a summary of the elastic constants as evaluated for the 1.8% relative density hexagonal aluminum honeycomb. Recall that these have been estimated for all loading directions according to the analytical expressions given in the textbook by Gibson and Ashby [1997].

As far as the determination of $s_{TT}(\varepsilon_{TT}^P)$ and $s_{TW}(2\varepsilon_{TW}^P)$ is concerned, it is noteworthy that the cell walls of the aluminum honeycomb buckle elastically before yielding plastically. It is reasonable to assume that macroscopic yield initiates as the stress level reaches the characteristic initial peak of the stress-strain curves [Mohr and Doyoyo 2004a]. Upon evaluation of the experimental results, we obtain the initial yield stresses $s_{TT}(\varepsilon_{TT}^P = 0) = 1.95$ MPa and $s_{TW}(2\varepsilon_{TW}^P = 0) = 0.69$ MPa for crushing and shearing, respectively. The experimental curves from Figures 4 and 6 (a) have been converted into the functions $s_{TT}(\varepsilon_{TT}^P)$ and $s_{TW}(\varepsilon_{TW}^P)$ by assuming nonevolving elastic moduli, that is,

$$\varepsilon_{TT}^P = \varepsilon_{TT} - \frac{s_{TT}}{E_{TT}} \quad \text{and} \quad 2\varepsilon_{TW}^P \cong E_{TW} - \frac{s_{TW}}{G_{TW}}. \tag{7}$$

The approximation sign is used in the latter equation since it does not account for the rotation of the principal axes of the stretch tensor in the shear test. The validity of this approximation is examined by simulating the pure shear test using the constitutive model. The comparison of the solid and dotted curves in Figure 6 (a) confirms the validity of this simplification. Note from Figure 6 (b) that the shear-induced compaction of the core material may not be captured by the present model. The model response to uniaxial loading along the T-direction is identical to the experimental curve shown in Figure 4.

5.2. ***Modeling of the wide sandwich beam.*** In the development of the macroscopic constitutive model, it is assumed by the definition of the macroscopic strains (see Equation (3)) that the displacement field is linear along the core thickness (T-direction). Therefore, the core is discretized using only one row of elements with linear shape functions along the thickness direction. Using a single linear element along the thickness implies the assumption that initially flat cross-sections remain flat throughout bending. However, it is important to note that commonly used numerical integration schemes may not be accurate enough to capture substantial

variations in the stress field along the thickness direction. Therefore, the present modeling approach is only recommended when the contribution of the core material to the overall bending resistance of the sandwich sheet is negligible.

In the case of sandwich structures with curved mid-planes, the element edges must be aligned with the thickness direction of the core layer. The number of elements along the sandwich mid-axis on the other hand shall be chosen such that the continuum boundary value problem is solved with satisfactory accuracy. In the constitutive model, the honeycomb core is considered as a so-called simple material body. The model calibration experiments are almost stress gradient free (for example, $\delta\sigma_{TT}/\delta X_W \cong 0$). However, from a physical point of view, it may be expected that large macroscopic stress gradients affect the material response due to the discreteness of the cellular core structure along W- and L-directions, which indicates the need for enriched Cosserat type of theories [Onck 2002]. Therefore, it is emphasized that the present model predictions may not be satisfactory in regions where the continuum solution indicates large gradients in either the stress or strain field.

Another consideration in modeling sandwich structures as a three layer shell-solid-shell assembly is the continuity of the displacement field which is enforced at the common nodes of the face sheets and the core layer. These nodes are positioned in the face sheet mid-plane whereas in reality, the displacement continuity is enforced at the contact surfaces between the core and face sheets. There are basically three modeling options: (1) using the exact core thickness while the face sheet separation in the model is smaller than in reality; (2) using the exact face sheet separation, while artificially increasing the core thickness; (3) programming a user-defined sandwich element with enhanced kinematics to take this effect into account. With respect to sandwich sheet failure, two key mechanical quantities depend directly on either the face sheet separation $C + t_f$ or the core height C: the overall plastic bending moment, M_{pl}, and the shear strength, F_s, may be respectively approximated as

$$M_{pl} = \sigma_f t_f (C + t_f) W \quad \text{and} \quad F_s = \tau_{max} C W. \tag{8}$$

Both quantities show a linear dependence which demonstrates that the error associated with the model assumptions (1) or (2) is small if $t_f/C \ll 1$. In the present problem, we have $t_f/C \cong 1\%$.

5.3. ***Modeling of the punching experiments.*** The punching of the wide beam is treated as a two-dimensional problem. We hypothesized that the deformation of the core material in the L-direction can be neglected. Consequently, four-node plane strain elements with reduced integration (element CPE4R in [Abaqus 2005]) are employed for the honeycomb core layer. The thin face sheets are discretized by a

two-node Timoshenko beam element (element B21 in [Abaqus 2005]). Each beam element has a rectangular cross section of height $t_f = 0.2$ mm and a unit width.

Only one half of the whole system is analyzed due to the symmetry of the structure and the loading conditions. Symmetry boundary conditions are applied to the center cross section of the wide beam. The horizontal displacements of all nodes along each edge of the sandwich beam are restricted to be zero. The punch and all support structures are modeled by rigid elements with frictionless contact between each pair of contact surfaces. The support structures are fixed, while the punch loads is applied at a constant vertical velocity. The calculations are performed using ABAQUS/explicit. In comparison with the standard implicit algorithm, the explicit scheme is chosen due to its advantages in handling sliding contact conditions and the overall softening behavior of the honeycomb core due to the presence of stabilizing inertia. Oscillations due to this dynamic stabilization have been found to be negligibly small as compared to the static force level.

Note that the propagation velocities of uniaxial waves in the sandwich material are about 5000 m/s for both longitudinal waves along the face sheets and waves through the thickness of the honeycomb material. In order to ensure quasistatic loading conditions, the characteristic durations for elastic waves traveling from the punch center to the clamping support of the sandwich plate (about 30 μs) and through the thickness of the sandwich sheet (about 3 μs) must be several orders of magnitudes smaller than the total duration of the punching simulations. Here, the numerical simulations are carried out for a constant punch velocity of 1 mm/s, which corresponds to a total duration of 60 s. Regarding the computational efficiency of the simulations, it is worth noting that the stable time step is mostly governed by the wave propagation in the face sheets. Stability of the explicit time integration scheme requires the time step to be smaller than the duration of a wave propagating between two opposite sides of the element, that is, $\Delta t < l_e/c$ (in a nonrigorous sense), where l_e and c denote the characteristic element side length and wave speed, respectively. According to the continuum model of the core, the in-plane wave propagation speed in the present honeycomb core is extremely small (about 100 times slower than the out-of-plane wave). Thus, if the sandwich core height is larger than the element length along the sandwich mid-axis, the elements of the face sheets will control the critical time step.

5.4. ***Comparison of the results from experiments and simulations.*** The punching simulations are carried out for three different mesh densities along the sandwich mid-axis by employing 32, 64 and 128 elements along the sandwich mid-axis. No remarkable difference is observed between the force-displacement curves obtained using the three mesh densities. Even coarser meshes may be suitable for modeling the sandwich sheet, but the contact algorithm is likely to fail when the model no

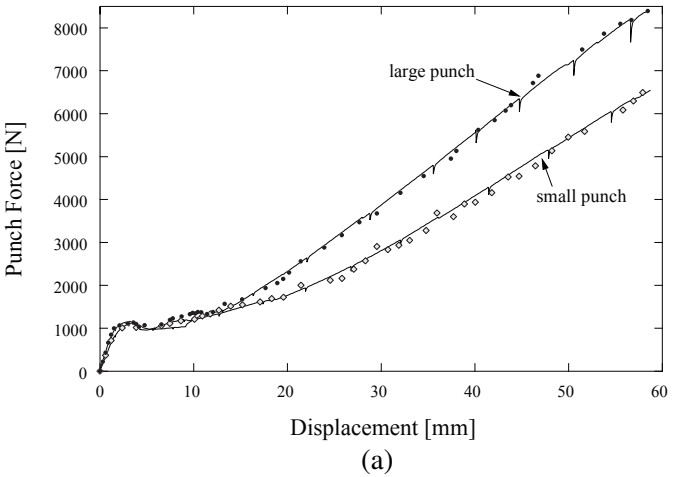

(a)

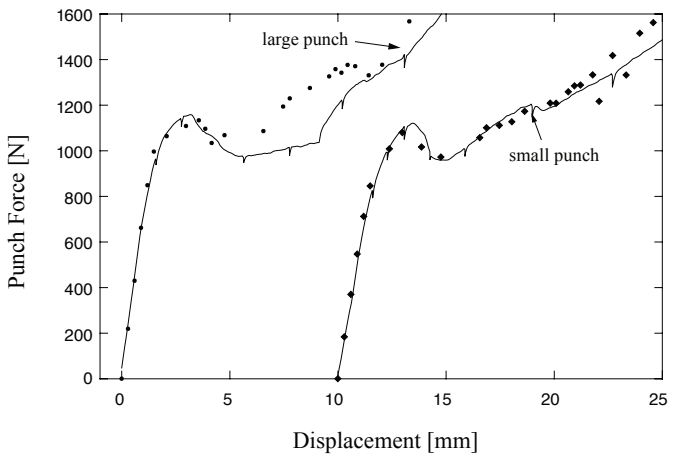

(b)

Figure 11. Comparison of the experimental results of the honeycomb core sandwich beam subject to quasistatic punch indentation (solid line) with the predictions from the numerical simulations based on the continuum modeling of the core. (a) Punch force-displacement curve for displacements of up to 60 mm; (b) detail of that curve for small displacements ($u_P \leq C = 16.3$ mm). The origin of the curve for the small punch has been shifted by 10 mm.

longer captures important details of the face sheet deformation near the rigid punch and support structures. The direct comparison of the experimental and computational force-displacement curves is shown in Figure 11 (a). The experimental and numerical curves are considerably close for small and large displacements. Both the initial slope in the elastic regime and the following peak load are accurately predicted by the numerical model (Figure 11 (b)). Similarly, excellent agreement is observed for large displacements, where the sandwich response is mostly governed by the stretching of the face sheets.

In order to compare the predicted displacement fields, we plotted the deformed *FE*-meshes next to selected photographs taken during the experiments at the same vertical displacements. Again, we observe good overall agreement of experiments and simulations. In particular, the development of two separate regions of shear-dominated and compression-dominated core deformation seems to be captured in close analogy with the experiment.

6. Discussion

The main result of this study is that this rather simple computational model can predict the response of a wide sandwich subject to punch loading with considerable fidelity. Due to the high orthotropy of the core material and the strength disparity between the core and face sheets, the sandwich core layer could be successfully modeled with only one element over the thickness. It is important to calibrate the plastic part of the core constitutive model from both uniaxial and pure shear test data. Recall that the punch force-displacement curve is governed by the shear behavior of the core material at the early stage of deformation.

Recent findings in cellular plasticity indicate that modeling of the fold propagation in honeycombs may require enriched constitutive theories [Mohr and Doyoyo 2003]. At the microscale, the through-the-thickness response of honeycomb sandwich sheets is characterized by the localization of deformation which may result in mesh dependency. This challenge has been successfully overcome by the present modeling approach through the use of only one element through the core thickness. This approach is suitable in sandwich applications when the stress and strain gradients along the in-plane directions are small. In the present study, this requirement is violated near the corners of the punch, but the comparison of experiments and simulations reveals that such local violations are still acceptable in a larger system. Another important outcome of preceding experimental studies on aluminum honeycombs is the observation of nonassociated plastic flow at large strains [Mohr and Doyoyo 2004c; Hong et al. 2006]. The present model assumes associated plastic flow which appears to be a suitable assumption for small deformations (Figure 6 (b)). Initially, the measured normal strains are almost zero,

which corresponds to associated flow with respect to the ellipsoidal yield surface, while for large shear strains substantial normal strain arises as described by the finite-strain constitutive model of Mohr and Doyoyo [2004c]. In the present experiments, the shear strains do not exceed 0.2, which explains the applicability of the present model. Furthermore, there is no difference between the nonassociated and associated flow models for uniaxial compression within the large deformation zone directly underneath the punch.

7. Conclusion

A detailed study has been performed to evaluate the predictive capabilities of a newly developed constitutive model for sandwich core materials [Xue et al. 2005]. A new pure shear test for cellular solids has been presented and used to obtain the material model parameters for a thin-walled hexagonal aluminum honeycomb. All-metal sandwich beams have been constructed by bonding a 16 mm thick slice of this honeycomb to a pair of 0.2 mm thick stainless steel face sheets. Using a special clamping fixture, these wide sandwich beams have been loaded under quasistatic loading conditions with punches of different widths. The response of sandwich beams to punch loading has been analyzed in detail and predicted from finite element simulations by employing a continuum constitutive model for the sandwich core. The computational model exploits a single linear solid element for the core material in conjunction with two beam elements for the face sheets, which leads to a significant reduction of the computational time as compared to detailed modeling of the cellular core structure. The comparison of the numerical and experimental results demonstrates the good predictive capabilities of this simple computational model for studying the structural performance of metal sandwich beams.

Acknowledgments

The authors would like to thank Professors T. Wierzbicki and J.W. Hutchinson for valuable discussions. Mark Shorey from Instron (Canton, MA) is thanked for his help in designing the two-actuator testing machine. Financial support through ONR grants N00014-02-01-0700 and GG10376-114934 is gratefully acknowledged.

References

[Abaqus 2005] Abaqus, *Abaqus version 6.5 reference manuals*, Providence, R.I: Abaqus Inc., 2005.

[Deshpande and Fleck 2000] V. S. Deshpande and N. A. Fleck, "Isotropic constitutive models for metallic foams", *J. Mech. Phys. Solids* **48**:6-7 (2000), 1253–1283.

[Doyoyo and Mohr 2003] M. Doyoyo and D. Mohr, "Microstructural response of aluminum honeycomb to combined out-of-plane loading", *Mech. Mater.* **35**:9 (2003), 865–876.

[ESI 1999] ESI, *PamCrash reference manuals*, France: Engineering Systems International, 1999.

[Gibson and Ashby 1997] L. J. Gibson and M. F. Ashby, *Cellular solids: structure and properties*, 2nd ed., Cambridge University Press, Cambridge, 1997.

[Hong et al. 2006] S.-T. Hong, J. Pan, T. Tyan, and P. Prasad, "Quasi-static crush behavior of aluminum honeycomb specimens under compression dominant combined loads", *Int. J. Plast.* **22**:1 (2006), 73–109.

[Hutchinson and Xue 2005] J. W. Hutchinson and Z. Xue, "Metal sandwich plates optimized for pressure impulses", *Int. J. Mech. Sci.* **47**:4-5 (2005), 545–569.

[LSTC 2000] LSTC, *LS-DYNA reference manuals*, Livermore, CA: Livermore Software Technology Corporation, 2000.

[Mohr 2005] D. Mohr, "Mechanism-based multi-surface plasticity model for ideal truss lattice materials", *Int. J. Solids Struct.* **42**:11-12 (2005), 3235–3260.

[Mohr and Doyoyo 2003] D. Mohr and M. Doyoyo, "Nucleation and propagation of plastic collapse bands in aluminum honeycomb", *J. Appl. Phys.* **94**:4 (2003), 2262–2270.

[Mohr and Doyoyo 2004a] D. Mohr and M. Doyoyo, "Deformation-induced folding systems in thin-walled monolithic hexagonal metallic honeycomb", *Int. J. Solids Struct.* **41**:11-12 (2004), 3353–3377.

[Mohr and Doyoyo 2004b] D. Mohr and M. Doyoyo, "Experimental investigation on the plasticity of hexagonal aluminum honeycomb under multiaxial loading", *J. Appl. Mech. (Trans. ASME)* **71**:3 (2004), 375–385.

[Mohr and Doyoyo 2004c] D. Mohr and M. Doyoyo, "Large plastic deformation of metallic honeycomb: orthotropic rate-independent constitutive model", *Int. J. Solids Struct.* **41**:16–17 (2004), 4435–4456.

[Onck 2002] P. Onck, "Cosserat modeling of cellular solids", *C. R. Mécanique* **330**:11 (2002), 717–722.

[Ponte Castañeda and Suquet 1998] P. Ponte Castañeda and P. Suquet, "Nonlinear composites", *Adv. Appl. Mech.* **34** (1998), 171–302.

[Rabczuk et al. 2004] T. Rabczuk, J. Y. Kim, E. Samaniego, and T. Belytschko, "Homogenization of sandwich structures", *Int. J. Numer. Methods Eng.* **61**:7 (2004), 1009–1027.

[Vaziri et al. 2006] A. Vaziri, Z. Xue, and J. W. Hutchinson, "Metal sandwich plates with polymer foam-filled cores", *Journal of Mechanics of Materials and Structures* **1**:1 (2006), 97–127.

[Wang and McDowell 2005] A. J. Wang and D. L. McDowell, "Yield surfaces of various periodic metal honeycombs at intermediate relative density", *Int. J. Plast.* **21**:2 (2005), 285–320.

[Xue and Hutchinson 2004a] Z. Xue and J. W. Hutchinson, "A comparative study of impulse-resistant metal sandwich plates", *Int. J. Impact Eng.* **30**:10 (2004), 1283–1305.

[Xue and Hutchinson 2004b] Z. Xue and J. W. Hutchinson, "Constitutive model for quasi-static deformation of metallic sandwich cores", *Int. J. Numer. Methods Eng.* **61**:13 (2004), 2205–2238.

[Xue et al. 2005] Z. Xue, A. Vaziri, and J. W. Hutchinson, "Non-uniform hardening constitutive model for compressible orthotropic materials with application to sandwich plate cores", *Comput. Model. Eng. Sci.* **10**:1 (2005), 79–96.

[Zok et al. 2005] F. W. Zok, H. Rathbun, M. He, E. Ferri, C. Mercer, R. M. McMeeking, and A. G. Evans, "Structural performance of metallic sandwich panels with square honeycomb cores", *Philos. Mag.* **85**:26-27 (2005), 3207–3234.

Received 16 Dec 2005. Revised 19 Jan 2006.

DIRK MOHR: mohr@mit.edu
Impact and Crashworthiness Laboratory, Massachusetts Institute of Technology, Cambridge, MA, United States
http://web.mit.edu/mohr/www

ZHENYU XUE: xue@deas.harvard.edu
Division of Engineering and Applied Sciences, Harvard University, Cambridge, MA, United States

ASHKAN VAZIRI: avaziri@deas.harvard.edu
Division of Engineering and Applied Sciences, Harvard University, Cambridge, MA, United States
www.deas.harvard.edu/~avaziri

SUBMISSION GUIDELINES

ORIGINALITY

Authors may submit manuscripts in PDF format on-line. Submission of a manuscript acknowledges that the manuscript is *original and has neither previously, nor simultaneously, in whole or in part, been submitted elsewhere.* Information regarding the preparation of manuscripts is provided below. Correspondence by email is requested for convenience and speed. For further information, write to:

Marie-Louise Steele
Division of Mechanics and Computation
Durand Building, Room 262
Stanford University
Stanford CA 94305

LANGUAGE

Manuscripts must be in English. A brief abstract of about 150 words or less must be included. The abstract should be self-contained and not make any reference to the bibliography. Also required are keywords and subject classification for the article, and, for each author, postal address, affiliation (if appropriate), and email address if available. A home-page URL is optional.

FORMAT

Authors are encouraged to use LaTeX and the standard article class, but submissions in other varieties of TeX, and, exceptionally in other formats, are acceptable. Electronic submissions are strongly encouraged in PDF format only; after the refereeing process we will ask you to submit all source material.

REFERENCES

Bibliographical references should be listed alphabetically at the end of the paper and include the title of the article. All references in the bibliography should be cited in the text. The use of BibTeX is preferred but not required. Tags will be converted to the house format (see a current issue for examples), however, in the manuscript, the citation should be by first author's last name and year of publication, e.g. "as shown by Kramer, et al. (1994)". Links will be provided to all literature with known web locations and authors are encoraged to provide their own links on top of the ones provided by the editorial process.

FIGURES

Figures prepared electronically should be submitted in Encapsulated PostScript (EPS) or in a form that can be converted to EPS, such as GnuPlot, Maple, or Mathematica. Many drawing tools such as Adobe Illustrator and Aldus FreeHand can produce EPS output. Figures containing bitmaps should be generated at the highest possible resolution. If there is doubt whether a particular figure is in an acceptable format, the authors should check with production by sending an email to:

production@mathscipub.org

Each figure should be captioned and numbered so that it can float. Small figures occupying no more than three lines of vertical space can be kept in the text ("the curve looks like this:"). It is acceptable to submit a manuscript with all figures at the end, if their placement is specified in the text by means of comments such as "Place Figure 1 here". The same considerations apply to tables.

WHITE SPACE

Forced line breaks or page breaks should not be inserted in the document. There is no point in your trying to optimize line and page breaks in the original manuscript. The manuscript will be reformatted to use the journal's preferred fonts and layout.

PROOFS

Page proofs will be made available to authors (or to the designated corresponding author) at a web site in PDF format. Failure to acknowledge the receipt of proofs or to return corrections within the requested deadline may cause publication to be postponed.

JOURNAL OF
MECHANICS OF MATERIALS AND STRUCTURES

Volume 1 No. 3 March 2006